



THE UNIVERSITY OF QUEENSLAND  
AUSTRALIA

# **Investigation of All-fibre Methane Sensors for Underground Coal Mines**

Mohammad Amanzadeh

B.Eng. and M.Eng. (Electrical Engineering)

*A thesis submitted for the degree of Master of Philosophy at*

*The University of Queensland in 2014*

School of Mechanical & Mining Engineering

## **Abstract**

Methane gas is a potential hazard in underground coal mines, which may cause incidents resulting in injuries and fatalities. Methane gas naturally occurs in coal seams during its formation from organic materials. Rich methane is released into a mine environment during the extraction process and from coal seams in roadways. Methane is extremely flammable and may provoke explosions in the presence of oxygen and an ignition source. Moreover, with the introduction of the new greenhouse gas emission legislation, it has become crucial to accurately monitor and measure emissions from underground coal mining operations. Underground coal mines require accurate and real-time measurement of methane concentrations at various locations to ensure the safety of both the miners and the operation.

Different sensing systems have been employed to detect gas concentrations in the mining industry; however, there are still fatalities occurring due to the failure of sensors or lack of sufficient data. The systems currently in use suffer from cross sensitivity, high maintenance costs, the requirement for trained personnel to run the measurement units, and a lack of accuracy in real time data values. Accordingly, there is a pressing need for the development of a distributed, real time, low cost, sensing system; and fibre optic technology holds great promise towards this end.

The main aim of this thesis is to develop and test various fibre-optic based sensors: (i) tapered single mode fibres (SMFs), (ii) drilled SMFs; and (iii) drilled hollow core fibres (HCFs). These sensors are known as all-fibre sensors. For the first type sensor, SMFs are tapered by stretching them over an oscillating flame to different lengths and oscillation functions. For the second type sensor, SMFs are drilled by applying a focused ion beam (FIB) to remove material and contour the appropriate dimensions on the interior surface of fibre. For the third type sensor, HCFs are drilled using an FIB in a similar fashion to that used in the SMF drilling.

An experimental gas concentration apparatus was designed and developed to test the all-fibre sensor heads using various methane concentrations. The sensor heads have been tested and compared to conventional open path gas cells as candidates for remote methane sensors in underground coal mines. Wavelength modulation spectroscopy (WMS) and direct absorption

spectroscopy (DAS) at 1665.961 nm absorption line centre of methane have been conducted by a DFB laser source for all sensor heads.

Both the open path gas cells and the drilled HCFs proved to be able to detect methane with the required sensitivity, accuracy, and response time demonstrating that they both have the potential for being developed into commercial sensors. The open path gas cell method demonstrated greater sensitivity and is more robust than the drilled HCF sensor. The drilled HCF also has excellent accuracy but has a more complex structure; light coupling and reflection between HCF and SMF splice point are still an issue.

As both the open path gas cells and HCF sensors were shown to have sufficient sensitivity, accuracy, and response times, they may well lend themselves to being used as components of underground mine gas sensing systems. The goal of this study is to investigate novel, previously untested, experimental sensor head designs for underground coal mine applications. The drilled HCFs seem to have a great potential for this application since they only need a micro-scale volume of sample gas for a real time measurement and could potentially offer as little as a few seconds response time. In addition, the drilled HCF sensor heads are more amenable to forming part of a sensing network consisting of many sensor heads connected via SMFs throughout a mine and even in inaccessible areas.

## **Declaration by Author**

This thesis is composed of my original work, and contains no material previously published or written by another person except where due reference has been made in the text. I have clearly stated the contribution by others to jointly-authored works that I have included in my thesis.

I have clearly stated the contribution of others to my thesis as a whole, including statistical assistance, survey design, data analysis, significant technical procedures, professional editorial advice, and any other original research work used or reported in my thesis. The content of my thesis is the result of work I have carried out since the commencement of my research higher degree candidature and does not include a substantial part of work that has been submitted to qualify for the award of any other degree or diploma in any university or other tertiary institution. I have clearly stated which parts of my thesis, if any, have been submitted to qualify for another award.

I acknowledge that an electronic copy of my thesis must be lodged with the University Library and, subject to the General Award Rules of The University of Queensland, immediately made available for research and study in accordance with the *Copyright Act 1968*.

I acknowledge that copyright of all material contained in my thesis resides with the copyright holder(s) of that material. Where appropriate I have obtained copyright permission from the copyright holder to reproduce material in this thesis.

Mohammad Amanzadeh

February 2014

## **Publications during candidature**

### *Industry Reports:*

- 1) S.M. Aminossadati, W.P. Bowen, E. Sheridan, M. Amanzadeh, and M.S. Kizil, “An Innovative Fibre Optic Based Methane Sensor”, *ACARP (Australian Coal Association Research Program)*, C20014, Feb 2013.
- 2) S. Adam, J. Devlin, M. Amanzadeh, E. Prochon, S.M. Aminossadati, and M.S. Kizil, “Fibre Optic Sensing in Underground Coal Mines: The Possibilities and Opportunities”, *CRCMining Internal Report*, Jul 2013.

### *Conference papers:*

- 1) S.M. Aminossadati, M. Amanzadeh, M.S. Kizil and T. Liu, “Development and utilisation of fibre optic-based monitoring systems for underground coal mines”, *In: Naj Aziz, 2014 Coal Operators’ Conference*, Wollongong, NSW, Australia, (369-380). 12-14 Feb 2014.
- 2) S.M. Aminossadati, M. Amanzadeh, E. Prochon, J Kok and S. Adam, “Step change approaches in coal technology and fugitive emissions research”, *In: Ting Ren and Jialin Xu, The 6th international symposium on green mining*, Wollongong, NSW, Australia, (332-337). 24-26 Nov 2013.
- 3) M. Amanzadeh, E. Sheridan, S.M. Aminossadati, M.S. Kizil, and W.P. Bowen, “Microfabricated hollow core fibres for gas sensing using wavelength modulation spectroscopy”, *OSA Imaging and Applied Optics CLEO: Laser Application & Technology*, 2013, San Jose, California, United States, (6.1-6.2). 9-14 Jun 2013.
- 4) M. Amanzadeh, S.M. Aminossadati, M.S. Kizil, E. Sheridan, W.P. Bowen, “A microfabricated fibre optic sensor for methane gas measurement in underground coal mines”, *In: , 2012 Photonics Global Conference (PGC), 2012*, Singapore, Singapore, (1-5). 13-16 Dec. 2012, IEEE Xplore, DOI: 10.1109/PGC.2012.6457999.
- 5) E. Sheridan, M. Amanzadeh, S.M. Aminossadati, M.S. Kizil, and W.P. Bowen, “Characterization of microfabricated optical fibre for gas sensing”, *In: , Australian Conference On Optical Fibre Technologies*, Sydney, NSW, Australia, (). 9-13 Dec 2012.
- 6) M. Amanzadeh, E. Sheridan, S.M. Aminossadati, M.S. Kizil, and W.P. Bowen, “Methane sensing in underground coal mines using a microstructured optical fibre”, *In: Paul Lever, Stuart Thompson, 2012 Australian Mining Technology Conference Proceedings*, Perth, WA, Australia, (141-150). 8-10 Oct 2012.
- 7) E. Sheridan, M. Amanzadeh, S.M. Aminossadati, M.S. Kizil, and W.P. Bowen, “Fibre microfabrication and characterization for gas sensing”, *Imaging and Applied Optics Technical Digest OSA. Optical Sensors*, Monterey, CA, United States, (). 24-28 June 2012.

## **Publications included in this thesis**

- 1) S.M. Aminossadati, W.P. Bowen, E. Sheridan, M. Amanzadeh, and M.S. Kizil, “An Innovative Fibre Optic Based Methane Sensor”, *ACARP (Australian Coal Association Research Program)*, C20014, Feb 2013. Partially incorporated as paragraphs in Sections 7.1 and 7.2 in Chapter 7, and Section 8.2 in Chapter 8.

<b>Contributor</b>	<b>Statement of contribution</b>
S.M. Aminossadati	Initiated the idea (20%)
	Designed experiments (20%)
	Carried out analysis (20%)
	Wrote and edited the report (20%)
W.P. Bowen	Initiated the idea (20%)
	Designed experiments (20%)
	Carried out analysis (20%)
	Wrote and edited the report (20%)
E. Sheridan	Initiated the idea (20%)
	Designed experiments (20%)
	Carried out analysis (20%)
	Wrote and edited the report (20%)
M. Amanzadeh	Initiated the idea (20%)
	Designed experiments (20%)
	Carried out analysis (20%)
	Wrote and edited the report (20%)
M.S. Kizil	Initiated the idea (20%)
	Designed experiments (20%)
	Carried out analysis (20%)
	Wrote and edited the report (20%)

- 2) M. Amanzadeh, E. Sheridan, S.M. Aminossadati, M.S. Kizil, and W.P. Bowen, “Microfabricated hollow core fibres for gas sensing using wavelength modulation spectroscopy ”, *OSA Imaging and Applied Optics CLEO: Laser Application & Technology*, 2013, San Jose, California, Unites States, (6.1-6.2). 9-14 Jun 2013. Partially incorporated as paragraphs in Chapters 7 and 8.

<b>Contributor</b>	<b>Statement of contribution</b>
M. Amanzadeh	Initiated the idea (40%) Designed experiments (40%) Carried out analysis (50%) Wrote and edited the paper (20%)
E. Sheridan	Initiated the idea (15%) Designed experiments (15%) Carried out analysis (50%) Wrote and edited the paper (20%)
S.M. Aminossadati	Initiated the idea (15%) Designed experiments (15%) Carried out analysis (0%) Wrote and edited the paper (20%)
M.S. Kizil	Initiated the idea (15%) Designed experiments (15%) Carried out analysis (0%) Wrote and edited the paper (20%)
W.P. Bowen	Initiated the idea (15%) Designed experiments (15%) Carried out analysis (0%) Wrote and edited the paper (20%)

- 3) M. Amanzadeh, S.M. Aminossadati, M.S. Kizil, E. Sheridan, W.P. Bowen, “A microfabricated fibre optic sensor for methane gas measurement in underground coal mines”, *In: , 2012 Photonics Global Conference (PGC), 2012, Singapore, Singapore, (1-5). 13-16 Dec. 2012, IEEE Xplore, DOI: 10.1109/PGC.2012.6457999.* Partially incorporated as paragraphs in Section 3.1 in Chapter 3, and Section 7.2.3 in Chapter 7.

<b>Contributor</b>	<b>Statement of contribution</b>
M. Amanzadeh	Initiated the idea (40%) Designed experiments (40%) Carried out analysis (50%) Wrote and edited the paper (20%)
S.M. Aminossadati	Initiated the idea (15%) Designed experiments (15%) Carried out analysis (50%) Wrote and edited the paper (20%)
M.S. Kizil	Initiated the idea (15%) Designed experiments (15%) Carried out analysis (0%) Wrote and edited the paper (20%)
E. Sheridan	Initiated the idea (15%) Designed experiments (15%) Carried out analysis (0%) Wrote and edited the paper (20%)
W.P. Bowen	Initiated the idea (15%) Designed experiments (15%) Carried out analysis (0%) Wrote and edited the paper (20%)



- 4) E. Sheridan, M. Amanzadeh, S.M. Aminossadati, M.S. Kizil, and W.P. Bowen, “Characterization of microfabricated optical fibre for gas sensing”, *In: ,Australian Conference On Optical Fibre Technologies, Sydney, NSW, Australia, (). 9-13 Dec 2012. Partially incorporated as paragraphs in Section 7.2.2 Chapter 7.*

<b>Contributor</b>	<b>Statement of contribution</b>
E. Sheridan	Initiated the idea (40%) Designed experiments (40%) Carried out analysis (50%) Wrote and edited the paper (20%)
M. Amanzadeh	Initiated the idea (15%) Designed experiments (15%) Carried out analysis (50%) Wrote and edited the paper (20%)
S.M. Aminossadati	Initiated the idea (15%) Designed experiments (15%) Carried out analysis (0%) Wrote and edited the paper (20%)
M.S. Kizil	Initiated the idea (15%) Designed experiments (15%) Carried out analysis (0%) Wrote and edited the paper (20%)
W.P. Bowen	Initiated the idea (15%) Designed experiments (15%) Carried out analysis (0%) Wrote and edited the paper (20%)

- 5) M. Amanzadeh, E. Sheridan, S.M. Aminossadati, M.S. Kizil, and W.P. Bowen, “Methane sensing in underground coal mines using a microstructured optical fibre”, *In: Paul Lever, Stuart Thompson, 2012 Australian Mining Technology Conference Proceedings*, Perth, WA, Australia, (141-150). 8-10 Oct 2012. Partially incorporated as paragraphs in Chapters 2 and 7.

<b>Contributor</b>	<b>Statement of contribution</b>
M. Amanzadeh	Initiated the idea (40%) Designed experiments (40%) Carried out analysis (50%) Wrote and edited the paper (20%)
E. Sheridan	Initiated the idea (15%) Designed experiments (15%) Carried out analysis (50%) Wrote and edited the paper (20%)
S.M. Aminossadati	Initiated the idea (15%) Designed experiments (15%) Carried out analysis (0%) Wrote and edited the paper (20%)
M.S. Kizil	Initiated the idea (15%) Designed experiments (15%) Carried out analysis (0%) Wrote and edited the paper (20%)
W.P. Bowen	Initiated the idea (15%) Designed experiments (15%) Carried out analysis (0%) Wrote and edited the paper (20%)

- 6) E. Sheridan, M. Amanzadeh, S.M. Aminossadati, M.S. Kizil, and W.P. Bowen, “Fibre microfabrication and characterization for gas sensing”, *Imaging and Applied Optics; Technical Digest OSA. Optical Sensors*, Monterey, CA, United States, (). 24-28 June 2012. Partially incorporated as paragraphs in Chapter 7.

<b>Contributor</b>	<b>Statement of contribution</b>
E. Sheridan	Initiated the idea (40%) Designed experiments (30%) Carried out analysis (50%) Wrote and edited the paper (20%)
M. Amanzadeh	Initiated the idea (15%) Designed experiments (25%) Carried out analysis (50%) Wrote and edited the paper (20%)
S.M. Aminossadati	Initiated the idea (15%) Designed experiments (15%) Carried out analysis (0%) Wrote and edited the paper (20%)
M.S. Kizil	Initiated the idea (15%) Designed experiments (15%) Carried out analysis (0%) Wrote and edited the paper (20%)
W.P. Bowen	Initiated the idea (15%) Designed experiments (15%) Carried out analysis (0%) Wrote and edited the paper (20%)

## **Contributions by others to the thesis**

Dr. Eoin Sheridan contributed in microfabrication of fibres.

**Statement of parts of the thesis submitted to qualify for the award of another degree**

None

## **Acknowledgements**

I am pleased to thank everyone who supported me. First and foremost, I would like to express my deep appreciation to Dr. Aminossadati. This thesis was made possible due to his masterly guidance during the past two years. Throughout my MPhil degree, I was fortunate enough to have Dr. Saïied M. Aminossadati, A/Prof. Mehmet Kizil, and A/Prof. Warwick Bowen as my advisory team. The knowledge they shared with me has been invaluable. I want also to express my sincere appreciation to Dr. Eoin Sheridan for his great work and much needed assistance during this project.

I am very much grateful to Professor Tongyu Liu, Director of the Laser Laboratory of the Shandong Academy of Science, China for allowing access to their facilities and sites. I cherish this as an amazing international opportunity in terms of my career going forward, but more importantly as an amazing chance to see firsthand the implementation of fibre optic-based gas sensors in the mining industry.

I had the opportunity to meet and be inspired by some outstanding and well known experts in the area of photonics. It is a lifetime honour for me to be acknowledged by Professor Rachel Won, Editor in Chief of Nature Photonics for choosing my paper at PGC-2012 as the best student paper. Professor Nader Engheta, University of Pennsylvania, who inspired me not only with his publications but also with the thoughts he shared with me, opening new perspectives and teaching me approaches to conceptual thinking in photonics research.

I would also like to thank Mr. Peter Brisbane (ACARP project monitor), Prof. Peter Knights, Prof. Paul Lever (CRCMining), Mr. Scott Adam (CRCMining), Mr. Ramtin Ghodsi (ABB Australia), Mr. Saju Pothen (ABB Australia), and Dr. Stuart Thompson for all their mentoring and support during my studies. Special thanks should go to the Australian coal association research program (ACARP) and CRCMining Australia for the financial support of the project (Project number C20014). CRCMining granted a living cost scholarship through my study and top-up to my scholarship.

Also, I should thank the University of Queensland for providing me with a UQI scholarship to cover my tuition fee. In addition, the University of Queensland's graduate school provided me

with a GSITA scholarship to visit Shandong Academy of Science and Xinglongzhuang mine in Shandong, China in April 2013 as part of my study. I need also give thanks to the UQ Mining Division for all their kind support and for providing me the chance to visit central Queensland mines, including Oaky creek, Clement, and Blackwater mines in October 2012. Without this support, my research could never have come to fruition. I sincerely hope that the work presented in this thesis justifies the financial commitment made by the University.

I would like to express my enormous gratitude to my family (Nosrat, Ali, Azam, Bahar, Azadeh, Maryam, Wakan, and Viona) who have been a constant source of inspiration, support, and optimism on the long journey that started with my MPhil project and continues up to this day.

My greatest thanks go out to my dear friends and colleagues who have stood by me and buoyed my spirits during my studies, especially Nima, Marjan and Brianne for their unwavering support throughout the difficulties of my study and research. I owe a lot to my colleagues in the Queensland Quantum Optics Laboratory and the UQ Mining division who supported me, and I thank them for their interesting and fruitful scientific discussions.

Thank you all

## **Keywords**

spectroscopy, underground coal mine, wavelength modulation spectroscopy, direct absorption spectroscopy, mine safety, gas detection, methane gas measurement, hollow core fibre, photonic crystal fibre, microstructured fibre, micromachining, focused ion beam milling, all-fibre sensor



## **Australian and New Zealand Standard Research Classifications (ANZSRC)**

ANZSRC code: 091405, Mining Engineering, 50%

ANZSRC code: 090605, Photodetectors, Optical Sensors and Solar Cells, 30%

ANZSRC code: 020502, Lasers and Quantum Electronics, 20%

## **Fields of Research (FoR) Classification**

FoR code: 0999, Mining Engineering, 50%

FoR code: 0205, Optical Physics, 30%

FoR code: 0906, Electrical and Electronic Engineering, 20%

# **Table of Contents**

<b>Abstract .....</b>	<b>i</b>
<b>Declaration by Author .....</b>	<b>iii</b>
<b>Publications during candidature .....</b>	<b>iv</b>
<b>Publications included in this thesis.....</b>	<b>v</b>
<b>Contributions by others to the thesis.....</b>	<b>xi</b>
<b>Statement of parts of the thesis submitted to qualify for the award of another degree .....</b>	<b>xii</b>
<b>Acknowledgements.....</b>	<b>xiii</b>
<b>Keywords.....</b>	<b>xv</b>
<b>Australian and New Zealand Standard Research Classifications (ANZSRC).....</b>	<b>xvi</b>
<b>Fields of Research (FoR) Classification.....</b>	<b>xvi</b>
<b>Table of Contents .....</b>	<b>xvii</b>
<b>List of Figures.....</b>	<b>xxi</b>
<b>List of Tables .....</b>	<b>xxvi</b>
<b>List of Abbreviations used in the thesis.....</b>	<b>xxvii</b>
<b>1 INTRODUCTION.....</b>	<b>1</b>
1.1 Background .....	1
1.2 Motivation for All-fibre Methane Sensing.....	4
1.3 Aims and Objectives .....	5
1.4 Scope of Work.....	5
1.5 Significance to Industry .....	6
1.6 Overview .....	7
<b>2 GAS MONITORING IN UNDERGROUND COAL MINES.....</b>	<b>8</b>
2.1 Introduction .....	8
2.2 Gases in Underground Coal Mines.....	11

2.2.1 Major Mine Gases .....	11
2.2.2 Methane in Underground Coal Mines .....	12
2.3 Gas Monitoring Systems .....	15
2.3.1 Methane Gas Sensor Technologies .....	15
2.3.2 Portable Gas Detectors .....	16
2.3.3 Fixed Gas Monitoring Systems .....	18
2.3.4 Comparison of Methane Monitoring Systems .....	23
2.4 Proposed Methane Gas Monitoring System.....	24
<b>3 SPECTROSCOPIC GAS SENSING .....</b>	<b>27</b>
3.1 Introduction .....	27
3.2 Spectroscopy Techniques.....	30
3.2.1 Theory of Absorption Spectroscopy.....	30
3.2.2 Direct Absorption Spectroscopy .....	32
3.2.3 Wavelength Modulation Absorption Spectroscopy .....	35
3.2.4 Other Gas Spectroscopy Techniques.....	45
<b>4 ALL-FIBRE GAS SENSORS .....</b>	<b>48</b>
4.1 Introduction .....	48
4.1.1 Single-mode Fibres.....	49
4.1.2 Photonic Crystal Fibre (PCF).....	50
4.2 All-fibre Gas Sensing Methods .....	51
4.2.1 Tapered Fibre .....	52
4.2.2 Drilled SMF .....	56
4.2.3 Drilled HC-PCF .....	57
<b>5 THEORETICAL ANALYSIS OF METHANE ABSORPTION BANDS.....</b>	<b>63</b>
5.1 Introduction .....	63

5.2 Methane Absorption Lines .....	63
5.3 Methane Spectroscopic Measurement in Underground Coal Mines .....	69
5.4 Methane Sensing in $2\nu_3$ Band Using HC-PCF .....	71
<b>6 EXPERIMENTAL SETUP AND PROCEDURES.....</b>	<b>73</b>
6.1 Introduction .....	73
6.2 Methane Gas Concentration Test Setup.....	74
6.3 Spectroscopy Measurement Setup.....	78
6.4 Experimental procedures.....	81
<b>7 ALL-FIBRE SENSOR DEVELOPMENT.....</b>	<b>86</b>
7.1 Introduction .....	86
7.2 Fibre Optic Sensor Head Fabrication.....	88
7.2.1 Tapered Single-mode Fibres .....	88
7.2.2 Drilled SMFs.....	91
7.2.3 Drilled Hollow Core Fibres .....	95
7.3 Fibre Coupling and Splicing of HCF to SMF .....	98
<b>8 EXPERIMENTAL ANALYSIS.....</b>	<b>101</b>
8.1 Introduction .....	101
8.2 Sensing Experimental Results .....	101
8.2.1 Open Path Gas Cells.....	101
8.2.2 Tapered Fibres.....	104
8.2.3 Drilled SMFs.....	105
8.2.4 Drilled Hollow Core Fibres .....	106
8.3 Comparison of Measurements.....	117
<b>9 CONCLUSIONS AND RECOMMENDATIONS.....</b>	<b>119</b>
9.1 Conclusions .....	119

9.2 Recommendations for Future Work .....	120
<b>References.....</b>	<b>122</b>
<b>Appendix I: Risk Assessments .....</b>	<b>131</b>
<b>Appendix II: Certificates of Merit Awarded During Study .....</b>	<b>136</b>
<b>Appendix III: Hollow Core Fibre Specification Sheet .....</b>	<b>139</b>
<b>Appendix IV: Gas Concentration Setup.....</b>	<b>140</b>
<b>Appendix V: Single Mode Fibre Specification Sheet .....</b>	<b>142</b>
<b>Appendix VI: DFB Laser Source Datasheets and Drawings .....</b>	<b>144</b>

## **List of Figures**

Figure 2.1: (a) Canary bird in cage, and (b) safety lamp for gas detection in underground coal mine .....	9
Figure 2.2: Molecular structure of methane gas .....	12
Figure 2.3: Formation of explosive mixture of methane .....	13
Figure 2.4: Depiction of methane being diluted into ventilation air in mine atmosphere.....	14
Figure 2.5: Catalytic sensor, (a) Wheatstone bridge circuit, and (b) a cutaway view .....	15
Figure 2.6: Typical design of an IR gas sensor .....	15
Figure 2.7: OdaLog7000 multi gas detector .....	17
Figure 2.8: Calibration of catalytic instrument for different gases.....	17
Figure 2.9: Dräger Xzone5000 multi gas detector, area monitoring and confined entry.....	18
Figure 2.10: Installed real-time gas detector in a Queensland underground coal mine.....	19
Figure 2.11: Filters and gas measurement unit of tube bundle system.....	20
Figure 2.12: Tube-bundle system's pump. (a) in operation, and (b) after event.....	21
Figure 2.13: A typical ultra-fast Gas Chromatograph utilised in a Queensland underground coal mine ...	22
Figure 2.14: Telemetric against tube-bundle methane measurement .....	23
Figure 2.15: A risk assessment case study (a) sample as measured by tube bundle; (b) sample as measured by GC .....	24
Figure 2.16: Proposed fibre optic based methane gas detection system.....	26
Figure 3.1: Schematic of laser absorption through a gas .....	28
Figure 3.2: (a) A tuneable laser scan across a methane absorption feature (b) and the normalised absorbance near 1666 nm .....	29
Figure 3.3: Schematic of a spectroscopic based (a) extrinsic optical (open-path) gas sensor and (b) intrinsic fibre based (all-fibre) gas sensor.....	29
Figure 3.4: Sample line shape function as a function of frequency.....	32
Figure 3.5:A schematic of scanned-wavelength direct absorption spectroscopy with a tuneable laser .....	33
Figure 3.6: An example of WMS output VCSEL scan with absorption.....	35
Figure 3.7: A schematic of wavelength modulation spectroscopy to detect second harmonic (2f) and first harmonic (1f) .....	36
Figure 3.8: WMS measurements. (a) Normalised DC scan through gas absorption. (b) Fundamental frequency (1f) signal and, second harmonic (2f) signal .....	36
Figure 3.9: An example of best fit for 1 and 2f to intensity modulation .....	38
Figure 3.10: Second harmonic profile broadening for different modulation depth.....	42

Figure 3.11: Second harmonic amplitude ( $S_{2,ampl}$ ), Second harmonic maximum ( $S_{2,max}$ ), and first harmonic amplitude ( $S_{1,ampl}$ ) as a function of modulation index ( $m$ ) .....	43
Figure 3.12: Normalisation against laser intensity disturbance .....	44
Figure 3.13: A simple photoacoustic gas measurement setup .....	46
Figure 3.14: Cavity ring-down (CRD) schematic .....	46
Figure 3.15: (a) fibre cavity using linear FBG cavity setup, (b) setup of a fibre loop cavity .....	46
Figure 4.1: Typical optical fibres used for data transmission .....	49
Figure 4.2: Conventional single mode fibre attenuation in different bands .....	49
Figure 4.3: Photonic Crystal Fibre (PCF) arrangements. (a) index guiding; (b) PBG .....	50
Figure 4.4: Photonic crystal band gap effect found in <i>Cyanophrys remus</i> butterflies .....	51
Figure 4.5: Scanning electron microscopy (SEM) image of HC-PCF .....	51
Figure 4.6: Schematic of gas detection based on evanescent field .....	52
Figure 4.7: various all-fibre gas sensor heads: (a) a short gap in a fibre, (b) a tapered fibre, (c) a removed cladding section of a fibre, (d) a side-polished fibre (e) a SMF fibre with Long Period Gratings (LPGs) (f) a PCF fibre to provide gas and light interaction inside fibre .....	52
Figure 4.8: Propagation of light in a tapered fibre .....	53
Figure 4.9: Calculated fraction of laser power in the evanescent field near surface of a tapered SMF .....	54
Figure 4.10: Microscopy image of a 4 $\mu\text{m}$ dia. drilled hole through a SMF .....	56
Figure 4.11: Interferometric-based gas sensing from a drilled hole on SMF .....	56
Figure 4.12: A specially designed gas sensing PCF .....	58
Figure 4.13: Microchanneled HC-PCF for gas sensing .....	59
Figure 4.14: Schematic of femtosecond laser drilling in an optical fibre .....	59
Figure 4.15: SEM cross-section image of micro-hole drilled in HC-1550-02 fibre (a) in coated fibre with a UV removed hole on polymer surface (b) in a stripped fibre .....	60
Figure 4.16: Schematic of a dual-beam FIB-SEM system suitable for micromachining and imaging of solid materials .....	60
Figure 4.17: SEM images of side hole by FIB with diameter of (a) 12 $\mu\text{m}$ and (b) 15 $\mu\text{m}$ , on side of PCFs .....	61
Figure 5.1: Absorption features for five main mine gases in from 100 nm to 16000 nm region .....	64
Figure 5.2: Methane absorbance (a) for under 10000 nm, and (b) for under 2000 nm, vibrational bands are labelled .....	65
Figure 5.3: Absorption spectra of methane at $2\nu_3$ band, R, P and Q branches are tagged .....	66
Figure 5.4: Methane absorbance at R branch of $2\nu_3$ band in NIR for 0.01% and 100% methane in air (a) from 1650 nm to 1660 nm, and (b) at 1653.7 nm line centre .....	67

Figure 5.5: Methane absorbance at Q branch of $2\nu_3$ band for 0.01% and 100% methane in air from 1664 nm to 1668 nm .....	68
Figure 5.6: Methane WMS second harmonic signal at Q-branch of $2\nu_3$ band for 0.01%, 0.1%, and 100% methane in air for 1665.961 nm, 1666.201nm, and 1666.483 nm line centres .....	69
Figure 5.7: Spectrum showing the significant absorption lines for methane ( $\text{CH}_4$ ) and other common mine gases in NIR region .....	70
Figure 5.8: Normalised spectral absorbance of methane at $2\nu_3$ band (red), attenuation and dispersion of HC-1550-02 .....	72
Figure 5.9: Typical near field intensity of HC-1550-02 fibre at 1550 nm.....	72
Figure 6.1: General schematic of experimental setup .....	73
Figure 6.2: Schematic of methane gas concentration setup .....	74
Figure 6.3: (a) 3D AutoCAD design with open top, (b) with closed top, and (c & d) Photos of the developed gas chamber.....	75
Figure 6.4: Teflon connection to feed fibre optics to the chamber.....	75
Figure 6.5: High pressure gas cylinders and fittings .....	76
Figure 6.6: The built gas chamber and other connections .....	77
Figure 6.7: Schematic diagram of spectroscopic methane measurement setup .....	78
Figure 6.8: DFB laser package .....	79
Figure 6.9: Lock-in amplifier (LIA) model SR830 .....	80
Figure 6.10: Tektronix DOP 3034Oscilloscope.....	80
Figure 6.11: Photo of the experimental setup .....	81
Figure 6.12: Schematic of fixed-wavelength absorption spectroscopy experiment .....	82
Figure 6.13: Schematic of scanned-wavelength absorption spectroscopy experiment.....	83
Figure 6.14: Schematic of Wavelength Modulation Spectroscopy (WMS) experiment .....	83
Figure 6.15: A screenshot of oscilloscope showing WMS signal (blue), 2f-WMS (green), and 1f-WMS (red) from a 5% methane filled reference gas cell .....	84
Figure 6.16: Normalised and filtered WMS-1f and WMS-2f signal of a reference gas cell.....	84
Figure 7.1: Profile illustrations of the four types of sensor head investigated in this project (left), and images (photograph/micrograph) of real examples of the sensor head (right).....	87
Figure 7.2: (a) Schematic diagram, (b & c) Photographs of taper pulling rig.....	88
Figure 7.3: Images of (a) tapered fibre in stainless steel clamp, (b) tapered fibre clamped inside the gas chamber, (c) scanning electron micrograph showing the narrowing of the fibre .....	89
Figure 7.4: Screenshot of the LabView Flame oscillation program (a) linear tapered profile setting, (b) linear exponential tapered profile.....	90



Figure 7.5: Australian microscopy & microanalysis research facility (AMMRF) at Queensland University of Technology, (a) Leica EMSCD005 gold coating vacuum chamber, (b) EDAX FEI Quanta 3D SEM/FIB dual beam system in, (c) gold coated fibre placed inside the FIB chamber for drilling ..... 91

Figure 7.6: Scanning electron microscope images showing the progress of a 10  $\mu\text{m}$  diameter hole drilled into a single mode fibre using a beam current of 7 nA. .... 92

Figure 7.7: Optical micrographs showing a 10  $\mu\text{m}$  dia. hole drilled in a standard optical fibre by focused ion beam milling (a) imaged from above the hole, (b) imaged from the side of the hole ..... 92

Figure 7.8: Optical microscopy setup and a piezo stage to insert a tapered fibre tip for characterisation of the drilled hole ..... 93

Figure 7.9: (a) Schematic representation of a tapered fibre tip inserting into a hole drilled in a standard fibre. (b) Optical micrograph showing a tapered fibre tip inserting into a hole drilled in a standard fibre. 93

Figure 7.10: Transmission intensity of 1666 nm light passing through drilled standard optical fibres as a probe was inserted into the drilled hole until it touched the base of the hole. The depth of the hole was 96  $\mu\text{m}$  (black), 35  $\mu\text{m}$  (grey) ..... 94

Figure 7.11: Cross section of a cleaved HC-1550-02 fibre (a) SEM image, (b) optional microscopy image ..... 95

Figure 7.12: Scanning electron micrograph (SEM) showing the cross section of a hollow core fibre that has had a 10  $\mu\text{m}$  dia. hole drilled into its core ..... 96

Figure 7.13: Scanning electron micrographs showing a 10  $\mu\text{m}$  diameter hole drilled in a hollow core fibre (HCF) using focused ion beam drilling at the indicated magnification. False colour has been added to the 12,000x image to increase contrast ..... 97

Figure 7.14: Side view of HFC (left) to SMF (right) splice attempt using SMF splice program on FSU-975 splicer..... 98

Figure 7.15: Image of HCF (Left) splice to SMF-28 (Right); (a) optical microscopy image, (b) SEM image ..... 99

Figure 7.16: Back reflection from splice point which causes a Fabry-Perot cavity between splice point of the HCF and the SMF in a drilled HCF sensor head ..... 100

Figure 7.17: A screenshot of oscilloscope showing noise on WMS signal due to cavity between two splice fusion between a 40mm HCF ends and SMFs ..... 100

Figure 8.1: General experimental setup (simplified) for methane detection in an open path gas cell..... 102

Figure 8.2: Open path gas cell calibration curve from direct absorption measurements of methane peak at 1665.9 nm at different concentrations ..... 103

Figure 8.3: Open path gas cell calibration curve from normalised peak signal of second harmonic measurement of methane peak at 1665.9 nm at different concentrations. Wavelength modulation depth was 0.10cm <sup>-1</sup> .....	104
Figure 8.4: Experimental setup (simplified) for methane detection with a tapered fibre sensor head .....	105
Figure 8.5: Experimental setup (simplified) for methane detection with a drilled single mode fibre sensor head .....	106
Figure 8.6: An 85 mm drilled HCF placed in the methane gas test chamber .....	107
Figure 8.7: Experimental setup (simplified) for methane detection with a drilled hollow core fibre (HCF) sensor head.....	107
Figure 8.8: Normalised transmitted signal of scanned-wavelength absorption spectroscopy over one scan using an 85 mm drilled HCF.....	108
Figure 8.9: Fixed-wavelength absorption spectroscopy signal over time for various methane concentrations using an 85 mm drilled HCF.....	109
Figure 8.10: Calibration curve from direct absorption measurements of methane peak at 1665.961 nm at various concentrations using a drilled HCF .....	110
Figure 8.11: WMS second harmonic of methane for different concentrations from HITRAN database. ....	111
Figure 8.12: HITRAN database calibration curve from normalised peak to peak signal of second harmonic measurement of methane absorption at 1665.961 nm in 0% to 100% methane .....	111
Figure 8.13: HITRAN database calibration curve from normalised peak to peak signal of second harmonic measurement of methane absorption at 1665.961 nm in various concentrations (0%-10%)....	112
Figure 8.14: Calibration curve from wavelength modulation spectroscopy measurements of methane second harmonic peak to peak signal at 1665.961 nm at different concentrations using a drilled hollow core fibre (HCF) sensor head .....	113
Figure 8.15: A screenshot of oscilloscope showing WMS signal (green), 2f-WMS (blue), and 1f-WMS (red) from a 345 mm drilled HCF in 5% methane .....	114
Figure 8.16: Calibration curve from WMS measurements of methane normalised second harmonic peak to peak signal at 1665.96 nm at different concentrations using a drilled HCF sensor head .....	114
Figure 8.17: Calibration curve from WMS measurements of methane first harmonic peak to peak signal at 1665.961 nm at different concentrations using a drilled HCF sensor head .....	115
Figure 8.18: Transmission transients showing the change in transmission at 1665.961 nm upon release of 2% methane into the gas chamber at t = 190 s.....	116

## **List of Tables**

Table 1.1: Some of the major underground coal mines explosions.....	1
Table 1.2: Advantage and disadvantages of gas measurement systems for underground coal mines .....	3
Table 2.1: Major underground coal mine gases .....	11
Table 3.1: Sources of uncertainties in wms-2f measurement.....	45
Table 4.1: List of previous tapered fibre gas sensing studies.....	55
Table 4.2: Previous works on SMF micromachining .....	57
Table 4.3: Gas sensing projects using Hollow core fibres (HCFs) in short .....	62
Table 6.1: Flow meter specifications .....	77
Table 6.2: The IR detector specifications (Dräger X-am 7000).....	77
Table 6.3: Laser system tuning specifications .....	79
Table 7.1: Comparison of measured fibre hole depths with depth programmed into FIB.....	94
Table 7.2: Specifications of the SMF and HC-PCF used in the experiments .....	98
Table 7.3: SMF-28 to SMF-28 and HC-1550-02 splice parameters used in this study .....	99
Table 8.1: Summary of results of methane detection with different sensor heads .....	117

## **List of Abbreviations used in the thesis**

<i>1f</i>	First Harmonic
<i>2f</i>	Second Harmonic
<i>2f-WMS / 2f-WMS</i>	Second Harmonic-Wavelength Modulation Spectroscopy
<i>APC</i>	Angle-Polished Connector for Fibre Optics
<i>AR</i>	Anti-Reflection
<i>atm</i>	Atmospheric Pressure
<i>AMMRF</i>	Australian Microscopy And Microanalysis Research Facility
<i>BNC</i>	Type of Connector
<i>BQW</i>	Buried Quantum Well
<i>C</i>	Centigrade
<i>CMATSP</i>	Coal Mining Abatement Technology Support Package
<i>CMM</i>	Coal Mine Methane
<i>CRDS/CRD</i>	Cavity Ring Down Spectroscopy
<i>DA</i>	Direct Absorption
<i>DAC</i>	Direct Absorption Concentration
<i>DAQ</i>	Data Acquisition
<i>DAS</i>	Direct Absorption Spectroscopy
<i>DBR</i>	Distributed Bragg Reflector
<i>DC</i>	Direct Current
<i>DFB</i>	Distributed Feedback
<i>DLAS</i>	Diode Laser Based Absorption Spectroscopy
<i>DSA</i>	Direct Scanned Absorption
<i>DSP</i>	Digital Signal Processing
<i>EC-QCL</i>	External-Cavity Quantum Cascade Laser
<i>EL</i>	Explosive Limits
<i>FBG</i>	Fibre Bragg Grating
<i>FFP-TF</i>	Fibre Fabry-Perot Tunable Filter
<i>FIB</i>	Focused Ion Beam
<i>FMS</i>	Frequency Modulation Spectroscopy

<i>FPI</i>	Fabry-Perot Interferometer
<i>FS</i>	Femtosecond
<i>FWHM</i>	Full-Width Half Maximum
<i>GC</i>	Gas Chromatograph
<i>GHz</i>	Giga Hertz
<i>GPIB</i>	General Purpose Interface Bus- IEEE 488
<i>GRIN</i>	Gradient-Index
<i>HITRAN</i>	High Resolution Transmission Molecular Absorption database
<i>HCF</i>	Hollow Core Fibre
<i>HWHM</i>	Half Width At Half Maximum
<i>IR</i>	Infrared
<i>TEC</i>	Temperature Controller
<i>TLV</i>	Threshold Limit Value
<i>LIA</i>	Lock In Amplifier
<i>LPG</i>	Long Period Grating
<i>MSHA</i>	Mine Safety And Health Administration
<i>NIR</i>	Near-Infrared
<i>NDIR</i>	Non-Dispersive Infrared
<i>OEM</i>	Original Equipment Manufacturer
<i>PBG</i>	Photonic Band Gap
<i>PD</i>	Photo Detector
<i>PPM</i>	Part Per Million
<i>RMS</i>	Root Sum Square
<i>S/Sec</i>	Second
<i>SEM</i>	Scanning Electron Microscope
<i>SNR</i>	Signal To Noise Ratio
<i>UEL</i>	Upper Explosive Limit
<i>UPS</i>	Uninterruptible Power Supply
<i>VAM</i>	Ventilation Air Methane
<i>VCSEL</i>	Vertical Cavity Surface Emitting Laser
<i>WMS</i>	Wavelength Modulation Spectroscopy

# CHAPTER 1

## INTRODUCTION

### 1.1 Background

Methane is a highly volatile and potentially hazardous gas that occurs naturally in coal seams during the formation of coal from organic substances. Because methane gas is extremely flammable in the presence of oxygen, it poses a considerable danger in underground coal mines. The risk of explosions is particularly high in underground coal mine environments where methane concentrations can rise quickly during the extraction process. Table 1.1 shows a list of major incidents from 2005 to 2010, where methane was the main contributing factor.

Table 1.1: Some of the major underground coal mine explosions (2005-2010) [1, 2]

<b>Country</b>	<b>Date</b>	<b>Coal Mine</b>	<b>Fatalities</b>
<b>New Zealand</b>	19-November-2010	Pike River mine, Greymouth	29
<b>Turkey</b>	17-May-2010	Karadon, Zonguldak	30
<b>USA</b>	5-April-2010	Upper Big Branch, West Virginia	29
<b>Ukraine</b>	19-November-2007	Zasyadko, Donetz	80
<b>Russia</b>	19-March-2007	Ulyanovskaya, Kemerovo	108
<b>Kazakhstan</b>	20-September-2006	Lenina, Karaganda	43
<b>USA</b>	2-January-2006	Sago, West Virginia	12
<b>China</b>	14-February-2005	Sunjlawan, Haizhou shaft, Fuxin	214

The presence of such a dangerous gas, which affects both safety and productivity in mine environments, calls for adopting an intrinsically safe, fast-response, reliable, and accurate gas monitoring system. There are three primary incentives for maintaining accurate methane gas measurements throughout underground coal mines [1]. The first is to improve mine operation safety. In the past century, there have been thousands of deaths worldwide [3], including many hundreds in Australia [4], caused by methane explosion in underground coal mines.

The second is that a distributed methane monitoring system in underground coal mines would contribute to a reduction of the environmental impacts of methane emissions. Coal mines emit a significant amount of methane into the atmosphere, which has more than 20 times the global warming potential than carbon dioxide [2, 5, 6]. Due to the growth of global coal demand, coal excavations are going ever deeper; and there are ever more underground coal mines operating all around the world—thus exacerbating the associated issues of both safety and gas emissions [7]. The implementation of systems that can provide adequate information on emissions would contribute to more effective approaches to methane gas drainage, ventilation, and utilisation.

The third is that underground methane gas measurement may contribute to mining economics. An accurate and well-distributed methane monitoring system could improve coal mine methane (CMM) recovery and utilisation [8, 9]. This would also increase mine productivity by reducing downtimes due to high methane levels [1]. The withdrawal of underground coal miners is mandated if methane concentrations reach 1% in China, Germany, and U.S.A; 1.25% in Australia, India and United Kingdom; and 1.4% in South Africa [2, 10]. In addition, a variety of emissions credits and tax regimes under the Kyoto protocols in some countries, such as Australia, require accurate ventilation air methane (VAM) measurements [2, 11].

For centuries, miners used canaries and mice, due to their faster reactions to the presence of a poisonous atmosphere, as a means of warning to evacuate the mining area [12]. Nowadays, thanks to modern technology, detectors and monitoring systems are utilised to recognise the gas concentrations. As differing systems provide particular information essential for the safe operation of a mine, utilising various techniques—including real-time gas monitoring, accurate gas trace monitoring, and portable gas detectors—is required. Moreover, in order to manage each system's weakness, a combination of all systems is the ideal solution; however, not all mines require or utilise them [13, 14]. Currently, tube bundle and telemetry systems are utilised in most

Australian underground coal mines [14]. Table 1.2 shows a summary of the different gas measurement systems presently utilised in underground coal mines, their advantages and disadvantages. Different technologies and gas detection systems are discussed in detail in Chapter 2.

Table 1.2: Advantage and disadvantages of gas measurement systems for underground coal mines [12-15]

<b>Measurement System</b>	<b>Advantages</b>	<b>Disadvantages</b>
1. <b>Portable devices</b>	Multi gas detection, offers affordable prices for personal and machine protection in high risk areas.	Cross-sensitivity, fault readings, require regular maintenance, 20% of miners fail to use them properly.
2. <b>Fixed devices</b>		
2.1. <b>Telemetric</b>	Instantaneous, long distance, continuous gas measurement at strategic locations. Easy diagnosing of failure.	Constant calibration, cross-sensitivity, relatively expensive, high maintenance, active sensing head which is not suitable for high risk, such as goaf area. Not functional in high methane concentrations due to power shutdowns. Limited sensor life time. Poisoning of methane sensor can happen.
2.2. <b>Tube bundle</b>	High stability and analytical capability, perfect for gas trace monitoring at different points including goaf and road ways	Delays involved due to sample drawing time, difficult/impossible to diagnose faulty tube parts, relatively expensive, post event damage.
2.3. <b>Chromatography</b>	Very accurate measurement of most mine gases. Essential for gas monitoring during operation. Critical for decision making during events	Require expert attention, gas sampling required (timely), slow analysis

A review of the latest disaster reports reveals that methane gas monitoring is still an issue for underground coal mines. Recently, the Park River mine incident judgement reported that inadequate methane gas monitoring contributed significantly to the 2010 event [16]. The coal mining abatement technology support package (CMATSP), a program linked to the Australian carbon pricing scheme, particularly addressed the need for novel reliable methane monitoring systems to help predict methane emission sources and long term magnitude for optimised coal mining in Australia [17]. Fibre optic sensors have provided unique solutions to measuring



different parameters in industrial applications. Fibre optic technology has revolutionised many industries and fostered new applications for use in communications, oil and gas, electrical power grid monitoring, wind turbine monitoring, structural health monitoring, and many other fields.

## **1.2 Motivation for All-fibre Methane Sensing**

The mining industry is feeling increasingly distressed by a combination of factors including: the worldwide economic weakness, a decrease in average ore-grades, and the higher costs of underground operations. This situation will not be improved unless cost-effective, innovative technologies can transform the mining industry. Deploying an optical fibre sensor network provides a passive sensing element which can be remotely located and monitored, promising an intrinsically safe technique in harsh underground coal mine environments. In addition, this capability can be expanded via multiplexing methods, where a single control unit can monitor many passive sensors through an optical fibre network. This offers a cost effective sensing solution relative to the number of sensor heads. Thus far, fibre optic sensor systems are still in the development stage and undergoing trials for underground coal mine applications. Remote methane detection by laser absorption spectroscopy (first proposed by Moore in 1965) and the development of diode lasers in near-infrared (NIR) opened the way for remote methane measurements using optical fibres in the late 20<sup>th</sup> century [18].

Lately, there have been many research projects aiming to develop and take to trial fibre optic based methane gas monitoring systems using open-path gas cell sensor heads for underground coal mine application [19-26]. The proposed, all-fibre sensor heads have several advantages over conventional open-path gas cell sensor heads. These benefits include, but are not limited to, minimal temperature effects on the physical characteristics of a sensing head, fibre size and flexibility, real-time and fast response gas detection due to the low gas volume samples required for measurement, relatively lower costs, and the potential for networkability and easier installation. These properties hold the promise of easing the adoption and commercialization of fibre optic based methane sensors within the mining industry. The motivation for this investigation is three-fold: recent disasters due to methane explosions, the global warming effects of methane, and recent advances in the field of fibre optic sensors. This study developed and conducted laboratory tests to evaluate the methane gas detection capability of three different

all-fibre sensor head candidates for underground coal mines. However, further research is required to improve the mine environment compatibility of successful sensor heads addressing, for example, issues such as hazardous area operation capability and dust and humidity proof filtering minimisation against response time.

### **1.3 Aims and Objectives**

The main aim of this investigation and conducted experiments was to evaluate the applicability of using all-fibre sensor heads to measure methane concentrations in underground coal mines towards the end of improving mine safety via gas monitoring systems. This aim is achieved by answering a single research question (as stated below) and by meeting the project objectives.

*Can an all-fibre methane sensor system be used in underground coal mines?*

The objectives can be classified as follows:

- Gaining a comprehensive knowledge of gas sensing systems currently used in underground coal mines;
- Identifying potential methods by which to develop all-fibre gas sensors;
- Developing gas chamber apparatuses and appropriate experimental methodologies;
- Implementation of an absorption spectroscopy setup to measure gas concentrations;
- Fabrication of all-fibre sensor heads including tapered fibres, drilled single mode fibres (SMF) and drilled hollow core fibres (HCF); and
- Testing the developed sensor heads and analysing their sensing capabilities.

### **1.4 Scope of Work**

This project has focused on the analysis of all-fibre methane gas sensing systems for underground coal mining applications. The scope of this study is limited to development of three kinds of all-fibre sensing heads. The following facilities have been utilised in this study: tapered fibres using the tapering facility available at Queensland Quantum Optics Laboratory, drilled single mode and drilled HCFs using the FEI Quanta 3D scanning electron microscope (SEM) / focused ion beam (FIB) dual beam system in the Australian microscopy and microanalysis research facility (AMMRF) at Queensland University of Technology. The gas detection

techniques were limited to direct absorption spectroscopy (DAS) and harmonic wavelength modulation spectroscopy (WMS). The modified sensor heads were tested exposing them to various methane concentrations of fewer than 10% in a chamber within a laboratory environment. The actual methane concentration in the chamber was verified using a calibrated Dräger X-am 7000 gas detector equipped with a methane infrared (IR) sensor. The exclusives to the scope of this study are coal mine compatibility tests, prototype sensor head development with proper filtering, comprehensive response time study and sensor heads development with different arrangements and properties.

### **1.5 Significance to Industry**

To the best of the author's knowledge as of the date of this writing, there have been no commercially available all-fibre methane gas sensor heads developed for underground coal mines. This has been confirmed by a thorough search of all industry sources. However, there are a few optical methane gas sensing systems using open path gas cell sensor heads which are under trial in China and the U.S. [27, 28]. The properties of all-fibre sensor heads could notably advance the development of innovative pre-trial technologies that may benefit the coal mining industry. Although there have been other research projects and experiments done on all-fibre methane gas sensor heads [29-35], the current state of research has not been sufficient to move these types of sensors into the industry. Development of all-fibre methane gas sensing systems could deliver the following benefits to the underground coal mining industry:

- A distributed methane gas sensing system;
- A reliable gas sensing method with no cross-sensitivity to other gases;
- Relatively cheap sensor heads and system costs per extracted data at various points;
- A monitoring system that works in the absence of oxygen making it perfect for use in unventilated and inaccessible areas such as goafs and sealed areas;
- An intrinsically safe network with no ignition source in system;
- The prospect of developing distributed real-time methane gas sensing systems that will improve gas monitoring and safety at reasonable prices; and
- Easy and fast diagnostics of system faults. Optical time domain reflectometry could provide a time effective failure detection system that reduces maintenance time and costs.

## 1.6 Overview

This Thesis is presented in eight chapters as follows:

**Chapter 1** describes the motivation for developing all-fibre optic based methane gas sensing for underground coal mines, the thesis aims and objectives, and the thesis overview.

**Chapter 2** presents a comprehensive review of different mine gases and gas monitoring systems employed in underground coal mines. Methane gas characteristics and sensing technologies are discussed.

**Chapter 3** discusses fibre optic-based gas detection using absorption spectroscopy and different associated techniques.

**Chapter 4** various potential fibres and all-fibre methane gas sensors are presented.

**Chapter 5** presents theoretical analysis of methane absorption bands using the HITRAN database. Suitable line centres are considered for detecting methane using fibre optics—most specifically, hollow core fibres are discussed and analysed.

**Chapter 6** describes methane concentration tests and spectroscopy measurement setups. The specifications and simulations for choosing the right laser source and optical components are also described and discussed. In the last section, procedures and experimental arrangements are presented.

**Chapter 7** provides a detailed description of the development of all-fibre sensor heads, including fabrication processes. Fibre coupling and splicing between single mode fibre (SMFs) and hollow core fibres (HCFs)—as well as their optical properties—are discussed in the second section. This chapter includes sensor head images and splicing results.

**Chapter 8** presents an in-depth description of the experimental processes and characterisation of fibre sensor heads. The experimental results from tests using pre-filled open path gas cells and the developed sensor heads are examined and discussed. These results were obtained using absorption spectroscopy techniques (WMS and DAS).

**Chapter 9** concludes the thesis with some suggestions and recommendations for future work.

# CHAPTER 2

## GAS MONITORING IN UNDERGROUND COAL MINES

### 2.1 Introduction

A number of gases can be found in underground coal mines. Mine gases are variously released into the mine atmosphere from coal seams, rock strata, combustion, fires, blasting, diesel engines, and coal oxidation. The main underground coal mining gases of interest are methane, carbon monoxide, oxygen, nitrogen, hydrogen sulphide, carbon monoxide, oxides of nitrogen, oxides of hydrogen, and higher hydrocarbons. Among mine gases, methane poses one of the greatest dangers to underground coal miners. It is the main reason for many fatalities in underground coal mines, as it is a highly volatile gas that can cause underground fires and explosions [36, 37]. Therefore, methane gas management is vital to operating underground coal mines safely.

Sufficient air quality is essential to provide a safe, healthy, and comfortable working environment in successful underground mining operations. Adequate air supply is required to maintain oxygen, dust, pollutant gas concentrations, temperature, and humidity at appropriate levels and well below or above statutory limits [38]. Traditionally, mine ventilation is utilised to

keep gas concentrations at desired levels throughout the mines. In addition to ventilation in gassy mines, pre-mining and post-mining drainage are employed to reduce coal seam gas emission. In order to ensure that the mine is safe and adequate ventilation and drainage are in place, the coal mine environment and working atmosphere need to be thoroughly and constantly monitored.

Since the earliest underground coal mining, various techniques have been used to monitor air quality—from canary birds and safety lamps to the portable and fixed electronic based sensors currently available in the market [39]. Canary birds are very sensitive to low levels of carbon monoxide and methane, which kept them in mines as hazard detectors up till the 20<sup>th</sup> century [40]. A singing canary was the sign of a safe working place, while a dead or listless canary was cause for immediate evacuation. Miners carried canaries in cages during operations and post-events to assure them the air supply was safe (Figure 2.1a). The miners' safety lamp was the first specifically methane measurement device and an icon of the industrial revolution from the early 18<sup>th</sup> century [41, 42]. Safety lamps consist of a flame which is surrounded by an iron plate with small holes to prevent ignition. The intensity and colour of the light's flame were a measure of gas concentrations, particularly methane concentrations [12]. Figure 2.1b shows miners carrying a safety lamp after an event.



Figure 2.1: (a) Canary bird in cage, and (b) safety lamp for gas detection in underground coal mine [11]

Thanks to a succession of newer technologies, various kinds of electronic and electro-chemical gas measurement systems replaced canaries and safety lamps. Nowadays, mature safety systems are deployed in mines owing to continuous changes in mine safety legislation. These legal mandates are a result of lessons learnt from past mine accidents and new technological

developments [43]. However, there is still no unique system to meet all industry mandates for a well-distributed multi gas sensing system with the required sensitivities and response time.

An efficient gas monitoring system is critical to detect, analyse, and predict the hazards associated with mine gases such as spontaneous outbursts and fires [39]. Generally, there are two different kinds of gas detection systems that have been used in underground coal mines: fixed gas monitoring systems and portable gas monitoring systems.

Fixed gas monitoring systems provide adequate information on different gasses in exhaust shafts, entry points, and all other critical areas required by legislations. A combination of three different fixed monitoring systems are currently used in most Queensland underground coal mines to collect essential gas concentration data: telemetric, tube-bundle, and onsite ultra-fast gas chromatography (GC) systems. These systems not only provide information that can predict and help prevent outbursts and fires, ensure safe operation during exploration, and treat fires; but also can provide data to determine the status of underground coal mine environments following major incidents such as methane explosions and mine fires [15, 43]. On the other hand, portable gas detectors are used for personal safety during normal operations, for reopening sealed areas, near battery charging stations, and entering abandoned work areas. Portable gas monitoring systems are also installed on equipment and machinery to be triggered at unsafe methane concentrations.

This chapter reviews various gases present in underground coal mines, particularly methane, as well as the current state of gas monitoring technologies. First, different mine gases are examined. Later in chapter 4, the list of mine gases is used to choose the right wavelength for methane detection with no cross-sensitivity to other mine gases. Then, in Section 2.3 various methane sensor technologies and gas monitoring systems are studied to highlight their advantages and disadvantages. Subsequently, methane gas properties, monitoring in underground coal mines, and the effectiveness of different systems is covered. In the last section, current issues in methane gas monitoring in underground coal mines are addressed. Finally, a well-distributed fibre optic-based methane sensing system is proposed to fill in the current gaps in methane monitoring in underground coal mines.

## 2.2 Gases in Underground Coal Mines

### 2.2.1 Major Mine Gases

Table 2.1 shows major underground coal mine gases, their health hazards for miners, sources of emissions, and explosive limits (EL) or their threshold limit value (TLV) if applicable.

Table 2.1: Major underground coal mine gases [24, 44, 45]

<b>Gas(Symbol)</b>	<b>Explosive</b>	<b>Toxic</b>	<b>Health Hazard</b>	<b>Source</b>	<b>EL/TLV</b>
<b>Methane</b> (CH <sub>4</sub> )	Yes	No	Asphyxiant (Rare)	strata, carbonaceous shale	5%–15%
<b>Oxygen</b> (O <sub>2</sub> )	No	No	Oxygen deficiency: 17% panting 15% dizziness and headache 9% unconsciousness 6% & below death.	21% of atmosphere	-
<b>Carbon-Dioxide</b> (CO <sub>2</sub> )	No	Yes	Increases breathing rate. May cause death in high concentrations.	diesel engines, fires, coal oxidation, blasting	TLV=5000 ppm
<b>Carbon-Monoxide</b> (CO)	Yes	Yes	Highly toxic. Can be an Asphyxiant.	diesel engines, fires, blasting, explosions	12.5%–74% TLV= 50 ppm
<b>Ammonia</b> (NH <sub>3</sub> )	No	Yes		blasting, cooling plants	
<b>Nitrogen-Dioxide</b> (NO <sub>2</sub> / N <sub>2</sub> O <sub>4</sub> )	No	Yes	Highly toxic. Corrosive effect on lungs. Can be an Asphyxiant.	blasting, diesel engines, electrical discharge, welding	TLV = 5 ppm
<b>Hydrogen-Sulphide</b> (H <sub>2</sub> S)	Yes	Yes	Highly toxic. Can be an Asphyxiant.	strata, stagnant water	4.5%–45% TLV=10 ppm
<b>Acetylene</b> (C <sub>2</sub> H <sub>2</sub> )	Yes		Only slightly toxic. Asphyxiant (Rare)	-	-
<b>Hydrogen</b> (H <sub>2</sub> )	Yes	No	Asphyxiant(O <sub>2</sub> Depletion)	strata, battery charging	4%–74%
<b>Sulphur-Dioxide</b> (SO <sub>2</sub> )	No	Yes	Highly toxic. Can be an Asphyxiant.	sulphide dust explosions	TLV=5 ppm
<b>Ethane</b> (C <sub>2</sub> H <sub>6</sub> )	Yes	No	Asphyxiant (Rare)	-	-
<b>Propane</b> (C <sub>3</sub> H <sub>8</sub> )	Yes	No	Asphyxiant (Rare)	-	-
<b>Butane</b> (C <sub>3</sub> H <sub>8</sub> )	Yes	No	Asphyxiant (Rare)	-	-
<b>Nitrogen</b> (N <sub>2</sub> )	No	No	Asphyxiant (O <sub>2</sub> Depletion)	78% of atmosphere	



Atmospheric air is a mixture of several gases including 79.04% nitrogen (N<sub>2</sub>), 20.93% oxygen (O<sub>2</sub>), and a small amount of carbon dioxide (CO<sub>2</sub>) [46]. There is also a very small amount of methane, 2 ppm, in normal air [47]. Various gases influenced by mining activities and events are emitted into underground coal mine atmosphere. There are three main hazards arising from mine gases: some gases are combustible, some are toxic, and large volumes of gases emitted into the mine workings could cause asphyxiation of miners. In addition to methane, the trends of oxygen, carbon monoxide, and carbon dioxide are continuously recorded at particular points in a mine. These gases are produced or consumed during combustion, so their accurate concentration trending is necessary. This information is used to calculate fire ratios, including Graham's ratio, CO/CO<sub>2</sub> ratio, and CO- that detect and monitor heating progressions and spontaneous combustions. Ratios' plotting has been found very valuable for events management due to their steady change with heating progress, which gives information on intensity and temperature [14].

### 2.2.2 Methane in Underground Coal Mines

It is important to gain a basic knowledge about methane gas and its physical and chemical characteristics in order to develop a methane gas detection system. Methane is a hydrocarbon gas with the chemical formula of CH<sub>4</sub>. It is the most important gas among mine gases produced and liberated from coal seams [1]. It needs to be controlled and monitored throughout a mine in order to eliminate explosions and/or asphyxiation risks [2]. Methane is odourless, lighter than air, highly flammable, and explosive. Figure 2.2 shows the methane gas structure which consists of four carbon-hydrogen bonds with 108.70 pm length.

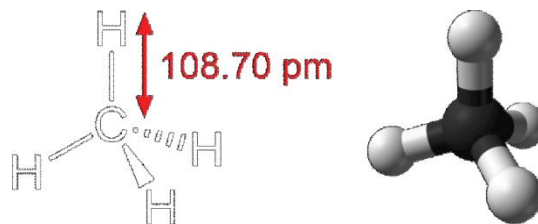


Figure 2.2: Molecular structure of methane gas (After [48])

Methane, in the presence of a certain amount of oxygen and an ignition source, burns with a pale blue flame and produces carbon dioxide, water, and heat. The lower explosive limit (LEL) of methane is 5% and the upper explosive limit (UEL) is 15% when mixed with air at the standard temperature and pressure, namely 20°C and 1 atmosphere, respectively. An air mixture of 5% to

15% methane and at least 12% oxygen is explosive. The most powerful mixture is 9.5% methane in air. These limits can change slightly with variations in temperature and pressure. However, this is not a serious concern as a considerable margin of safety is usually taken. A methane level below 2% is required for the safe operation of underground coal mines, an insight gained from industry experience with methane in the last century [47]. As Figure 2.3 illustrates, methane is not an explosion hazard except when mixed with enough oxygen (air). Such conditions—fuel rich zones—occur in sealed goafs. Methane leakage from sealing, roadways, and coal faces in mine environments needs to be watched carefully to prevent the formation of explosive mixtures, as shown in the red triangle in Figure 2.3 [2]. As the figure shows, introducing more oxygen and methane in fuel rich mixtures and fuel lean zones respectively, will cause an explosive mixture.

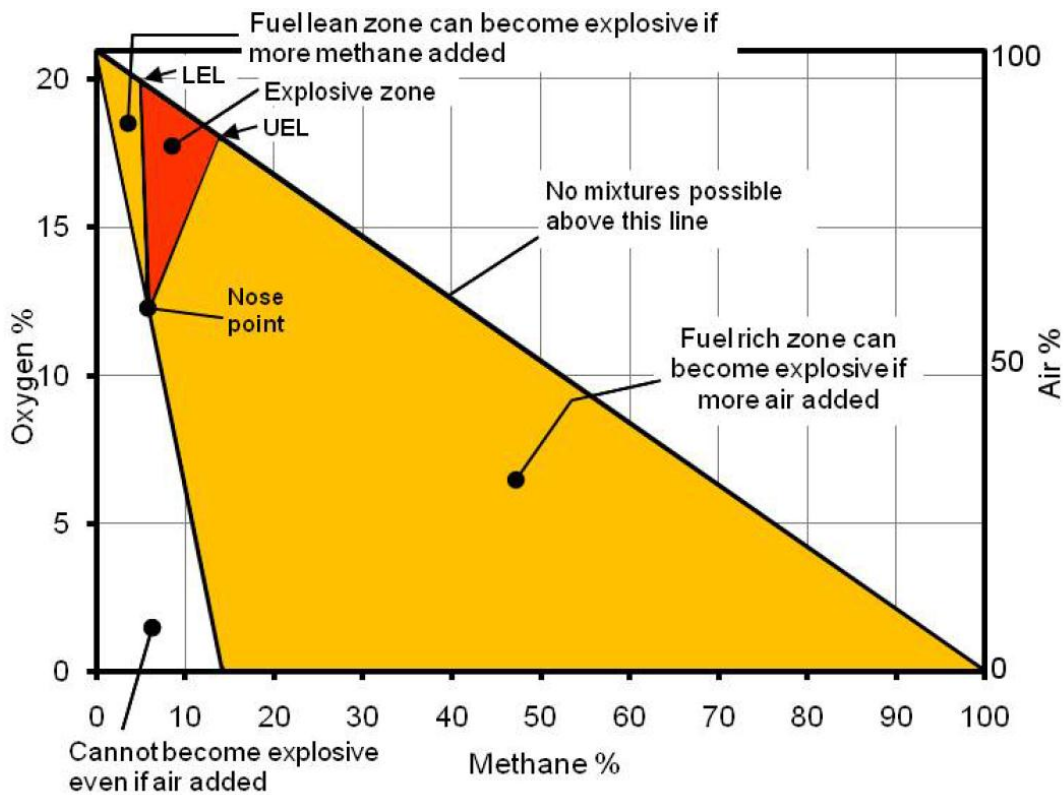


Figure 2.3: Formation of explosive mixture of methane (Based on Coward, 1928 chart) [2]

Methane in high concentrations enters a mine atmosphere from rocks and coal seams in roadways, ceilings, roofs, ribs, walls, goaf sealing, and coal faces. There are three basic elements that reduce methane hazards in underground coal mines. Firstly, fresh air replaces mine air by circulating the air through intake and return mine entries using the main ventilation system, and then by using brackets and ducts for face ventilation [19, 49]. Secondly, if gas concentrations

exceed safe operational levels, it is necessary to have subsequent protocols in place along with a reliable methane monitoring system [14]. Thirdly, mines need to have restrictive regulations to prevent the introduction of any possible ignition sources including materials, machinery, and equipment taken underground and to keep tabs on worker-related actions [49].

A mine safety program requires making sure that adequate drainage, goaf sealing inspections, and ventilation are in place at working faces and return airways to keep methane concentrations below acceptable levels [19]. Methane enters the mine atmosphere in high concentrations from various local points. Then, the methane gas is diluted by the moving air stream, assuming an appropriate air stream is provided [47]. Figure 2.4 illustrates the methane gas from a crack in the mine roof. As it shows, a safe methane measurement is required at 30 centimetres out [49].

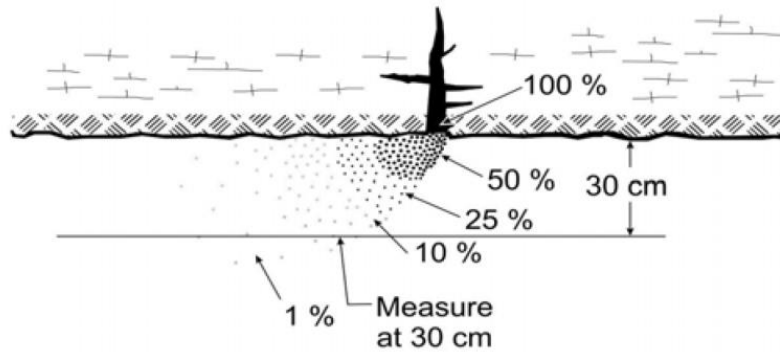


Figure 2.4: Depiction of methane being diluted into ventilation air in mine atmosphere [49]

The density of methane is almost half of air, so the methane gas may accumulate at the mine roof forming a floating layer that does not mix easily with ventilation air. If the location is liable to layering, gas monitoring should be taking place to safely deal with methane layers [14, 49]. The Coal Mining Safety and Health Regulation Act 2001 mandates risk assessments in order to identify and classify different risk zones in underground coal mines. Based on general body concentration of methane risk zones are defined as: Explosion risk zone zero (greater than 2%), explosion risk zone one (from 0.5% to 2%), and negligible explosion risk zone (less than 0.5%) [50]. There are designated points for methane measurements based on risk zones which are directly outlined in legislations to assure safe operations in mines.

All electrical equipment needs to be shut down when methane concentrations reach a set level of 1.25% (in Australia) and the mine should be evacuated if the methane concentration is over 2%

[2, 10]. These limits and measurement points vary based on state regulator, and sometimes different companies have more restrictive safety standards than state standards. In addition to the above-mentioned facts, it should be noted that each sensor merely shows the gas concentration of the air at the sampling point. Sensor response time is critical in order to predict or prevent further accidents by taking essential actions timely.

## 2.3 Gas Monitoring Systems

### 2.3.1 Methane Gas Sensor Technologies

The most common methane detectors use electro-catalytic sensors known as Pellistors or catalytic bead systems. All gas sensing technologies have been comprehensively reviewed by Liu *et al.* [51]. The principle behind catalytic sensors is the resistance change due to heat generation from oxidation of hydrocarbons on catalytic bead filaments [52]. These sensors work accurately only where methane is under 8% and oxygen is over 10% [47]. Figure 2.5a shows the sensor's Wheatstone bridge circuit consisting of a catalytic bead detector and a compensator; Figure 2.5b shows a cutaway view of a catalytic sensor [53]. Another limitation associated with this type of detector is that it cannot distinguish between different combustible gases. The active design of the sensor is subject to baseline drift caused by corrosion; as a result, the efficiency of the unit is directly linked to a maintenance and calibration program.

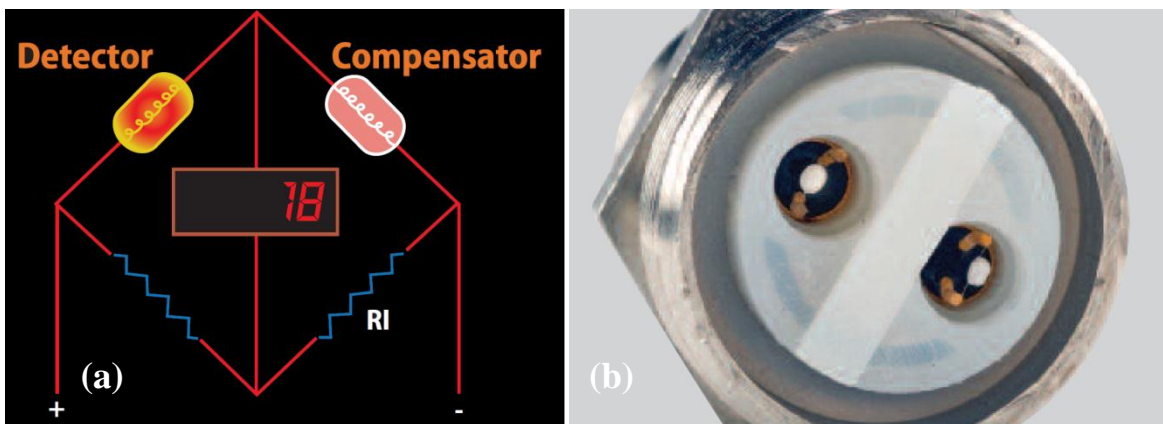


Figure 2.5: Catalytic sensor, (a) Wheatstone bridge circuit, and (b) a cutaway view [53]

The most recent methane sensors function on IR absorption which is a well-developed measurement technology. IR gas analysers are known for being complicated, cumbersome, and expensive [52]. They are certainly more expensive than catalytic sensors. The main advantage of IR instruments is that the detector does not directly interact with the gas (or gases) to be detected,

so there is no chance for the gas to cause electronic parts of the sensor to drift or die prematurely [54]. The IR beam passes through two cells—one cell containing the sample gas and a reference cell to minimise interference and increase stability. These sensors have low cross sensitivity to humidity, dust, and other gases while supporting full-range detection and operational functionality without the presence of oxygen [47]. The components of such sensors are designed to be resistant to corrosion, and they are easily removable for maintenance or replacement. A typical design for an IR gas sensor is illustrated in Figure 2.6 [53].

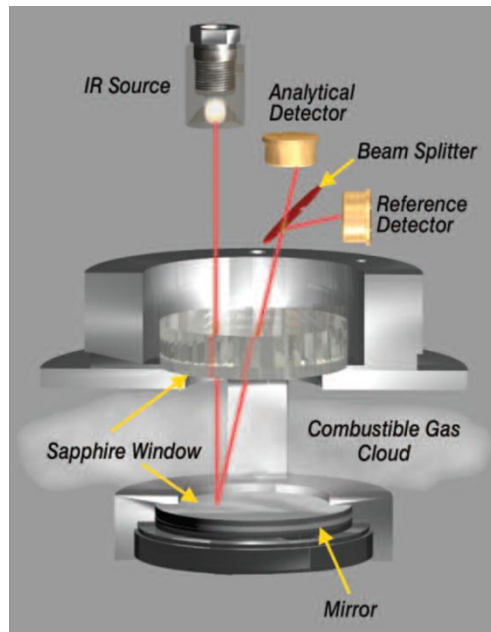


Figure 2.6: Typical design of an IR gas sensor [53]

There are also flame ionization systems, which are similar to pellistors, that use flame ionization to trace methane concentrations [52]. Moreover, there are other gas measurement techniques such as colorimetric stain tubes (these are still used for high concentration measurements) and electrochemical sensors; however, these are not used for methane detection.

### 2.3.2 Portable Gas Detectors

Most commonly, field measurements and surveys of methane gas are obtained using portable detectors capable of multi gas tracing. The main applications of hand-held detectors are personal air monitoring, confined space entry, gas accumulation detection, ventilation survey, and area monitoring. The methane sensitivity is typically in the range of 0.005% to 0.1% by volume [52].

According to the new south wales department of primary industries reports, the main portable gas monitoring units used in Australian underground coal mines are the Dräger MiniWarn, the Dräger X-am7000, the OdaLog7000, and the ITX [55]. These kinds of detectors can continuously measure multi-gases (mainly CH<sub>4</sub>, CO<sub>2</sub>, CO, H<sub>2</sub>S, NO and O<sub>2</sub>) and have been programmed to automatically alarm when exposed to high or low gas concentrations, explosive prone atmospheres, and risky gas ratios. Figure 2.7 shows an OdaLog7000 hand-held detector with a resolution of 0.01% of volume for methane measurements in the range of 0% to 5%, and 1% Vol sensitivity in the range of 5% to 100% [56].



Figure 2.7: OdaLog7000 multi gas detector [56]

Hand-held detectors utilise catalytic sensors which suffer from cross sensitivities where, for example, carbon monoxide sensors give false readings in the presence of hydrogen sulphide or hydrogen. The latest detector models utilize IR sensors. Calibration and inspection are regularly needed to keep the sensors in the correct range and avoid false alarms. Figure 2.8 shows an on-site calibration unit. However, it should be noted, some detectors require being sent back to the manufacturer for calibration purposes.



Figure 2.8: Calibration of catalytic instrument for different gases [12]

An area monitoring task is the monitoring of a defined working area where more than one worker is active for a long period of time. During maintenance and repair work, it is often necessary to enter confined spaces that have weak ventilation. Gas measurement is required to avoid hazards prior to entering confined spaces. In addition, real-time gas monitoring is compulsory in longwall operations. Therefore, specific portable multi-gas detectors have been designed and are being used in the industry to detect hazardous gases from a distance. Figure 2.9 shows a Dräger unit which is networkable and adoptable to mine monitoring systems allowing for its use during failure or maintenance of fixed monitoring systems in longwall mining as well as for use in confined space monitoring [51].



Figure 2.9: Dräger Xzone5000 multi gas detector, area monitoring and confined entry [51]

There are also machine mounted monitors which must be fitted to all mining machinery according to Australian legislation [13]. In the presence of hazardous gases, these monitoring systems alarm and shut down the power.

### **2.3.3 Fixed Gas Monitoring Systems**

#### **2.3.3.1 Telemetric Systems**

Telemetric systems are utilised at strategic locations in underground coal mines to monitor gas concentrations in real-time. The data extracted from a real-time sensor at each individual point is sent to the central control unit of the mine on the surface [39]. The major gases that need to be monitored for instantaneous warning of sudden decreases or increases in gas or risk of fire are methane, carbon monoxide, carbon dioxide, and oxygen, respectively [43]. A combination of catalytic, electrochemical, and simple IR sensors is used in this system. However, compared with analyser type sensors used in tube-bundle systems, the sensors used in telemetric systems often have lower detection ranges, less stability, lower life times, and higher cross sensitivity [14].

Figure 2.10 shows real-time detectors installed in a Queensland underground coal mine. It shows that the sampling point is at an acceptable distance from the ceiling to avoid false readings (as discussed in Section 2.2.2). The dust and harsh environment of a mine makes the detector unsuitable for precise measurements over long periods of time. This photo gives some indication of the harsh environmental conditions in which a real-time monitoring system needs to work.



Figure 2.10: Installed real-time gas detector in a Queensland underground coal mine [48, 51]

### 2.3.3.2 Tube-bundle Systems

Tube-bundle systems, that use pumps, draw gas from different points underground to the surface through plastic tubes and analyse the samples sequentially using paramagnetic and IR techniques. Surface analysers offer more accurate and higher quality analysis. While paramagnetic analysers are generally used for oxygen monitoring, non-dispersive infrared (NDIR) analysers are used for methane, carbon monoxide and carbon dioxide [14]. The standard size of such a system would be in the range of 20 to 40 tubes with a maximum tube length of up to 8000 meters [13]. Figure 2.11 shows a tube bundle system including filters, analysers and all the tubing coming in from underground.





Figure 2.11: Filters and gas measurement unit of tube bundle system [53]

Tube-bundle systems are used to monitor goaf areas, operating long-walls, pillar extraction panels, and selective points along conveyor belts in return ways [13]. One of the advantages of this system is that there is no requirement for maintenance at underground sampling points. This is a big advantage especially for gas monitoring of goafs and sealed areas. The main advantages of tube- bundle systems are as follows [14, 15, 39, 43, 47, 52, 57]:

- Suitable for long term trending;
- No explosion-proof certificate for parts is required;
- High accuracy as low as 1 ppm;
- The functionality in emergency situations. The status of tubes can be determined using vacuum pressure monitoring. This is invaluable data in case of an explosion;
- The samples obtained from tube-bundles can be used for further analysis such as gas chromatography. This is mainly important in case of an emergency when miners are prohibited from re-entering the mine; and
- Easy, on-the- surface maintenance, including changing filters and calibrating all equipment right in the control room with no underground access necessary.

Below are disadvantages of this system in brief:

- Considerable time delay in providing gas data that is used for prevailing underground condition monitoring. It takes about 1 to 2 hours for measuring one point depending on the size and number of sampling points being analysed;
- Not suitable for explicability measurements in areas affected by fire or overheating;

- Not suitable for instantaneous incident detection;
- It requires a complicated flow setup in all tubes to get the right mix of oxygen for paramagnetic analysers; this necessitates monthly leakage tests; and
- The system can be damaged or inoperable during overheating events or when exposed to hazardous concentrations.

Figure 2.12 shows tube-bundle sampling pumps before and after the surface ignition of methane in high concentrations [15].

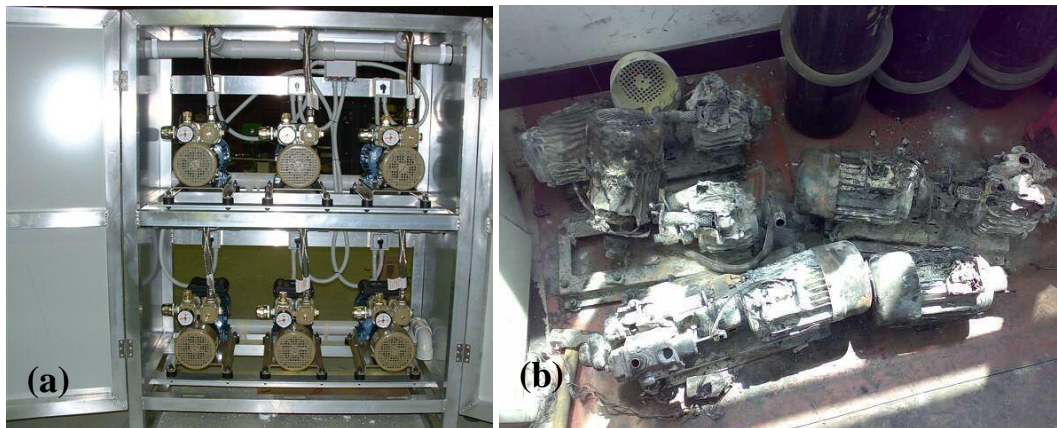


Figure 2.12: Tube-bundle system's pump. (a) in operation, and (b) after event [15]

### 2.3.3.3 Gas Chromatography

In 1947, gas chromatograph (GC) was developed by Mikhail Semenovich who was awarded the Nobel Prize for his work on chromatography [58]. GC involves the separation of all components of a gas sample then making precise measurements by various sensors. A specially packed column is used to separate gases and a suitable detector—usually thermal conductivity or flame ionization is used—to measure each gas as it elutes from the column. Specificity of different components identified by the separation rather than the detection system is what makes the GC very accurate and different from other techniques [43].

GC is vital for gas analysis in the interpretation of extemporaneous combustion events in underground coal mines as it provides accurate measuring of hydrogen, nitrogen, ethylene, and ethane. The sample gases are injected into a gas chromatograph from tube-bundles, or a sample can be taken using special bag samples from underground [57]. In case of collapses that disable tube bundles in tunnels, samples can be taken from predrilled boreholes.

Underground coal mines need access to a gas chromatography system for spontaneous combustion detection and analysis. In Australia, some sites utilise micro GCs (the first one having been installed in Moranbah North in 1997), while some others have access to mobile gas monitoring laboratories for immediate deployment in emergency situations [43, 59]. Figure 2.13 shows a typical ultra-fast GC, capable of gas sample analysis in 2 to 3 minutes, being utilised in a mine [15].



Figure 2.13: A typical ultra-fast Gas Chromatograph utilised in a Queensland underground coal mine [15]

The GC has particular advantages [14, 57]:

- No cross-sensitivity from other gases;
- Ability to separate all spontaneous combustion components including hydrogen, carbon monoxide, and higher hydrocarbons with ppm sensitivity and up to %100 percentage levels;
- Ability to measure all general mine gases, as discussed in Section 2.1; and
- Accurate measurements of most of the gases (from very low to very high concentrations) that occur or are produced underground by heating or in a fire [43].

Its disadvantages include [14, 43, 57]:

- Comparatively slow analyses similar to tube-bundle systems;
- Periodical maintenance and calibration are essential;
- Complicated hardware and control system;
- Requires a highly trained, on-site operator to operate and analyse the data; and
- Interference in some gas levels is unavoidable. High methane percentages affect low level CO measurements which are critical for ratio calculations.

### 2.3.4 Comparison of Methane Monitoring Systems

In this section, a case study is presented to compare different fixed methane monitoring systems [43]. Methane measurements collected from the same location using tube-bundle and real-time systems over a one week period are compared in Figure 2.14. The results show good correlation in the magnitude and trends of the two measurements. Due to the kind of the analysers used in tube-bundle system, the measurements have higher variations and are more reliable for post-events decision making. On the other hand, the immediate availability of telemetric sensor information is critical for immediate gas outburst detection; however, they are not operational in post-events due to power shut downs. The tube-bundle data is used to validate the telemetric sensor readings in normal operations. The difference between magnitudes of measurements could be a sign of faulty calibration or telemetry sensor drift.

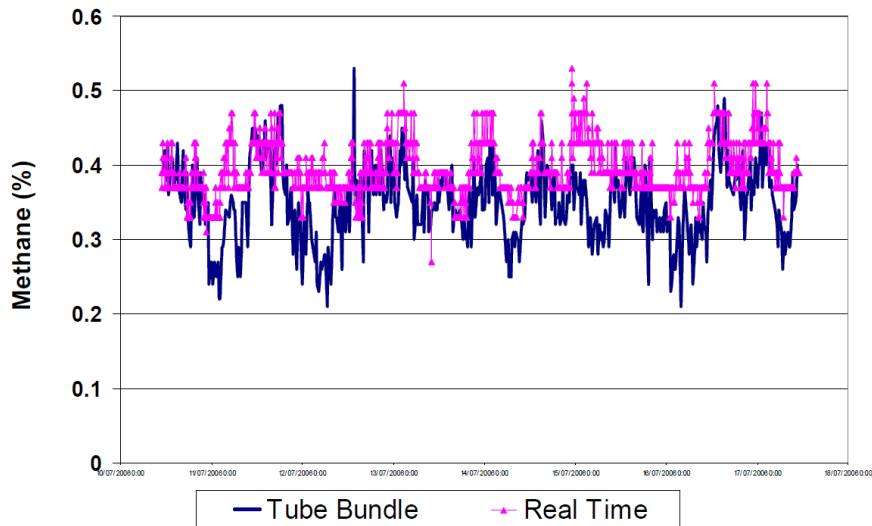


Figure 2.14: Telemetric against tube-bundle methane measurement [43]

Suitable gas monitoring information is critical to mine management. In case of emergencies, such as fire and combustion events, the only reliable source of decision making information is GC. The critical measurements of tube-bundle and telemetry systems are unreliable in emergencies. Typical problems include oxygen in tube-bundles, due to flow dependency; and methane measurement in telemetry systems which drift over time. Figure 2.15 shows a case-study comparing mine atmosphere combustibility based on data measured by tube-bundle and GC systems [43]. As can be seen, relying on the tube-bundle system results could significantly underestimate the combustibility of the mine atmosphere.

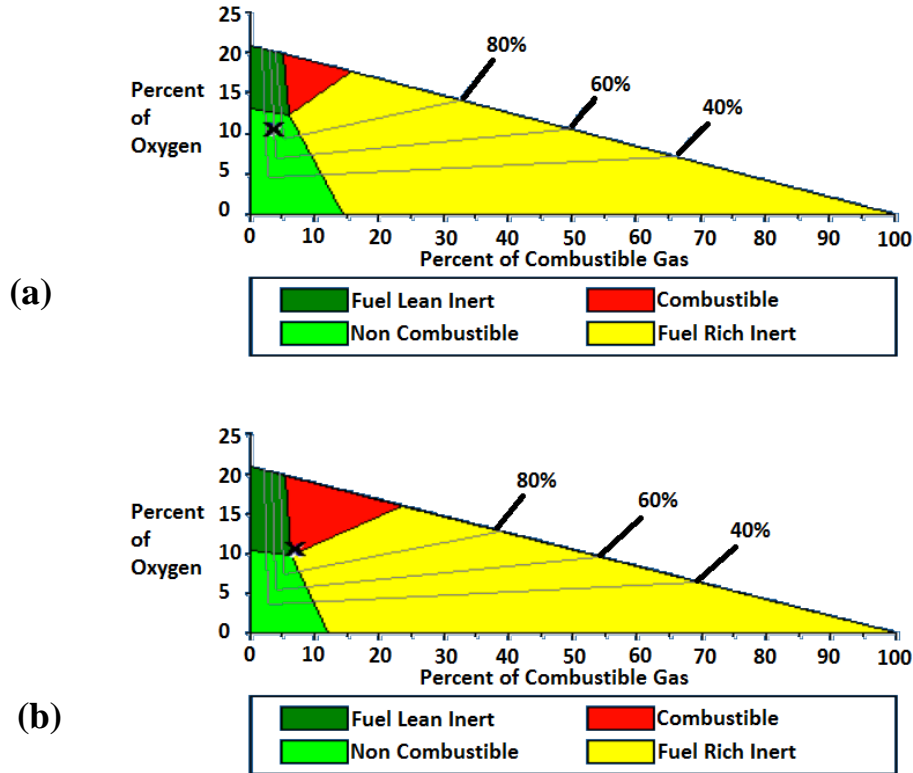


Figure 2.15: A risk assessment case study (a) sample as measured by tube bundle; (b) sample as measured by GC [43]

## 2.4 Proposed Methane Gas Monitoring System

The mining industry is currently dealing with increasing growth in coal mining production and consequently higher rates of gas release during operations. The main challenge for the mining industry in terms of gas sensing is a lack of a robust real-time gas monitoring system which is able to accurately measure concentration of all required gases—most importantly methane—with minimum levels of maintenance and at a reasonable price [39]. After studying currently utilised gas measurement systems in the mining industry, downsides and benefits are identified. This study may help to identify the issues and problems that a novel system needs to address.

Different mine gases were studied among which the properties of methane, as the most important underground coal mine gas, are discussed in detail. In order to fully understand the industry needs, currently used sensors and gas monitoring systems are studied and their benefits and weaknesses are outlined. It is apparent that methane gas monitoring in underground coal mines is critical for prediction, detection and treatment of explosions, fires, spontaneous combustions and

outbursts. A combination of gas monitoring systems is used for different purposes and to cover each individual system's weaknesses.

The literature shows that the following issues need to be addressed in a successful distributed methane gas monitoring system to fill the gaps in the industry: sensitivity, interferences and cross sensitivity, ease of use (minimum expert attention), robustness, and data handling [2, 14-16, 39, 43, 47]. In order to overcome these technical hitches, a remote all-fibre system based on the absorption spectroscopy technology has been found promising. Using an all-fibre gas sensing system could very well satisfy all the requirements of a distributed, real-time gas sensing system in underground coal mines. Also, the developed sensing method may be used to develop novel instruments and techniques in pre-mining and post-mining processes.

U.S. federal regulations mandate the accuracy level required for underground mine methane detectors to have a maximum permissible relative error of 10% at 2.0% alarm level (i.e.  $2.0 \pm 0.2\%$ ) [60]. The mine safety and health administration (MSHA) also requires 0.25% minimum level of detection, with minimum accuracy of 20% over most ranges [47]. In order to safely detect methane alarm levels in a timely manner, an ideal distributed real-time methane monitoring system should have accuracy and sensitivity levels of 0.1% or less, and a response time of under one minute [61]. These properties are achievable using the proposed fibre optic based methane monitoring system which is shown in Figure 2.16. Similar arrangements have been previously proposed by other research groups for land field gas monitoring and underground coal mines [22, 62, 63]. However this study focuses on the development of all-fibre sensor heads for this detection system for the first time. The long pass sensor heads in the design are intended for areas requiring higher sensitivity of detection.

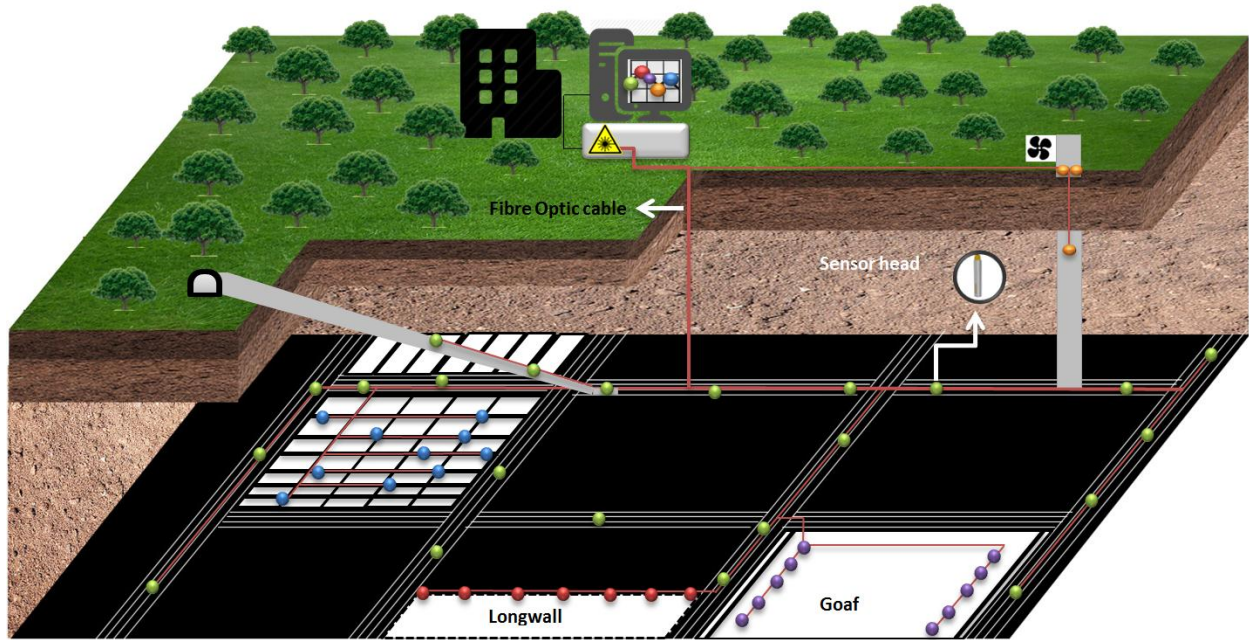


Figure 2.16: Proposed fibre optic based methane gas detection system

This system has the potential to fill the identified gaps in the industry. It uses the same principles as the IR detectors do; however, there are no electronic components underground. The final cost of gas measurements per measuring point is expected to be cheaper than currently used methane telemetry systems. As a matter of fact, this system is viable for use with one laser source multiplexed for several detection points. Also, the detector host and laser are remote from gauging points, which promises easy maintenance and operation. This study particularly investigates all-fibre sensor heads for the proposed methane sensing system. The principles of spectroscopy techniques and various all-fibre gas concentration measurement sensor heads are comprehensively reviewed in the next chapter.

# CHAPTER 3

## SPECTROSCOPIC GAS SENSING

### 3.1 Introduction

The main goal of this chapter is to review all-fibre optic sensing technology and various spectroscopy gas sensing techniques that are capable of making distant measurements of methane gas concentrations. In the first section, gas spectroscopy techniques chosen specifically for the scope of this project—namely wavelength modulation spectroscopy (WMS) and direct absorption spectroscopy (DAS), along with principle mathematical analysis—are described. Following that, a brief review of other spectroscopy techniques is provided. In the second section, the state of the art fibre optic technology is outlined followed by a comprehensive review of the literature available on different all-fibre gas sensors.

Absorption spectroscopy using a tuneable diode laser has been tested as a reliable method of measuring gas concentrations in various applications for more than a decade [64-68]. In this technique, the laser wavelength is rapidly tuned around absorption features of the gas and the laser light output is recorded by a photo detector (PD) to determine line shapes of spectral absorption.



Gas molecules have different natural frequencies; as a result, they absorb light at particular frequencies. These absorptions are known as gases finger prints. As shown in Figure 3.1, laser beam intensity changes passing through a gas. As the light passes through a particular gas, it loses intensity in specific frequencies at the centre of an absorption line. The intensity alteration is correlated to gas concentration, temperature, pressure, and interaction length. The fundamental equation ruling gas absorption spectroscopy is the beer-lambert relation (Equation 1).

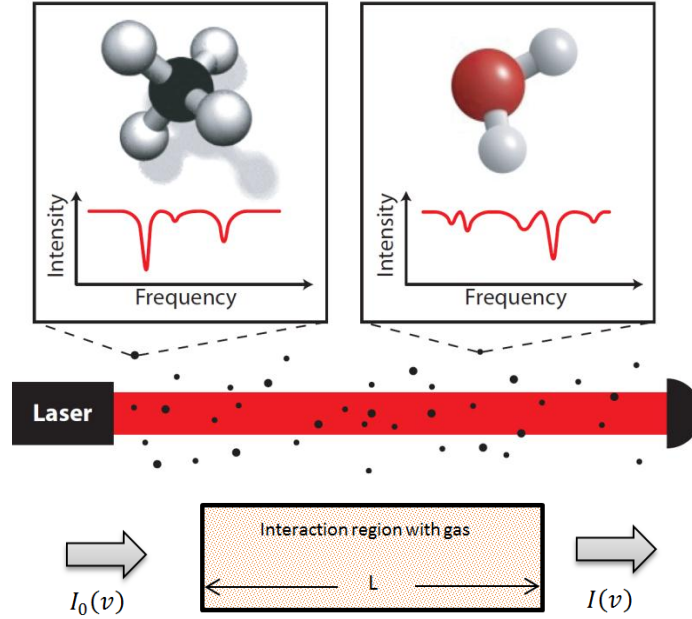


Figure 3.1: Schematic of laser absorption through a gas

$$T_v = \frac{I(v)}{I_0(v)} = e^{-k_v L} \quad (1)$$

The Beer-Lambert equation relates monochromatic (single frequency) laser beam transmission,  $T_v$ , over a known gas to interaction length,  $L$ , and spectral absorption coefficient,  $k_v$ , of the analyte gas [65]. Fractional transmission,  $T_v$ , is the ratio of incident laser intensity,  $I_0(v)$ , over transmitted laser intensity,  $I(v)$ , at a single laser beam frequency of  $v$ . Absorption coefficient,  $k_v$ , can be expressed with unit of  $\text{cm}^{-1}$  and  $L$  indicates in unit of  $\text{cm}$  [69]. Product of  $k_v$  and  $L$  is called absorbance and is a function of gas concentration, temperature and pressure. The laser amplitude is rapidly tuned around absorption features of the gas to determine the line shapes of the spectral absorption and the laser light output is recorded by a photo detector. Figure 3.2 shows (a) a simple scan of laser intensity that was recorded in our laboratory and (b) the normalised absorbance for methane around a wavelength of 1666 nm.

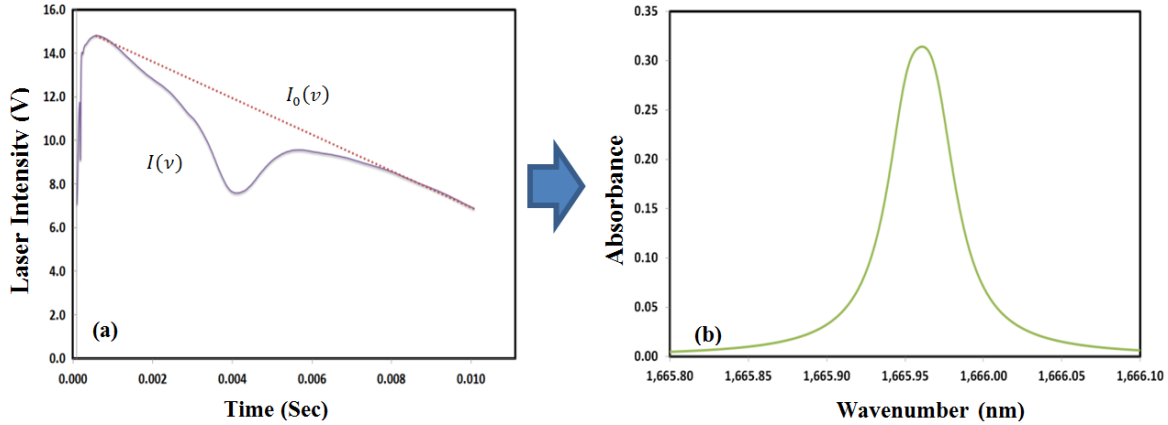


Figure 3.2: (a) A tuneable laser scan across a methane absorption feature (b) and the normalised absorbance near 1666 nm

As shown in Figure 3.2a,  $I$  is transmitted laser intensity and  $I_0$  is the incident laser intensity. The deepest point in Figure 3.2a, time=0.004 Sec, corresponds to 1666 nm laser wavelength. As explained from Beer-Lambert law transmission in 1666 nm line centre,  $I/I_0$ , corresponds to methane gas concentration. Normalised absorbance peak in Figure 3.2b, which is calculated using the high resolution transmission molecular absorption (HITRAN) database for 10 % methane in a 10 cm interaction length, demonstrates the transmission in Figure 3.2a.

The proposed system in this study (all-fibre methane sensors) operates based on NIR absorption spectroscopy using distributed feedback (DFB) laser sources. In this method, the laser beam interacts with the gas in the sensor head and is absorbed if its wavelength corresponds to a methane transition. There are two basic types of sensor heads: extrinsic and intrinsic. Extrinsic sensor heads are sensors in which the laser beam interacts with the gas outside of the fibre (Figure 3.3a). Intrinsic (all-fibre) gas sensor heads operate based on the interaction of gas with a section of the fibre core or its evanescent field (Figure 3.3b).

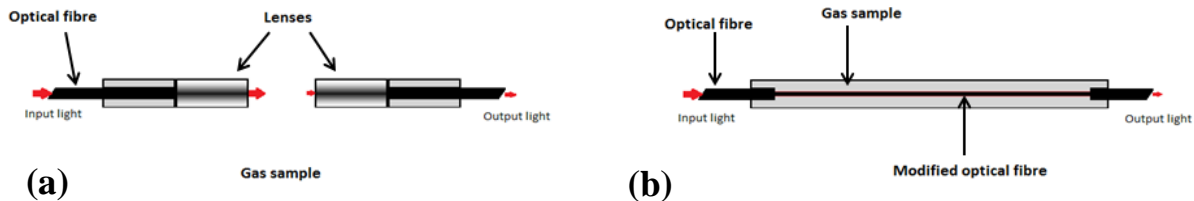


Figure 3.3: Schematic of a spectroscopic based (a) extrinsic optical (open-path) gas sensor and (b) intrinsic fibre based (all-fibre) gas sensor

The length of interaction is critical for spectroscopic measurements. Due to the nature of lenses, extrinsic sensor heads are involved with optical losses. All-fibre sensor heads have the advantage of flexibility in implementation, being electromagnetically passive with lower optical losses, over extrinsic sensor heads. There are numerous types of all-fibre sensor heads that allow laser light transmitting through the fibre to interact with the surrounding atmosphere including: bended fibres [70], one side polished or D-fibres [71], sol-gel cladded fibres [72], tapered fibres [33, 71, 73], U-shaped fibres, coil shape sensors [74], and micro drilled Hollow core fibres (HCFs) [75]. In this study, three different types of all-fibre sensor heads (namely tapered fibre, drilled single mode. and drilled HCF) have been developed and experimentally tested. In Section 3.3, different kinds of all-fibre sensor heads are explained and previous works are studied.

## 3.2 Spectroscopy Techniques

### 3.2.1 Theory of Absorption Spectroscopy

Recent development and implementation of narrow band laser light has simplified absorption spectroscopy measurement of gases, as it can be treated as a monochromatic beam [76]. Diode laser absorption spectroscopy of a gas depends on spectral absorption line characteristics, including line position, strength, and shape. These features are the basics of spectroscopic measurements [77]. In this section, the basic theory of these parameters is explained. An understanding of the theory is particularly important in choosing appropriate laser wavelengths and in the study of temperature or pressure effects on the absorption measurements.

#### 3.2.1.1 Line Strength

In the Beer-Lambert equation, Equation 1, the spectral absorption coefficient is the main function relating gas characteristics to light intensity change. If there are several absorption features in a particular spectral region that are adequately wide-ranging in the way they overlap each other, the total absorption coefficient at the given frequency (wavelength) is calculated by summing up the spectral absorption coefficients of each transition [69]. Equation 2 shows a formula for multi absorption features, where  $i$  is the index of a known transition and  $N$  is the number of investigated transitions [78].

$$k_{\nu} = \sum_{i=1}^N S_i(T) \cdot \varphi(T, P, X_i) \cdot P \cdot X_i \quad (2)$$

Hence, the spectral absorption coefficient,  $k_\nu$ , is related to line shape function ( $\varphi[\text{cm}]$ ), line strength ( $S[\text{cm}^{-2}/\text{atm}]$ ), and partial pressure ( $P_i[\text{atm}]$ ) [69, 79]. If a narrow absorption band is chosen, small transitions could be neglected in comparison with the main absorption band. Absorption coefficient is a function of line strength, temperature and partial pressure. Partial pressure is a measure for gas concentration in a mixture. Partial pressure ( $P_i[\text{atm}]$ ) is a product of total gas mixture pressure,  $P$ , multiplied by target gas mole fraction,  $X_i[\text{mol/mol}]$ . Species mole fraction is correlated to the target gas concentration in a mixture. Therefore mole fraction and concentration are used interchangeably in this study. Line strength and line shape function need to be calculated in order to have this relation as a function of environmental characteristics.

Line strength can be expressed in the unit of  $\text{cm}^{-2}/\text{atm}$ . Equation 3 shows the line strength as a function of temperature for a known absorption feature [65]:

$$S(T) = \frac{h\nu_0 B_{12}}{k_B T} \cdot \frac{g_1 \cdot e^{\left(\frac{-hc E''}{k_B T}\right)}}{Q(T)} \cdot \left(1 - e^{\left(\frac{-hc\nu}{k_B T}\right)}\right) \quad (3)$$

Where,  $h$  is Planck's constant  $6.63 \times 10^{-34} \text{ J}\cdot\text{s}$ ,  $\nu_0[\text{cm}^{-1}]$  is the transition frequency,  $B_{12}$  is Einstein's coefficient for probability deduce absorption from state 1 to 2,  $c[3 \times 10^{10} \text{ cm/sec}]$  is the light speed, Boltzmann's constant is presented by  $k_B[1.381 \times 10^{-23} \text{ J/K}]$ , the lower state energy of transition is denoted by  $E''[\text{cm}^{-1}]$  and  $Q(T)$  is the absorbing molecule's temperature-dependent partition function. [69, 77]. Equation 4 delineates partition function. Coefficients a, b, and c are calculated for different molecules and are given in HITRAN database [80, 81].

$$Q(T) = a + bT + cT^2 + dT^3 \quad (4)$$

### 3.2.1.2 Line Shape Function

Line shape function shows the way each atom and molecule interacts with laser light in different frequencies [69]. Line shape function  $\varphi(\nu)$  expresses the variation of the spectral absorption coefficient for a particular transition line as a function of frequency. A sample line shape function is shown in Figure 3.4. Frequency variation of line shape function results from broadening mechanisms in the gas environment that disturb the energy transitions.

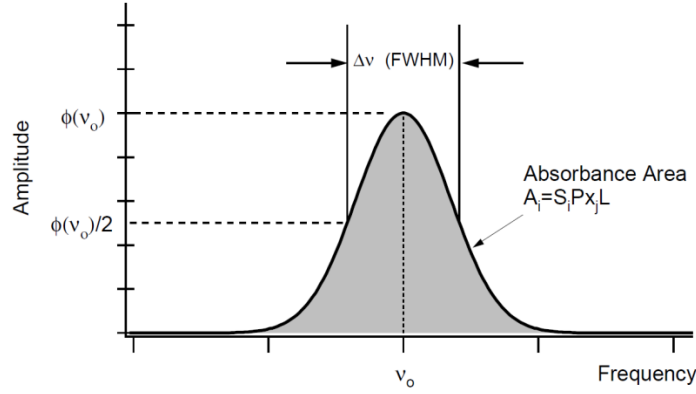


Figure 3.4: Sample line shape function as a function of frequency [80]

Line shape function is affected by medium parameters such as pressure, temperature, and gas composition. The dependence of the line shape function on different physical mechanisms can be described and can be evaluated using Gaussian, Lorentzian, or Voigt line shape functions depending on the temperature and pressure range of interest [77]. As Equation 5 shows, Gaussian, Lorentzian, and Voigt functions are all defined as unity functions.

$$\int_{-\infty}^{\infty} \varphi(\nu) d\nu = 1 \quad (5)$$

Equation 6 can be derived from Equations 5 and 2. In this equation,  $A$  [ $\text{cm}^{-1}$ ] is defined as integrated absorbance where integration upon frequency space is applied on  $k_\nu L$ . Integrated absorption is obtained as a function of partial pressure, line strength and transmission length.

$$A = \int_{-\infty}^{\infty} k_\nu L d\nu = \int_{-\infty}^{\infty} S(T) \cdot P_i \cdot L \cdot \varphi(\nu) \cdot d\nu = S(T) \cdot P_i \cdot L \quad (6)$$

Besides HITRAN database, other models and many studies have measured line strength and broadening effects of methane transition bands in various temperatures and pressures [78, 82-85].

### 3.2.2 Direct Absorption Spectroscopy

Direct absorption spectroscopy (DAS) has two main techniques which are: fixed wavelength and scanned wavelength absorption measurements. Scanned wavelength has more advantages over the fixed wavelength absorption measurement since complicated quantitative calculations of line shape is required for accurate measurements using fixed wavelength DAS. Moreover, in fixed

wavelength, calibration is necessary to ensure the right laser frequency. Each technique is explained and the basic theory is presented in this section.

### 3.2.2.1 Scanned-Wavelength Absorption

Scanned wavelength absorption spectroscopy has proved to be more effective for narrow absorption features. It is the mostly used method for DAS due to its simplicity and accuracy of measurements [86]. Unlike the fixed wavelength, laser frequency is adjusted upon the absorption and non-absorbing wings [69]. The shape of this output is like a saw tooth, also known as a ramp wave. The advantage of this technique is that its result includes all of the absorption line shape, which provides the opportunity to omit uncertainties from the line shape function by calculating the integration over frequency. Moreover, it eliminates the need for non-absorbing beam measurements. In Figure 3.5, a schematic of a scanned wavelength gas absorption spectroscopy is illustrated.

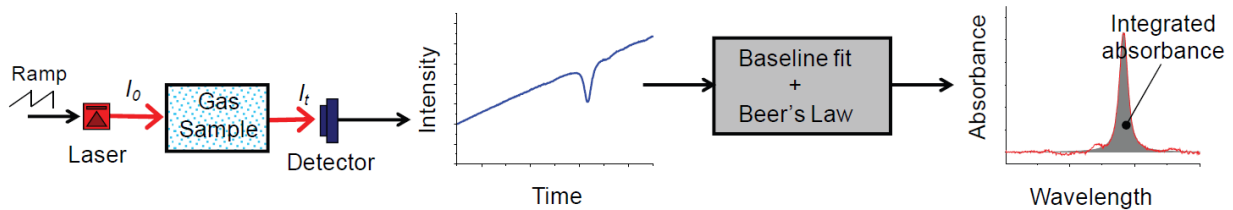


Figure 3.5: A schematic of scanned-wavelength direct absorption spectroscopy with a tuneable laser [86]

There are two major gas characteristic tracing methods using scanned wavelength absorption and extracted integrated absorbance information; they are direct absorption thermometry and concentration. As discussed in the previous section, line strength varies with the temperature for a particular absorption transition (refer to Equation 5). In ratio-based thermometry, the ratio of integrated absorbance in two different line strengths at a reference temperature is used to determine an unknown temperature using its measured ratio. The ratio-based thermometry technique has been used in harsh environments and utilised as an effective technique [69].

Direct absorption concentration (DAC) is used where temperature and pressure are known or do not have significant effects; gas concentration can be determined from the absorption of a transmission (using a laser with either a fixed or a scanned wavelength). Equation 7 shows the direct absorption concentration calculation using integrated absorbance of a scanned wavelength.

$$X_i = \frac{A}{S(T).P.L} \quad (7)$$

### 3.2.2.2 Fixed-Wavelength Absorption

The fixed-wavelength method is known as an uncomplicated and simple technique to utilize. This technique can be found by a laser source with a tuned frequency at the absorption transition peak of the gas specie. The system is fixed for the gas of interest and transmitted laser intensity is recorded directly from PD in an oscilloscope or in a computer based system with a high speed A/D, with frequency around MHz. Transmitted intensity is recorded for different gas concentrations and temperatures.

From the Beer-Lambert law, Equation 1, the formulation for a fixed-wavelength laser system could be run as found in Equation 8:

$$I(v_{Line\ Centre}) = I_0(v_{Line\ Centre}).\beta.\exp(-k_v L) \approx I_0.\beta.(1 - k_v L) \quad (8)$$

Where,  $I_0$  is input intensity and  $\beta$  is all losses except absorption line losses (e.g. optical losses). Equation 8 is expanded for weak absorptions with Taylor series (where  $k_v.L \ll 1$ ).

If all losses, laser intensity input, and wavelength are constant, Equation 8 can be changed to a linear relation between gas concentration ( $X_i$ ) and measured signal amplitude, as shown in Equation 9.

$$I(v_{LineCentre}) \propto 1 - S(T).\phi_{Linecentre}.P.X_i.L \quad (9)$$

Significant advantages of this technique are the fast responses and uncomplicated nature of the design. This technique is used in this study for estimation of developed sensor head response time. There are also some disadvantages involved with this method. Firstly, this system needs calibration. Secondly, there are difficulties in obtaining the intensity of a non-absorbing baseline. Lastly, complicated quantitative calculations are needed to obtain environmental results. In order to overcome the second problem, a non-absorbing beam should be used to detect the intensity of the baseline, which is used in transmission calculations. Calibration for a non-absorbing cell at various temperatures and concentrations could be used as a predetermined factor in a database that can obtain both temperature or concentration with a good approximation [69].

### 3.2.3 Wavelength Modulation Absorption Spectroscopy

This section provides an overview of WMS theory and previous studies on methane gas WMS measurements. Formulations and different methods based on WMS are reviewed and discussed in depth. Wavelength modulation spectroscopy is very similar to the DAS with scanned-wavelength method. The main difference between these methods is the additional sinusoidal laser modulation in WMS.

#### 3.2.3.1 Measurement of WMS Second Harmonic

In the wavelength modulation method, the wavelength of a laser is modulated using a low frequency ramp signal with an additional high frequency sine wave ( $f$ ), with the frequency to half width of the absorption features (HWHM) of less than  $0.05 \text{ cm}^{-1}$  or  $1.5 \text{ GHz}$  [65]. The laser beam intensity changes after passing through the absorbing gas at the central absorption wavelength. Figure 3.6 shows a low slope linear WMS scan and the additional high frequency sinusoidal signal using VCSEL (vertical cavity surface emitting laser) with absorption from oxygen recorded at Stanford wind tunnel WMS laboratory [65].

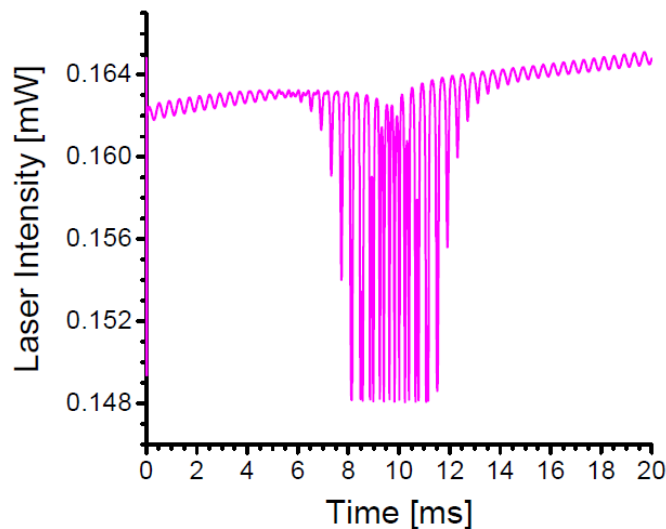


Figure 3.6: An example of WMS output VCSEL scan with absorption ( $m=1.8, 50\text{Hz}$  ramp,  $2500\text{Hz}$  modulation) [65]

Fourier analysis of the transmitted laser beam gives harmonic components of the signal. The detected WMS signal needs to pass from several lock in amplifiers (LIAs), with reference to sinusoidal signals at the desired frequency ( $2f$  or  $1f$ ), then a low pass filter should be applied to remove all noises outside its bandwidth. The interaction between the additional sinusoid modulation and the nonlinear absorption characteristic cause a stronger second harmonic signal



in the output beam. Generally, the second and first harmonic signals of WMS have been used to sensitively trace gas species attributes [87]. Figure 3.7 illustrates inputs and outputs of the WMS system [86].

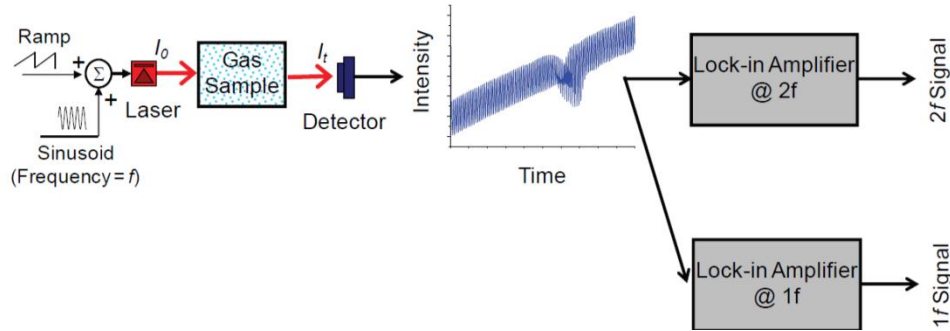


Figure 3.7: A schematic of wavelength modulation spectroscopy to detect second harmonic (2f) and first harmonic (1f) [86]

The second harmonic is sensitive to the entire absorption feature of the gas; therefore, it is suitable for high density spectra and broadened absorptions. Moreover, to detect the second harmonic the LIA is used, which decreases noises associated with intensity modulation and electronics [86]. It is critical to either tune phase the LIA reference with the same phase as the detected harmonics signal or use a lock in approach with intensive phase [64, 86, 88]. Figure 3.8 illustrates second harmonic and first harmonic signals obtained from a WMS signal at a gas absorption centre.

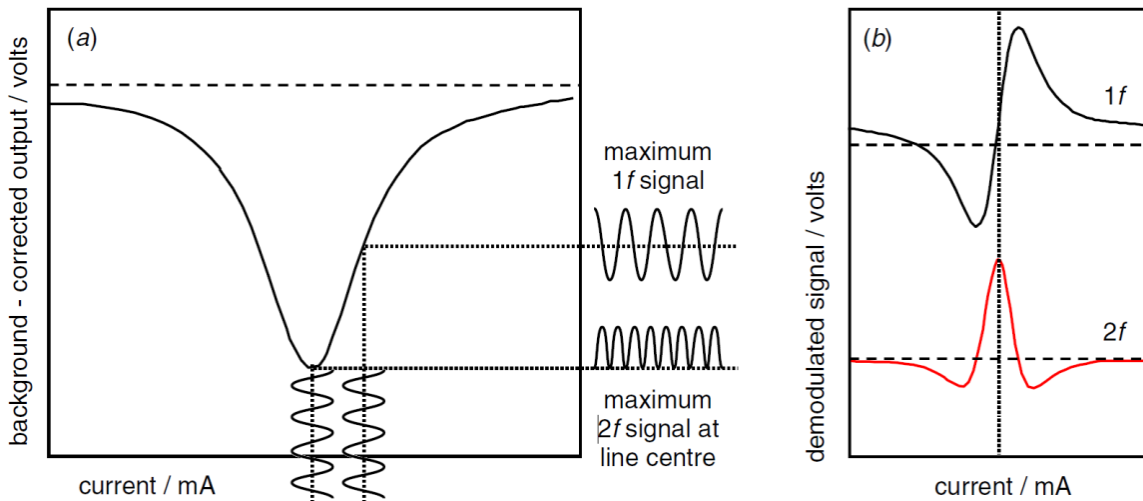


Figure 3.8: WMS measurements. (a) Normalised DC scan through gas absorption. (b) Fundamental frequency (1f) signal and, second harmonic (2f) signal (after[89])

The following backgrounds should be subtracted or avoided before measurements can be directly used in the WMS model:

- Background signal along light pass (Etalon effects);
- Background laser signal produced by nonlinear intensity modulation; and
- Absorption by other gases.

Etalon effects along an optical pass are caused by the reflection of parallel parts which by the nature of their wavelength dependency can cause false 2f signals. Firstly, these effects should be taken into consideration during sensor design because an incorrect design produces an unstable signal and cannot be completely removed from a measured second harmonic. It has been found, using a 1° to 3° wedge on the face of windows or fibres along the optical pass, that the Etalon effects can be effectively reduced below other noise sources [86]. However, by their nature, all-fibre sensors do not express Etalon effects when used as sensing heads. The other two background noises would be avoided by choosing an appropriate signal generator or WMS model and an interference-free absorption centre for the laser wavelength.

### 3.2.3.2 Wavelength Modulation Spectroscopy Model

Using a simulation of the experimental processes, incident laser intensity can be written as:

$$I_0(t) = \bar{I}_0 [1 + i_0 \cos(\omega t + \varphi_1) + i_2 \cos(2\omega t + \varphi_2)] \quad (10)$$

Hence average of laser intensity is  $\bar{I}_0$ ,  $i_0$  is amplitude of linear (1f) and  $i_2$  is amplitude of nonlinear modulation, phase shifts between wavelength modulation and laser intensity modulation is presented by  $\varphi_1$  and  $\varphi_2$  for linear and nonlinear modulations, respectively. All of these parameters ( $i_0, i_2, \varphi_2, \varphi_1$ ) are just related to laser characteristics and need to be measured in the laboratory. Li [87] has presented a complete procedure for measuring these parameters. In this method, the nonlinear term of intensity modulation phase shift and amplitude are determined with the best first order fit to modulation. An example of this fitting is presented in Figure 3.9.

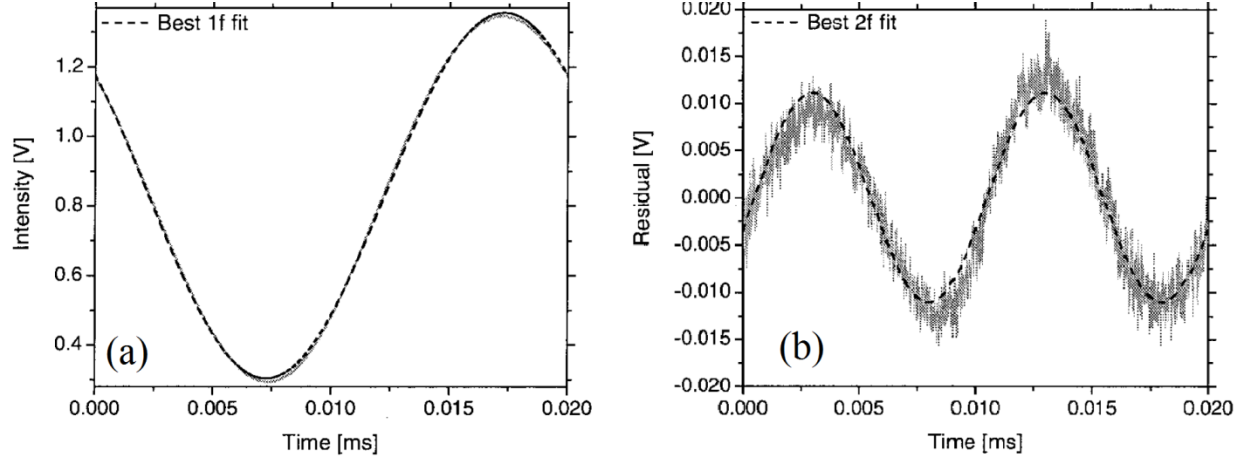


Figure 3.9: An example of best fit for 1 and 2f to intensity modulation [87]

### 3.2.3.3 Second Harmonic Normalisation to First Harmonic

Calibration could be a big drawback for commercializing a detection system. Thus, many studies recently have been done to develop a calibration free WMS-2f method to detect gas traces [90-93]. This section will discuss all aspects of second harmonic normalisation by first harmonic centre. Nonlinear intensity modulation introduces noise in the second harmonic of absorption and non-absorption signals. WMS-2f has been modelled to subtract nonlinear modulation from measured 2f (and simulated models) to find a linear relationship between the second harmonic and gas concentration. The lock in phase-intensive measurement is used to model the laser modulation characteristics for finding the output signal of 2f/1f as a function of known parameters. This model has been used and verified in many other similar studies [81, 86-88, 93], for example  $CO_2$  and  $H_2O$  are modelled for different frequencies and modulation amplitudes at different pressures and temperatures (up to 900K and 30 atm) [87]. The measured second harmonic needs to be normalised if there is a background noise or nonlinear modulation noise which may, in practice, exist. One approach is second harmonic normalisation using the first harmonic signal as shown in Equation 11 [86].

$$\frac{WMS_{2f}}{WMS_{1f}} = \sqrt{\left[ \left( \frac{X_{2f}}{R_{1f}} \right)_{raw} - \left( \frac{X_{2f}}{R_{1f}} \right)_{bg} \right]^2 + \left[ \left( \frac{Y_{2f}}{R_{1f}} \right)_{raw} - \left( \frac{Y_{2f}}{R_{1f}} \right)_{bg} \right]^2} \quad (11)$$

Hence,  $X_{2f}$  and  $Y_{2f}$  are X and Y components of the lock in amplifier outputs at 2f frequency and  $R_{1f}$  is the Root Sum Square (RMS) magnitude of X and Y components of the LIA output at the frequency of 1f. Raw refers to the WMS signal contains interest signal and background (bg)

noises, and  $bg$  refers to the signal measurement in the absence of absorption or without the optical path. This method was first suggested by Li [87]. It explains a calibration free WMS measurement, which uses a synchronized modulated laser source to come up with a method that has fewer drawbacks than all other previous methods and is also suitable for harsh environments. The first harmonic is used to normalise the second harmonic signal. This normalisation removes many disturbances of laser intensity and fibre optics which cannot be neglected in harsh environments, especially at high pressures and high temperatures.

While there is a saw tooth current in addition to intensity modulation (as described in previous sections), values of  $\bar{I}_0, i_0, i_2$  vary through the ramp. The values need to be calculated just at the second harmonic peak to determine gas traces. Hence, the modulated laser frequency over time is  $\nu(t) = \bar{\nu} + a\cos\omega t$ . Where  $\bar{\nu}$  is the average laser wavelength, and frequency modulation amplitude is denoted by  $a$ .

Insensitive phase lock in components (X and Y),  $\cos 2\omega t$  and  $\sin 2\omega t$  signals functioning as reference signals, are multiplied by detector signals to respectively simulate X and Y components of the second harmonic. These are shown in equations 12 and 13. Since there is a low pass filter in lock in, only DC components come out [86].

$$X_{2f} = \frac{G\bar{I}_0}{2} \left[ H_2 + \frac{i_0}{2} (H_1 + H_3) \cos \phi_1 + i_2 \left( H_0 + \frac{H_4}{2} \right) \cos \phi_2 \right] \quad (12)$$

$$Y_{2f} = \frac{G\bar{I}_0}{2} \left[ \frac{i_0}{2} (H_1 - H_3) \sin \phi_1 + i_2 \left( H_0 - \frac{H_4}{2} \right) \sin \phi_2 \right] \quad (13)$$

Hence, the detection system has an electro-optical gain of  $G$ ; and  $H_k$  shows  $k^{\text{th}}$  harmonic components. Electro-optical gain does not need to be calculated or measured because it will be cancelled by normalisation of the second harmonic. In the same way, X and Y components of the first harmonic can be modelled as:

$$X_{1f} = \frac{G\bar{I}_0}{2} \left[ H_1 + i_0 \left( H_0 + \frac{H_2}{2} \right) \cos \phi_1 + \frac{i_2}{2} (H_1 + H_3) \cos \phi_2 \right] \quad (14)$$

$$Y_{1f} = \frac{G\bar{I}_0}{2} \left[ i_0 \left( H_0 - \frac{H_2}{2} \right) \sin \phi_1 + \frac{i_2}{2} (H_1 - H_3) \sin \phi_2 \right] \quad (15)$$

The RMS (Root Mean Square) value of the first harmonic is calculated, as follows:

$$R_{1f} = \sqrt{X_{1f}^2 + Y_{1f}^2} = \frac{GI_0}{2} \left[ \left[ H_1 + i_0 \left( H_0 + \frac{H_2}{2} \right) \cos \varphi_1 + \frac{i_2}{2} (H_1 + H_3) \cos \varphi_2 \right]^2 + \left[ i_0 \left( H_0 - \frac{H_2}{2} \right) \sin \varphi_1 + \frac{i_2}{2} (H_1 - H_3) \sin \varphi_2 \right]^2 \right]^{\frac{1}{2}} \quad (16)$$

Reiker [86] used these equations to develop a pre-calculated model to simulate the first and second harmonics of a known tuned laser for a specific absorption feature and a non-absorbing condition. It was shown that all hardware related parameters, such as G optical gain, sensitivity of detector, lock-ins gain, and modulation intensity variations, could be eliminated using this model.

This model is simplified to calculate gas parameters as Equation 17. The Taylor series' first two terms are used in Beer-Lambert law to abridge the second harmonic to the first harmonic for absorbance less than 0.05, as shown in Equation 17. A proper absorption feature and modulation index (m=2.2) could reduce uncertainties to almost %5 [87, 94]. This is valid for almost all absorbance features of methane in the Near Infrared (NIR).

$$\frac{WMS_{2f}}{WMS_{1f}} \approx \frac{H_2}{i_0} = \frac{S(T).P.X_i.L}{i_0\pi} \int_{-\pi}^{\pi} \varphi(v(t)) \cos 2\theta d\theta \quad (17)$$

### 3.2.3.4 WMS-2f Peak to Peak Ratio Normalisation to DC Output

Henningsen *et al.* [95] developed a quantitative method to analyse the second harmonic signal for absorption features with no distortion on the wings. The devised algorithm has been used to derive the absolute concentration (where pressure and temperature are known) from a peak to peak ratio, line width and modulation depth of second harmonic signal (2f) measurements [86].

In wavelength spectroscopy, laser frequency is modulated such that  $v(t) = v + v_m \sin \omega_m t$ , so the second harmonic line shape (which is detected by an LIA) is recovering an RMS value of 2f as shown in Equation 18. It is assumed that the DC detector voltage is normalizing the output of lock in.

$$WMS_{2f} = \frac{1}{\sqrt{2}} .L.P.X_i.S.\varphi_{2h} \quad (18)$$

Where:

$$\varphi_{2h} = \frac{1}{\pi} \int_0^{2\pi} \varphi(v + v_m \sin(\omega_m t) - v_0) \cos(2\omega_m t) d\omega_m t \quad (19)$$

From the Taylor series, where line width is much larger than the modulation amplitude  $v_m$ , the line shape function can be written as:

$$\varphi(v + v_m \sin(\omega_m t) - v_0) = \varphi(v - v_0) + \varphi'(v - v_0) \cdot v_m \cdot \sin(\omega_m t) + \varphi''(v - v_0) \cdot v_m^2 \cdot (1 - \cos(2\omega_m t)) \quad (20)$$

Hence,  $\varphi(v - v_0)$  is the area normalised by the line shape function. From Equations 19 and 20, the second harmonic signal is found to be proportional to the second derivative of line shape function in weak modulations.

$$WMS_{2f} = \frac{1}{4\sqrt{2}} \cdot L \cdot P \cdot X_i \cdot S \cdot v_m^2 \cdot \varphi''(v - v_0) \quad (21)$$

Where  $g_v(0)$  is the maximum of the Voigt profile for normalised line shape function, peak absorbance is expressed in Equation 22:

$$\gamma(0) = 2.171 \cdot 10^{20} * X_i [mol/mol] * L [m] \frac{P [Pa]}{T [K]} S [cm/mol] * g_v(0) [GHz^{-1}]$$

(22)

At ambient pressure, using Lorents limit, a good approximation of the Voigt profile in maximum point can be written as Equation 23.

$$g_v(0) \approx g_L(0) = \frac{1}{\pi \Delta v_L} \quad (23)$$

In Equation 24, the function F is introduced based on the Voigt profile for half width at half maximum (HWHM) values. F is a function of modulation depth ( $b = \frac{v_m}{\Delta v}$ ), where  $0.5 < \Delta v < 2.5 GHz$  and modulation amplitude is  $0.1 < v_m < 12.5 GHz$ .

$$(g_1 + g_2) \pi \Delta v = F(b) \quad (24)$$

Hence, the second harmonic upper and lower amplitude peaks are  $g_1$  and  $g_2$ , respectively (Figure 3.10).

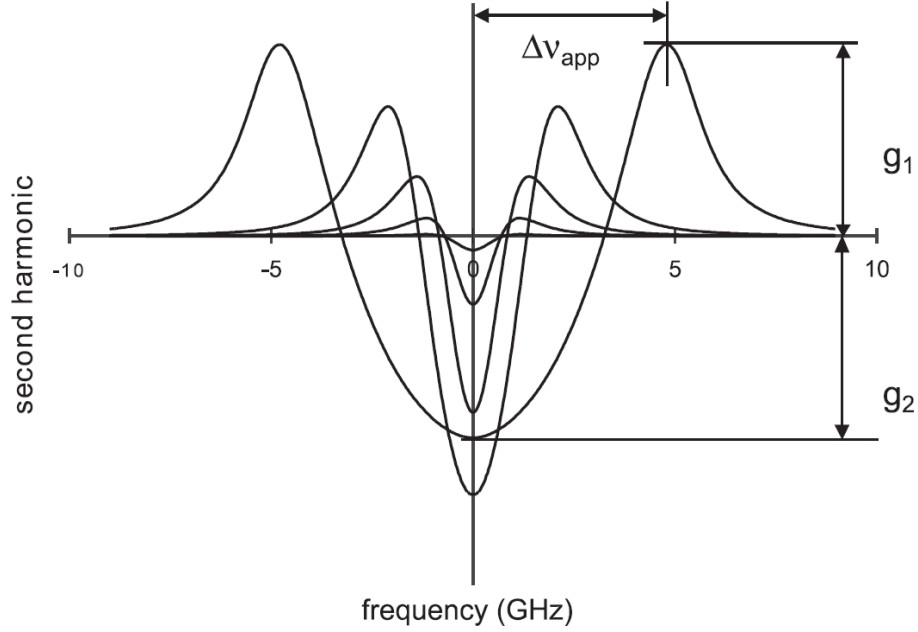


Figure 3.10: Second harmonic profile broadening for different modulation depth ( $b=0.2,0.5,1,2,5$ ) [95]

Using above equations the second harmonic peak to peak as a function of maximum absorbance is calculated [95].

$$WMS_{2f}^{P-P} = \gamma(0) \frac{F(b)}{\sqrt{2}} \quad (25)$$

From Equations 22, 23 and 25, the second harmonic peak to peak amplitude is obtained as follows:

$$WMS_{2f}^{P-P} = \frac{F(b)}{\sqrt{2\pi \Delta\nu[\text{GHz}]}} * 2.171 * 10^{20} * X_i [\text{mol/mol}] * L[\text{m}] \frac{P[\text{Pa}]}{T[\text{K}]} S[\text{cm/mol}] \quad (26)$$

From Equation 26, where the unknown parameter is concentration and other parameters are known, concentration can be obtained by measuring the peak to peak of the second harmonic output. Also the average DC modulation should be used to normalise the output and minimize the power fluctuation effects. In addition to absorption, the second harmonic magnitude varies with modulation depth, affected by function F. A high signal to noise ratio is feasible when the second harmonic signal is maximized in regards to the optimum modulation index. The modulation index is shown as below:

$$m = \frac{a}{\Delta\nu/2} \quad (27)$$

Here,  $a$  is modulation depth and  $\Delta\nu$  is the FWHM (full length at half the maximum) of absorption feature, which can be described by any of the line shape functions. The modulation index is known as the standard index to maximum sensitivity. Cao *et al.* [76] presented the harmonic amplitude ( $S_{2,amp}$ ), the second harmonic maximum ( $S_{2,max}$ ), and the first harmonic amplitude ( $S_{1,amp}$ ) of a methane WMS at 1654 nm as a function of the modulation index ( $m$ ) in Figure 3.11. The signals are maximised in the modulation index of 3.1, 2.2, and 2, respectively. Lyle [65] calculated a similar graph for the normalised second harmonic with the first harmonic as a function of at a  $2f/1f$  peak height as a function of the modulation index for a Voigt function. It has been proved that the maximum normalised second harmonic is achievable when the modulation index is  $m=2.2$ .

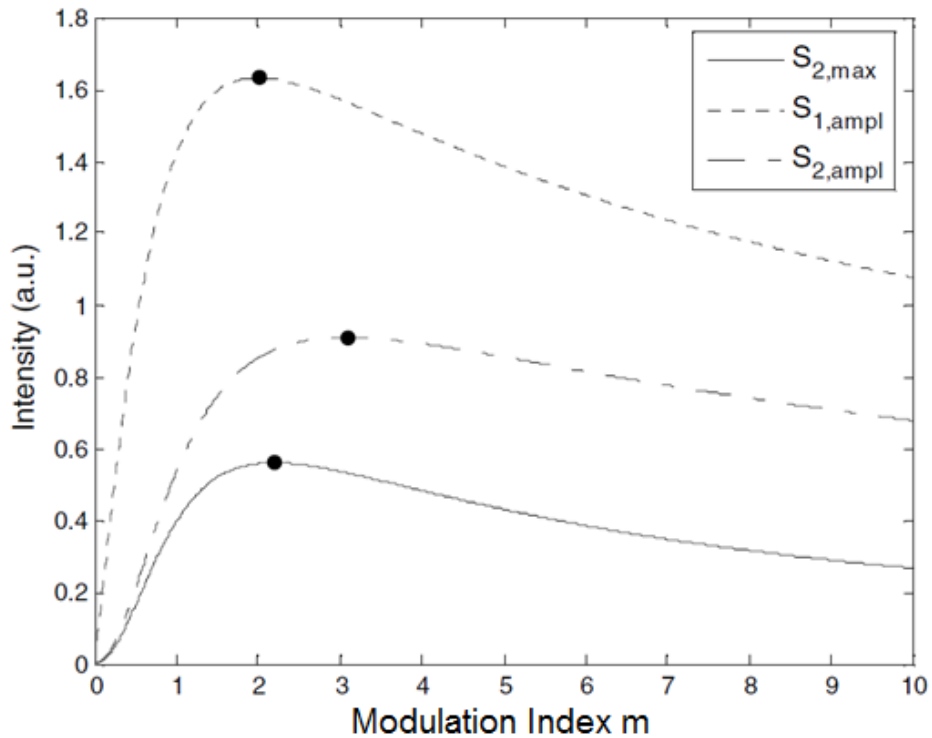


Figure 3.11: Second harmonic amplitude ( $S_{2,amp}$ ), Second harmonic maximum ( $S_{2,max}$ ), and first harmonic amplitude ( $S_{1,amp}$ ) as a function of modulation index ( $m$ ) [76]

### 3.2.3.5 Advantage and Uncertainties of Normalised WMS-2f

As shown in the last two sections, the first harmonic signal value at the peak of the second harmonic is highly correlated to the intensity modulation; therefore, they could be used interchangeably for normalisation. The first harmonic signal is detected with another LIA with reference to a  $1f$  frequency signal. This normalisation has the advantage of removing optical



disturbances in an optical system. The normalised second harmonic techniques are capable of producing accurate results in different environmental conditions (temperature, concentration, pressure, or path length) with any set of laser parameters as long as the model and experiment are compatible [86].

Figure 3.12 illustrates the normalised second harmonic signal advantages over an unadjusted second harmonic signal. The input beam has been partially blocked and vibrated, which didn't considerably disturb the  $2f/1f$  signal. Thus using  $2f/1f$  omits the uncertainties from rapid changes in laser intensity and voltage vibrations. Moreover, it minimizes the disturbance caused by dust in the sensor area. This contributes to less maintenance of the sensor head.

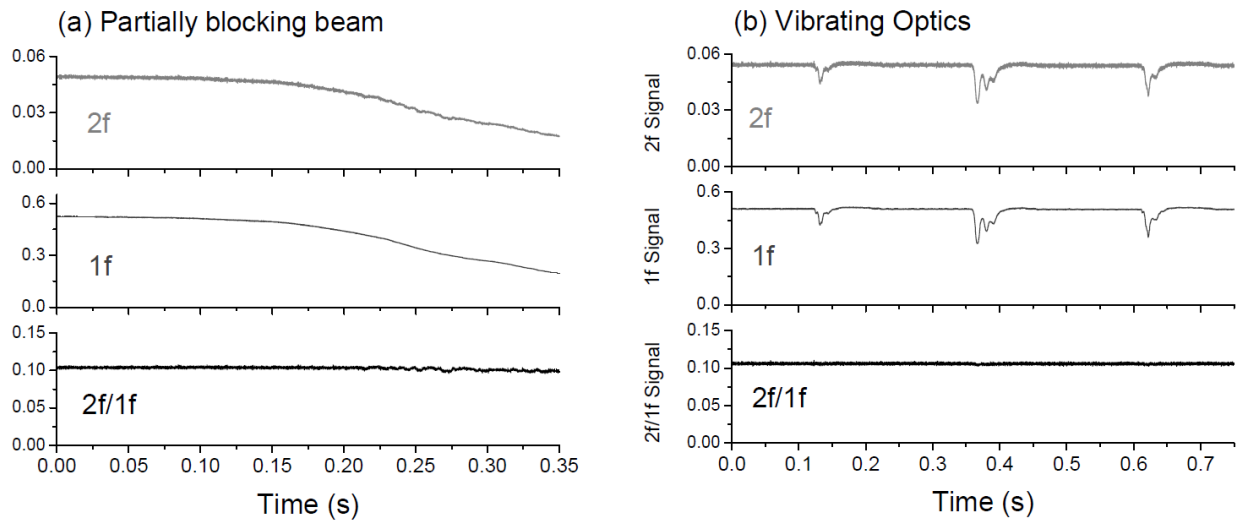


Figure 3.12: Normalisation against laser intensity disturbance [86]

There are still more advantages of a normalised second harmonic over other techniques, as a result of higher signal to noise ratio (SNR) of the second harmonic. This improvement depends on the conditions of a particular experiment, but it is between 2 to 100 times better than direct absorption's SNR. On the other hand, the second harmonic approximation with the first two orders of the Taylor series is not enough when wide optical depth is used to increase the signal to noise ratio. The general uncertainties, sources, and mitigations in this method have been presented in Table 3.1.

Table 3.1: Sources of uncertainties in wms-2f measurement [87, 96, 97]

<b>Source of Uncertainty</b>	<b>Description</b>	<b>Mitigation</b>
<b>Spectral parameters</b>	Absorption line features changes, Line strength and line shape broadening effect by temperature and pressure	Study the changes of pressure and temperature effects under controlled laboratory and use the parameters introduced in Section 3.2.3.2
<b>Laser tuning characteristics</b>	Error in laser tuning parameters could affect the calibration curve	Do not change laser modulation parameters for same calibration curve
<b>Background absorption</b>	Background absorption from other gases can affect the measurement	Choose appropriate wavelength with no cross-sensitivity
<b>Etalon effects</b>	Constructive/destructive interference arising from reflection in optical path can effect WMS measurements	APC Fibre connections and angled design of parts will minimise cavity to shape. Choosing modulation index is critical to minimize the effects. Also using HCF has less effect than GRIN lens in open-path
<b>Modulation amplitude</b>	Choosing large modulations could reduce linearity of WMS-2f signal relation to concentration	Choosing optimum modulation depth and amplitude, maximizing SNR and minimizing broadening effects

### 3.2.4 Other Gas Spectroscopy Techniques

There are other techniques employed to trace gas concentrations. However, in this study, WMS and DAS techniques are used due to their simplicity and suitability for fibre optic based gas concentration measurement. In this section some other techniques are briefly outlined to consider the possible value that other techniques might reveal in future studies.

McGettrick *et al.* [91, 92] developed a technique for a calibration-free WMS to measure gas concentrations with the first harmonic. This method recovers the line shape of direct absorption from the first harmonic. The recovered line shape can be used in data reduction methods the same as a direct absorption problem. This technique works very well in small modulation amplitudes, but the algorithm becomes very complicated when modulation amplitude is increased to obtain a higher signal to noise ratio. Additionally, like the peak to peak method, the laser must be tuned within all absorption features to detect and remove non-absorbing base lines

to normalise the laser intensity. This technique is challenging when the gas absorbing features are overlapped or the pressure broadening effect is presented [86].

Photoacoustic gas measurement is also known as the sensitive gas analysis technique [98]. Figure 3.13 shows a simple photoacoustic gas measurement setup. In this technique, an IR beam passes through the target gas and causes temperature and pressure variations. The beam is periodically disturbed by a chopper. Periodic changes in pressure produce an acoustic wave which is recorded by a capacitive microphone [98]. Despite the fact that this technique is highly sensitive as compared to WMS, it is not suitable for remote detection in environments with vibrations and acoustic noises [99].

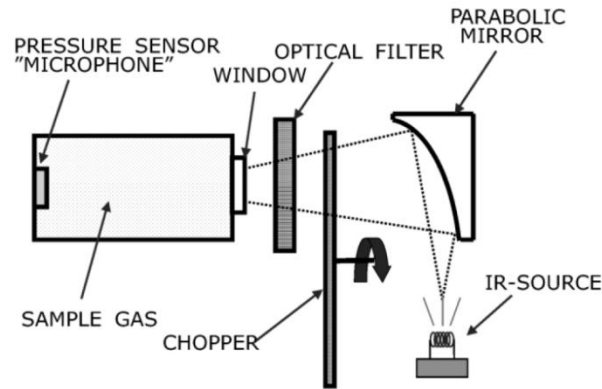


Figure 3.13: A simple photoacoustic gas measurement setup [100]

Cavity ring-down (CRD) spectroscopy has been used for high sensitivity gas absorption concentration measurements in the last decade [25, 101-103]. This method works based on the oscillation of a single frequency laser on absorption features of the target gas between two ideal mirrors. The oscillation cavity increases the interaction length to tens of kilometres [104]. The ring-down signal loss and time are correlated to gas concentration. Figure 3.14 illustrates a CRD schematic.

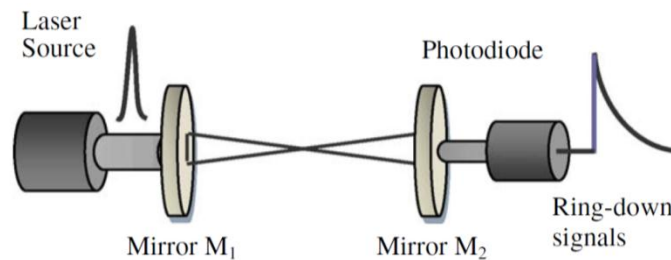


Figure 3.14: Cavity ring-down (CRD) schematic [25]

There are mainly two approaches to forming cavities: fibre bragg grating (FBG) and fibre loop. A fibre could be simply looped to form a cavity (Figure 3.15b), or two commercially available narrow band FBGs could be used as a cavity mirror in a single fibre (Figure 3.15a). The fibre loop method is broad band, which is ideal for multi gas detection using multi wavelength detection. A micro-cell between two mirrors or couplers can accommodate gas interaction with laser light. The PCF-microcell has received a great deal of attention in the last few years for all-fibre CRD gas sensing [105-107].

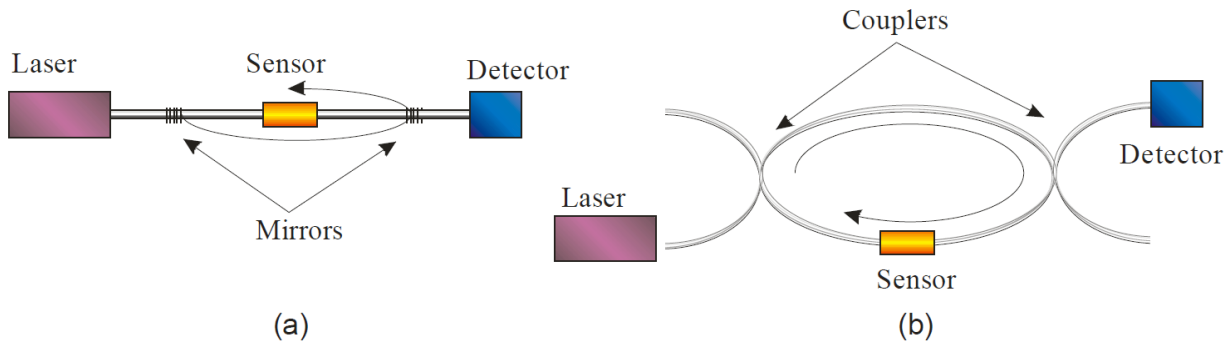


Figure 3.15: (a) fibre cavity using linear FBG cavity setup. (b) Setup of a fibre loop cavity [101]

To the best of the author’s knowledge, as of this date, there has been no research conducted that takes full advantage of the potential CRD offers for multi gas detection—neither the advantages of FBG-microcells nor the PCF-microcells [101]. Investigations into a very sensitive multi-gas all-fibre sensor using CRD for underground coal mines present a great opportunity for future works.

# CHAPTER 4

## ALL-FIBRE GAS SENSORS

### 4.1 Introduction

This chapter focuses on the characteristics and basics of optical fibres and gas sensors developed based on optical fibres. Optical fibres are used to guide a light beam through a small size and flexible media. Plastic and silica in various settings are used to design optical fibres. The major applications of fibre optics have been in the telecommunication industry; they have been used as a low consumption data transmission solution with high bandwidths over long transmission distances. Optical fibres usually have a main core and a cladding. Normally the core guides the main portion of light and the cladding is used to reflect the light and keep it guided within the core. Figure 4.1 shows typical fibre optics designed for data transmission.

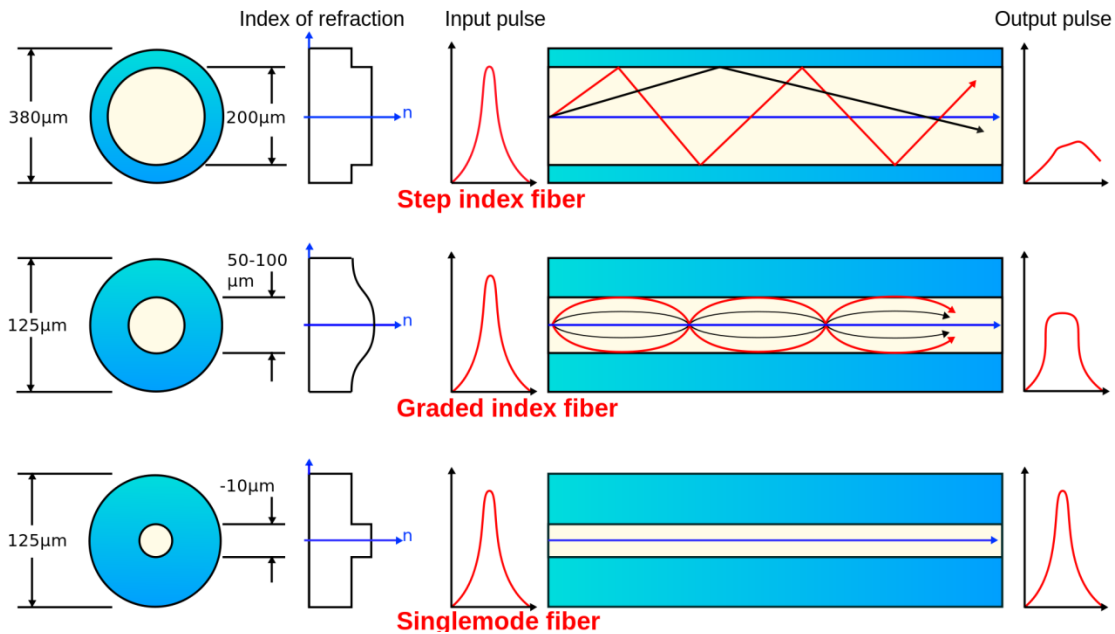


Figure 4.1: Typical optical fibres used for data transmission [108]

### 4.1.1 Single-mode Fibres

Single mode fibre (SMF) has been the most common and cheapest fibre on the market since the mid-20<sup>th</sup> century [109]. The wide use of SMFs in telecommunications—aside from the industry’s research and development activities—has steered the current SMF technology very close to the basic theory. As shown in Figure 4.1, SMFs function according to the different reflection indices of the silica material used in the core and cladding. Attenuation and dispersion, as a result of scattering and material absorption, limit the transmission distance. Attenuation depends on applied wavelength. Figure 4.2 presents a conventional SMF attenuation graph. Attenuation is around 0.3db/km within U-band (1652nm-1675nm) which is a methane absorption wavelength.

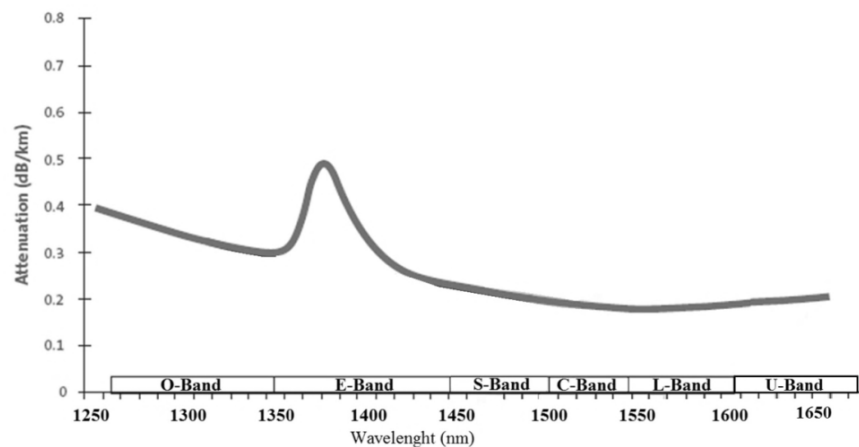


Figure 4.2: Conventional single mode fibre attenuation in different bands (After SMF-28 datasheet [110])

SMFs have been used in many different arrangements including fibre gratings [109, 111, 112], and tapered fibres [113-115], to develop sensor heads. Detailed specifications of the SMFs used in our experiments can be found in Appendices III and V.

#### 4.1.2 Photonic Crystal Fibre (PCF)

Photonic crystal fibres (PCFs), first developed in 1999, are specially designed fibres with multiple enclosed channels running inside the length of the silica fibre [116]. They have opened a wide range of applications in sensing and telecommunications. There are mainly two kinds of PCFs including the index guiding and the photonic band gap (PBG) (Figure 4.3) [117].

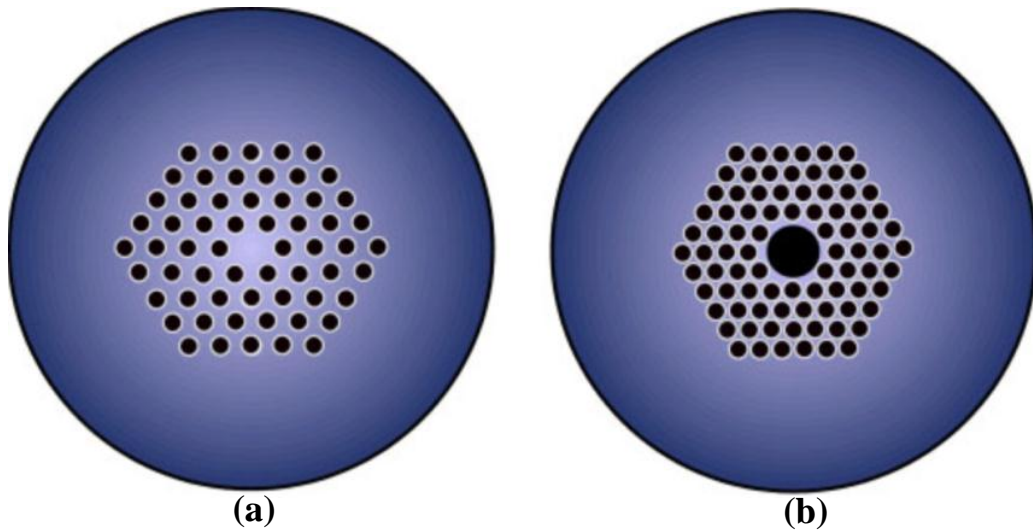


Figure 4.3: Photonic Crystal Fibre (PCF) arrangements. (a) index guiding; (b) PBG [117]

The photonic band gap fibres have a hollow core which is surrounded by microstructure air holes. Thus, these fibres are also named hollow core photonic crystal fibres (HC-PCFs). Multilayer holes with specific angles and sizes reflect a range of wavelengths which make a perfect mirror called a PBG. HCFs guide the light based on the PBG that occurs due to the periodic structure of the cladding [118]. Unlike SMFs, most of the light is confined in the hollow core owing to the shaped PBG in the cladding [119]. This effect can also be seen in nature. Butterfly wings have micro holes shaping a PBG which produces a colourful reflection of light (Figure 4.4).

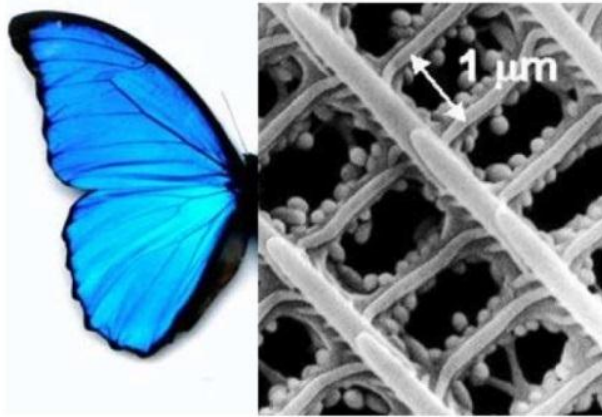


Figure 4.4: Photonic crystal band gap effect found in *Cyanophrys remus* butterflies [30]

There are different characteristics (air hole diameters, holes separation, and structure) to be considered in the design of HCFs which result in various arrangements and types of HC-PCFs [120]. There are two major commercially developed HCFs including HC-1550-02 and HC19-1550-01 with core diameters of  $10\mu\text{m} \pm 1\mu\text{m}$  and  $20\mu\text{m} \pm 2\mu\text{m}$ , respectively [121]. Scanning electron microscopy (SEM) images of cross sections of commercialised HCFs are illustrated in Figure 4.5. The black areas are hollow, filled with presented gas or air.

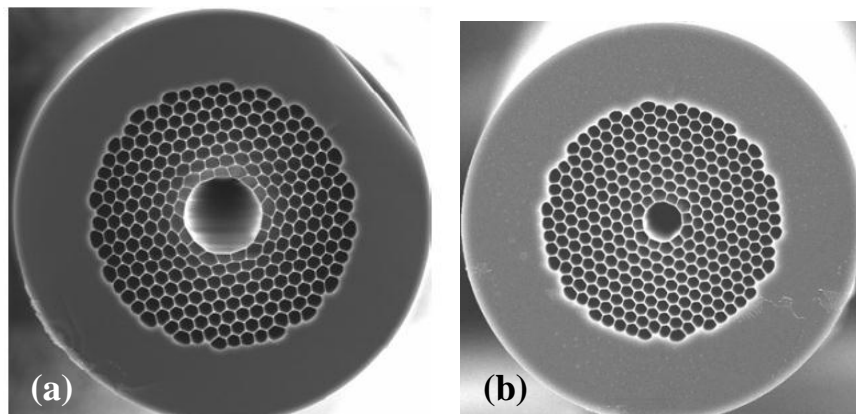


Figure 4.5: Scanning electron microscopy (SEM) image of HC-PCF. (a) HC19-1550-01, (b) HC-1550-02 [119]

## 4.2 All-fibre Gas Sensing Methods

Gas measurement using the interaction of light and the target gas within a fibre is called all-fibre gas absorption sensing. In an optical fibre, light propagates inside fibre core and some in the cladding. This forms an evanescent field in fibre cladding (Figure 4.6). If a gas is introduced to the evanescent field, it will absorb a part of the light and the rest will be reflected back into the



fiber core. Light intensity variations are related to gas concentrations using the Beer-Lambert law, Equation 1, with an additional factor of the evanescent field strength.

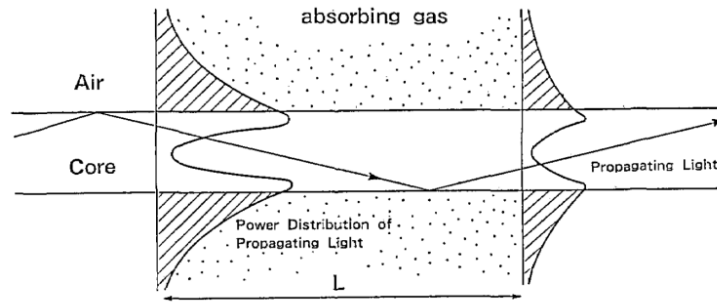


Figure 4.6: Schematic of gas detection based on evanescent field [122]

Different methods have been employed to provide the interaction between a gas and the light in an optical fibre. Waechter *et al.* [101] have completely reviewed the all-fibre sensors as illustrated in Figure 4.7.

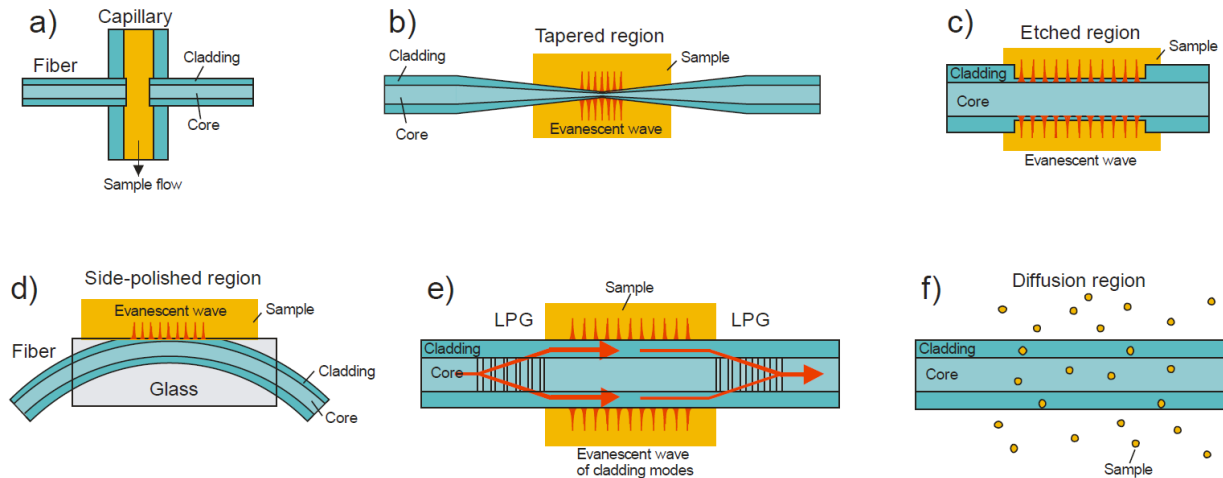


Figure 4.7: various all-fibre gas sensor heads: (a) a short gap in a fibre, (b) a tapered fibre, (c) a removed cladding section of a fibre, (d) a side-polished fibre (e) a SMF fibre with Long Period Gratings (LPGs) (f) a PCF fibre to provide gas and light interaction inside fibre [89]

In the current study, the scope of investigation is focused on tapered SMFs (Figure 4.7b), drilled HC-PCFs (Figure 4.7f), and drilled SMFs. Previous studies and the basis for these methods are reviewed in the following sub-sections.

#### 4.2.1 Tapered Fibre

One of the techniques that use an evanescent field sensor is tapering. The propagation of laser light in a sub-micro tapered fibre allows light, as a magnetic field, to propagate in the region

close to the fibre surface [123]. Evanescent spectroscopy is formed by the total reflection of the laser light with the gas around the surface of a tapered fibre. By reducing the diameter of the cladding and core a large fraction of the light propagates in the cladding. Under single mode conditions, a large amount of light leaves the cladding, which creates a powerful evanescent field [124]. Figure 4.8 illustrates light power propagations in a tapered fibre.

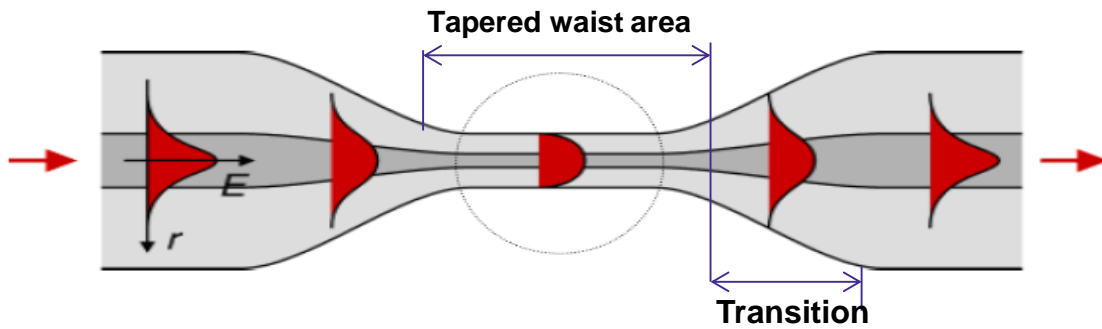


Figure 4.8: Propagation of light in a tapered fibre (after [125])

Previous theoretical and experimental studies show that evanescent field absorption strengths are a function of waist diameter, waist length, transition profile, laser wavelength, refractive index of presence gas, and protective layer (e.g. aerogel) in the evanescent field [73, 126]. In addition to these factors, Takemoto *et al.* [70] showed that improvement of absorption in tapered fibres is feasible by the bending of tapered regions. Difficulties involved in using tapered fibres are their fragile configuration and the surface sensitivity to dust and moisture. It is also complicated to produce a long sub-micro tapered fibre with the desired characteristics.

The presence of contamination on the fibre surface has significant effects on the measurement and can cause misinterpretation of gas concentrations [127]. Recently, protection of tapered fibres against structure-breakage, contamination, and moisture has been achieved using a spongy nanostructure aerogel layer which allows gas diffusion within the evanescent field [33, 128]. Figure 4.9 illustrates evanescent field intensity as a function of wavelength for various waist diameters. The sensitivity of the sensor could be improved by a stronger evanescent field. The fraction of the evanescent field in the tapered region is maximised near the U-band to more than 95% for an SMF tapered waist of 0.5  $\mu\text{m}$ .

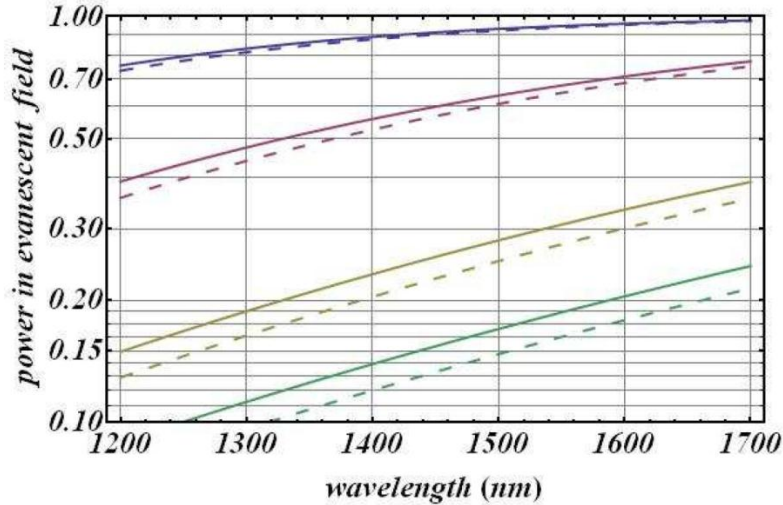


Figure 4.9: Calculated fraction of laser power in the evanescent field near surface of a tapered SMF. For waist of diameter 0.5, 0.7, 1.0 and 1.2  $\mu\text{m}$ , from top to bottom, in air (dashed ones) and silica aerogel (solid line) [33]

Tapered fibres have been used in different arrangements for absorption sensing of gases and biomolecules. Hydrogen detection is possible using a tapered fibre with an over-layer of palladium which changes the light intensity in different hydrogen concentrations [129]. For the first time, Tai *et al.* [122] presented direct absorption methane gas sensing using a tapered fibre sensor in the strong 3.392  $\mu\text{m}$  line centre of methane. However, Badru [124] failed in attempting methane detection with a 1666 nm line centre using a tapered fibre developed by a splicer. Insufficient tapered characteristics are stated as the reason for failure. The literature shows that tapered fibres have not been used in many different arrangements as sensors; a summary and the results of previous works are presented in Table 4.1.

Table 4.1: List of previous tapered fibre gas sensing studies

<b>Setup/Method</b>	<b>Result significant</b>	<b>Reference/Year</b>
CH <sub>4</sub> detection using 3.392 μm He-Ne laser	1.8 μm dia. in 10mm length tapered SMF Minimum CH <sub>4</sub> detected ≤5%	[122], 1987
Theoretical evaluation of tapered fibres	Sensitivity is a function of taper profile; laser wavelength and target gas refractive index. Exponential –linear taper profile has higher sensitivity	[126], 1994 [73], 2003
Theoretical study	Tapered fibre with porous cladding has higher sensitivity and less response time than a uniform fibre	[130], 1995
Modelling and Fabrication using an oscillating flame	20-35 μm dia. in 10mm length uniform-waist tapered SMF	[131], 2003
First H <sub>2</sub> detector using tapered with nano-palladium layer	1.3 μm dia. in 2mm length tapered SMF with a 4nm palladium layer, Minimum H <sub>2</sub> detected ≤4%	[132], 2005
Antibody detection using coated tapered fibre	Tapered with waist of 6-12 μm dia. and waist length of 100μm	[115], 2007
Molecules absorption detection	0.5 μm dia. in 3 mm length tapered SMF	[123], 2007
CH <sub>4</sub> detection using 1.65 μm DFB laser and tapered fibre	11 μm dia. in 0.3 mm length tapered SMF Failed in CH <sub>4</sub> detection	[124], 2008
Novel long tapered fabrication facility	SMF & PCF tapering with minimum 0.5 μm dia. Waist and length from cm to ten meter.	[133], 2008
Tapered fibre surrounded by silica aerogel	1 μm dia. in 10 mm length tapered SMF	[128], 2009
Acetylene detection using micro-tapered fibre in a hydrophobic aerogel	0.7 μm dia. in 1cm length tapered SMF; Response time 30 s	[33], 2010

### 4.2.2 Drilled SMF

Drilled SMFs have the potential to be utilised as gas absorption detection sensors. Important characteristics of drilled SMFs are the depths and diameters of holes—another consideration is accurate drilling position which may cause strokes or crosses in the fibre core (Figure 4.10).

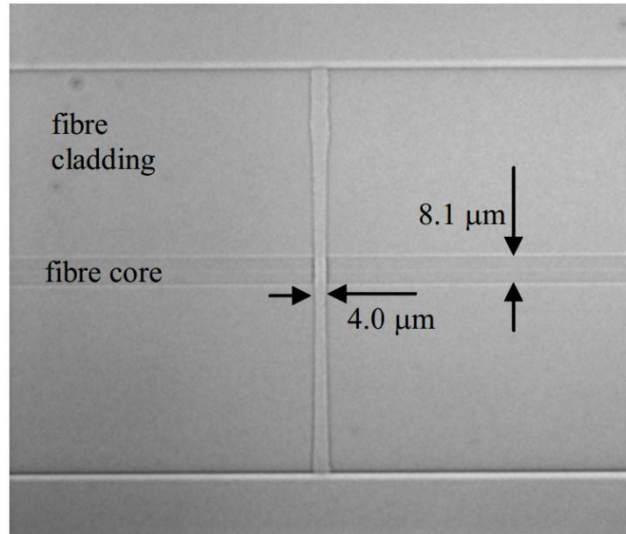


Figure 4.10: Microscopy image of a 4 μm dia. drilled hole through a SMF [134]

A drilled hole allows a microcell to have interaction between the laser beam and a sample gas (similar to Figure 4.7a). The gas detection is possible either by transmitted light absorption or by reflected light employing an interferometric-based sensing regime (Figure 4.11).

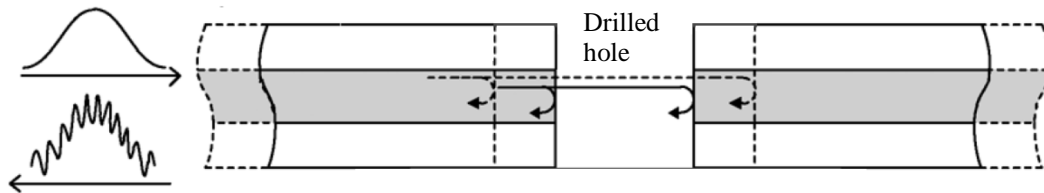


Figure 4.11: Interferometric-based gas sensing from a drilled hole on SMF (After [129])

The literature shows different SMFs are drilled adopting different methods, mostly femtosecond (FS) lasers [10, 60, 90, 134-136] and Focused Ion Beams (FIBs) [109, 137, 138], to develop Fibre Gratings and refractive index (RI) sensors. To the best of the author's knowledge, no attempt has been made to use drilled SMFs for absorption spectroscopy gas sensing as of this date. Fibre fabrication for the development of sensors and experimental results are discussed in Section 7.1.2. Table 4.2 presents different approaches and the results of previous studies on micromachining of SMF.

Table 4.2: Previous works on SMF micromachining

Setup/Method	Result significant	Reference/Year
FS micro drilling	4 $\mu\text{m}$ channel for RI sensing	[134], 2006
FIB micro drilling	10 $\mu\text{m}$ diameter hole with 8 $\mu\text{m}$ depth. First long period gratings (LPG)	[138], 2007
FS drilling aided chemical etching	fibre bragg grating (FBG)	[90], 2008
FS micromachining	1.2 $\mu\text{m}$ (width)x125 $\mu\text{m}$ (depth)x500 $\mu\text{m}$ (length) micro-slit	[139], 2008
FS laser drilling	relationship between the transmission the RI is critically dependent on the size of the micro-hole in the fibre core region	[10], 2009
FS laser drilling	4.5 $\mu\text{m}$ channel passed core for RI sensing in a CRD setup	[61], 2009
FIB micromachining	10 $\mu\text{m}$ x 25 $\mu\text{m}$ micro-cavity in 32 $\mu\text{m}$ diameter taper for RI sensing	[109], 2011
FIB micro drilling	LPG and micro-cavity drilling for RI sensing	[137], 2012

### 4.2.3 Drilled HC-PCF

HC-PCFs have attracted the interest of many research groups due to their unique characteristics. The well controlled interactions, flexibility, selective wavelength options, high power transmission capability, and small sample volume requirements offer benefits which have opened the door to many new sensing applications using HC-PCFs [125]. There have been many studies carried out on gas sensing based on HC-PCF fibres. The major feature of HC-PCFs in gas sensing is the ability to provide interaction between gases and light beams in the air holes. In PCFs, more than 98% of the light is guided through the holey core, which makes it a perfect gas cell if the gas is presented in the hollow core. This is unlike evanescent sensors which have a weaker evanescent field and gas/light interaction. Using holey core fibres has the advantages of small size, small sample volume requirement, insensitivity to bending, low cost, and possible distributed gas sensing [140].

HCFs were first employed in gas sensing applications in the late 90's and have since been studied for different HC-PCF designs and configurations [141]. Monro *et al.* [118] presented the

design criteria for efficient gas interaction in the air holes. Later, Ritari *et al.* [140] illustrated gas sensing with an open end HC-PCF in a vacuum chamber. They investigated methane detection in a 10 meter long PBF1300 fibre at 630 mbar at the Q-branch of a 1330 nm methane absorption band. The HCF was spliced to an SMF, and loss was estimated to be about 1 db. The absorption spectrum was obtained using a broadband LED and an optical spectrum analyser. The time response for 90% of presented gas was about 20 minutes [140].

To fill the fibre core with gas, different techniques—such as micro-channelling the fibre cladding [75, 142], open end fibre, the use of a vacuum to fill the fibre, and gapped hollow core connections for gas diffusion—have been applied. Ho *et al.* [143-146] theoretically and experimentally investigated microstructured fibre gas sensing using these techniques. A specially fast response PCF, as shown in Figure 4.12, was suggested to overcome fabrication process complexity [145].

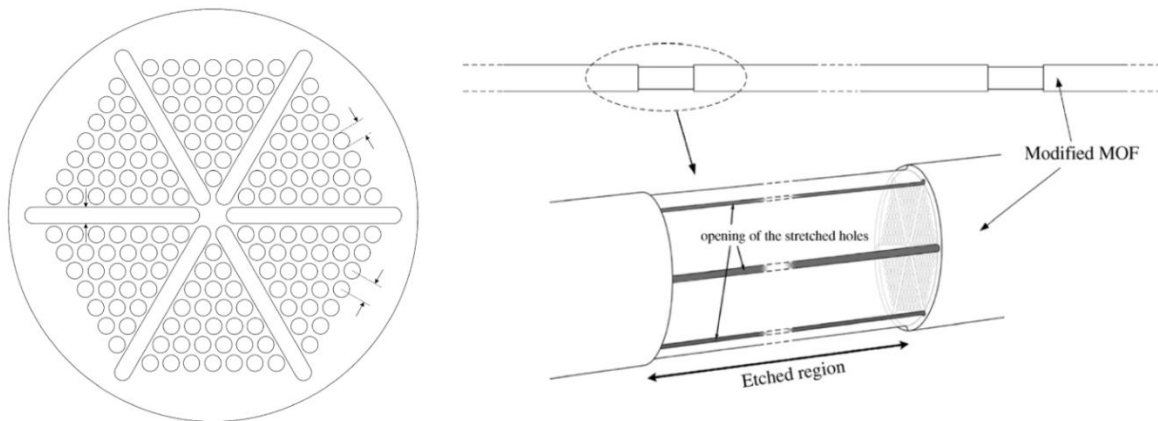


Figure 4.12: A specially designed gas sensing PCF [145]

This arrangement presents a good evanescent field sensor with a lower loss and faster diffusion time when compared to conventional PCFs; however, this design is difficult to manufacture. HC-PCF design has matured enough that different types are now commercially available. The advantage of using HC-PCFs over other methods is the versatility of having an all fibre cell with small size and a high interaction between the light and gas. As discussed, different methods are used to enter the gas in a hollow core. A hole on the side of a fibre facilitates the gas diffusion into a fibre's hollow core for interaction with the light. It has also been demonstrated that a micro hole on the side of an HC-PCF has a negligible effect on transmission loss which makes it a preferable method [142]. Figure 4.13 illustrates gas sensing using a side drilled HC-PCF.

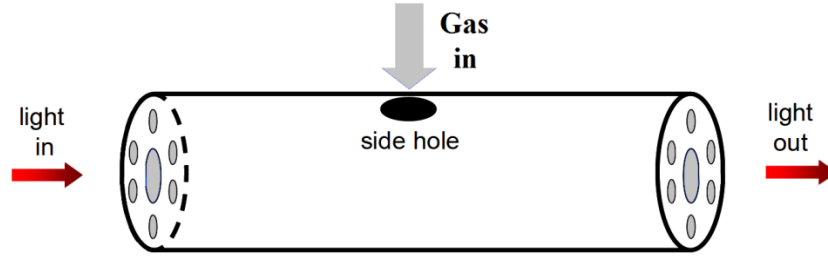


Figure 4.13: Microchanneled HC-PCF for gas sensing (after [147])

There are mainly two micromachining methods used to drill HC-PCFs, namely femtosecond (FS) laser drilling and focused ion beam (FIB) drilling. FS drilling uses a tightly focused FS laser beam with kHz shoot frequency to destroy the holey structure of HC-PCFs. Figure 4.14 illustrates a schematic of fibre drilling using an FS laser where the fibre surface is covered by an index-matching fluid to eliminate distortion caused by the cylindrical shape of the fibre [148].

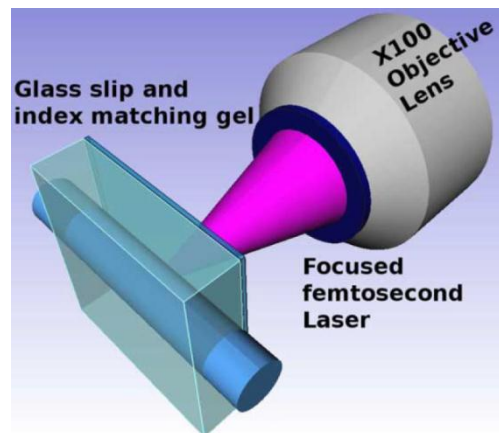


Figure 4.14: Schematic of femtosecond laser drilling in an optical fibre [148]

FS micromachining is faster as compared to FIB drilling. It has been demonstrated that 20 minutes of FS radiation can produce a micro channel breaching in the holey core using a Ti:sapphire laser with a 110 FS pulse at 800 nm wavelength and 1 kHz frequency [142]. Also an inline fabrication setup could be used to produce multi holes on PCFs [135, 149]. A paper by Gattass and Mazur [150] published in the journal, *Nature*, has extensively reviewed FS laser micromachining principles and their main experimental parameters. Figure 4.15 shows SEM images of a milled hole in an HC-1550-02 fibre using the FIB method. The channel diameter varies from 20  $\mu\text{m}$  on the fibre surface to few micro meters in the fibre core.



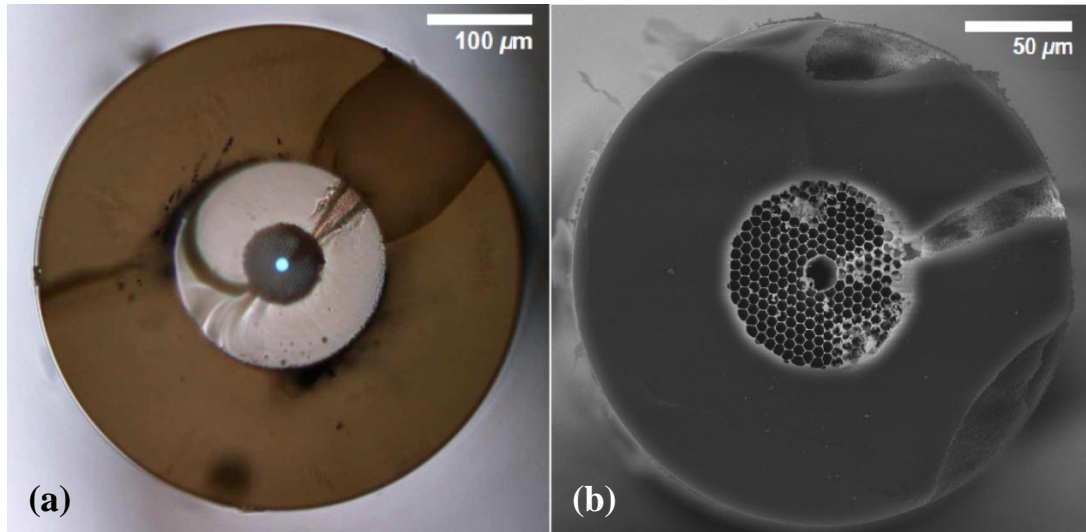


Figure 4.15: SEM cross-section image of micro-hole drilled in HC-1550-02 fibre (a) in coated fibre with a UV removed hole on polymer surface (b) in a stripped fibre [142]

The fairly recent commercial development of FIB systems, with the advantages of both micromachining and imaging at the same time, has led to the development of many applications in optical fibre micromachining. Figure 4.16 shows a Dual-beam FIB-SEM system which consists of an FIB column with  $\text{Ga}^+$  ions for removal of particles and an electron column for SEM to obtain high resolution images [151].

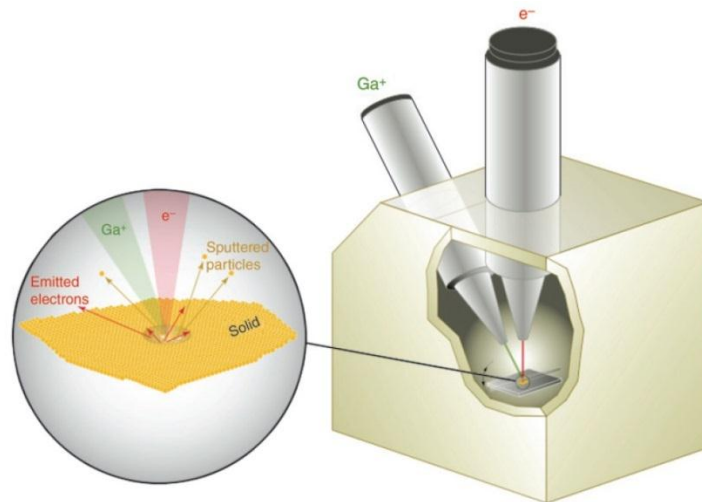


Figure 4.16: Schematic of a dual-beam FIB-SEM system suitable for micromachining and imaging of solid materials [151]

The basics of FIB and SEM have been extensively reviewed by Volkert *et al.* [151], Fu *et al.* [152], and Tseng *et al.* [153]. Martelli *et al.* [154] presented FIB micromachining of PCFs for the first time. The main advantage of using FIB is the clean material removal with no deposits or

damage to the structure (in contrast to FS drilling). Figure 4.17 shows SEM images of milled holes on the side of PCFs using FIB. Note there is no deposition of materials is observed.

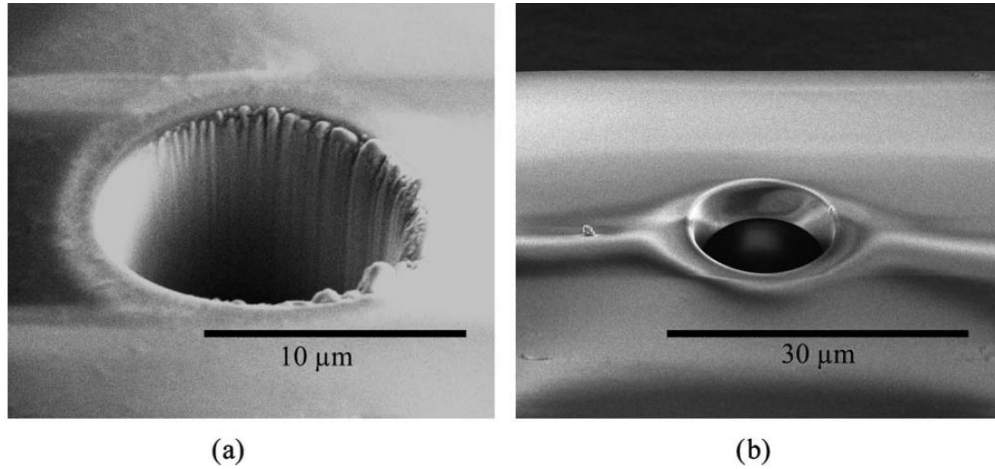


Figure 4.17: SEM images of side hole by FIB with diameter of (a) 12  $\mu\text{m}$  and (b) 15  $\mu\text{m}$ , on side of PCFs [154]

The literature shows that response time is a function of the sample gas, HC-PCF length, number of drilled holes, and their positions. Table 4.3 presents previous gas sensing studies using PCFs. The range of achieved response times (3 seconds to 20 minutes) and sensitivities (158 ppm to 647 ppm for methane) are promising for employment of drilled HC-PCF methane sensors in an underground coal mine.

Table 4.3: Gas sensing projects using Hollow core fibres (HCFs) in short

<b>Setup/Method</b>	<b>Result significant</b>	<b>Reference/Year</b>
10 m PCF 1300 with one open side in a vacuum chamber	30 minutes response time with 10 mbar pressure- CH <sub>2</sub> and CH <sub>4</sub> detection	[140], 2004
FIB Micromachining in PCF	12 μm diameter and 68μm depth in four-ring PCF	[154], 2007
1.15 m two holes each 40 cm from ends	FS drilling in HC-PCF with minor loss 3 hours response time for Acetylene (C <sub>2</sub> H <sub>2</sub> )	[142], 2007
5.1 m HC-PCF with one side open in a vacuum chamber 1645 nm multiline DFB detection	10 ppm CH <sub>4</sub>	[34], 2007
5.6 m HC1300 and 5.1 m HC1600 with one open side in a vacuum chamber Broadband laser source	98 ppm CH <sub>4</sub> at 1.33 μm band and 10 ppm at 1.66 μm band	[35], 2009
13.7 cm with angled distance of 176 μm at fibre ends (mechanically attached) 1666 nm DFB laser source	248 sec – 158 ppm CH <sub>4</sub>	[32], 2009
7 cm HC-PCF with 7 holes (FS Laser)	3 sec - 647 ppm CH <sub>4</sub>	[29], 2010
90 cm HC-PCF with two end open	11 minute - 300 ppm CO <sub>2</sub>	[31], 2011
FIB end modified HC-1550-02 and HC19-1550-01 with a broadband laser source	Sensitive detection of CH <sub>2</sub> and CH <sub>4</sub> , angle cleaving of HC-PCF using FIB for first time	[155],2013

# CHAPTER 5

## THEORETICAL ANALYSIS OF METHANE ABSORPTION BANDS

### 5.1 Introduction

In order to determine the best wavelength for all-fibre methane gas detection in underground coal mines a detailed spectral analysis of methane and other mine gases using the HITRAN database was conducted is outlined in this chapter. Section 5.2 briefly overviews absorption lines for major mine gases and discusses the main methane absorption bands. Section 5.3 presents methane spectra measurements in NIR for underground coal mine conditions. Cross-sensitivity to other mine gases, and temperature and pressure effects are also examined.

### 5.2 Methane Absorption Lines

Gas molecules have different natural frequencies depending on their structure. The HITRAN [156] database contains high resolution spectral absorption parameters for 42 different gas molecules, including methane. This database uses either theoretical calculated spectroscopic information or highly accurate measurements. It is an international standard used for the study of gas absorption spectroscopy and remote sensing. The 2008 edition of the HITRAN database is used in this thesis as the main source of information for theoretical analysis of methane and other

mine gases. The HITRAN 2008 contains more accurate experimental results between 1650 nm and 1670 nm in comparison to the HITRAN 2004 [156]. The associated software was used for spectral line shape computations and the display for the HITRAN 2008 database is SWSpectrum.

As shown in Figure 5.1, finger prints of major mine gases in the IR region consist of narrow features as a result of discrete molecular vibration levels. The NIR region (700 nm to 2500 nm) has weaker bands (100 times weaker for methane); however, the availability of telecommunication equipment with lower loss and higher signal to noise ratio of measurements in the NIR make these features feasible for fibre optic based spectroscopy [89].

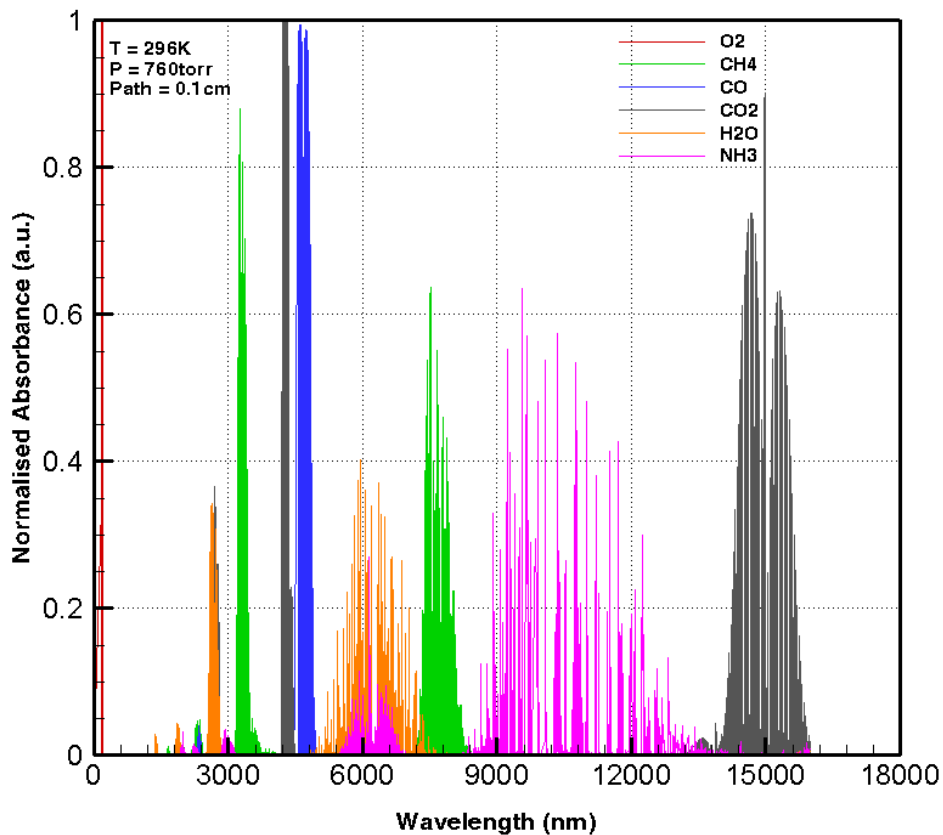


Figure 5.1: Absorption features for five main mine gases in from 100 nm to 16000 nm region (all at 100% concentration, T= 296 K, P= 760 Torr, and in a 0.1 cm path length)

Methane molecules vibrate in four modes as a result of molecular symmetric stretch at 3.43  $\mu\text{m}$  ( $\nu_1$ ), twisting at 6.52  $\mu\text{m}$  ( $\nu_2$ ), anti-symmetric stretch at 3.31  $\mu\text{m}$  ( $\nu_3$ ), and scissoring at 7.62  $\mu\text{m}$  ( $\nu_4$ ) [110]. Absorption bands happen as a result of these vibration frequencies and their combinations. Methane spectrum absorption is mainly composed of five bands, as shown in Figure 5.2a. The strongest bands are centred at 3.31  $\mu\text{m}$  ( $\nu_3$ ), and 7.62  $\mu\text{m}$  ( $\nu_4$ ), respectively.

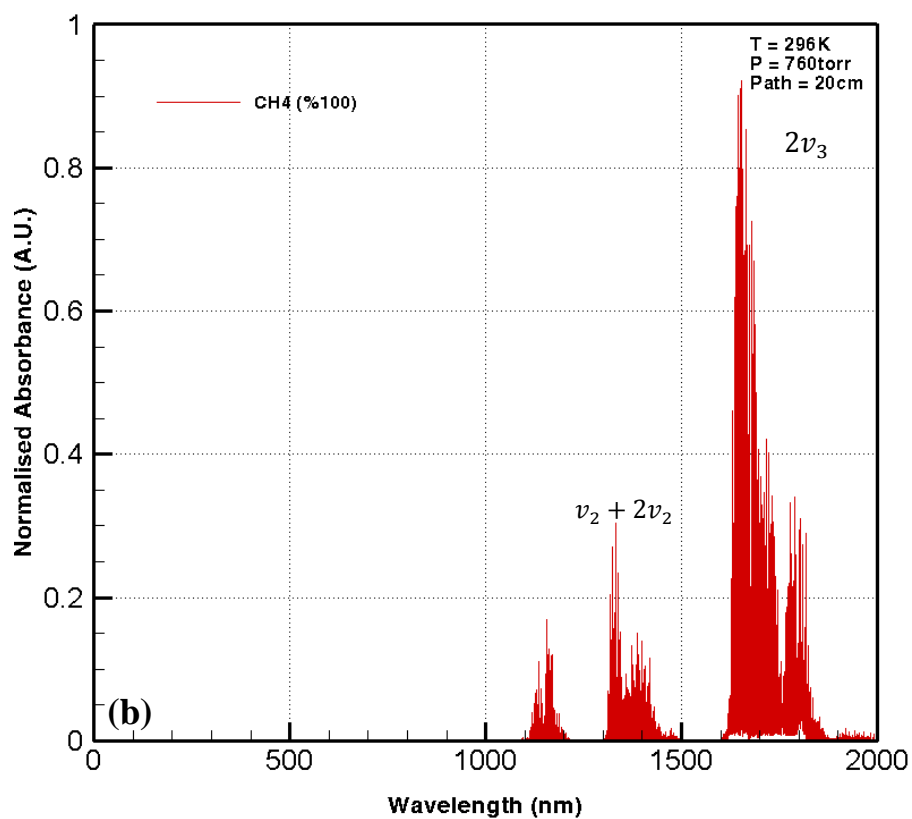
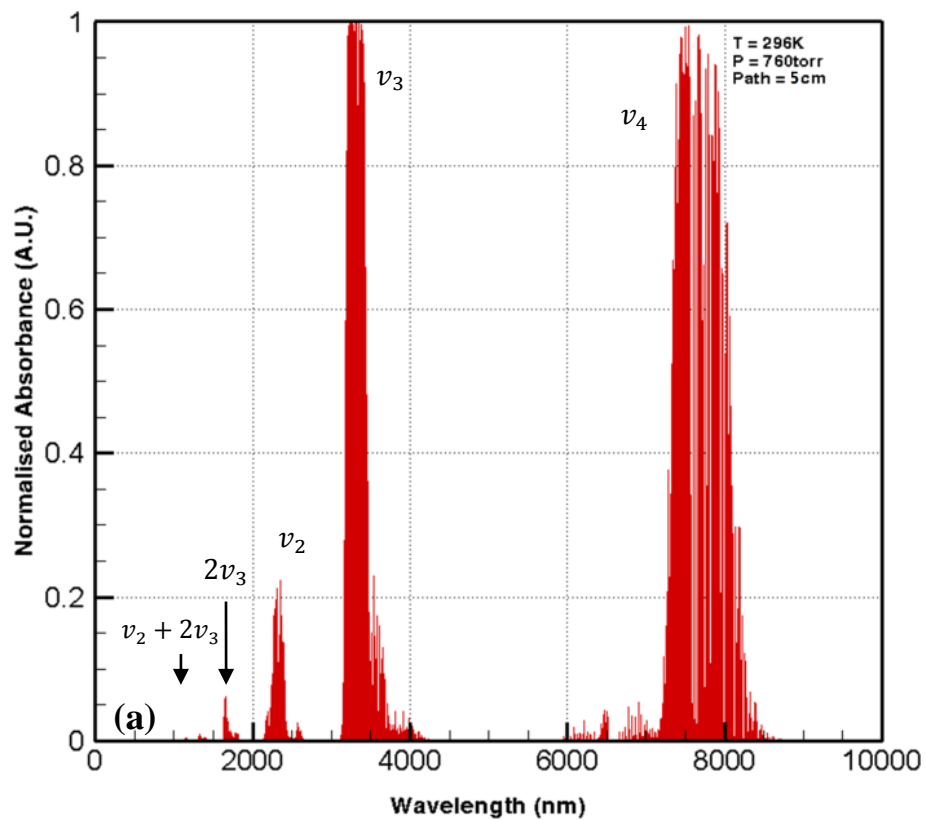


Figure 5.2: Methane absorbance (a) for under 10000 nm, and (b) for under 2000 nm, vibrational bands are labelled (for 100% methane at T= 296 K, P= 760 Torr, and in (a) 5 cm and (b) 20 cm path length)

The strongest absorption in the conventional fibre optic transmission region (NIR) is at around 1.66  $\mu\text{m}$  ( $2\nu_3$ ) and 1.33  $\mu\text{m}$  ( $\nu_2+2\nu_3$ ), as can be seen in Figure 5.2b. The methane  $\nu_2+2\nu_3$  band has closely spaced and weaker absorption compared to the 1.66  $\mu\text{m}$  band. The strongest methane absorption of the  $\nu_2+2\nu_3$  band is at 1331.55 nm. It is a very broad line which is insufficient for accurate concentration measurements and also has interference with water vapour absorption bands. Therefore, this band is not suitable for industrial gas sensing; however, high performance and cost-effective telecommunication equipment is available in this range [35]. There are three main branches at the  $2\nu_3$  absorption band of methane shown in Figure 5.3, namely R-branch (1630 nm -1664 nm), Q-branch (1665 nm -1668 nm), and P-branch (1669 nm -1680 nm) [85].

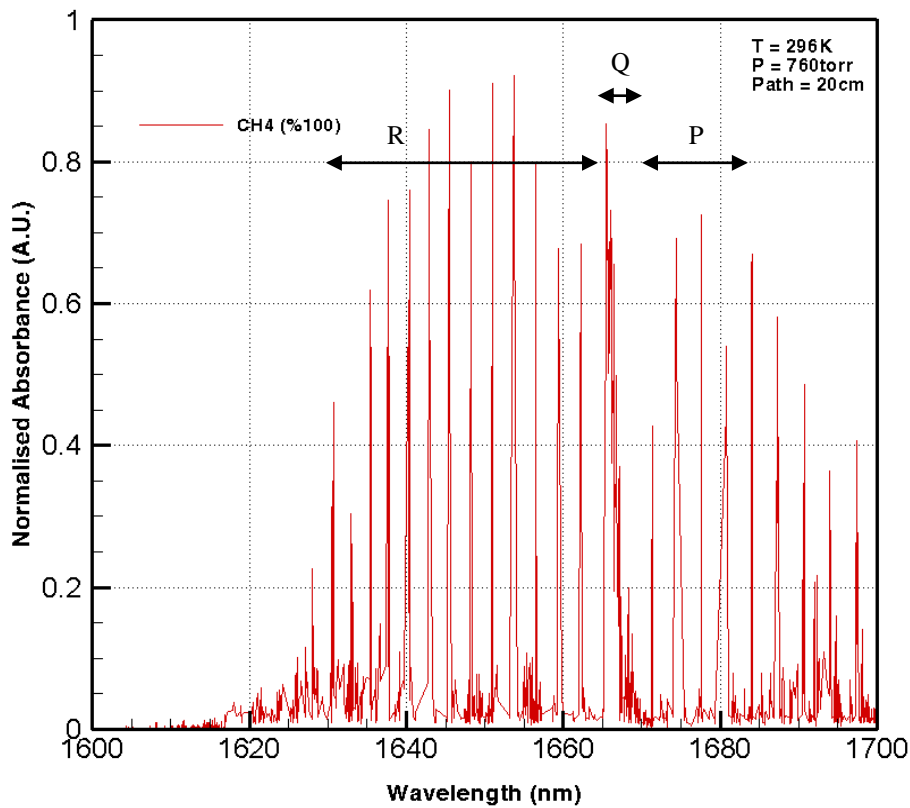


Figure 5.3: Absorption spectra of methane at  $2\nu_3$  band, R, P and Q branches are tagged

The three main absorption lines of the R-branch happen at the 1645.56 nm (R6), 1650.96 nm (R4), and 1653.7 nm (R3) line centres. The R6 line centre is the strongest of the three, and it is used in other studies [34, 157, 158]. As Figure 5.4 illustrates, methane absorption at the R3 line centre has less cross over with small lines around it, and it also has a narrower absorption which makes it more suitable for WMS measurements. There have been many studies using the R3 line centre for methane concentration measurements [71, 83, 99, 159-163].

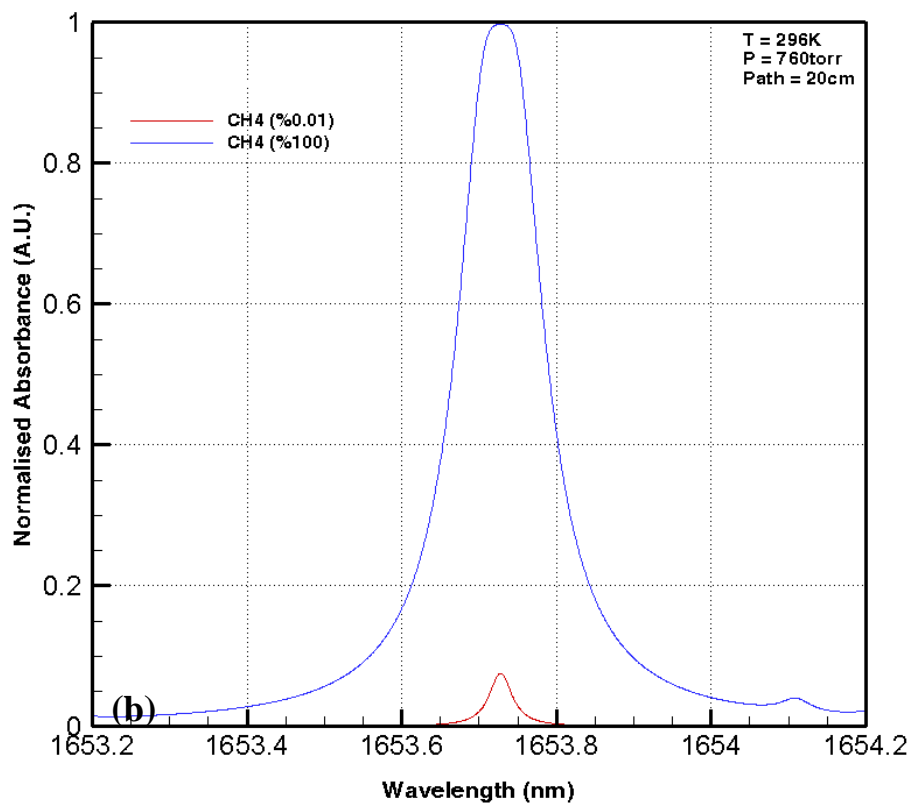
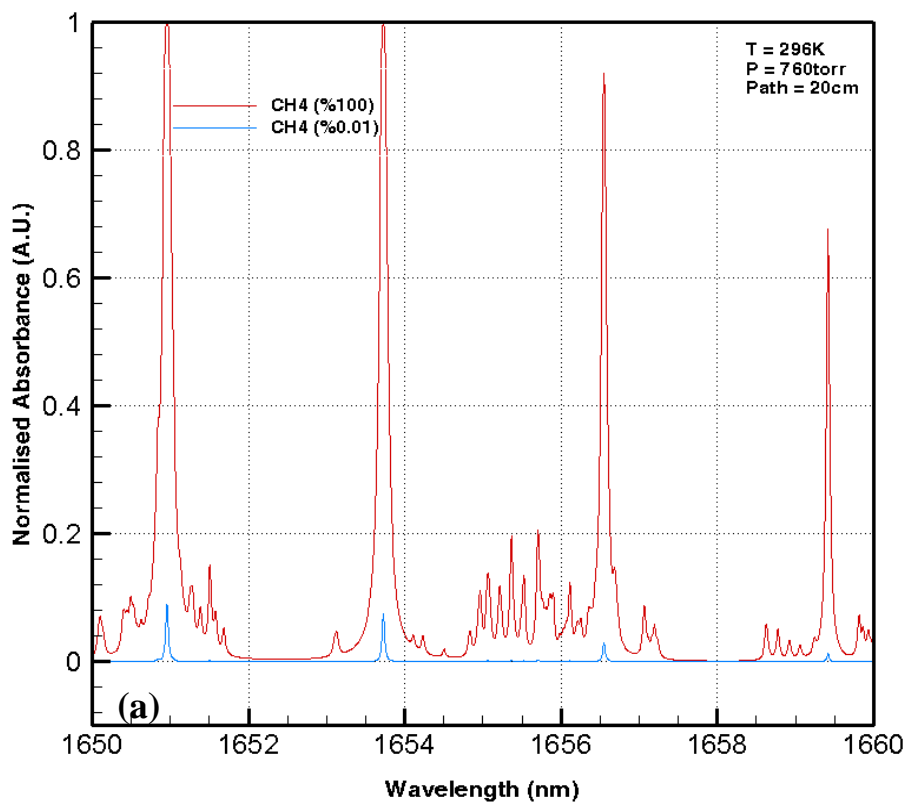


Figure 5.4: Methane absorbance at R branch of  $2\nu_3$  band in NIR for 0.01% and 100% methane in air (a) from 1650 nm to 1660 nm, and (b) at 1653.7 nm line centre (at T= 296 K, P= 760 Torr, and in a 20 cm path length)



As Figure 5.5 demonstrates, the Q-branch consists of many strong lines which have strong absorbance even for methane concentrations at concentrations as low as 0.01% in air (more than 5% absorbance) at ambient conditions. The four major lines at the Q-branch are 1665.961 nm (Q6), 1665.48 nm (Q4), 1666.201 nm (Q7), and 1666.483 nm (Q8).

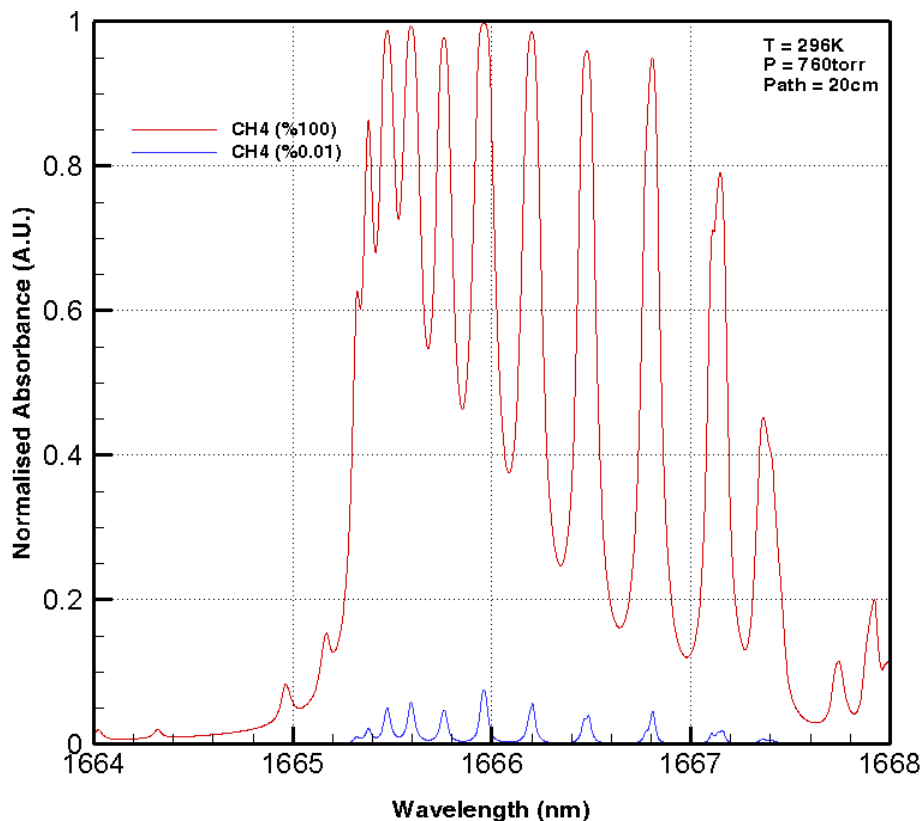


Figure 5.5: Methane absorbance at Q branch of  $2\nu_3$  band for 0.01% and 100% methane in air from 1664 nm to 1668 nm (at  $T= 296$  K,  $P= 760$  Torr, and in a 20 cm path length)

The close and narrow lines in the Q-branch makes it suitable for multiline detection and quantitative calculations [164]. There was a study done using the line centre at 1665.48 nm (Q4) for methane concentration measurements [29]; the Q6 line centre is the strongest line and the most used in other studies using the Q-branch [22, 71, 165-167]. The WMS second harmonic signal at the Q-branch of the  $2\nu_3$  band for 0.01%, 0.1%, and 100% methane in air for the 1665.961 nm, 1666.201 nm, and 1666.483 nm line centres are presented in Figure 5.6. The methane second harmonic WMS at the Q6 line centre has less cross over with other lines around it (specifically in low concentrations), and it also has a narrower absorption (less than 0.03 nm) which makes it more suitable for WMS measurements. This plot suggests that the second

harmonic WMS signal has a better signal to noise ratio at the Q6 line centre than other line centres in the Q-branch.

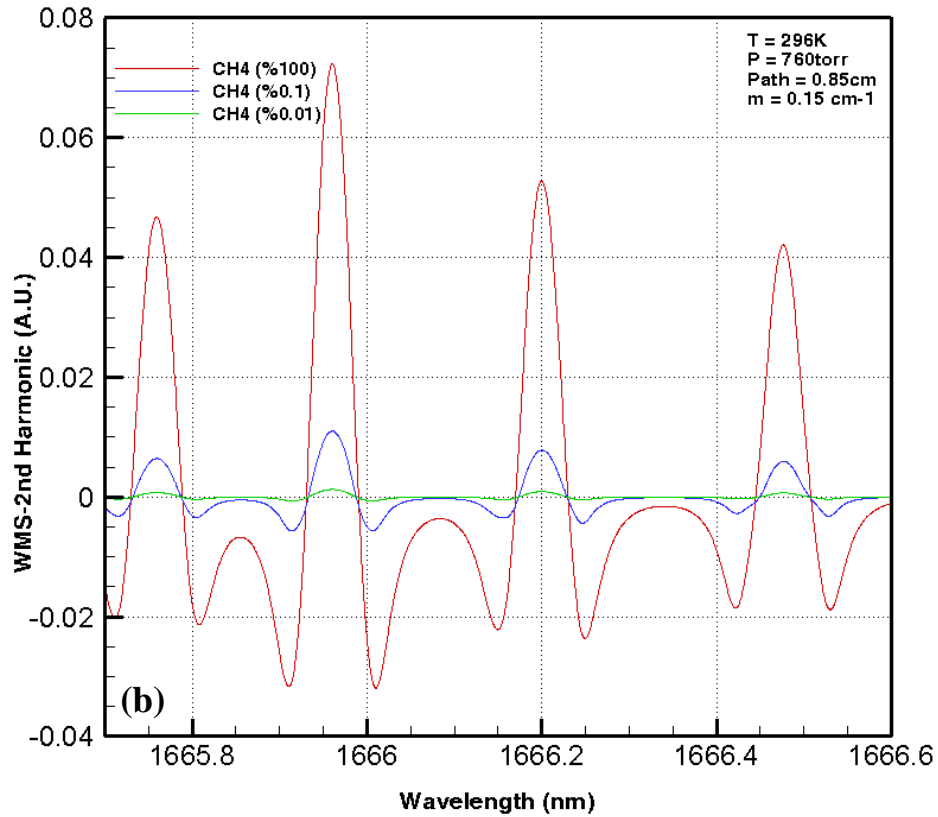


Figure 5.6: Methane WMS second harmonic signal at Q-branch of  $2\nu_3$  band for 0.01%, 0.1%, and 100% methane in air for 1665.961 nm, 1666.201nm, and 1666.483 nm line centres (at T= 296 K, P= 760 Torr, and in 0.85 cm path length)

### 5.3 Methane Spectroscopic Measurement in Underground Coal Mines

There were a number of factors that needed to be considered when selecting the laser wavelength at which to perform methane gas absorption spectroscopy experiments. The first consideration was that the laser light must be absorbed by methane so that it could be detected spectroscopically. As explained in the previous section, methane has strong absorption features at wavelengths of 1330 nm, 1666 nm, and 3310 nm. At these wavelengths, methane absorbs light and can be quantified according to the Beer-Lambert equation (Equation 1). At other wavelengths, such as visible light (380 nm – 740 nm), methane does not absorb light and cannot be detected or quantified. Another consideration is the wavelengths of light accessible to optical fibres. As optical fibres are silica based, they can only transmit light within the transmission range of silica (~300 nm – 1900 nm). Therefore, a fibre optic based sensor cannot interrogate the

3310 nm methane spectral feature because it is not possible to transmit light through a fibre optic device at this wavelength using standard fibre optics.

A final consideration for the choice of laser wavelength is the sensing environment. In Section 2.2.1 the common gases found in an underground mine are listed. In a practical application of methane sensing in a mining environment, it is very important that the sensing technique selectively detects methane and does not give false positive results due to interference from other mine gases. Figure 5.7 shows the spectral features of the common mine gases in the NIR region. The data for this analysis was obtained from the HITRAN 2008 database. The methane absorptions at 1330 nm occur close to some strong water vapour absorptions, so that it is possible that the methane signal could be masked if there is a high vapour content in the atmosphere. On the other hand, at 1666 nm there are numerous strong methane absorptions that do not coincide with absorptions of the other common mine gases. This means that absorption at 1666 nm can be associated only with the presence of methane, so this is the ideal wavelength for these experiments.

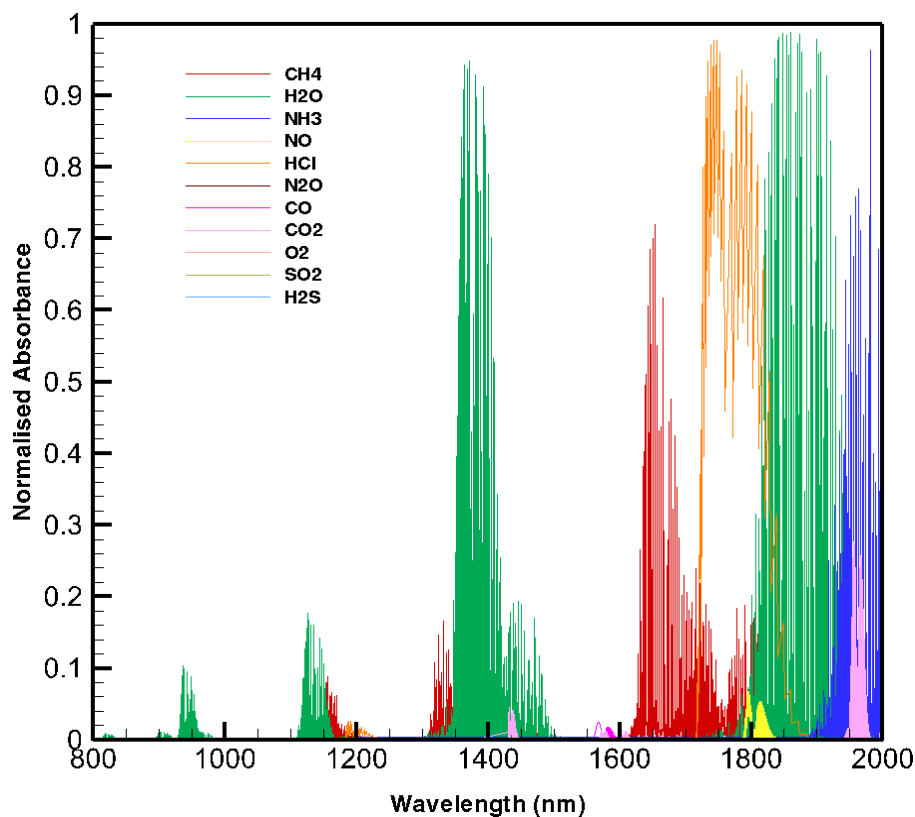


Figure 5.7: Spectrum showing the significant absorption lines for methane ( $\text{CH}_4$ ) and other common mine gases in NIR region (all gases at 100% concentration individually, data obtained from HITRAN database [156])

Pressure and temperature variations could also affect absorption line characteristics and therefore introduce errors in spectroscopic measurements. Shemshad *et al.* [24] has shown that there is no cross-sensitivity between mine gases spectra with methane and no considerable effects from pressure and temperature variations on methane WMS measurements in underground coal mine conditions using previous versions of the HITRAN database.

#### **5.4 Methane Sensing in $2\nu_3$ Band Using HC-PCF**

As mentioned in Section 4.1.2, there are two main commercial HC-PCFs available for the U-band (from 1500 nm to 1700 nm). In our range of interest for methane sensing, the  $2\nu_3$  methane absorption band, HC19-1550-01 has a considerable attenuation which makes it unsuitable for methane sensing. However, HC-1550-02 has attenuation less than 0.03 dB/m and dispersion less than 300 ps/nm/km around methane spectral absorbance in the  $2\nu_3$  band (Figure 5.8). The high attenuation in PCFs as compared to SMFs is due to the PBG based guidance limitations [30]. The attenuation in the designed wavelength is not considerable for developing sensor heads of only a few meters length at most.

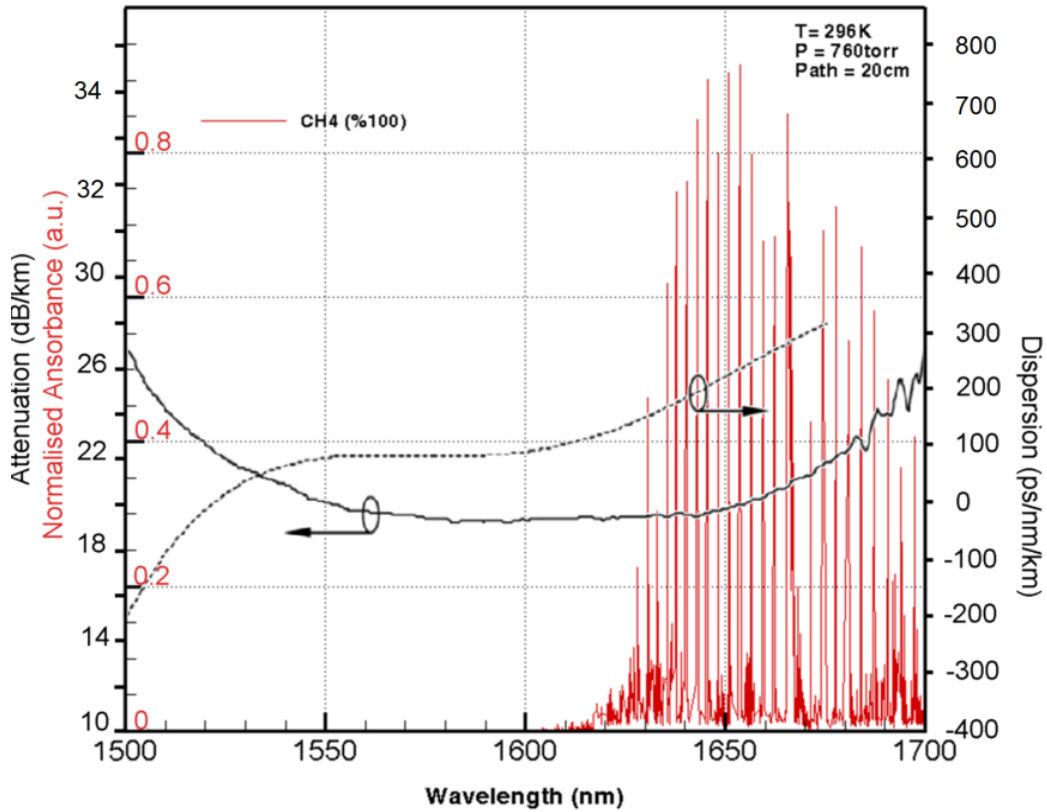


Figure 5.8: Normalised spectral absorbance of methane at  $2\nu_3$  band (red), attenuation and dispersion of HC-1550-02 (data extracted from [156, 168])

In addition, a similar core diameter to single mode fibres (SMFs) and its gaussian distribution (Figure 5.9) facilitates its coupling to SMFs. These characteristics make it an appropriate micro scale methane gas spectroscopy cell. On the other hand, there are practical challenges involved in using HC-PCFs for gas sensing—particularly, joining SMFs to PCFs, fabricating side holes, and creating proper dust-proof and humidity-proof filters [120].

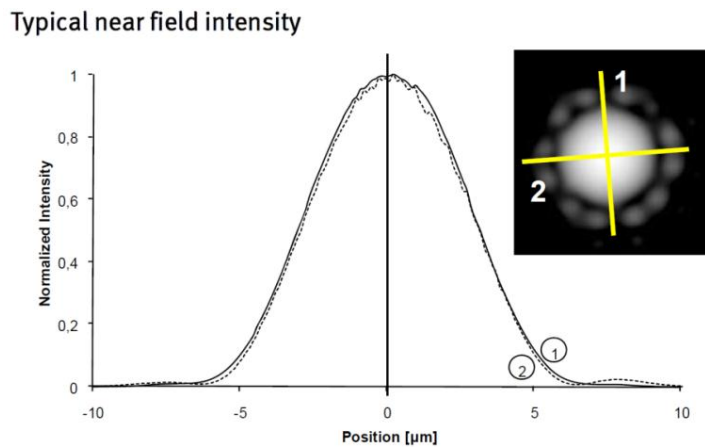


Figure 5.9: Typical near field intensity of HC-1550-02 fibre at 1550 nm [168]

# CHAPTER 6

## EXPERIMENTAL SETUP AND PROCEDURES

### 6.1 Introduction

This chapter presents the experimental design and setup that were used to test the all-fibre sensors using a DFB laser system. Figure 6.1 is a schematic of the experimental setup consisting of a gas concentration setup and a spectroscopy measurement setup.

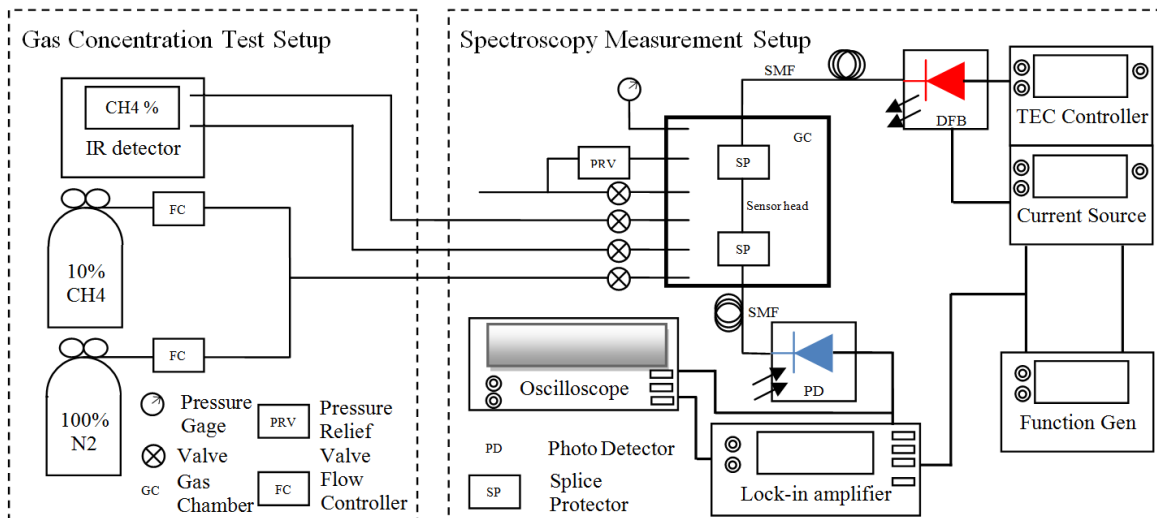


Figure 6.1: General schematic of experimental setup

## 6.2 Methane Gas Concentration Test Setup

A methane gas concentration experimental setup has been specially developed to test all-fibre sensor heads in a safe controlled manner at various known methane concentrations. This system was built mostly from stainless steel 316 and was manufactured in the school of physics workshop and then modified in the school of chemical engineering workshop at The University of Queensland. The methane concentration setup consists of a chamber, two gas cylinders, two flow meters, and other fittings (Figure 6.2). All the parts are connected through stainless steel pipes and flexible hoses. Flexible hoses are used to connect an IR detector to monitor methane concentration inside the chamber.

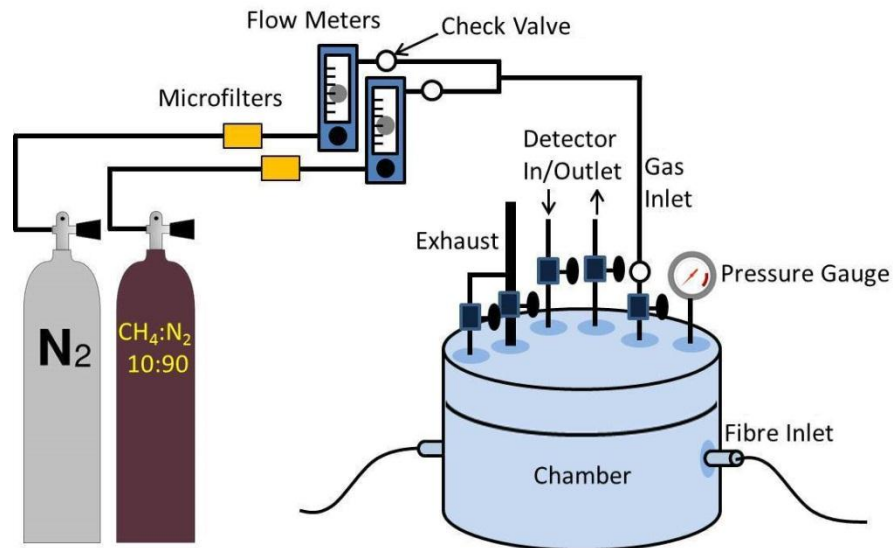


Figure 6.2: Schematic of methane gas concentration setup

**Chamber:** The bottom layer of the chamber is built from a machined cylindrical stainless steel pocket and also has grooves for O-rings machined around the top edge (Figure 6.3). The sitting top (with a locating step) is a circular machined stainless steel disk that accommodates a silicon O-ring around the top edge. The top side is affixed with six screws to the chamber walls. Four valves at the top of the chamber are used for the entry and discharge of the gas mixture. An outlet and a pressure relief valve are utilised to avoid any pressure excess more than 45 Psi. A plastic exhaust pipe line is connected to the chamber that takes the gas out of the laboratory from chamber output. The pressure relief valve, chamber, and fittings were assembled and tested at the school of chemical engineering workshop.

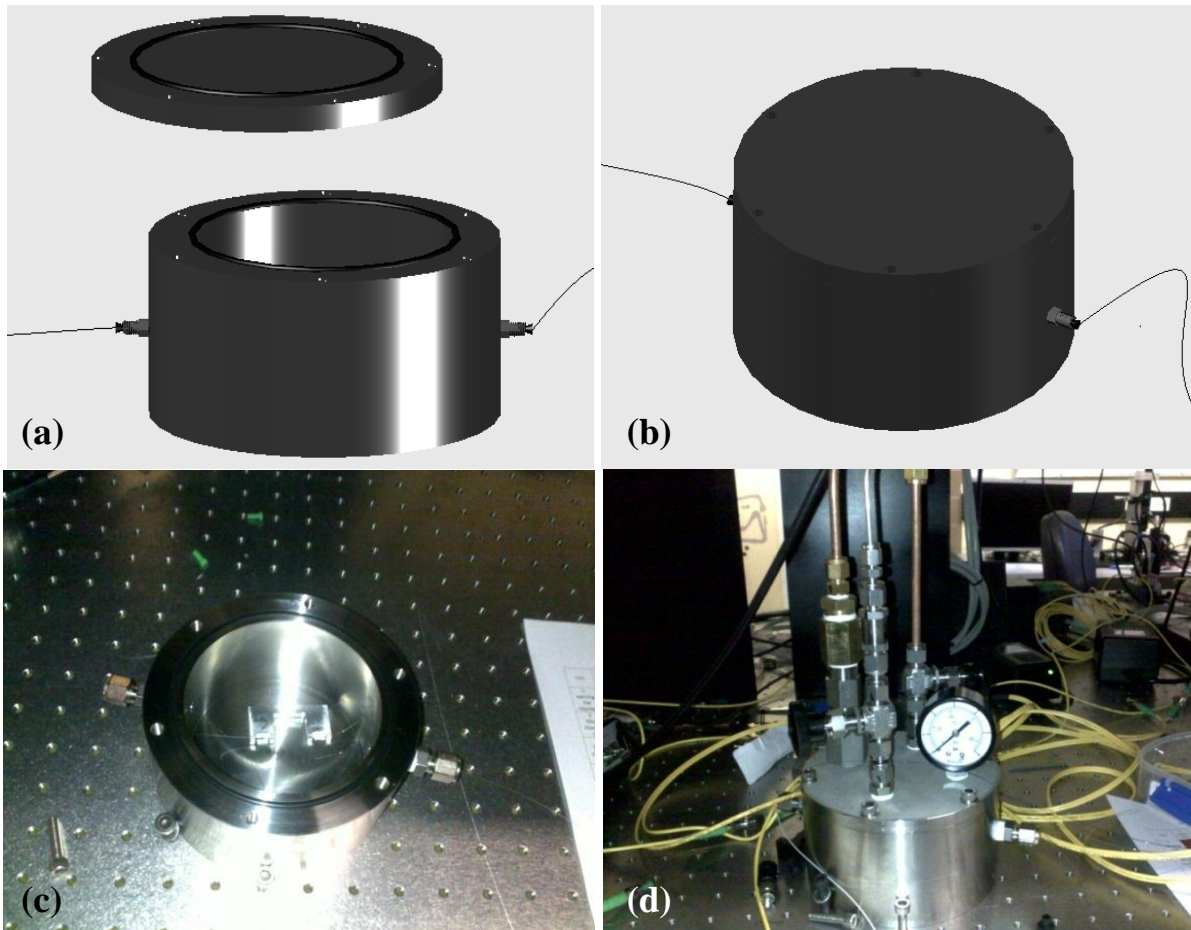


Figure 6.3: (a) 3D AutoCAD design with open top, (b) with closed top, and (c & d) Photos of the developed gas chamber. Fibre optic inlet and outlet on sides of chamber and fittings can be seen in photos

There are two optical fibres feeding connectors across each-other on the chamber body. The optical fibres are introduced to the chamber through micro-holed teflon connectors that are screwed into a stainless steel Swagelok connector attached to the chamber's wall. The teflon dimensions are designed with an additional 0.09 inch edge for better fixation and sealing of the chamber. A drawing of the Teflon connectors is shown in Figure 6.4.

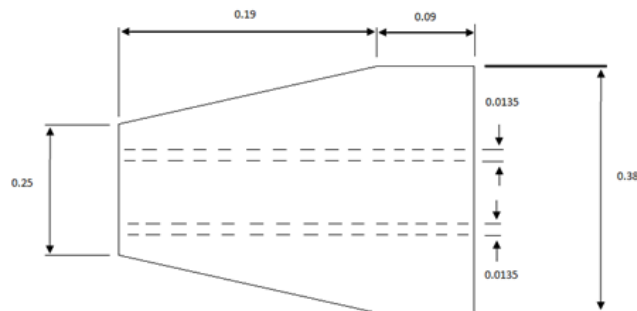


Figure 6.4: Teflon connection to feed fibre optics to the chamber (All dimensions are in inches)



**Gas Cylinders:** Two gas cylinders (Figure 6.5) filled with nitrogen and methane are utilised to supply the test chamber with specific amounts of gases. One of the cylinders is entirely filled with pure nitrogen, and the other cylinder is filled with 90% of nitrogen and 10% of methane which is also called “beta 10% CH<sub>4</sub> in N<sub>2</sub> mixture”. The gas mixture certificate is attached in Appendix IV. The cylinders are tied to a trolley so that the experiments can be conducted in safe conditions. The gas regulators are single-step output with a stainless steel diaphragm. The amount of the gases and flow rates supplied to the chamber depends on the experimental design. The two gas cylinders are connected to the chamber through strengthened stainless steel pipes with a flow meter between each cylinder and the chamber. There are two check valves installed after the flow meters to prevent any outside explosion going through the pipes to the highly pressurized cylinders. In addition, there is a micro-filter after each cylinder to filter the gas and prevent the probable long term leakage to the Swagelok valves. All the valves are oil free to prevent any leakage due to chemical reactions with methane. Figure 6.5 displays the cylinders, flow meters, and regulators placed on the trolley and their connections.

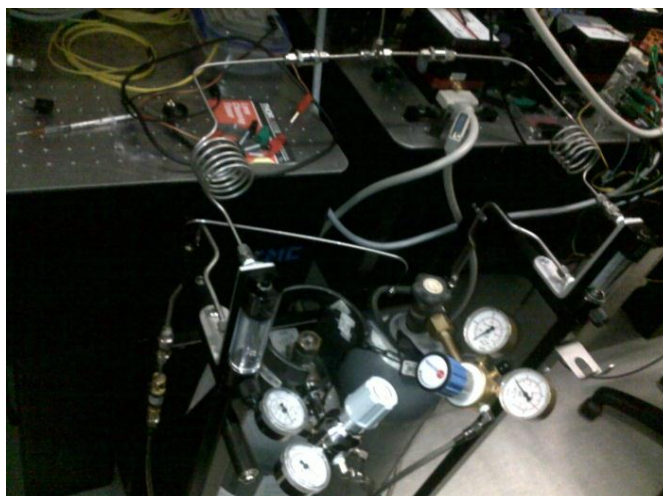


Figure 6.5: High pressure gas cylinders and fittings

**Flow meters:** Two mechanical flow meters are used to adjust the flow rate into the chamber (Table 6.1). The amount of the gas flow rate into the chamber depends on the experimental design. There is also a check valve after each flow meter as mentioned previously, which prevents the gas flow from returning back to the cylinders through the flow meters. These flow meters are used to estimate the methane concentration in the injected mixture.

Table 6.1: Flow meter specifications

<b>Manufacturer</b>	Key Instruments
<b>Max. Flow Rate</b>	5 L/min
<b>Minimum Flow Rate</b>	0.5 L/min
<b>Max. Operating Temperature</b>	+93°C

**IR Detector:** IR detectors are capable of detecting many gases and vapours. IR detectors are known for fast response time, high accuracy, and low cross-sensitivity in gas detection. In the experiments, a Dräger X-am 7000 unit which accommodates a methane IR detector is used to accurately monitor the methane concentrations in the gas chamber (Figure 6.6). This model has a pump which circulates the gas mixture (with a low flow) and returns the tested mixture to the chamber. This keeps the gas mixture consistent during gas monitoring. The technical data of the Dräger sensing unit used in the gas concentration test setup is presented in Table 6.2.

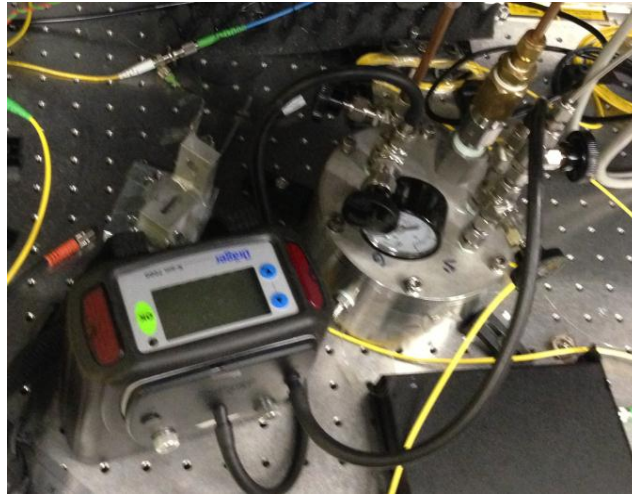


Figure 6.6: The built gas chamber and other connections

Table 6.2: The IR detector specifications (Dräger X-am 7000)

<b>Dimensions</b>		150 × 140 × 75 mm
<b>Weight</b>	Instrument	600 g
	Rechargeable battery	490 g (3.0 Ah)/730 g (6.0Ah)
	Temperature	-20 to +55°C
<b>Ambient conditions</b>	Pressure	700 to 1300 hPa
	Humidity	10 to 95% r.h.
<b>Pump mode</b>	Maximum hose length of 45 m	
<b>Methane sensor</b>	Dräger Smart IR Ex	0-100 Vol. % CH <sub>4</sub>

### 6.3 Spectroscopy Measurement Setup

A spectroscopy measurement system is set to test developed all-fibre sensor heads and reference gas cells. It consists of a DFB laser source, a laser temperature controller (TEC), a laser current source, a PD, a dual function generator, two LIAs, and an oscilloscope. Depending on the experimental design, an extra PD and splitter may be used. Figure 6.7 illustrates a general schematic of this system and component connections. The important characteristics and specifications of the individual parts are presented in this section.

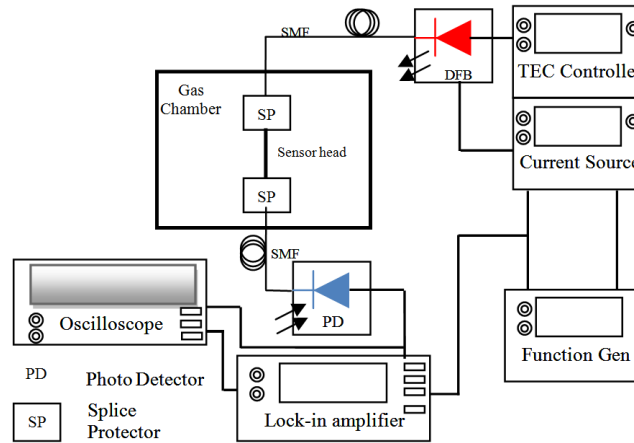


Figure 6.7: Schematic diagram of spectroscopic methane measurement setup; including DFB laser, laser drives, PD, function generator, LIA, oscilloscope

**DFB laser:** Based on the theoretical analysis in Chapter 5, a butterfly DFB laser (Model: LD-1665-0010-DFB-1) was chosen to operate in the 1666 nm region (from 1663.19 nm to 1669.25 nm) which covers the Q-branch of the  $2\nu_3$  methane spectral absorption band (1665 nm - 1668 nm). The DFB source is capable of accurate WMS methane measurements in this range due to the narrower linewidth of DFB (2 MHz) and methane absorption spectral band (few GHz). Shemshad [169] used and calibrated the same laser in his study to test reference methane gas cells in a sequential arrangement. The maximum laser power output is 10.7 mW which meets the Australian standards for operation of laser sources in hazardous explosive areas of underground coal mines. The DFB laser source is hosted in a compact butterfly package (DL DFB BFY), as can be seen in Figure 6.8, which has great heat management capability, a built-in 30 dB isolator, and an FC/APC optical output connector.



Figure 6.8: DFB laser package (DL DFB BFY)

The DFB source is connected to a digital current source and temperature controller (Model: SYS DCC/DTC110). The DFB laser source, package, and controllers were manufactured and tested by Toptica Photonics. The DFB’s technical test details and DL DFB BFY drawing are provided in Appendix VI. Important specifications included in the manufacturer’s test report are provided in Table 6.3.

Table 6.3: Laser system tuning specifications

<b>Coarse Tuning</b>		
<b>Minimum wavelength</b>	1663.19 nm	
<b>Lasing threshold</b>	7 mA	
<b>Minimum temperature</b>	3.0 °C	
<b>Maximum power</b>	13.2 mW	
<b>Maximum current</b>	83 mA	
<b>Maximum wavelength</b>	1669.25 nm	
<b>Lasing threshold</b>	23 mA	
<b>Maximum temperature</b>	48.0 °C	
<b>Maximum power</b>	8.0 mW	
<b>Maximum current</b>	100 mA	
<b>Tuning Rate</b>		
<b>Current tuning rate</b>	1.0 GHz/mA, 0.0090 nm/mA	
<b>Tuned range (pp)</b>	19 GHz	
<b>Temperature</b>	25 °C	
<b>Current</b>	90 mA	
<b>Mod. current (pp)</b>	20 mA	
<b>Mod. frequency</b>	0.1 Hz	
<b>Temperature tuning rate</b>	14.5 GHz/K, 0.13 nm/K	
<b>Current</b>	82 mA	
<b>Tmax/λmax</b>	48.0 °C /1669.25 nm	
<b>Tmin/λmin</b>	3.0 °C /1663.19 nm	
<b>MHFTR</b>	655 GHz	

**Lock-in amplifier (LIA):** Two LIAs were used to extract first and second harmonic signals from the WMS output signal of the PD. The model of the amplifiers shown in Figure 6.9 is SR830 manufactured by Stanford Research Systems. The advantage of LIAs lies in their ability to improve the signal to noise ratio. An intensive phase approach is adopted to detect harmonics, as described in Section 3.2.3. The LIAs and DFB laser source are both modulated with the same high frequency (kHz) sine signal from the function generator. There are two parallel signals from the detectors to be passed from the LIAs. The LIA internally computes the Y component of the harmonic from multiplication of the PD signal by the reference wave, and then the X component is recovered from the PD signal by a phase shifted reference signal. The RMS of the X and Y components provide the magnitude of the harmonic component without being affected by any phase shift between the detector and LIAs.



Figure 6.9: Lock-in amplifier (LIA) model SR830

**Oscilloscope:** A four channel digital oscilloscope is used to monitor and record variations of signal voltages from the LIAs and PD. The model of the oscilloscope used for the experiments is Tektronix DOP 3034 (Figure 6.10).

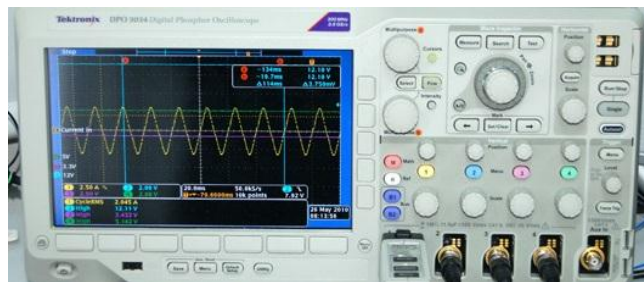


Figure 6.10: Tektronix DOP 3034 Oscilloscope

The described spectroscopy based methane gas concentration measurement system was installed at Queensland quantum optics laboratory of The University of Queensland (Figure 6.11).

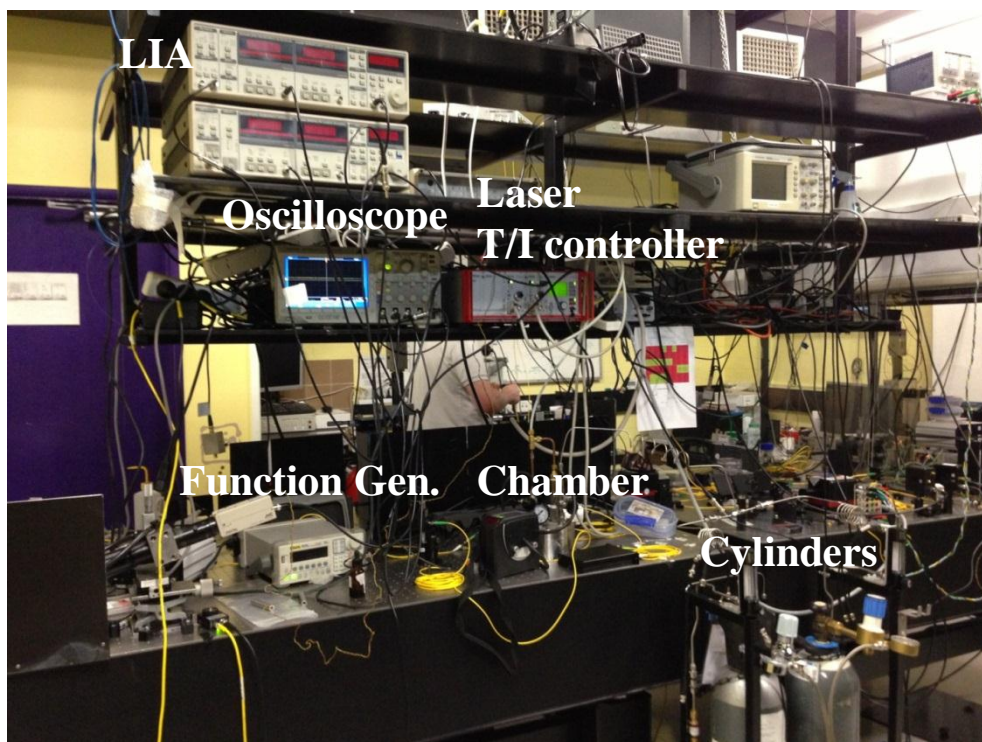


Figure 6.11: Photo of the experimental setup including LIAs, laser controllers, a digital oscilloscope, a function generator, chamber, cylinders, etc.

## 6.4 Experimental procedures

Prior to every experiment, a risk assessment has been performed to make sure that the risks associated with the experiments have been identified and proper measures have been taken to remove hazards. A number of hazards have been identified by a risk assessment which is covered in Appendix I. Some of these hazards are considered in the design stage and some others are controlled procedurally according to the job instructions included in the risk assessment.

**Stabilisation of electronics:** Electronics were operated in an isolated laboratory where minimum optical and electrical noises were presented. The electricity was supplied through an uninterruptible power supply (UPS) unit to protect the electronics.

**Measurements and recording process:** All the signals were recorded on a USB memory of the oscilloscope which was set for high data frequency recording (depending on the experiments).

**Adjustment of laser wavelength intensity output and modulation:** The laser was first tuned with a low frequency ramp signal over a broad laser wavelength range in the presence of a reference methane gas cell to see all methane absorption centres. Then, the modulation peak, the

laser current, and temperature were carefully setup in order to keep only the target methane line centre (1665.961 nm) in the window. There were some considerations from the laser source control manual which were considered, as follows:

- If temperature is set to values less than 15°C make sure the laser diode is switched on.
- The POS/NEG switch on the DCC module has to be set to NEG.

**Fixed-wavelength Absorption Spectroscopy:** As discussed in Section 3.2.2.2, the sensors' response times were calculated using the Direct Absorption Spectroscopy (DAS) method. The laser source was precisely set to operate at line centre of an absorption branch of methane around 1666 nm, mostly 1665.961 nm. To avoid fibre movement and intensity change other than methane absorption, the optical fibres and splice points were secured inside and outside of the chamber. Laser output was minimised at a line centre by adjusting the temperature and current. Figure 6.12 illustrates the experimental setup schematic for fixed-WMS.

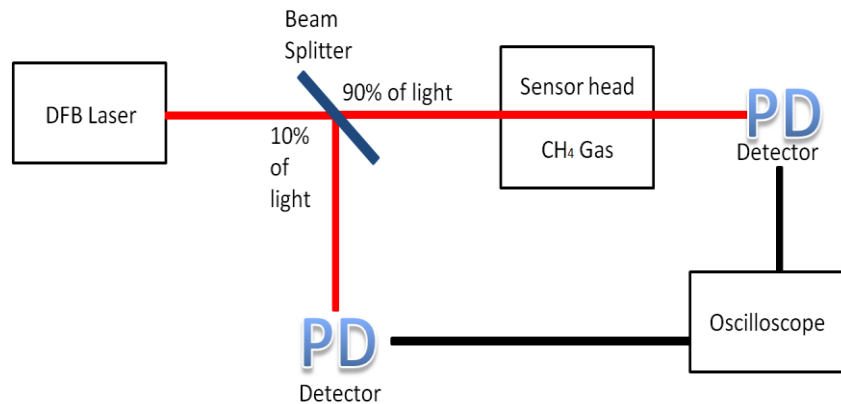


Figure 6.12: Schematic of fixed-wavelength absorption spectroscopy experiment

**Scanned-wavelength Absorption Spectroscopy:** For direct absorption measurements, the ramp was turned up to maximise the absorption in order to make sure that the laser source operated at the centre of absorption feature, and then the signal was recorded. Figure 6.13 shows a schematic of the arrangement used for this measurement using reference gas cells and drilled hollow core fibres. Data was normalised using the recorded signal before the sensor head.

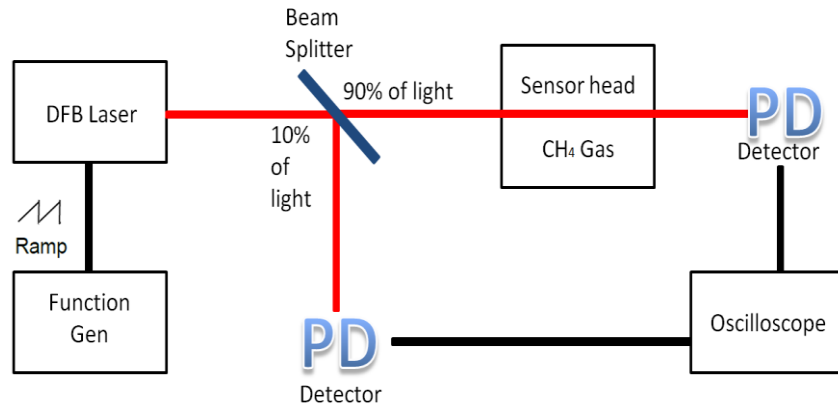


Figure 6.13: Schematic of scanned-wavelength absorption spectroscopy experiment

**Wavelength Modulation Spectroscopy:** The WMS signal was detected using an additional high frequency signal that was added to the DFB laser through T-bias. The modulation index was accurately adjusted to maximise the output signal as presented in Section 3.2.3.4. The PD output was delivered to the oscilloscope and the LIAs to detect the harmonics. The LIAs were referenced with the same sine signal modulated from the DFB laser source. The LIAs were set to have a higher signal to noise ratio with low pass filtering and amplification. The LIA outputs were delivered to the oscilloscope for recording. A schematic of the WMS measurement setup is illustrated in Figure 6.14.

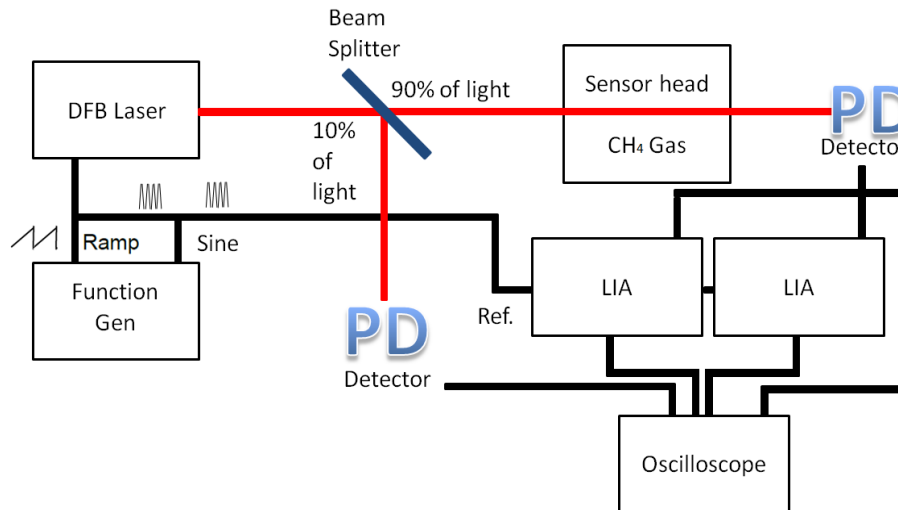


Figure 6.14: Schematic of Wavelength Modulation Spectroscopy (WMS) experiment

An actual screenshot of the oscilloscope with a WMS signal is illustrated in Figure 6.15. The blue signal is the WMS output from the PD after a 16.5 cm reference gas cell containing 5% of methane. The green and purple signals are displaying the second harmonic and first harmonic as detected by the LIAs, respectively.



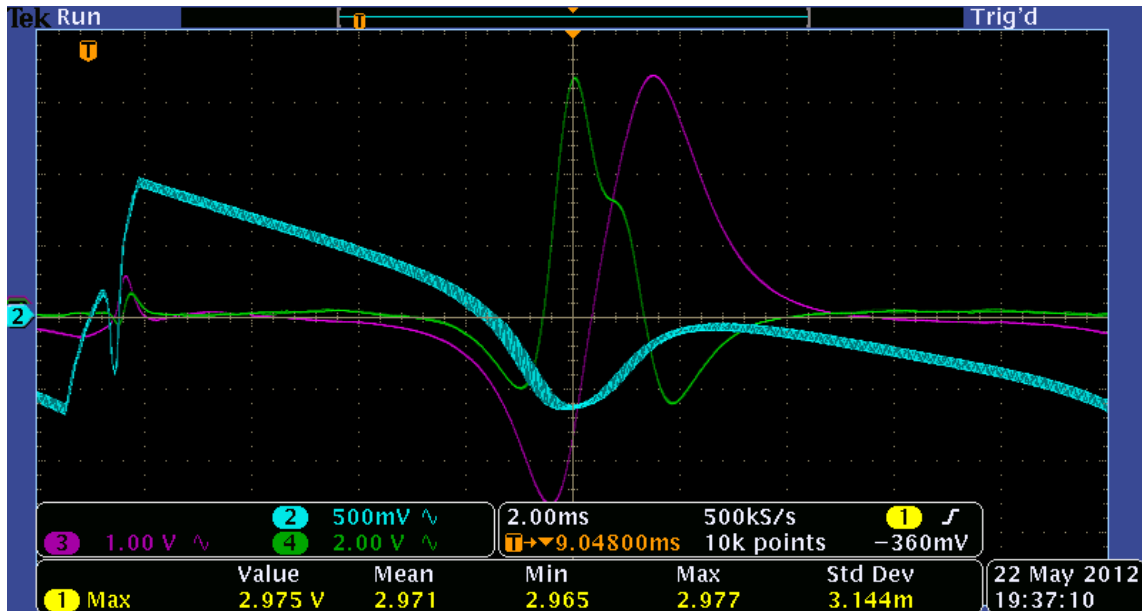


Figure 6.15: A screenshot of oscilloscope showing WMS signal (blue), 2f-WMS (green), and 1f-WMS (red) from a 5% methane filled reference gas cell

The oscilloscope's data is recorded on an external USB memory and is transferred to a computer for data analyses. A filtered and normalised sample of second and first harmonic WMS signals is presented in Figure 6.16.

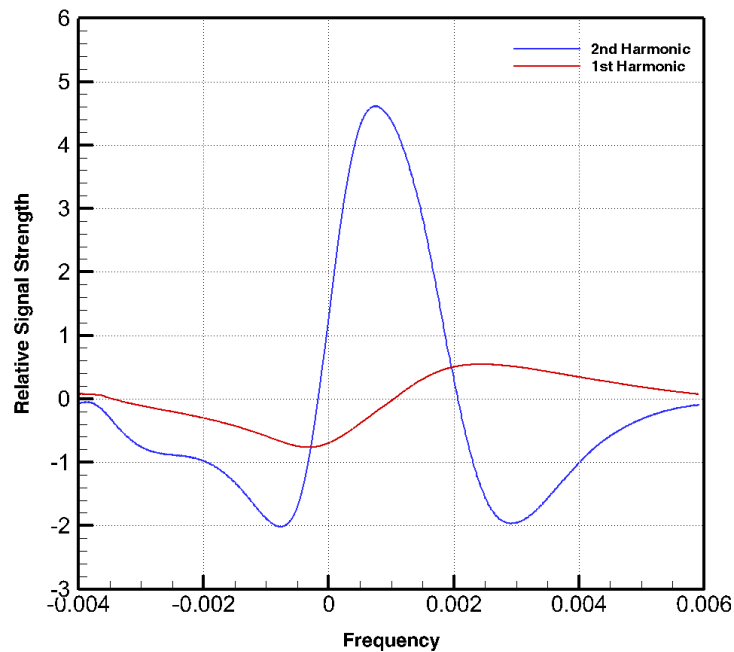


Figure 6.16: Normalised and filtered WMS-1f and WMS-2f signal of a reference gas cell

**Gas concentrations test:** At the beginning of each test, the gas mixture remaining from the previous test was evacuated from the chamber. The chamber was either filled with 100% nitrogen or exposed to air for a significant period of time with an open valve or top lead. A low flow rate of the gas mixture, usually one liter per minute, was injected for a pre-calculated time interval to reach the desired gas concentration in the chamber. The exhaust outlet valve was kept open to avoid chamber pressurisation. As soon as the injection was stopped, the inlet and outlet valves were set closed. The gas concentrations were recorded during the experiments using the IR detector while its pump was circulating the mixture. There were delays involved in the IR measurements, so the detector continued operating during the experiments.

**Cylinder replacement:** The following steps were followed to replace the cylinders:

- Open the gas regulator. Connect the cylinder to the regulator with a left turning connector for the mixture cylinder and a right turning connector the for nitrogen cylinder.
- Maintain the regulator in a safe position. Keep the side connected to the cylinder clear and with no scratch, as it does not have a ring on that side.
- Replace the bottle with a similar bottle.
- Design and perform a new risk assessment before increasing the percentage of any new mixture.

# CHAPTER 7

## ALL-FIBRE SENSOR DEVELOPMENT

### 7.1 Introduction

Optical fibres are very efficient light conduits, which makes them suitable for sensing applications. In an optical fibre, nearly all of the light travels in the core at the centre of the fibre. In order to perform sensing with fibres, the fibre must be modified to allow interaction between the light in the core and the surrounding gases. Whilst the gases simultaneously absorb the travelling light within the modified parts, the intensity changes can be monitored at the fibre end. Four types of sensor heads (Figure 7.1) were considered in this study:

- In the *open path gas cell* (Figure 7.1a), light was out-coupled from a single mode fibre (SMF) into free space. It was then allowed to propagate and interact with the methane before coupling back into a second SMF. A number of standard gas cells with various methane concentrations were purchased from Wavelength References Inc.
- In the *tapered optical fibre* sensor head (Figure 7.1b), the light remained guided by the optical fibre; but by drawing the fibre down to a diameter less than the optical

wavelength, a fraction of the field propagated externally to the fibre and thus was able to interact with the methane.

- In the *drilled SMF* (Figure 7.1c), a hole was drilled in the side of the fibre up to the edge of the core. This allowed some of the light to propagate into the hole and interact with the methane that diffused into the hole.
- The *drilled hollow core fibre* (Figure 7.1d) had a core of air instead of silica. A hole was drilled in the side of the fibre until the core was breached. This allowed the methane to diffuse directly into the path of the light so that it could be detected.

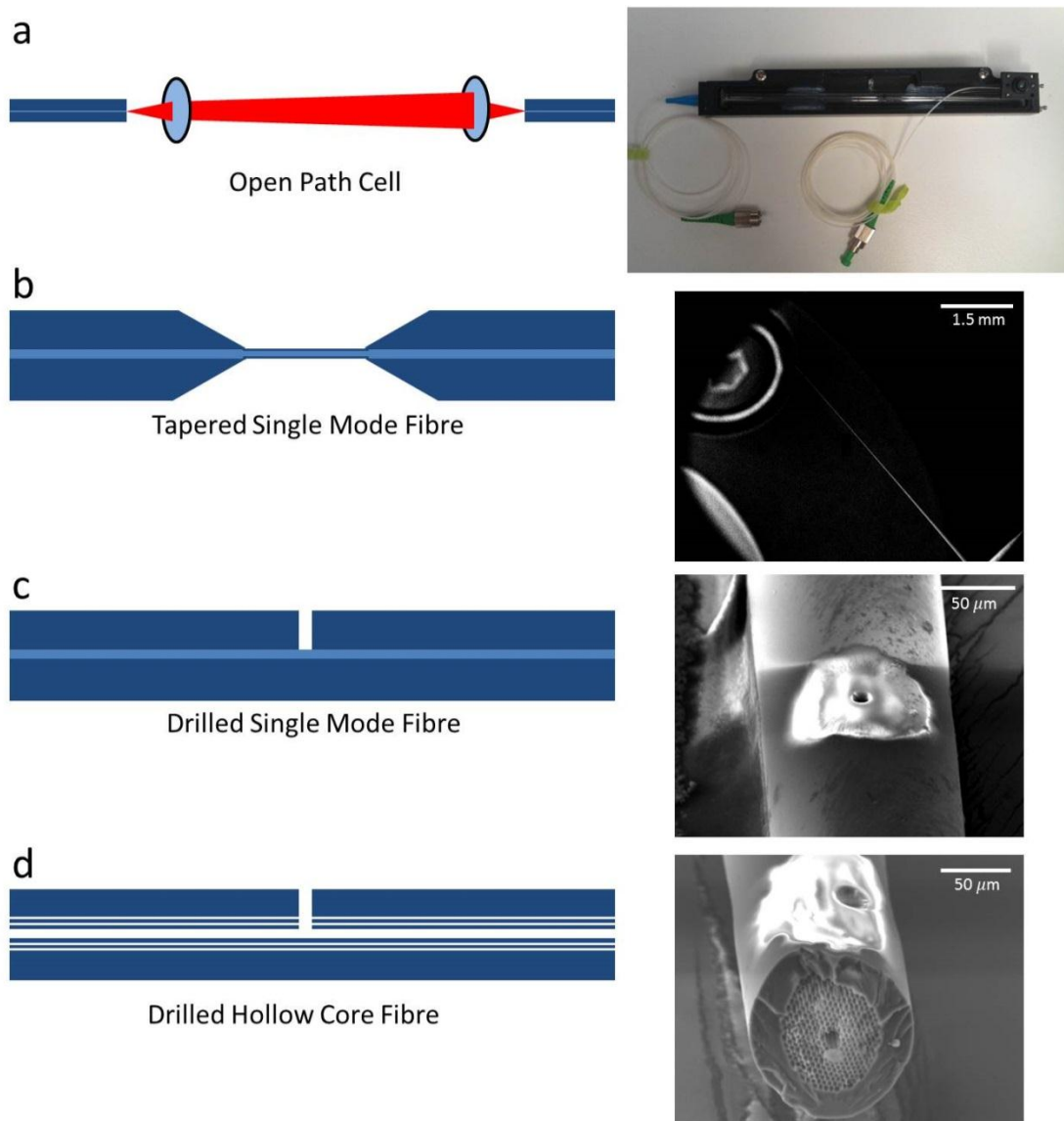


Figure 7.1: Profile illustrations of the four types of sensor head investigated in this project (left), and images (photograph/micrograph) of real examples of the sensor head (right).

In this section, the development stages of all-fibre sensor heads, including tapered fibres, drilled SMFs, and drilled hollow core fibres (HCFs) are presented.

## 7.2 Fibre Optic Sensor Head Fabrication

### 7.2.1 Tapered Single-mode Fibres

Tapered fibres were prepared in-house using a taper pulling rig (Figure 7.2) based on a standard method [122, 123]. A standard single mode optical fibre (SMF-28: as specification in Appendix V) was stretched over an oscillating hydrogen flame using a set of mechanical stages.

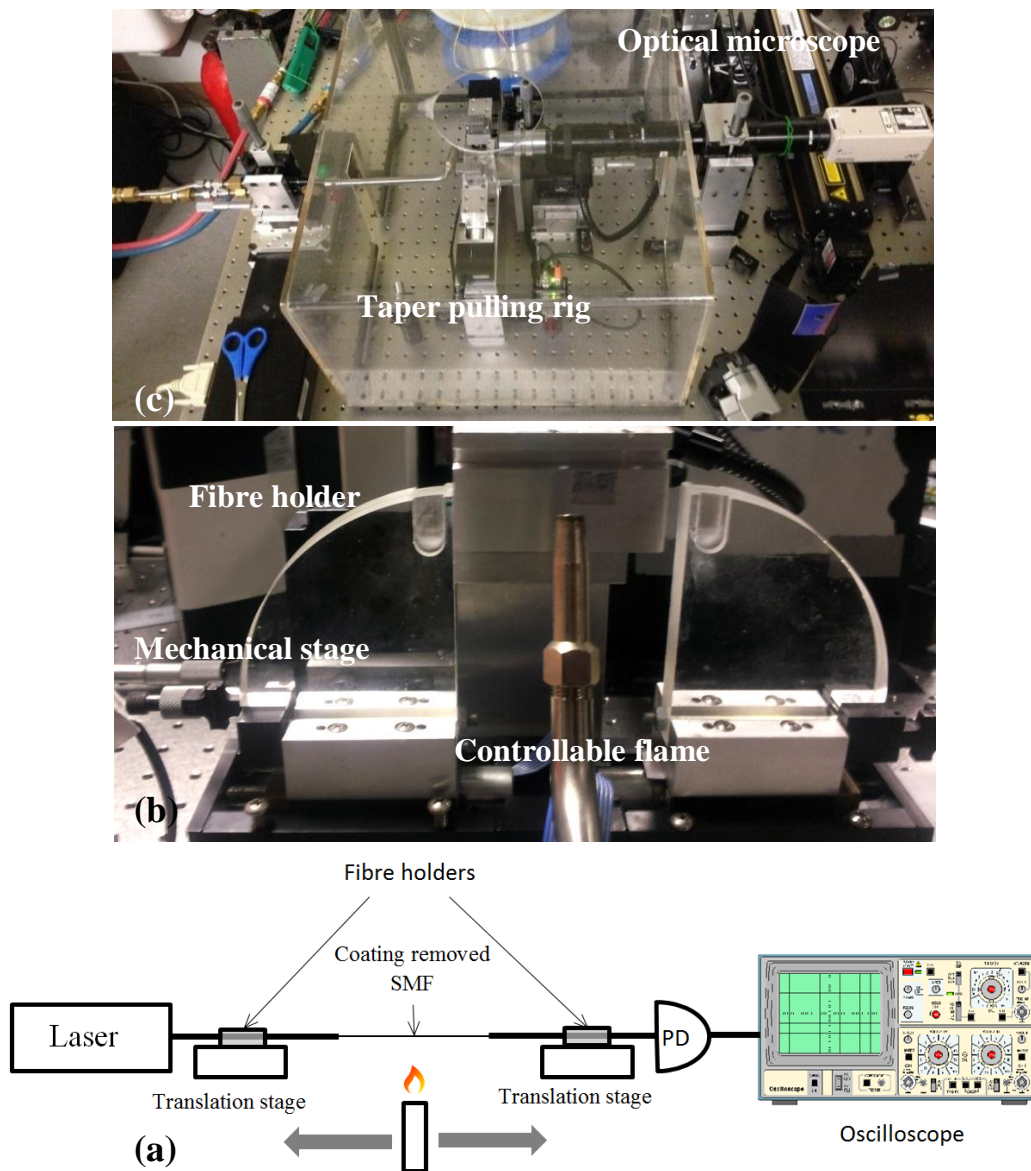


Figure 7.2: (a) Schematic diagram, (b & c) Photographs of taper pulling rig

The transmission through the fibre was monitored as the experiment progressed so that stretching could be stopped once the taper had been stretched to accommodate only a single optical mode. This ensured that the waist of the fibre was sufficiently narrow to induce some of the laser light to travel outside of the fibre and was indicated by an abrupt switch from an oscillating transmission pattern to a constant transmission.

Tapered fibres are extremely fragile due to having a very narrow waist ( $< 1.5 \mu\text{m}$ ). Therefore, in order to protect them, they were secured to a stainless steel clamp using epoxy. An example of the tapered fibres prepared in the laboratory is shown in Figure 7.3.

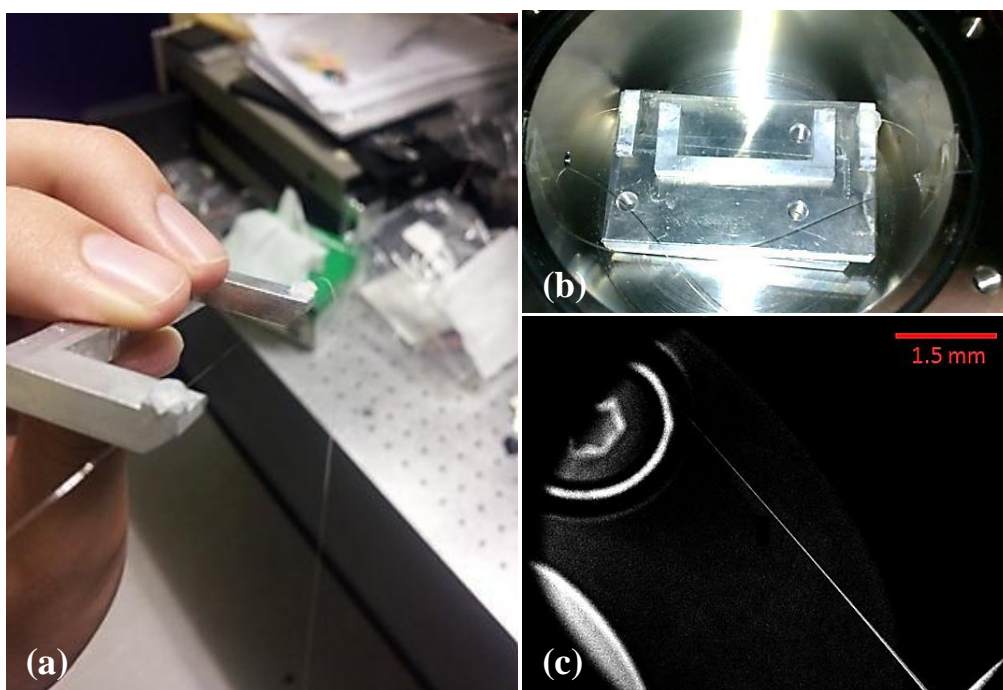


Figure 7.3: Images of (a) tapered fibre in stainless steel clamp, (b) tapered fibre clamped inside the gas chamber, (c) scanning electron micrograph showing the narrowing of the fibre

The length and diameter of the tapered region of the fibre could be controlled, to some extent, by varying the pulling parameters. For example, by pulling the fibre for a longer distance, whilst initially maintaining the flame in a single position before turning on the flame oscillation, it was possible to pull a tapered fibre with a tapered region twice as long (20 mm vs. 10 mm). Tapered optical fibres allow interaction of the surrounding gas with light passing through the optical fibre via evanescent coupling in the tapered region; therefore, an extended tapered region serves to increase the interaction volume with the surrounding atmosphere. As discussed in Section 4.2.1, different settings of the flame oscillator were used to achieve a gradual linear tapered profile

with minimum waist diameter (from 0.8  $\mu\text{m}$  to 1.5  $\mu\text{m}$ ) and maximum waist length (10 mm to 20 mm). Figure 7.4 illustrates the various setups used on a LabView program including the expected taper diameters, profiles, and amplitude of the oscillating stage drive over time.

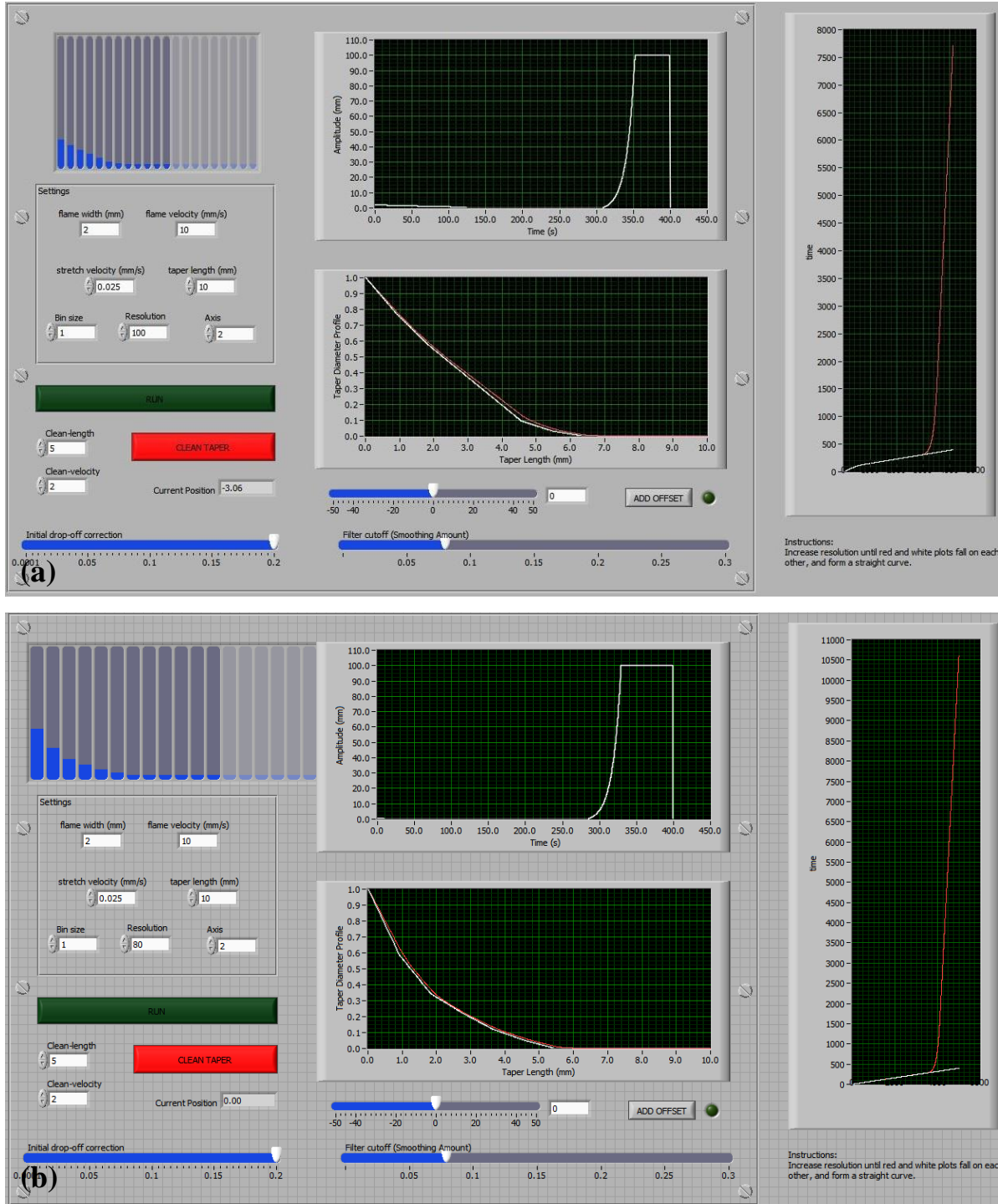


Figure 7.4: Screenshot of the LabView Flame oscillation program (a) linear tapered profile setting, (b) linear exponential tapered profile

### 7.2.2 Drilled SMFs

Standard SMFs were drilled using focused ion beam milling. This involved aiming a focused stream of ions (gallium) at the surface of the fibre within a vacuum chamber. When the gallium ions strike the surface of the fibre its atoms become ionised and are ablated from the surface. Focused ion beam milling is performed with an adapted scanning electron microscope so that the drilling process can be monitored during the course of the drill. The drilling speed depends on the substrate and also the size of the hole. While drilling a 10  $\mu\text{m}$  diameter hole into a silicon fibre, the drilling rate is approximately 1  $\mu\text{m}$  per minute (beam current = 7 nA). The experimental laboratory and equipment are shown in Figure 7.5.

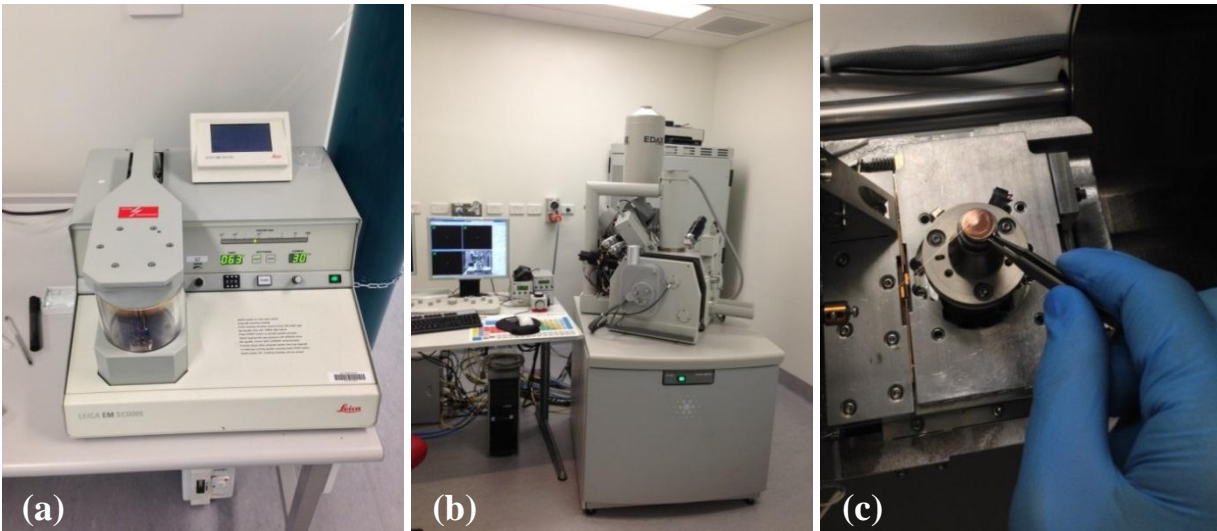


Figure 7.5: Australian microscopy & microanalysis research facility (AMMRF) at Queensland University of Technology, (a) Leica EMSCD005 gold coating vacuum chamber, (b) EDAX FEI Quanta 3D SEM/FIB dual beam system in, (c) gold coated fibre placed inside the FIB chamber for drilling

An example of the progress of one such drill is demonstrated in the scanning electron microscope images in Figure 7.6.



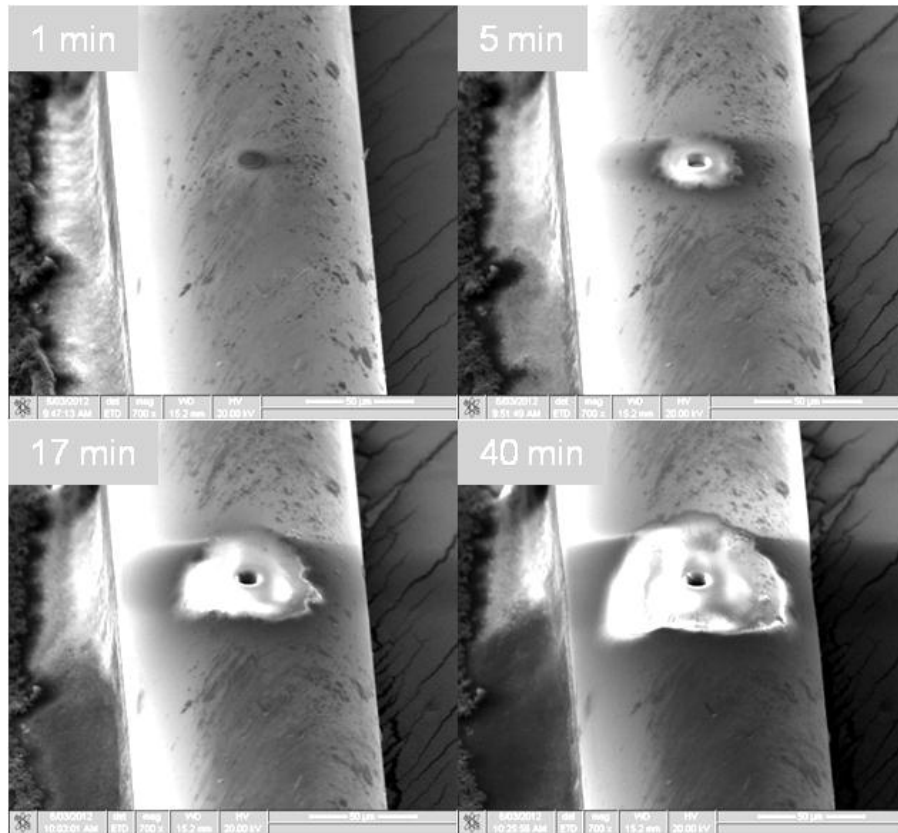


Figure 7.6: Scanning electron microscope images showing the progress of a 10  $\mu\text{m}$  diameter hole drilled into a single mode fibre using a beam current of 7 nA.

To make a useful sensor head, it is important that the drilled hole reaches the core of the fibre so that the light inside the core can interact with the gas diffused into the hole. This requires precise drilling and the ability to characterise the drilled hole. Due to the optical transparency of SMFs, it was not feasible to precisely measure the depth of the drilled hole using standard techniques such as microscopy or optical profilometry. For example, the image in Figure 7.7 demonstrates that the drilled hole can be seen, but its trajectory cannot be inferred from a 2 dimensional image.

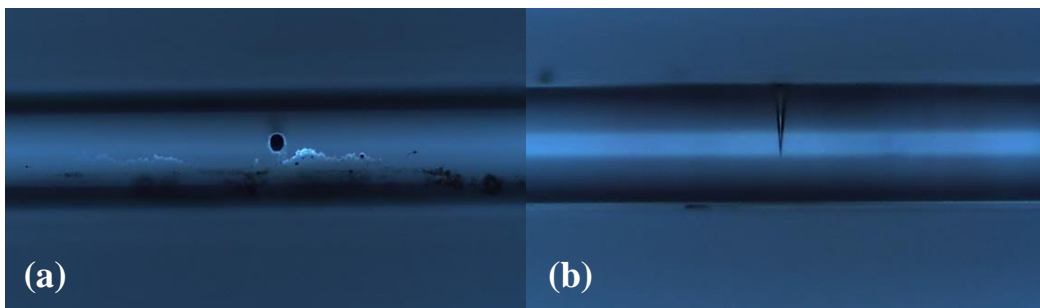


Figure 7.7: Optical micrographs showing a 10  $\mu\text{m}$  dia. hole drilled in a standard optical fibre by focused ion beam milling (a) imaged from above the hole, (b) imaged from the side of the hole

From the optical microscopy image, it was not possible to determine if the drilled hole was touching the fibre core. Standard probing techniques such as atomic force microscopy were also not possible to adopt due to the large aspect ratio of the drilled holes. Instead, micrometre scale drilled holes, a novel technique for probing high aspect ratios, was developed using a tapered fibre tip as the probe. The optical microscopy setup and piezo stage for probing the drilled fibre are presented in Figure 7.8.

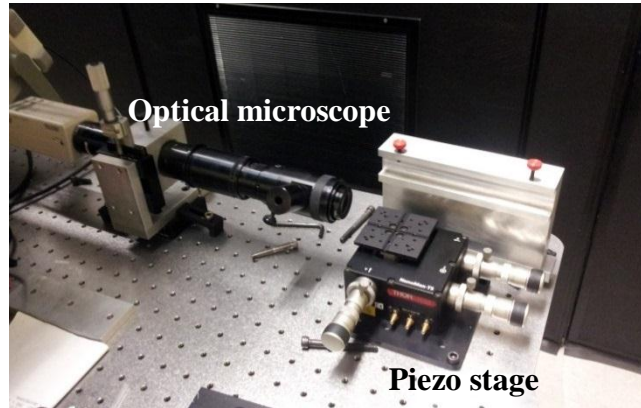


Figure 7.8: Optical microscopy setup and a piezo stage to insert a tapered fibre tip for characterisation of the drilled hole

The principles of this fibre probing technique are demonstrated in Figure 7.9. A tapered fibre tip, made by breaking a tapered fibre, was secured to a clamp. The fibre to be probed was secured to a piezo controlled stage such that it was positioned under the tapered tip. The stage was used to move the tapered tip into the drilled hole, whilst monitoring the experiment using optical microscopy. The tapered tip was selected such that it could reach the base of the drilled hole (dia.  $< 5 \mu\text{m}$ ). The depth of the hole could therefore be estimated based on the distance travelled by the piezo stage before the tapered tip flexed (indicating the base of the hole had been reached).

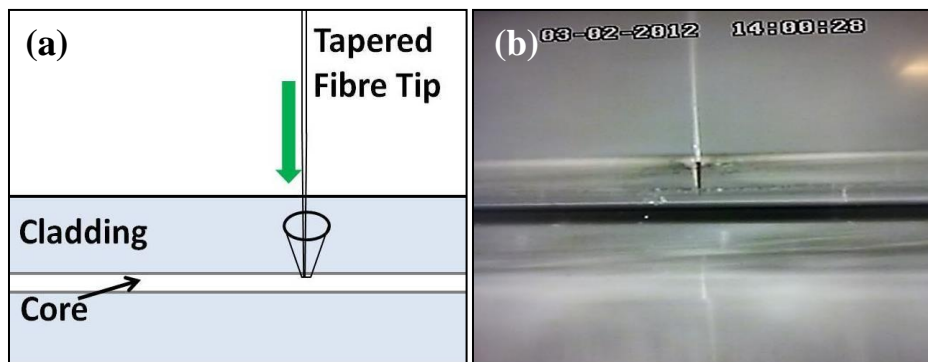


Figure 7.9: (a) Schematic representation of a tapered fibre tip inserting into a hole drilled in a standard fibre. (b) Optical micrograph showing a tapered fibre tip inserting into a hole drilled in a standard fibre.

A sampling of measured depths of drilled fibres is provided in Table 7.1. As expected, the measured depths of the holes are shorter than the depths programmed into the FIB (because the FIB is optimized to drill into silicon rather than glass). The distance between the edge of the cladding and the edge of the core is expected to be 60  $\mu\text{m}$ .

Table 7.1: Comparison of measured fibre hole depths with depth programmed into FIB

Programmed Drill Depth as per FIB ( $\mu\text{m}$ )	Probed Depth ( $\mu\text{m}$ )	Imaged Depth ( $\mu\text{m}$ )
60	24	18
120	96	81
150	93	73

Importantly, the probing technique could also determine if there was interaction between the drilled hole and the fibre core. If the hole was drilled close enough to the fibre core such that there was an interaction with the evanescent field of the core of the standard SMF, then touching the base of the hole with the probe tip produced changes in the intensity of light transmitted through the fibre due to scattering. A typical result is shown in Figure 7.10.

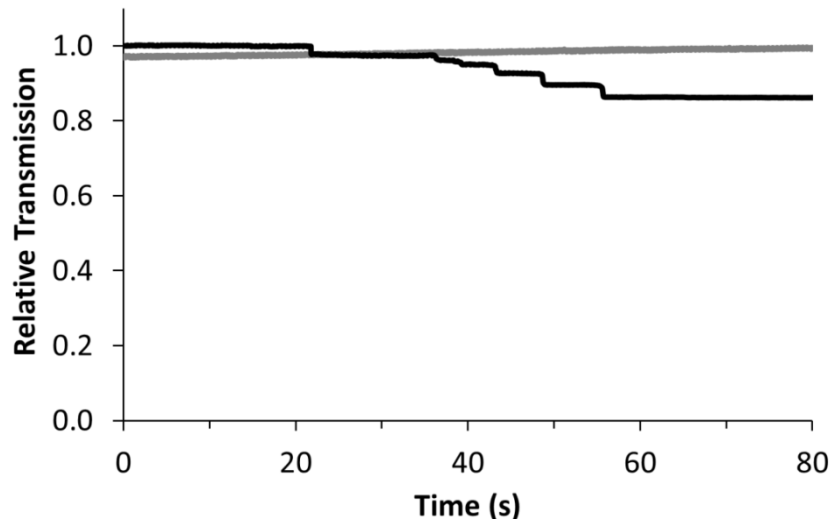


Figure 7.10: Transmission intensity of 1666 nm light passing through drilled standard optical fibres as a probe was inserted into the drilled hole until it touched the base of the hole. The depth of the hole was 96  $\mu\text{m}$  (black), 35  $\mu\text{m}$  (grey)

Figure 7.10 shows that as the fibre tip approached the base of the drilled hole, the transmission began to decrease as a result of the scattering of light by the tip. The amount of loss continued to increase as the tapered tip further approached the base of the hole. Each step-down in transmission, as evidenced by the black trace in Figure 7.10, corresponds to a movement of the

fibre probe 2  $\mu\text{m}$  closer to the base of the hole until the probe reached the base at about 55 sec. On the other hand, when the hole was drilled too short such that it did not interact with the evanescent field of the core, probing the entire depth of the hole did not result in any significant changes in the fibre transmission. This is evident in the grey trace in Figure 7.10. The important point is that the fibre probing technique allowed the identification of drilled holes that were close enough to the core to facilitate interaction between the light in the core and the hole. This allowed the most suitable candidates for sensing to be selected for experiments in the gas chamber.

### 7.2.3 Drilled Hollow Core Fibres

Hollow core fibre (HCF) consists of a silica cladding and an air core. The core of the fibre consists of a central air filled hole that runs through the length of the fibre, surrounded by smaller holes in a honey-comb arrangement. The light is guided through the air-core with 95% confined to the larger central core. These features are visible in the scanning electron microscope and optical microscope images in Figure 7.11. As discussed in sections 4.1.2, 4.2.3 and 5.4, HC-1550-02 is one of the fibres selected for methane gas sensing in this study.

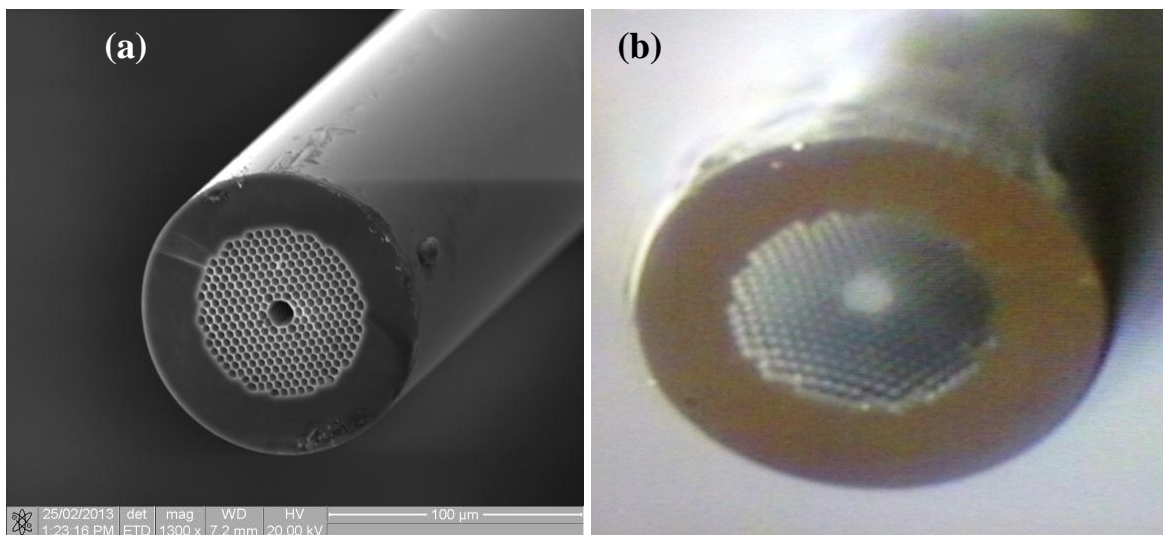


Figure 7.11: Cross section of a cleaved HC-1550-02 fibre (a) SEM image, (b) optical microscopy image

Unlike SMFs, the core of HCFs can act as a spectroscopic cell if the target gas is allowed to diffuse into the air core. This means that the interaction volume is potentially as large as full light interaction over the length of the HCF segment. In order to facilitate the diffusion of gas into the core of the fibre, holes must be drilled into the side of the fibre so that the gas penetrates into the

central core [29, 43, 136, 142]. Proper protection of the micro-channels against moisture and contaminants is necessary for use in a practical environment if an increase in response time is desired; however, a filtering design is not within the scope of this study. Figure 7.12 shows an SEM image of an HCF cross section with a 10  $\mu\text{m}$  diameter hole drilled into its core.



Figure 7.12: Scanning electron micrograph (SEM) showing the cross section of a hollow core fibre that has had a 10  $\mu\text{m}$  dia. hole drilled into its core (the fibre tip was broken)

Hollow core fibre sensor heads were drilled using focused ion beam drilling in a similar manner to the SMFs. The drilling time of HCFs was significantly less due to the microstructured nature of a significant portion of the fibre depth (as apparent in Figure 7.11 and 7.12). Some typical scanning electron microscopic images of the resulting drilled holes are shown in Figure 7.13. From the 12,000x magnification image of the drilled HCF, it is obvious that the fibre's central core was successfully breached. Therefore, unlike the SMFs, an additional probing technique was not required to determine the most suitable sensor heads for gas chamber testing. When the fibre core could be viewed through the drilled hole, it was clear that the gas could diffuse into the core.

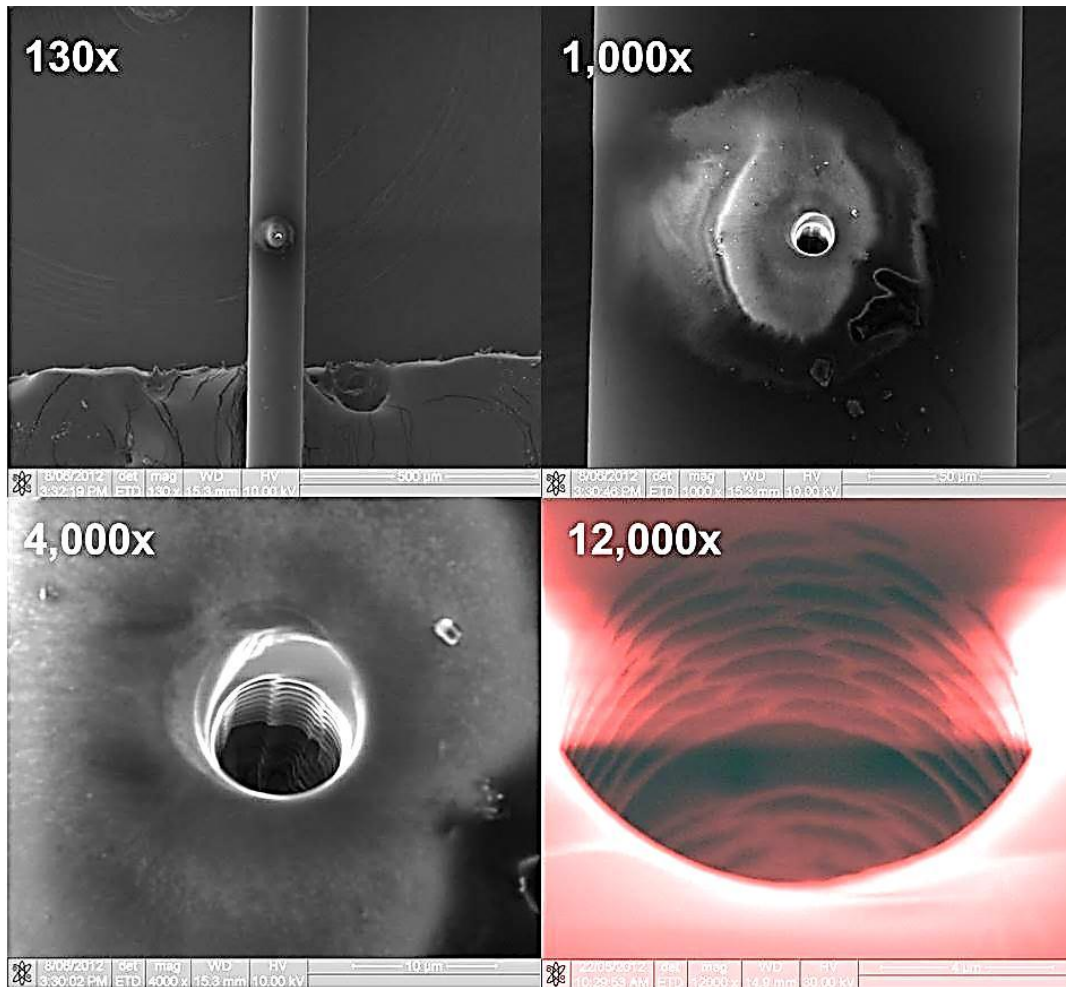


Figure 7.13: Scanning electron micrographs showing a 10 µm diameter hole drilled in a hollow core fibre (HCF) using focused ion beam drilling at the indicated magnification. False colour has been added to the 12,000x image to increase contrast

### 7.3 Fibre Coupling and Splicing of HCF to SMF

In order to use a drilled HCF in remote gas measurements, it is important to couple the HCF to an SMF. Proper fibre coupling and splicing should maximise power transmission through the fibres by avoiding back reflection from the splice and coupling points. Table 7.2 presents the specifications of the fibres used in our experiments. The mode shape overlap of the HCF (HC-1550-02) used with a SMF-28 is over 85%, and over 95% of the light fraction is in the air holes. In addition, choosing this type of HCF has the advantage of similar core diameter to the SMF (10  $\mu\text{m}$  vs. 8.2  $\mu\text{m}$ ).

Table 7.2: Specifications of the SMF and HC-PCF used in the experiments (According to appendices III & IV)

<b>Parameters</b>	<b>SMF-28</b>	<b>HC-1550-02</b>
<b>Core Diameter</b>	8.2 $\mu\text{m}$	10 $\mu\text{m} \pm 1 \mu\text{m}$
<b>Pitch</b>	N/A	3.8 $\mu\text{m}$
<b>Ring in the cladding</b>	N/A	7
<b>Cladding diameter</b>	125 $\mu\text{m} \pm 0.7 \mu\text{m}$	120 $\mu\text{m}$
<b>Coating diameter</b>	245 $\mu\text{m} \pm 5 \mu\text{m}$	220 $\mu\text{m}$
<b>Diameter of holey region</b>	N/A	70 $\mu\text{m}$
<b>Mode field diameter</b>	10.4 $\mu\text{m} \pm 0.5 \mu\text{m}@1625\text{nm}$	7.5 $\mu\text{m} \pm 0.5 \mu\text{m}@1550\text{nm}$
<b>Transmission loss</b>	0.20 dB/Km	0.03 dB/m

Using the same program as the SMF to SMF splice on the Ericson FSU-975 splicer causes collapsing and melting of both fibre heads (Figure 7.14). Calculating of the best arrangement for splicing HCFs to SMFs has attracted the attention of researchers in last few years. The major aims are to minimise the splice losses and strengthen the connections.

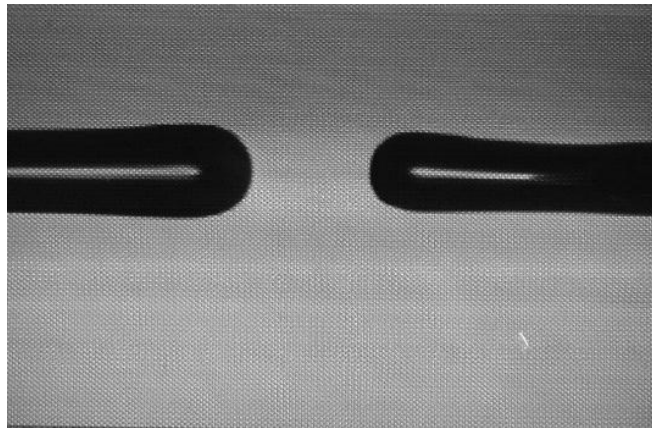


Figure 7.14: Side view of HCF (left) to SMF (right) splice attempt using SMF splice program on FSU-975 splicer

Among all the previous studies [30, 31, 107, 119, 155, 170-177], Xiao, *et al.*[178] have achieved the best possible setting for a successful splice between an HC-1550-02 and an SMF-28; consequently, we have used their fibre specifications in our study. Table 7.3 shows the optimised parameters for splicing an SM-28 to an HC-1550-02.

Table 7.3: SMF-28 to SMF-28 and HC-1550-02 splice parameters used in this study (based on [178])

<b>Splice parameters</b>	<b>SMF-28</b>	<b>HC-1550-02</b>
<b>Pre-fusion time</b>	0.2 s	0.2 s
<b>Pre-fusion current</b>	10 mA	5 mA
<b>Gap</b>	50 $\mu\text{m}$	50 $\mu\text{m}$
<b>Overlap</b>	10 $\mu\text{m}$	10 $\mu\text{m}$
<b>Fusion time one</b>	0.3 s	0
<b>Fusion current one</b>	10.5 mA	-
<b>Fusion time two</b>	2.0 s	0.3 s
<b>Fusion current two</b>	16.3 mA	9 mA
<b>Fusion time three</b>	2.0 s	0
<b>Fusion current three</b>	12.5 mA	-
<b>Centre position</b>	255	250

Figure 7.15 shows an optical microscopy image and an SEM image of a successful splice between an HC-1550-02 and an SMF-28 using an Ericson FSU-975 with the parameters provided in Table 7.3. The estimated loss is measured as 1.5 dB.

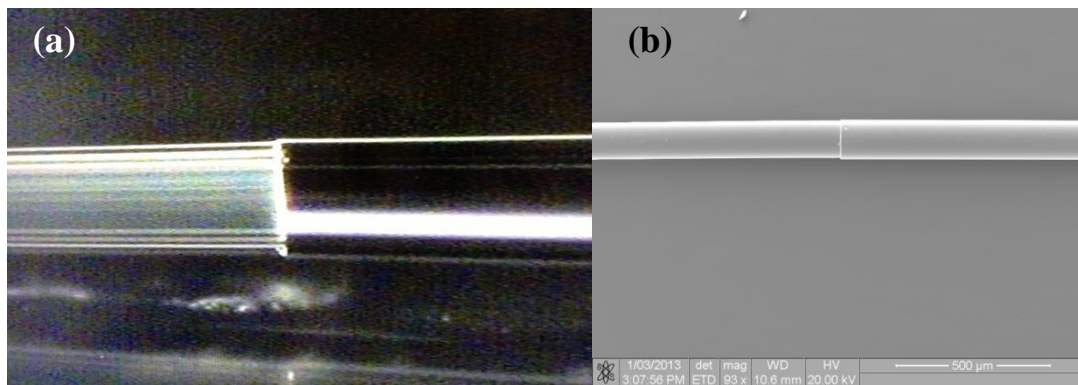


Figure 7.15: Image of HCF (Left) splice to SMF-28 (Right); (a) optical microscopy image, (b) SEM image

The splice between the SMF and the HCF reflects 4% of light due to the difference between refractive indexes of the cores (air core vs. silica core). As shown in Figure 7.16, these reflections result in a Fabry-Perot cavity between these two points.



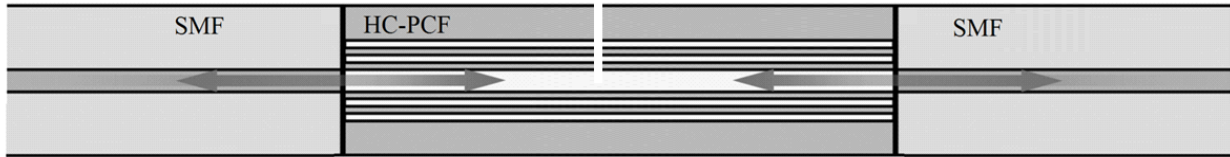


Figure 7.16: Back reflection from splice point which causes a Fabry-Perot cavity between splice point of the HCF and the SMF in a drilled HCF sensor head (after [176])

A Fabry-Perot cavity causes an extra oscillation on top of the WMS ramp signal (Figure 7.17). This oscillation prevents harmonic detections and may cause damages to the DFB laser source. One of our developed sensor heads (85mm) did not have a considerable Fabry-Perot cavity effect. In addition, a 345 mm long HCF was successfully spliced with an acceptable noise level for the first harmonic WMS measurements (Section 8.2.4.3). A number of subsequent attempts failed to produce a low reflection splice between the SMFs and the HCFs. The splice is either very weak or lead to collapse of holey cores at transition region. An angle cleaved connection or splice could reduce the back reflection considerably [176]. However, an angle cleaver was not available at our laboratory to experiment further with splicing HCF-SMF segments.

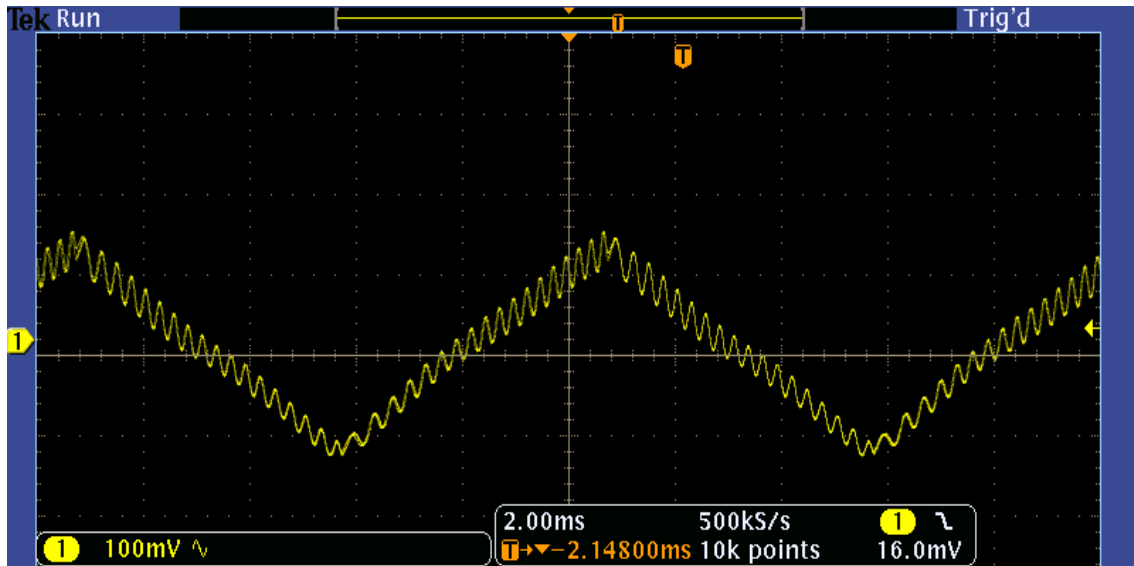


Figure 7.17: A screenshot of oscilloscope showing noise on WMS signal due to cavity between two splice fusion between a 40mm HCF ends and SMFs

# CHAPTER 8

## EXPERIMENTAL ANALYSIS

### 8.1 Introduction

In this section, the results of the developed all-fibre sensor heads and open path gas cell tests using the direct absorption spectroscopy (DAS) method and wavelength modulation spectroscopy (WMS) are presented.

### 8.2 Sensing Experimental Results

#### 8.2.1 Open Path Gas Cells

Open path gas cells containing certified concentrations of methane were purchased from Wavelength References Inc. These cells consisted of sealed chambers containing a known methane concentration (0.1% – 10%) in nitrogen. The cells had a fibre optic input and output so that the light could pass through the gas in the cell and then refocused back into a fibre and detected by a photo detector (PD). Thus, each individual cell simulated a situation where methane diffused from the environment into the cell for detection. However, the cell remained sealed for the initial tests. A general experimental setup used for open path gas cell test is shown in Figure 8.1. Light from a DFB laser was split so that 90% passed through the open path gas cell

and then reached a detector. The other 10% went straight to a detector so that the absorption intensity could be normalized to variations in the laser output intensity. Absorption at a particular wavelength was determined by subtracting the intensity of light transmitted through the gas cell ( $I$ ) from the intensity in the absence of methane ( $I_0$ ). The open path gas cells could be switched out so that the methane concentration would be varied.

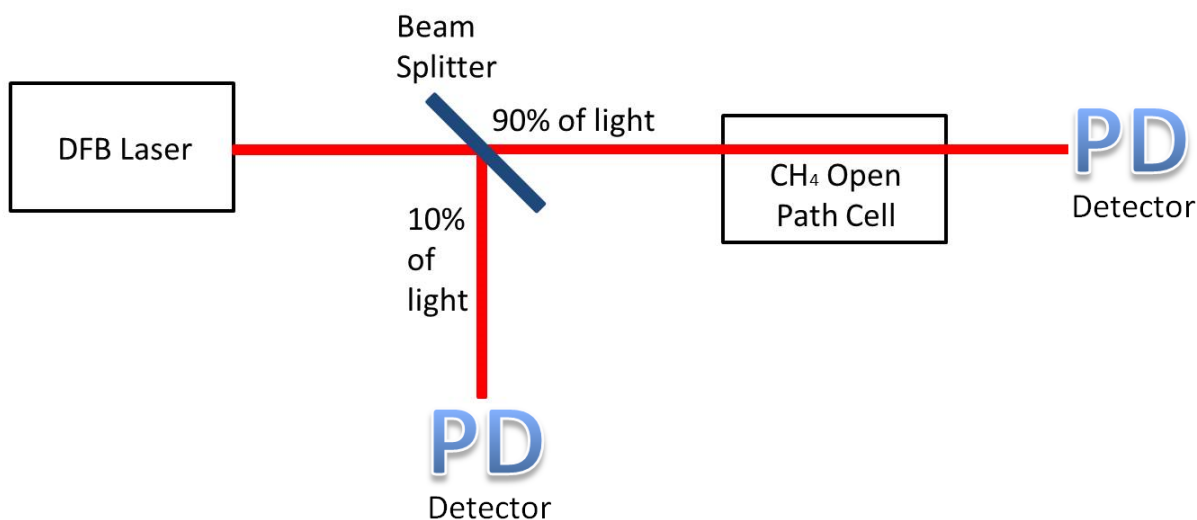


Figure 8.1: General experimental setup (simplified) for methane detection in an open path gas cell

### 8.2.1.1 Direct Absorption Spectroscopy

The prefilled open path gas cell has the advantage of having instantaneous response because the method does not rely on diffusion of gas into a hole or aperture. Using the DAS experimental setup explained in experimental procedures (Figure 6.13), the absorption peak in the methane spectrum at 1665.961 nm (Q6 branch) was monitored at different methane concentrations employing a scanned-wavelength absorption spectroscopy method. Figure 8.2 shows a methane calibration curve for DAS. The absorption intensity was demonstrated to increase with the methane concentrations. Linearity of the curve was relatively poor ( $R^2 = 0.9917$ ). This reduced the accuracy of the method; the relative error was 25.03%. For example, using this calibration curve, a sample of 2.00% methane gave a result of  $2\% \pm 0.5$ . Such an error at the 2% methane concentration level (a common mine alarm level) is unacceptable and could potentially result in false alarms or erroneous safe level readings. It is likely that the source of the calibration non-linearity and poor accuracy was a result of drifts in the laser frequency caused by small temperature fluctuations in the lab. Also, the different gas cell characteristics and Etalon effect could have introduced a significant error to this calibration curve. However, these noise sources

could be significantly reduced by employing WMS. Although accuracy was poor, sensitivity was not influenced by minor wavelength drifts of the laser in the same manner. Sensitivity using DAS was 0.01% which is impressive but was negated by the poor accuracy of the method.

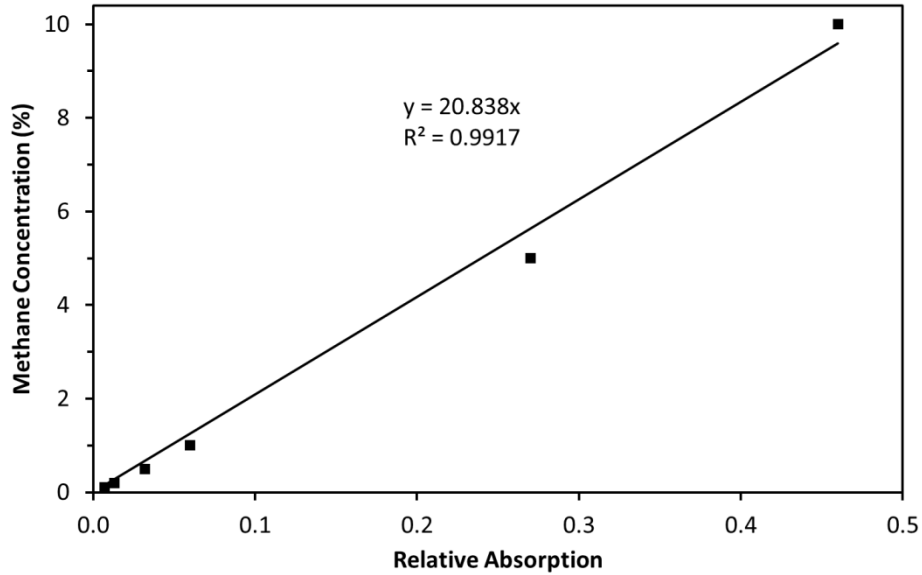


Figure 8.2: Open path gas cell calibration curve from direct absorption measurements of methane peak at 1665.9 nm at different concentrations. T = 296 K, P = 101.325 kPa, l = 16.5 cm

### 8.2.1.2 Wavelength Modulation Spectroscopy

Using WMS, it is possible to perform concentration measurements with greater accuracy because the method filters out sources of noise present in the direct absorption measurements (refer to Section 3.2.3). The experimental setup is shown in Figure 6.14 presented in Chapter 6. The improved accuracy of the wavelength modulation open path method is demonstrated in Figure 8.3. In this calibration curve, the linearity is significantly improved as compared to the direct absorption method ( $R^2 = 0.9995$  vs. 0.9917). This results in a much lower relative error (2.67%) so that a sample of 2.00% methane gives a response of  $2\% \pm 0.05$ . Therefore, at an alarm level of 2% methane, the response uncertainty is within the accuracy level of  $\pm 0.1\%$  and the method would not result in false alarms or erroneous all-clears. The sensitivity of this method is 0.004% which is well within acceptable limits for mining applications (0.1%).

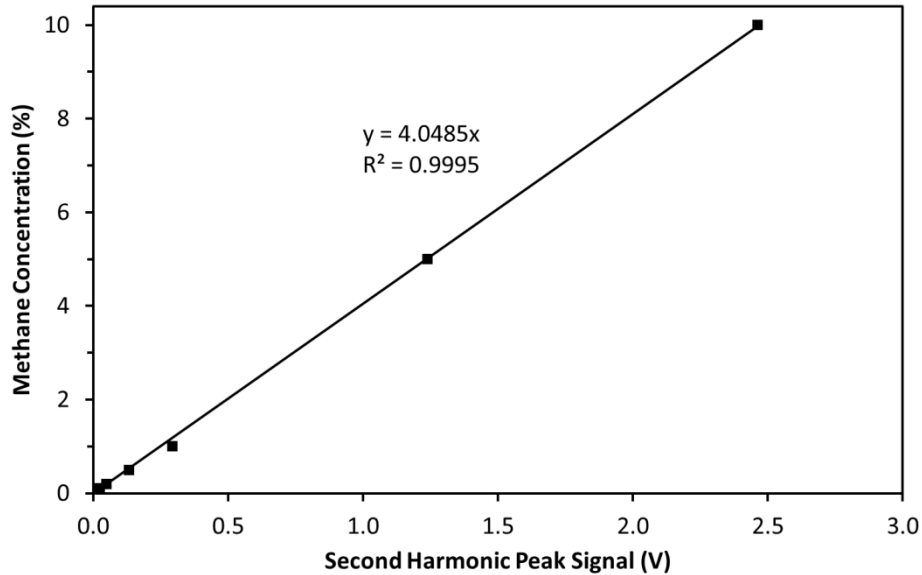


Figure 8.3: Open path gas cell calibration curve from normalised peak signal of second harmonic measurement of methane peak at 1665.9 nm at different concentrations. Wavelength modulation depth was 0.10cm-1. T = 296 K, P = 101.325 kPa, l = 16.5 cm

The dynamic range for the open path method (both direct absorption and WMS) is estimated to be 0-20% (based on the projected saturation of the detector at 20.6% methane). This is sufficient to cover all methane alarm levels for underground mining environments. The dynamic range of this method could easily be adjusted by changing the laser power or the optical path length.

### 8.2.2 Tapered Fibres

The fabrication of tapered optical fibres is described in detail in Section 7.2.1. An optical fibre is mechanically stretched over a flame to narrow its diameter. The experimental setup for the tapered fibre sensor heads is illustrated in Figure 8.4. Similar to the measurement method detailed in Section 4.3.1, light from the laser passed through the sensor head so that absorption by methane gas could be monitored. The methane concentration at the sensor head was controlled by using a gas chamber, as described in Section 6.2.

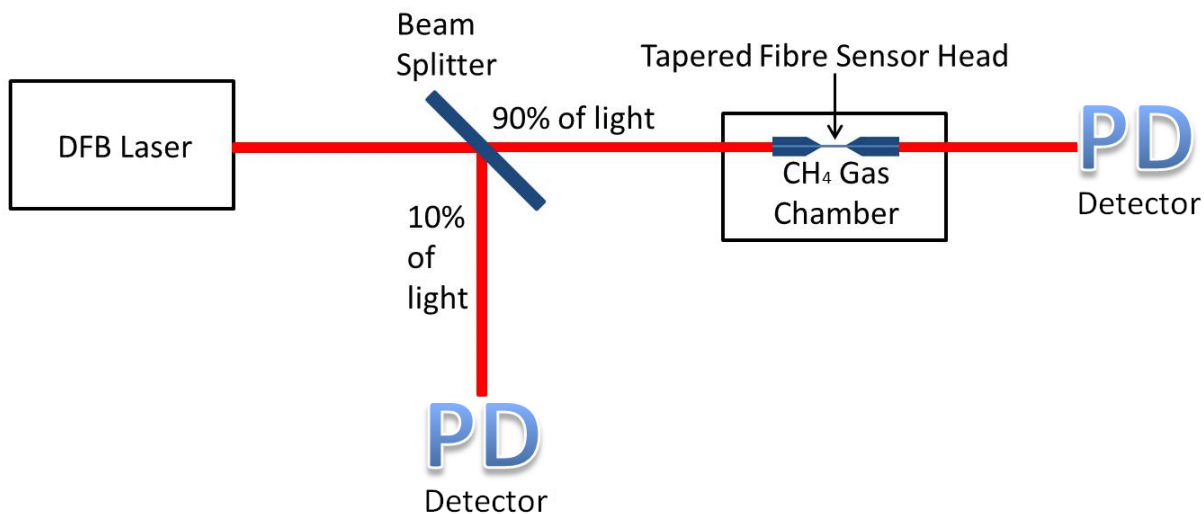


Figure 8.4: Experimental setup (simplified) for methane detection with a tapered fibre sensor head

Even using WMS, it was not possible to detect a signal corresponding to methane. A special taper with an extended tapered region was also pulled; and even with the additional interaction volume afforded by the extended taper, methane absorption could not be observed. This failure demonstrated that the interaction volume was not large enough to facilitate sufficient light absorption by methane in order to detect a signal. This is likely because the length of the tapered region was relatively small (<20 mm compared to 165 mm in the case of open path gas cells). Additionally, the nature of the interaction between the light and the gas was weak, relying on the evanescent field that propagates outside the fibre's core, as compared to a direct interaction in the case of open path gas cells. Therefore, tapered fibres provided a much shorter path length and allowed much less of the light to interact with the surrounding gas. This explains why the signal from methane absorption was not strong enough to be detected. The tapered fibres from our tapering facility (20 mm length limitation) were ruled out as candidate sensor heads for methane sensing in the  $2\nu_2$  band of methane spectral absorption. The reasons mentioned for our unsuccessful attempts at using tapered fibres in methane sensing using WMS in the  $2\nu_2$  band are in agreement with the reasons stated in Section 4.2.1 and 7.2.1.

### 8.2.3 Drilled SMFs

Drilled SMFs were produced by focused ion beam milling a 10  $\mu\text{m}$  diameter hole into the side of an optical fibre until the core was reached, as described in Section 7.2.2. The experimental setup used to test drilled SMFs was the same as that used to test tapered fibres (Figure 8.5).

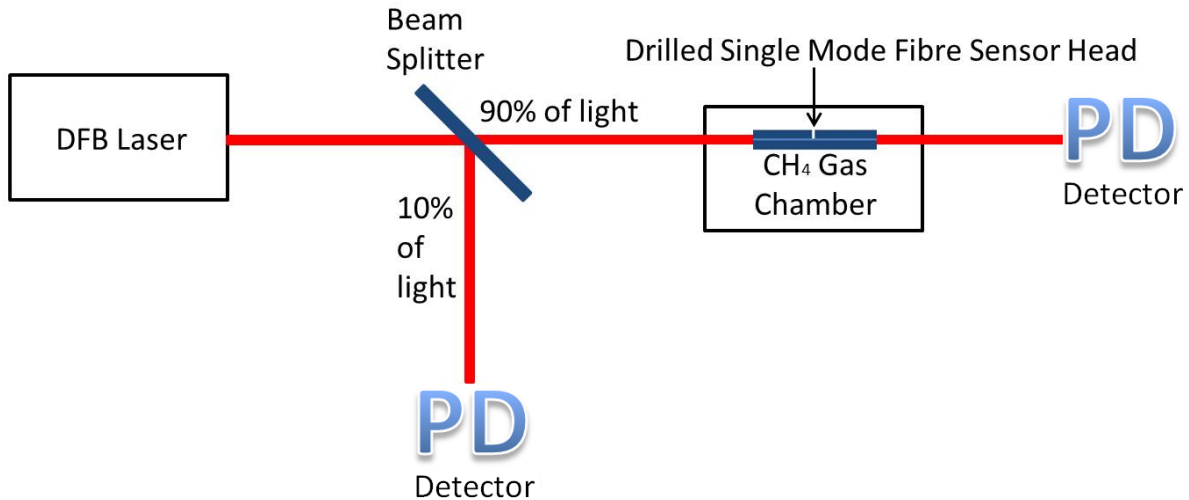


Figure 8.5: Experimental setup (simplified) for methane detection with a drilled single mode fibre sensor head

Gas measurement by drilled SMFs – similarly to tapered fibres- rely on interaction between the evanescent field and the gas molecules in the drilled hole. In the case of drilled SMFs, the interaction length is even smaller than that of tapered fibres, being equal to the diameter of the drilled hole (10  $\mu\text{m}$ ). Given that the strength of the interaction is approximately the same as for tapered fibres and the path length is even smaller (10  $\mu\text{m}$  vs. 20 mm), it is not surprising that it was not possible to detect a methane signal when the drilled SMFs were exposed to methane in the gas chamber. Therefore, drilled SMFs are not suitable candidates to be used as sensor heads for methane sensing using WMS and DAS methods in the  $2\nu_2$  band of methane.

#### 8.2.4 Drilled Hollow Core Fibres

Drilled HCFs provide a significantly longer interaction length (equal to the length of the HCF used) as compared to drilled SMFs. Furthermore, because the fibre core acts as a gas cell, direct absorption occurs inside the core. This is a much stronger interaction than the evanescent interaction in drilled SMFs and tapered fibres. Drilled HCFs were fabricated by drilling a 10  $\mu\text{m}$  diameter hole directly into the core of the fibres using focused ion beam drilling. As HCFs are significantly more expensive than SMFs (retail price per meter \$120 vs. \$0.80), it is preferable to splice a small segment (50-500 mm) of an HCF into a longer section of an SMF for the sensing experiments. This type of splicing also has the added advantage of allowing control over the path length and response time. The fabrication procedure is described in detail in Section 7.2.3. A section of a drilled HCF, 85 mm long, was spliced into a longer section of an SMF and fed into the gas chamber for testing (Figure 8.6).

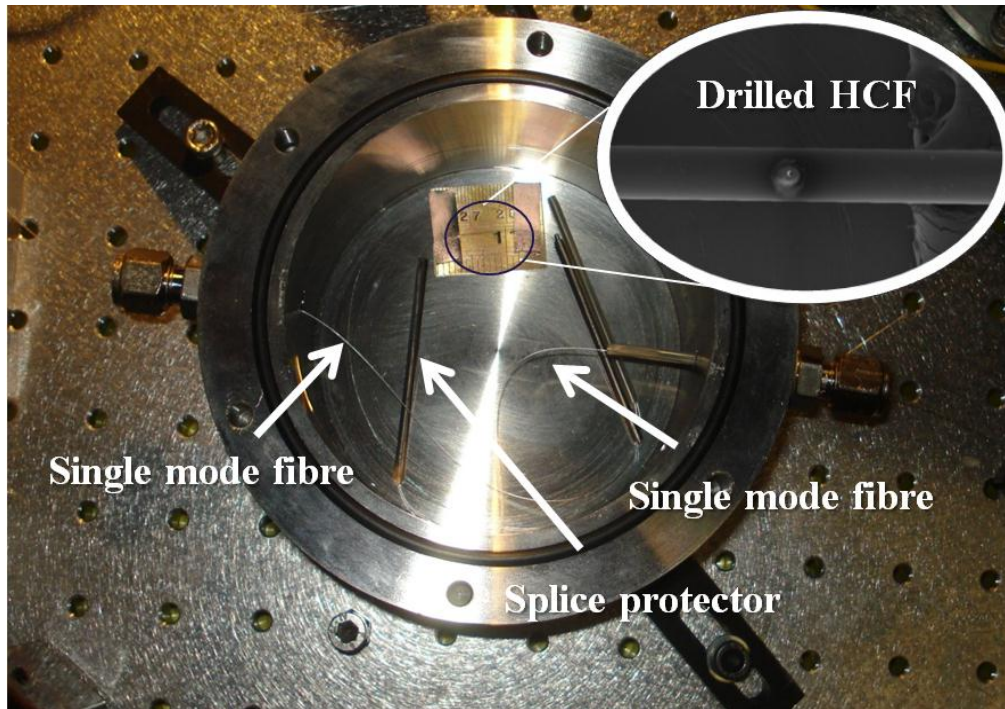


Figure 8.6: An 85 mm drilled HCF placed in the methane gas test chamber (circled image shows SEM of drilled HCF)

Full details of the experiments performed using the drilled HCF sensor heads in the gas chamber are explained in Sections 8.2.4.1 and 8.2.4.3. A simplified schematic of the experimental setup is shown in Figure 8.7.

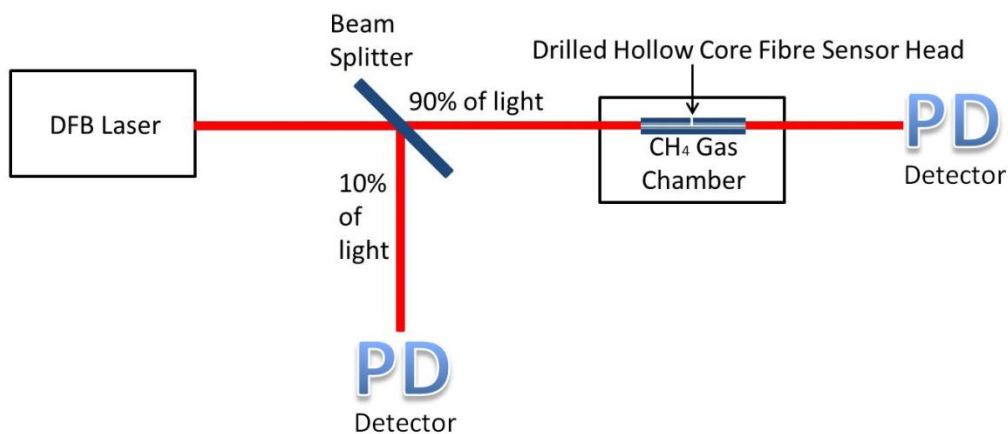


Figure 8.7: Experimental setup (simplified) for methane detection with a drilled hollow core fibre (HCF) sensor head

#### 8.2.4.1 Direct Absorption Spectroscopy

A drilled HCF with a single drilled hole on its side was tested using a scanned-wavelength spectroscopy setup (Figure 6.13). A normalised transmission signal was calculated at various



methane concentrations (Figure 8.8). As it was discussed in Section 3.2.2.1, the methane concentration of an unknown signal could be calculated from the absorption.

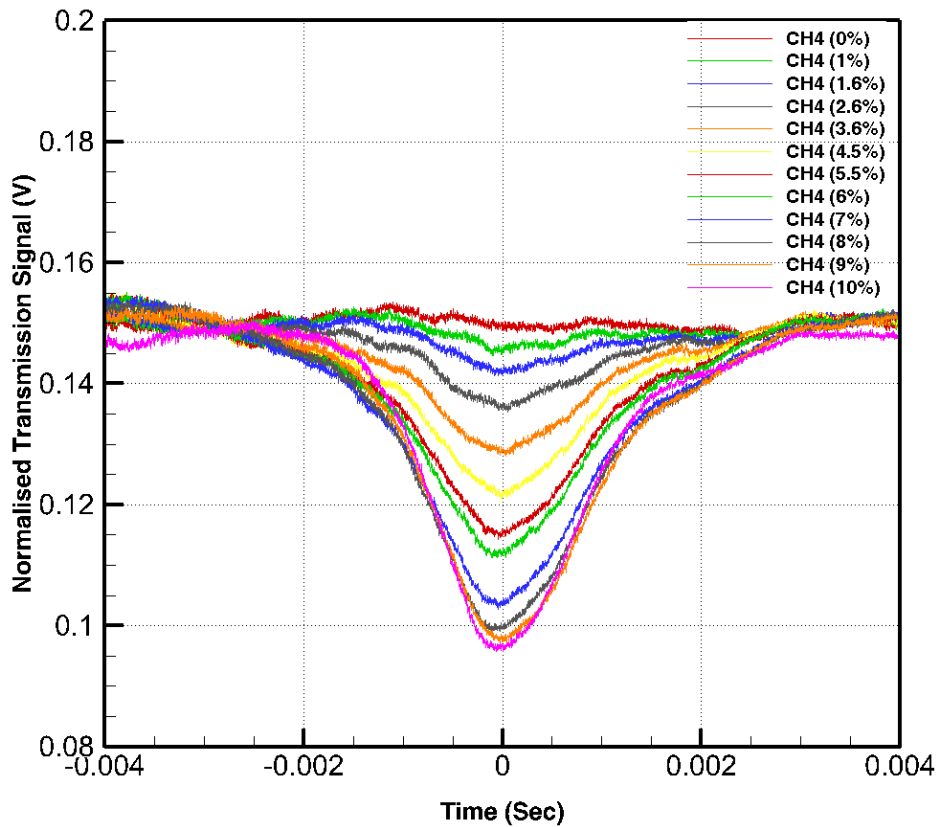


Figure 8.8: Normalised transmitted signal of scanned-wavelength absorption spectroscopy over one scan using an 85 mm drilled HCF ( $T = 296$  K,  $P = 101.325$  kPa,  $l = 8.5$  cm)

When direct absorption measurements were performed (Figure 6.12), a calibration curve was prepared by exposing the sensor head to a series of concentrations of methane while monitoring the relative absorption (% drop in laser intensity) at the wavelength of a strong methane absorption peak (1665.961 nm). The actual methane concentration in the chamber was verified using a calibrated Dräger IR methane detector (as explained in Chapter 6, experimental setup and procedures). The relative absorption recorded by the detector in the real experimental setup is presented in Figure 8.9 (the transmission concentrations are not plotted). The relative absorption is related to methane concentrations in Equation 9.

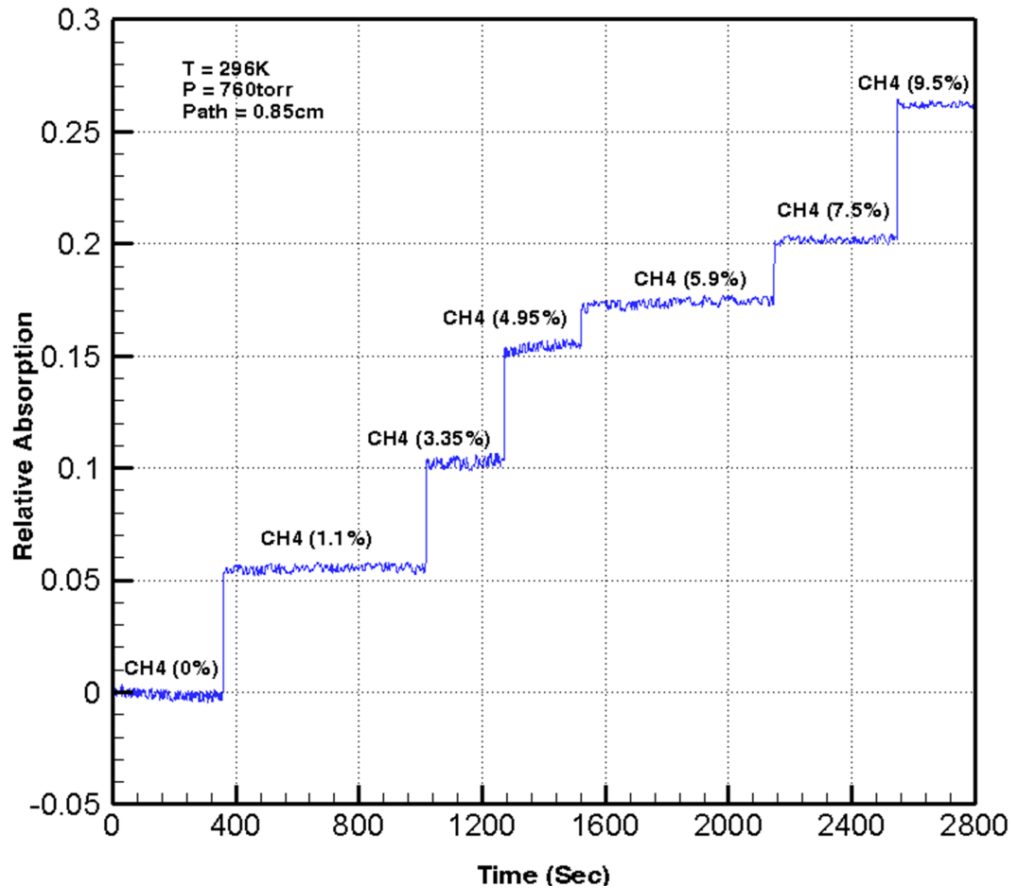


Figure 8.9: Fixed-wavelength absorption spectroscopy signal over time for various methane concentrations using an 85 mm drilled HCF (T = 296 K, P = 101.325 kPa, l = 8.5 cm)

The resulting calibration curve is presented in Figure 8.10. The curve shows relatively poor linearity ( $R^2 = 0.9815$ ). As with open path gas cell sensing (Section 8.2.1), this was likely due to laser wavelength drifts caused by minor temperature fluctuations. The poor linearity of the calibration curve is reflected in the accuracy of the method. There was a 26.45% relative error when measuring the methane concentration of 2.15%, giving a reading of 2.72%. Such a significant error is not acceptable for the purposes of detecting methane concentrations in an underground coal mine.

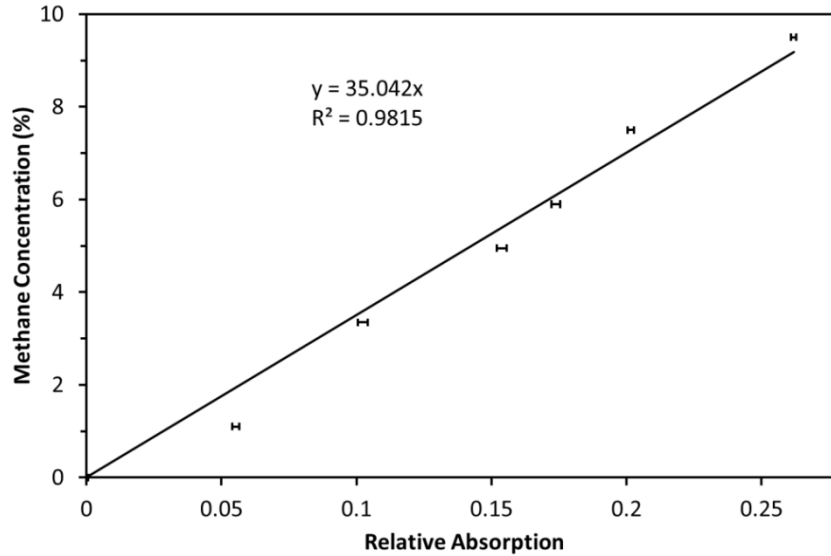


Figure 8.10: Calibration curve from direct absorption measurements of methane peak at 1665.961 nm at various concentrations using a drilled HCF. T = 296 K, P = 101.325 kPa, l = 8.5 cm. Error bars indicate standard deviation in measurement

#### 8.2.4.2 Wavelength Modulation Spectroscopy Calculations Based on HITRAN Database

The HITRAN 2009 database is used to evaluate the calculated calibration curves for the developed sensor heads. The second harmonic of WMS measurements with a modulation index of  $0.15 \text{ cm}^{-1}$  over a similar path length as developed drilled HCFs (85 mm) was calculated (Figure 8.11). It has been theoretically shown that small methane concentrations (as low as 0.01 %) up to the full range concentration (100%) can be simulated with no important distraction from neighbouring absorption spectra lines. The data was used to calculate the second harmonic WMS peak to peak signal in different concentrations to produce a calibration curve for different ranges (Figure 8.12 and Figure 8.13).

The red curve shows relatively poor linearity of  $R^2 = 0.9623$  (Figure 8.12). The poor correlation of the calibration curve in full range methane concentrations is reflected in the lower accuracy of the method at high concentrations. However, the second order polynomial fit has a high correlation to the data ( $R^2 = 0.998$ ).

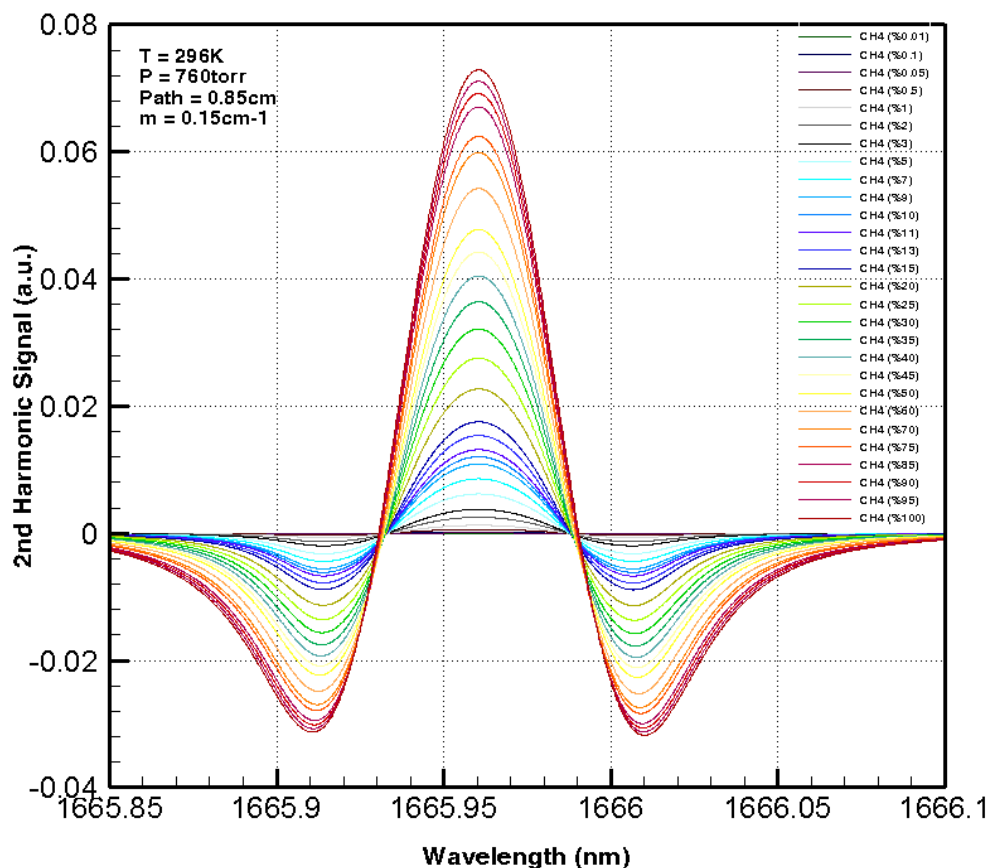


Figure 8.11: WMS second harmonic of methane for different concentrations from HITRAN database. Wavelength modulation depth was 0.15cm-1. T = 296 K, P = 760 Torr, l = 8.5 cm

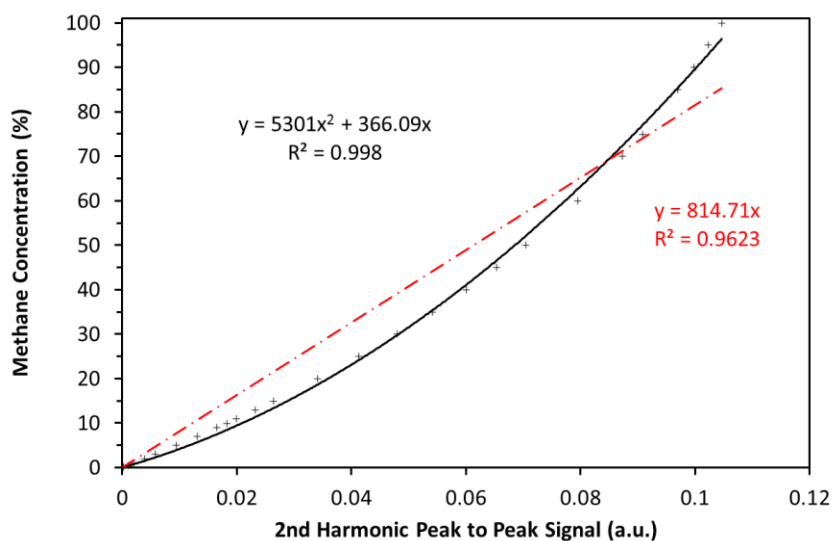


Figure 8.12: HITRAN database calibration curve from normalised peak to peak signal of second harmonic measurement of methane absorption at 1665.961 nm in 0% to 100% methane concentrations (linear fit in red and polynomial order 2 in black). Wavelength modulation depth was 0.15 cm-1. T = 296 K, P = 760 Torr, l = 8.5 cm

The data was plotted for a range of 0% to 10% methane (Figure 8.13). The curve shows a high correlation linearity ( $R^2 = 0.9996$ ). The data accuracy is expected to be similar in the same range.

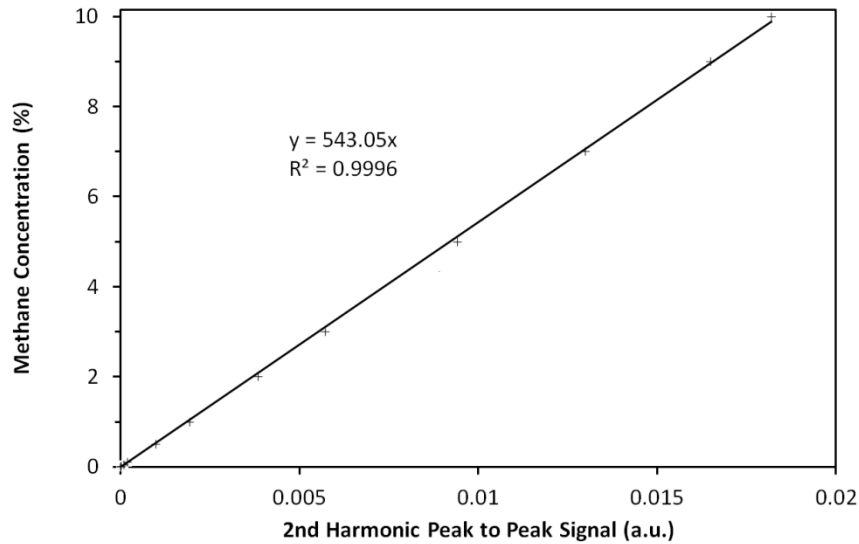


Figure 8.13: HITRAN database calibration curve from normalised peak to peak signal of second harmonic measurement of methane absorption at 1665.961 nm in various concentrations (0%-10%). Wavelength modulation depth was 0.15 cm<sup>-1</sup>. T = 296 K, P = 760 Torr, l = 8.5 cm

### 8.2.4.3 Wavelength Modulation Spectroscopy

As with open path gas cells, the sensing accuracy of drilled HCFs can be improved by utilising WMS. The calibration curve produced after employment of WMS is shown in Figure 8.14. This linear fit shows a similar correlation as theoretical data extracted from HITRAN (0.9994 vs. 0.9996). The reduced laser noise resulting from the use of WMS resulted in significant improvement of the linearity (0.9994 vs. 0.9815). The improved linearity of the curve resulted in significantly better accuracy of the measurements. The relative error was 0.25% when measuring 2.3% methane, giving a result of 2.306%. This level of accuracy at a typical methane alarm level is more than sufficient for underground coal mining applications. Such high accuracy was possible because the wavelength modulation method removed numerous sources of noise from the signal, most importantly, the drift in the laser wavelength. The removal of sources of noise from the signal also resulted in a decrease in the signal-to-noise ratio. This is reflected in the improved sensitivity of 0.03% (at 2.3% methane) when the wavelength modulation technique was used with the drilled HCF sensor head.

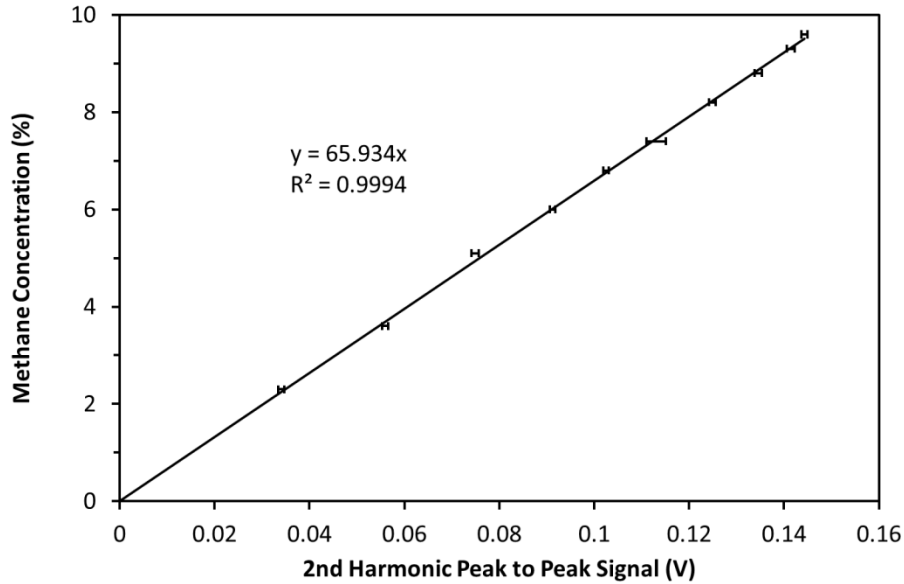


Figure 8.14: Calibration curve from wavelength modulation spectroscopy measurements of methane second harmonic peak to peak signal at 1665.961 nm at different concentrations using a drilled hollow core fibre (HCF) sensor head. T = 296 K, P = 101.325 kPa, l = 8.5 cm. Error bars indicate standard deviation in measurement

As with the direct absorption method, the response time of the wavelength modulation technique was limited by the diffusion of methane into the drilled HCFs. Hence, the response time remained at 59 seconds (Figure 8.18). The dynamic range of the drilled HCF technique was estimated to be 0-35% (based on the projected detector saturation). This is sufficient to cover all methane alarm levels in underground mining environments.

A 345 mm sensor head was also fabricated. The actual WMS signal output of this sensor head is illustrated in Figure 8.15. The Fabry-Perot cavity between two fusion splice points, as a result of reflection from the coupling points, introduced an oscillation noise to the WMS signal (green signal). This noise caused the second harmonic WMS (blue signal) to have significant noise on the left wing. However, the introduced noise from the cavity does not have any considerable effect on the first harmonic signal (red signal).

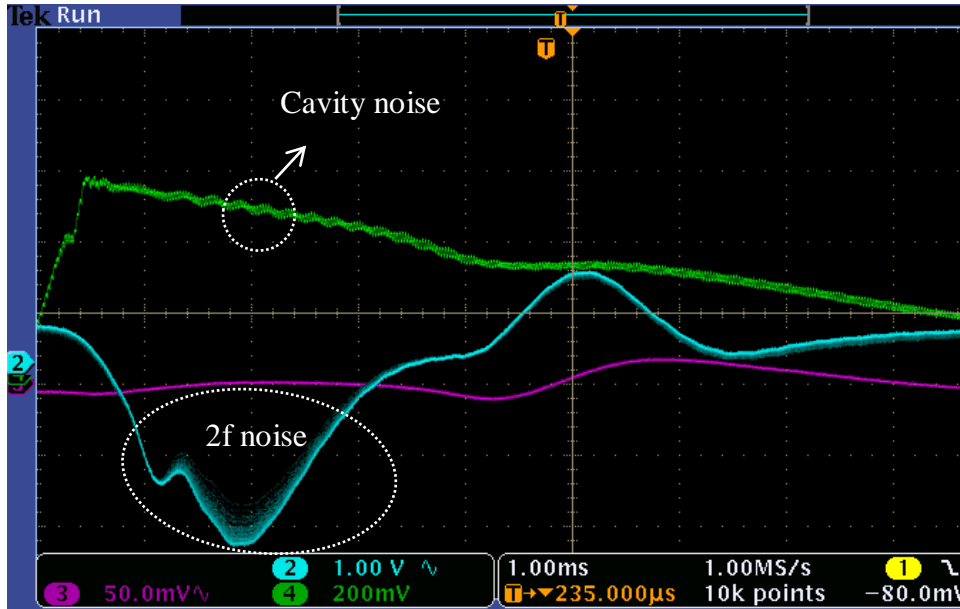


Figure 8.15: A screenshot of oscilloscope showing WMS signal (green), 2f-WMS (blue), and 1f-WMS (red) from a 345 mm drilled HCF in 5% methane

2f-WMS signals at 1665.961 nm (using right wing of 2f) were recorded for the drilled 345 mm HCF at various methane concentrations. A calibration curve of the resulting data is plotted in Figure 8.16. The curve shows relatively poor linearity ( $R^2 = 0.9748$ ).

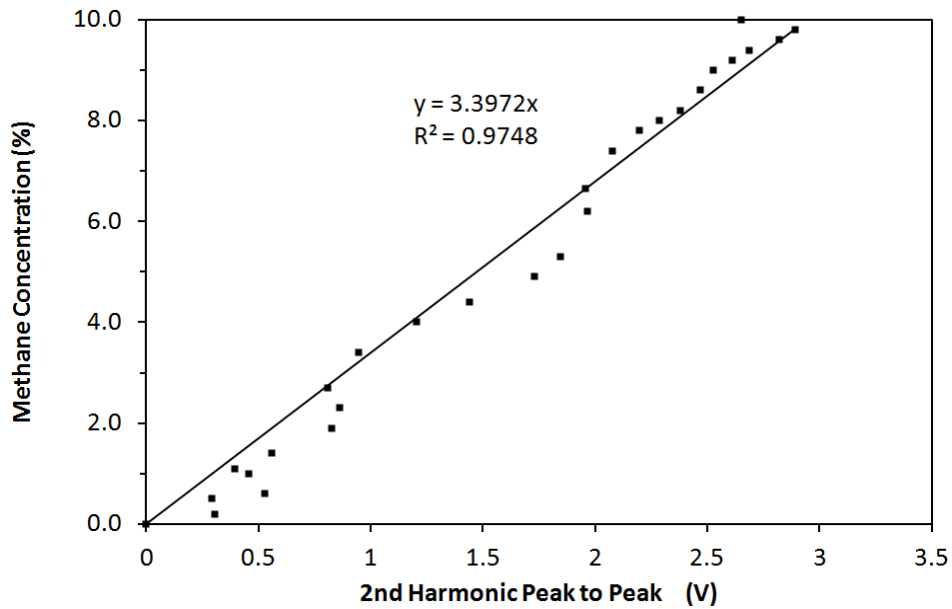


Figure 8.16: Calibration curve from WMS measurements of methane normalised second harmonic peak to peak signal at 1665.96 nm at different concentrations using a drilled HCF sensor head.  $T = 296$  K,  $P = 101.325$  kPa,  $l = 34.5$  cm

1f-WMS signals at 1665.961 nm were recorded for the drilled 345 mm HCF at various methane concentrations (Figure 8.17). As the first harmonic was less affected by the cavity noise, the calibration curve shows a higher correlation of linearity to methane ( $R^2 = 0.9947$  vs. 0.9748). Error bars indicate the standard deviation in measurement, which is within a satisfactory range.

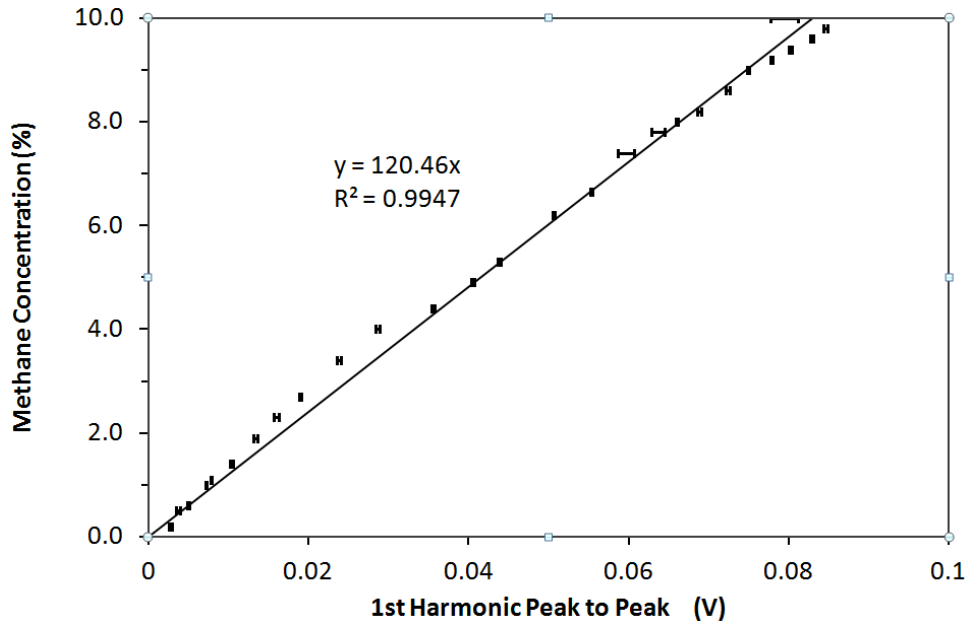


Figure 8.17: Calibration curve from WMS measurements of methane first harmonic peak to peak signal at 1665.961 nm at different concentrations using a drilled HCF sensor head.  $T = 296$  K,  $P = 101.325$  kPa,  $l = 34.5$  cm. Error bars indicate standard deviation in measurement

### 8.2.4.3 Effect of Changing the Sensor Head Length

According to the Beer-Lambert equation (Equation 1), the absorption intensity is directly proportional to the optical path length. This means that a longer sensor head should be more sensitive to methane concentrations and also more accurate. However, a longer HCF segment takes longer to fill through diffusion, meaning the response time is expected to increase when a longer sensor head is used. In order to investigate this, a longer HCF segment was employed to see how the response differed.

It should be mentioned that this was necessary to investigate both the respective rise and fall times due to increases or decreases in the concentrations. In order to do so, the drilled HCF needed to be exposed to atmospheric air to calculate the rise and fall times. It was challenging to calculate the response with our customised chamber. The volume of the chamber is considerable in comparison with the HCF volume; and consequently, it is dependent on the flushing time. It



was found that the flushing flow could pressurise the chamber and introduce noise into the system. This noise is from the splice point between the HCF and the SMF. The pressurised air could change the HCF structure in the splice point and cause more reflections. As the scope of this investigation did not include a comprehensive response time study, the following preliminary test was conducted (Figure 8.18).

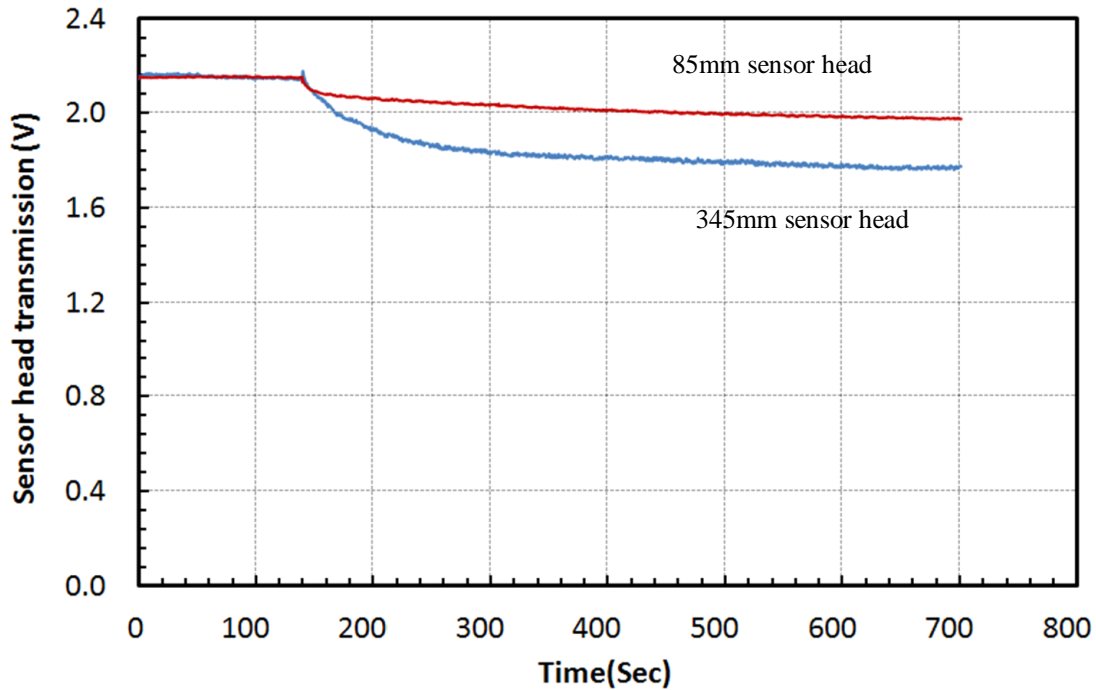


Figure 8.18: Transmission transients showing the change in transmission at 1665.961 nm upon release of 2% methane into the gas chamber at  $t = 190$  s

Figure 8.18 shows the transmission intensity at 1665.961 nm through two HCF sensor heads of different lengths upon sudden exposure to 2% methane in the customised chamber. The pressurising effects were minimised by keeping all the outputs open upon release of the gas. The longer sensor head took significantly more time to reach a steady state. The 85 mm sensor head took 59 s to reach 90% of its final transmission intensity ( $T_{90}$  is a common test for response time). The 345 mm sensor head took 145 s. The longer time resulted from the fact that the gas had to diffuse through a drilled hole and cover a longer distance in order to fill the hollow core of the sensor head. The response time for both sensor heads could be reduced by increasing the number of holes. Two or more evenly spaced holes in the fibre would significantly decrease the total diffusion distance, and consequently, the response time. However, each additional hole would cause a negligible optical loss (less than 0.03 dB per hole) so the total number of holes

would have to be optimised to minimise response time without causing significant losses that would negatively impact the effectiveness of the sensor. Producing more sensor heads with different arrangements and more drilled holes was not within the scope of this thesis. Nevertheless, due to the low volume of gas needed for HCF gas sensing, the response time is expected to decrease down to a few seconds when using multiple holes.

### 8.3 Comparison of Measurements

In this study, intrinsically safe fibre optic based prototype sensors were successfully demonstrated to have the potential to accurately measure methane concentrations in underground coal mines within a reasonable response time. Four fibre optic based sensing techniques were developed and assessed: one using pre-filled open path gas cells with known concentrations of methane (0.1% - 10%) in nitrogen; and three based on microstructure optical fibres. Two methods for methane detection were tested for each sensor head: direct absorption spectroscopy (DAS) and wavelength modulation spectroscopy (WMS). Table 8.1 shows the results achieved for each of the sensor heads developed in this project.

Table 8.1: Summary of results of methane detection with different sensor heads

Sensor Head	Detection Technique	Sensitivity <sup>a</sup>	Relative Error <sup>b</sup>	Response Time <sup>c</sup>
Open path gas cell	DAS	0.01%	25.03%	Instantaneous
	WMS	0.004%	2.67%	Instantaneous
Tapered fibre (20mm length and $\leq 1 \mu$ waist dia.)	DAS	No response	N/A	N/A
	WMS	No response	N/A	N/A
Drilled SMF (10 $\mu$ dia. hole)	DAS	No response	N/A	N/A
	WMS	No response	N/A	N/A
Drilled HCF (85mm)	DAS	0.08%	26.45%	59 s
	WMS	0.03%	0.25%	59 s

a: Sensitivity indicates the minimum methane concentration detectable above the background noise levels of the signal.

b: Relative error indicates the difference between the measured methane concentration and the actual methane concentration, expressed as a percentage of the actual concentration.

c: Response time indicates the time it took for the signal to reach 90% of its final, steady state, signal upon exposure to a certain concentration of methane.

Open path gas cells were able to measure methane concentrations with good sensitivity, but the accuracy was not acceptable when DAS was used. The sensitivity and the accuracy significantly improved when WMS was used. The response time for open path gas cells was effectively

instantaneous. This does not take into account the time required for gas to diffuse through a filter and housing that would be required in order to operate such a sensor in a real underground mining environment. Tapered fibre sensor heads have a simpler configuration than that of open path gas cells (no lenses/alignment), but at the cost of a much smaller interaction volume as compared to an open path gas cell. This resulted in these sensor heads being unable to detect methane. Drilled SMFs were simpler than open path gas cells and more robust than tapered fibres, but the interaction volume was even smaller. This meant that methane could not be detected with these sensor heads either. Drilled hollow core fibres offered the simplicity of an all-fibre set-up and the advantage of a large interaction volume, but are more expensive than SMFs. Drilled hollow core fibres had good sensitivity but unacceptable accuracy when DAS was used. When WMS was used, the accuracy levels improved significantly. The response time for drilled hollow core fibres was slower than open path gas cells due to the time required for methane to diffuse into the hollow core fibre. This response time is a function of the fibre sensor length and an inverse function of the number of holes in the fibre.

For all types of sensor heads, the dynamic range of the method was dependent on the optical path length. Those methods, for which methane detection was possible, were able to detect across a concentration range significantly greater than the standard alarm level ranges in underground mines (0.0%-5.0%). Given that the optical losses for the two successful sensors were relatively low, there is also a potential to adapt either of these sensor heads into a fibre optic network of sensors, providing multiple sensing locations throughout an underground mine from a single fibre. The mining environment is harsh; of particular concern to fibre optic based sensing is the high dust and particulate levels. A further study is required to assess the effects of a harsh mining environment (particulates, humidity, and other gases) to determine the design requirements for a commercial embodiment of these sensors.

# CHAPTER 9

## CONCLUSIONS AND RECOMMENDATIONS

### 9.1 Conclusions

The importance of methane gas monitoring in underground coal mines has been reviewed and the current gas monitoring system drawbacks have been studied. It has been found that development of an all-fibre methane gas monitoring system with all-fibre sensor heads may well lead to improved production and safety in underground coal mines.

This study has presented the design and development of three types of all-fibre microstructure sensor heads: tapered SMFs, drilled SMFs, and drilled hollow core fibres (HCFs). An experimental gas concentration setup was designed and developed to test developed all-fibre sensor heads in various methane concentrations. The sensor heads have been tested and compared to the conventional open path gas cells as candidates for remote methane sensors in underground coal mines. Wavelength modulations spectroscopy and direct absorption spectroscopy at the 1665.961 nm absorption line centre of methane have both been employed using a DFB laser source for all sensor heads. The open path gas cell and the drilled hollow core

fibre proved their ability to detect methane with the required sensitivity, accuracy, and response time demonstrating their potential for development into commercial sensors. The open path gas cell method demonstrates greater sensitivity and is more robust than the drilled hollow core fibre sensor. The drilled hollow core fibre also has excellent accuracy but has a more complex structure; light coupling and reflection between the HCF and SMF splice point are still an issue.

Both the open path gas cell and hollow core fibre sensors show promise for use as part of underground mine gas sensing systems. The aim of this study was to investigate mostly novel, previously untested, experimental sensor head designs for underground coal mine applications. The drilled hollow core fibre seems to be a good candidates for this type of application since it needs only a micro-scale volume of sample gas for a real time measurement and could potentially offer as little as a few seconds response time. In addition, the drilled hollow core fibre sensors show greater potential for integration into a sensing network consisting of many sensor heads connected via distributed SMFs throughout a mine—particularly in inaccessible areas.

## **9.2 Recommendations for Future Work**

As for the sensor heads that proved unsuccessful when using WMS and DAS methods, they still have the potential for gas sensing applications in other spectroscopic setups—for instance, using a cavity ring down or a sensitive back reflection method. As for the two sensor heads that proved successful, it is likely that with industry and the original equipment manufacturers (OEMs) consultation, it will be possible to identify specific applications for each one of which is best suited so that they can be further developed in those directions. A priority concern would also be in protecting the sensor heads from damage due to contaminates in underground mines such as coal dust and diesel particulate matter. Development of adequate filters for all types of all-fibre sensor heads is necessary to ensure accurate readings and fast response times. Many avenues of further research remain for extending the current work, seven of which are suggested and described below.

1. Improving spectroscopy setup: a LabView software program and associated hardware including a DFB laser source is suggested to ease all measurement setups into a computer based laboratory for gas spectroscopy sensing.

2. Improvements to gas concentration test setup: a micro scale chamber with a larger output is suggested for response time calculations of drilled HCFs.
3. Improvements to SMF-HCF splicing: the fibre splice remains the major limitation to using HCFs. It is proposed to follow up on the information currently available in the literature to reproduce the angle cleaved splice between an SMF and HCF in the lab.
4. Improvements to all-fibre methane sensors: drilling of multi holes on the sides of HC-PCFs using a femtosecond laser setup which has been used for inline FBG production.
5. Multi gas detection: using a coiled, multi-hole, drilled HC-PCF with a longer length to detect carbon monoxide, carbon dioxide, and methane all at once.
6. Alternative techniques for sensitive detection: employing cavity ring-down (CRD) gas detection using micro drilled SMFs could provide adequate interaction between light and gas. This would make a cheap microcell gas sensor.
7. Underground coal mine capability and networkability development: using hydrophobic silica gel as a filter on the surface of microstructured all-fibre sensors is suggested to produce robust, dust proof, water proof, and flexible sensor heads.

# References

- [1] C. Ö. Karacan, F. A. Ruiz, M. Cotè, and S. Phipps, "Coal mine methane: A review of capture and utilization practices with benefits to mining safety and to greenhouse gas reduction," *International Journal of Coal Geology*, vol. 86, pp. 121-156, 2011.
- [2] U. Nations, "Best Practice Guidance for Effective Methane Drainage and Use in Coal Mines," vol. ECE ENERGY SERIES No.31, U. N. E. C. f. Europe and M. t. M. Partnership, Eds., ed. New York and Geneva: UNITED NATIONS PUBLICATION, 2010.
- [3] K. M. Kowalski-Trakofler, D. W. Alexander, M. J. Brnich, Jr., L. J. McWilliams, and D. B. Reissman, "Underground coal mining disasters and fatalities - United States, 1900-2006," *Morbidity and Mortality Weekly Report*, vol. 57, pp. 1379-1383, 2008.
- [4] R. Kahler, "Fatalities in the West Australian Mining Industry 1970 – 2006," 2007.
- [5] A. K. Sovik, J. Augustin, K. Heikkinen, J. T. Huttunen, J. M. Necki, S. M. Karjalainen, *et al.*, "Emission of the greenhouse gases nitrous oxide and methane from constructed wetlands in Europe," *Journal of Environmental Quality*, vol. 35, pp. 2360-2373, Nov-Dec 2006.
- [6] M. A. Delucchi, "Methane Emissions From Natural Gas Production, Oil Production, Coal Mining, and Other Sources," *Appendix E to A Lifecycle Emissions Model: Lifecycle Emissions From Transportation Fuels, Motor Vehicles, Transportation Modes, Electricity Use, Heating and Cooking Fuels, and Materials, Institute of Transportation Studies, UC-Davis*, 2003.
- [7] T. Imgrund and R. Thomas, "International experience of gas emission and gas outburst prevention in underground coal mines," 2013.
- [8] P. Carothers and M. Deo, "Technical and economic assessment: mitigation of methane emissions from coal mine ventilation air," *Coalbed Methane Outreach Program, Climate Protection Division, United States Environmental Protection Agency (US EPA): Washington, DC*, pp. 28-30, 2000.
- [9] C. J. Bibler, J. S. Marshall, and R. C. Pilcher, "Status of worldwide coal mine methane emissions and use," *International Journal of Coal Geology*, vol. 35, pp. 283-310, 1998.
- [10] Worksafe-Australia, "Guidance Note on the Interpretation of Exposure Standards for Atmospheric Contaminants in the Occupational Environment NOHSC 3008(1995)," National Occupational Health and Safety Commission. Worksafe Australia 1995.
- [11] T. I. C. o. M. a. M. ICMM, "Fugitive methane emissions in coal mining " 2011.
- [12] A. Saunders, "Gas Detection Technology In Confined Spaces," in *ASSE Professional Development Conference and Exhibition*, 2008.
- [13] S. X. Hua Guo, David Reece, Srinivasa Yarlagadda. (2009, Identify and Collate Leading Safety Technologies. Available: <http://www.mirmgate.com/index.php?gate=appgate&pageId=document&docId=2&docItem=24>
- [14] M. S. O. B. I. a. I. NSW, "MDG1006-Technical Reference for Spontaneous Combustion Management Guideline," 2011.
- [15] P. Mason, "Challenges of gas monitoring and interpretation in underground coal mines following an emergency," 2012.
- [16] D. MUSSEN, "Critical Pike River failings revealed," in *Stuff National*, ed, 2013.
- [17] Australian Government and E. a. T. Department of Resources. (2012). *Coal Mining Abatement Technology Support Package (CMATSP)*.
- [18] K. Uehara and H. Tai, "Remote detection of methane with a 1.66- $\mu$ m diode laser," *Applied Optics*, vol. 31, pp. 809-814, 1992.
- [19] W. P. Diamond, *Methane control for underground coal mines*: US Department of the Interior, Bureau of Mines, 1994.

- [20] T. H. Dubaniewicz and J. Chilton, *Remote fiber-optic methane monitor*: US Department of the Interior, Bureau of Mines, 1992.
- [21] T. Minming, N. Jieru, H. Jifei, and J. Cunliang, "Study on a fiber optic sensor for CH<sub>4</sub> in mine," in *Photonics and Optoelectronic (SOPO), 2010 Symposium on*, 2010, pp. 1-4.
- [22] J. Ni, J. Chang, T. Liu, Y. Li, Y. Zhao, and Q. Wang, "Fiber methane gas sensor and its application in methane outburst prediction in coal mine," 2008, pp. 1-4.
- [23] T. Liu, "All fiber optic coal mine safety monitoring system," in *Optical Fiber Communication and Optoelectronics Conference, 2007 Asia*, 2007, pp. 174-176.
- [24] J. Shemshad, S. Aminossadati, W. Bowen, and M. Kizil, "Effects of pressure and temperature fluctuations on near-infrared measurements of methane in underground coal mines," *Applied Physics B: Lasers and Optics*, pp. 1-8, 2011.
- [25] M. Jiang, W. Zhang, Q. Zhang, Y. Liu, and B. Liu, "Investigation on an evanescent wave fiber-optic absorption sensor based on fiber loop cavity ring-down spectroscopy," *Optics Communications*, vol. 283, pp. 249-253, 2010.
- [26] V. Kumar, "Fiber optic methane and strain sensors for mines," in *Photonics (ICP), 2010 International Conference on*, 2010, pp. 1-4.
- [27] optosci. (2013, 27/6). *Optical methane gas monitoring system*. Available: <http://www.optosci.com/>
- [28] S. M.-s. P. Limited. (2013, 27/06). *Optical methane gas monitoring system*. Available: <http://www.iss-ms.com/English/>
- [29] Y. L. Hoo, S. Liu, H. L. Ho, and W. Jin, "Fast Response Microstructured Optical Fiber Methane Sensor With Multiple Side-Openings," *IEEE Photonics Technology Letters*, vol. 22, pp. 296-298, Mar 1 2010.
- [30] F. T. A. de Magalhães, "Development of gas detection systems based on microstructured optical fibres," Universidade do Porto, 2008.
- [31] H. Ding, X. Li, J. Cui, L. Yang, and S. Dong, "An All-Fiber Gas Sensing System Using Hollow-Core Photonic Bandgap Fiber as Gas Cell," *Instrumentation Science and Technology*, vol. 39, pp. 78-87, 2011.
- [32] H. Lehmann, H. Bartelt, Magalh, F. , R. Amezcua-Correa, R. J Van, *et al.*, "Remote System for Detection of Low-Levels of Methane Based on Photonic Crystal Fibres and Wavelength Modulation Spectroscopy," *Journal of Sensors*, vol. 2009, 2009.
- [33] L. Xiao, M. Grogan, R. England, W. Wadsworth, and T. Birks, "Gas sensing with a sub-micron tapered fibre embedded in hydrophobic aerogel," 2010.
- [34] A. Cubillas, M. Silva-Lopez, J. Lazaro, O. Conde, M. Petrovich, and J. Lopez-Higuera, "Methane detection at 1670-nm band using a hollow-core photonic bandgap fiber and a multiline algorithm," *Optics Express*, vol. 15, pp. 17570-17576, 2007.
- [35] A. M. Cubillas, J. M. Lazaro, O. M. Conde, M. N. Petrovich, and J. M. Lopez-Higuera, "Gas Sensor Based on Photonic Crystal Fibres in the 2 3 and 2+ 2 3 Vibrational Bands of Methane," *Sensors*, vol. 9, pp. 6261-6272, 2009.
- [36] P. MacNeill, "International Mining Fatality Database," NSW Department of Primary Industries 2008.
- [37] M. Brnich, K. Kowalski-Trakofler, and J. Brune, "Underground coal mine disasters 1900–2010: Events, responses, and a look to the future," *Extracting the Science: A Century of Mining Research*, 2010.
- [38] P. Darling, *SME mining engineering handbook*: SME, 2011.
- [39] C. Hester, "emerging technology in gas monitoring equipment," presented at the Queensland Coal and Energy Conference, 1996.
- [40] B. News. (1986, 28/05/2013). Coal mine canaries made redundant. Available: [http://news.bbc.co.uk/onthisday/hi/dates/stories/december/30/newsid\\_2547000/2547587.stm](http://news.bbc.co.uk/onthisday/hi/dates/stories/december/30/newsid_2547000/2547587.stm)
- [41] M. Adams, "Humphry Davy and the murder lamp (Miner's safety lamp)," *HISTORY TODAY*, vol. 55, pp. 4-5, 2005.



- [42] E. Edwards. (2009, 28/05/2013). *The miners' safety lamp (July 2009 ed.)*. Available: <http://england.prm.ox.ac.uk/englishness-miners-lamp.html>
- [43] D. Brady, "The role of gas monitoring in the prevention and treatment of mine fires," in *Coal 2008: Coal Operators' Conference*, University of Wollongong & the Australasian Institute of Mining and Metallurgy, 2008, pp. 202-208.
- [44] U. S. M. R. Association. (2011, 24/6/2013). *Mine gases and health effects*. Available: <http://www.usmra.com/download/minegases.pdf>
- [45] S. A. Raheem, "Remote Monitoring of Safe and Risky Regions of Toxic Gases in Underground Mines: a Preventive Safety Measures," 2011.
- [46] A. K. Singh, R. Singh, M. P. Singh, H. Chandra, and N. Shukla, "Mine fire gas indices and their application to Indian underground coal mine fires," *International Journal of Coal Geology*, vol. 69, pp. 192-204, 2007.
- [47] F. N. Kissell, *Handbook for Methane Control in Mining*: NIOSH, 2006.
- [48] Conspec, "Conspec Gas Facts • Methane (CH<sub>4</sub>) & Natural Gas," Conspec, Ed., ed, 2010.
- [49] F. N. Kissell, J. C. Tien, and E. D. Thimons, "Methods for Controlling Explosion Risk at Coal Mine Working Faces," in *32nd International Conference of Safety in Mines Research Institutes*, Beijing, China, 2007, pp. 161–168.
- [50] *Coal Mining Safety and Health Regulation* O. o. t. Q. P. Counsel, 2001.
- [51] X. Liu, S. Cheng, H. Liu, S. Hu, D. Zhang, and H. Ning, "A Survey on Gas Sensing Technology," *Sensors*, vol. 12, pp. 9635-9665, 2012.
- [52] K. K. Eltschlager, J. W. Hawkins, W. C. Ehler, and F. Baldassare, "Technical measures for the investigation and mitigation of fugitive methane hazards in areas of coal mining," Office of Surface Mining Reclamation and Enforcement 2001.
- [53] M. T. S. Company. (2011, 28/05/2013). Combustible Gas Detector SensorDrift: Catalytic vs. Infrared. Available: [http://s7d9.scene7.com/is/content/minesafetyappliances/07-0035-MC\\_CombustibleSensor](http://s7d9.scene7.com/is/content/minesafetyappliances/07-0035-MC_CombustibleSensor)
- [54] J. Chou, *Hazardous gas monitors :infrared gas sensors*: McGraw-Hill, 2000.
- [55] N. T. Investment, "list of registered gas detectors and monitors for use in NSW Underground coal mines," N. T. I. The Division of Resources and Energy, Ed., ed, 2012.
- [56] Odialog, "OdaLog® 7000 MkII Multi Gas Monitor," ed, 2011.
- [57] P. MacKenzie-Wood, "Mining and Quarrying," in *Encyclopaedia of occupational health and safety*, S. Jeanne Mager, J. R. Armstrong, and R. Menon, Eds., ed: International Labour Organization, 2011.
- [58] L. Bortolotto, *Direct Hydroxylation of Benzene to Phenol in a Microstructured Pd-Based Membrane Reactor*, 2011.
- [59] D. o. N. R. a. MInes, "Mining Journal," *Queensland Government Mining Journal*, vol. 110, 2013.
- [60] Office of the Federal Register, USA, *Code of Federal Regulations, Title 30, Mineral Resources, Pt. 200-699, Revised as of July 1 2011*: U.S. Government Printing Office, 2011.
- [61] P. Brisbane, "Personal Communication," S. M. Aminossadati, E. Sheridan, M. S. Kizil, W. P. Bowen, and M. Amanzadeh, Eds., ed, 2012.
- [62] T. H. Dubaniewicz, J. E. Chilton, and H. Dobroski Jr, "Fiber optics for atmospheric mine monitoring," *Industry Applications, IEEE Transactions on*, vol. 29, pp. 749-754, 1993.
- [63] Optosci. (2012). *Multipoint methaen monitoring system for landfill sites*.
- [64] G. B. Rieker, J. B. Jeffries, and R. K. Hanson, "Calibration-free wavelength-modulation spectroscopy for measurements of gas temperature and concentration in harsh environments," *Applied optics*, vol. 48, pp. 5546-5560, 2009.
- [65] K. Lyle, *Development of a real-time diode-laser mass flux sensor for simultaneous measurement of density and velocity of Oxygen* vol. 163: Stanford PhD. Thesis, TSD report, 2005.
- [66] S. I. Chou, D. S. Baer, and R. K. Hanson, "High-resolution measurements of HBr transitions in the first overtone band using tunable diode lasers," *Journal of Molecular Spectroscopy*, vol. 200, pp. 138-142, 2000.

- [67] S. I. Chou, "Diode-laser absorption spectroscopy of hydrogen halides for semiconductor plasma process diagnostics," 2000.
- [68] H. Edwards and J. Dakin, "Gas sensors using correlation spectroscopy compatible with fibre-optic operation," *Sensors and Actuators B: Chemical*, vol. 11, pp. 9-19, 1993.
- [69] D. W. Mattison, *Development and application of laser-based sensors for harsh combustion environments*: Stanford University. Palo Alto, CA, 2006.
- [70] Y. Takemoto, A. Seki, K. Takagi, H. Sasaki, M. Nishiyama, and K. Watanabe, "Bending effect on fiber optic evanescent absorption sensor for sensitivity enhancement in hetero-core structured fiber optic," 2011, p. 775349.
- [71] B. Culshaw, F. Muhammad, G. Stewart, S. Murray, D. Pinchbeck, J. Norris, *et al.*, "Evanescent wave methane detection using optical fibres," *Electronics Letters*, vol. 28, pp. 2232-2234, 1992.
- [72] C. A. Browne, D. H. Tarrant, M. S. Olteanu, J. W. Mullens, and E. L. Chronister, "Intrinsic sol-gel clad fiber-optic sensors with time-resolved detection," *Analytical Chemistry*, vol. 68, pp. 2289-2295, 1996.
- [73] C. Singh, Y. Shibata, and M. Ogita, "A theoretical study of tapered, porous clad optical fibers for detection of gases," *Sensors and Actuators B: Chemical*, vol. 92, pp. 44-48, 2003.
- [74] A. Armin, M. Soltanolkotabi, and P. Feizollah, "On the pH and concentration response of an evanescent field absorption sensor using a coiled-shape plastic optical fiber," *Sensors and Actuators, A: Physical*, vol. 165, pp. 181-184, 2011.
- [75] M. Petrovich, C. Grivas, F. Poletti, A. Van Brakel, E. Austin, and D. Richardson, "Microstructured optical fibres for gas sensing: design fabrication and post-fab processing," 2009.
- [76] J. Cao, K. Zhang, R. Yang, and Z. Wang, "Modulation coefficient analysis in optical fiber methane gas sensor based on wavelength modulation spectroscopy," in *Intelligent Control and Automation (WCICA), 2010 8th World Congress on*, 2010, pp. 7021-7025.
- [77] S. D. Wehe, *Development of a tunable diode laser probe for measurements in hypervelocity flows*: Stanford University Editor, 2000.
- [78] V. Nagali, S. Chou, D. Baer, R. Hanson, and J. Segall, "Tunable diode-laser absorption measurements of methane at elevated temperatures," *Applied optics*, vol. 35, pp. 4026-4032, 1996.
- [79] C. Soanes, A. Stevenson, and J. Pearsall, *Concise Oxford English Dictionary*: Oxford University Press, 2004.
- [80] M. E. Webber, "Diode laser measurements of NH<sub>3</sub> and CO<sub>2</sub> for combustion and bioreactor applications," stanford university, 2001.
- [81] A. Farooq, "EXTENDED-NIR LASER DIAGNOSTICS FOR GAS SENSING APPLICATIONS," Stanford University, 2010.
- [82] L. Wang, S. Kassi, A. Liu, S. Hu, and A. Campargue, "The 1.58  $\mu\text{m}$  transparency window of methane (6165–6750 $\text{cm}^{-1}$ ): Empirical line list and temperature dependence between 80 and 296K," *Journal of Quantitative Spectroscopy and Radiative Transfer*, vol. 112, pp. 937-951, 2011.
- [83] M. Gharavi and S. G. Buckley, "Diode laser absorption spectroscopy measurement of line strengths and pressure broadening coefficients of the methane 2 [nu] 3 band at elevated temperatures," *Journal of Molecular Spectroscopy*, vol. 229, pp. 78-88, 2005.
- [84] J. S. Margolis, "Line strength measurements of the 2v<sub>3</sub> band of methane," *Journal of Quantitative Spectroscopy and Radiative Transfer*, vol. 13, pp. 1097-1103, 1973.
- [85] C. Frankenberg, T. Warneke, A. Butz, I. Aben, F. Hase, P. Spietz, *et al.*, "Pressure broadening in the 2v<sub>3</sub> band of methane and its implication on atmospheric retrievals," *Atmos. Chem. Phys.*, vol. 8, pp. 5061-5075, 2008.
- [86] G. B. Rieker, "Wavelength-modulation spectroscopy for measurements of gas temperature and concentration in harsh environments," Stanford University, 2009.

- [87] H. Li, G. B. Rieker, X. Liu, J. B. Jeffries, and R. K. Hanson, "Extension of wavelength-modulation spectroscopy to large modulation depth for diode laser absorption measurements in high-pressure gases," *Applied optics*, vol. 45, pp. 1052-1061, 2006.
- [88] G. Rieker, H. Li, X. Liu, J. Jeffries, R. Hanson, M. Allen, *et al.*, "A diode laser sensor for rapid, sensitive measurements of gas temperature and water vapour concentration at high temperatures and pressures," *Measurement Science and Technology*, vol. 18, p. 1195, 2007.
- [89] J. Hodgkinson and R. P. Tatam, "Optical gas sensing: a review," *Measurement Science and Technology*, vol. 24, p. 012004, 2013.
- [90] C. JP, "Remote System for Detection of Low-Levels of Methane Based on Photonic Crystal Fibres and Wavelength Modulation Spectroscopy," *Journal of Sensors*, vol. 2009, 2009.
- [91] A. J. McGettrick, W. Johnstone, R. Cunningham, and J. D. Black, "Tunable Diode Laser Spectroscopy With Wavelength Modulation: Calibration-Free Measurement of Gas Compositions at Elevated Temperatures and Varying Pressure," *Lightwave Technology, Journal of*, vol. 27, pp. 3150-3161, 2009.
- [92] K. Duffin, A. J. McGettrick, W. Johnstone, G. Stewart, and D. G. Moodie, "Tunable diode-laser spectroscopy with wavelength modulation: a calibration-free approach to the recovery of absolute gas absorption line shapes," *Lightwave Technology, Journal of*, vol. 25, pp. 3114-3125, 2007.
- [93] H. Cai, Y. Wang, J. Geng, and Z. Fang, "Fiber optic methane sensing system based on wavelength modulation spectroscopy by using logarithm method," in *Lasers and Electro-Optics-Pacific Rim, 2007. CLEO/Pacific Rim 2007. Conference on, 2007*, pp. 1-2.
- [94] J. Reid and D. Labrie, "Second-harmonic detection with tunable diode lasers—comparison of experiment and theory," *Applied Physics B: Lasers and Optics*, vol. 26, pp. 203-210, 1981.
- [95] J. Henningsen and H. Simonsen, "Quantitative wavelength-modulation spectroscopy without certified gas mixtures," *Applied Physics B: Lasers and Optics*, vol. 70, pp. 627-633, 2000.
- [96] X. Liu, J. B. Jeffries, and R. K. Hanson, "Measurements of spectral parameters of water-vapour transitions near 1388 and 1345 nm for accurate simulation of high-pressure absorption spectra," *Measurement Science and Technology*, vol. 18, p. 1185, 2007.
- [97] G. Stewart, A. Mencaglia, W. Philp, and W. Jin, "Interferometric signals in fiber optic methane sensors with wavelength modulation of the DFB laser source," *Journal of Lightwave Technology*, vol. 16, p. 43, 1998.
- [98] J. Kauppinen, K. Wilcken, I. Kauppinen, and V. Koskinen, "High sensitivity in gas analysis with photoacoustic detection," *Microchemical journal*, vol. 76, pp. 151-159, 2004.
- [99] S. Schäfer, M. Mashni, J. Sneider, A. Miklós, P. Hess, H. Pitz, *et al.*, "Sensitive detection of methane with a 1.65  $\mu\text{m}$  diode laser by photoacoustic and absorption spectroscopy," *Applied Physics B: Lasers and Optics*, vol. 66, pp. 511-516, 1998.
- [100] J.-P. Besson, S. Schilt, and L. Thévenaz, "Multi-gas sensing based on photoacoustic spectroscopy using tunable laser diodes," *Spectrochimica Acta Part A: Molecular and Biomolecular Spectroscopy*, vol. 60, pp. 3449-3456, 2004.
- [101] H. Waechter, J. Litman, A. H. Cheung, J. A. Barnes, and H.-P. Looock, "Chemical sensing using fiber cavity ring-down spectroscopy," *Sensors*, vol. 10, pp. 1716-1742, 2010.
- [102] M. Lackner, G. Totschnig, F. Winter, M. Ortsiefer, M. Amann, R. Shau, *et al.*, "Demonstration of methane spectroscopy using a vertical-cavity surface-emitting laser at 1.68  $\mu\text{m}$  with up to 5 MHz repetition rate," *Measurement Science and Technology*, vol. 14, p. 101, 2003.
- [103] J. Morville, D. Romanini, A. Kachanov, and M. Chenevier, "Two schemes for trace detection using cavity ringdown spectroscopy," *Applied Physics B: Lasers and Optics*, vol. 78, pp. 465-476, 2004.
- [104] E. Coyne, Y. Chen, and H. Chen, "Trace Gas Detection Using a Broadband Continuous Wave-Cavity Ringdown Spectrometer," in *Applied Industrial Optics: Spectroscopy, Imaging and Metrology*, 2012.

- [105] N. V. Wheeler, M. D. Grogan, P. S. Light, F. Couny, T. A. Birks, and F. Benabid, "Large core acetylene-filled photonic microcells made by tapering the hollow-core fiber," in *Conference on Lasers and Electro-Optics*, 2010.
- [106] C. Wang, W. Jin, J. Ma, Y. Wang, H. L. Ho, and X. Shi, "Suspended core photonic microcells for sensing and device applications," *Optics Letters*, vol. 38, pp. 1881-1883, 2013.
- [107] N. V. Wheeler, M. D. W. Grogan, T. D. Bradley, F. Couny, T. A. Birks, and F. Benabid, "Multipass Hollow Core-PCF Microcell Using a Tapered Micromirror," *Journal of Lightwave Technology*, vol. 29, pp. 1314-1318, 2011.
- [108] (2007, 16/6). *Optical fiber types*. Available: [http://en.wikipedia.org/wiki/File:Optical\\_fiber\\_types.svg](http://en.wikipedia.org/wiki/File:Optical_fiber_types.svg)
- [109] M. M. Karbassian, "Introduction to Optical Communications," 2012.
- [110] Corning, "Corning SMF-28e+ 9/125/250um OS2 Single Mode Fiber," ed, 2012.
- [111] M. L. von Bibra, A. Roberts, and J. Canning, "Fabrication of long-period fiber gratings by use of focused ion-beam irradiation," *Optics letters*, vol. 26, pp. 765-767, 2001.
- [112] M. Yang, D. Wang, Y. Wang, and C. Liao, "Long period fiber grating formed by periodically structured microholes in all-solid photonic bandgap fiber," *Optics express*, vol. 18, pp. 2183-2189, 2010.
- [113] A. J. Fielding, K. Edinger, and C. C. Davis, "Experimental observation of mode evolution in single-mode tapered optical fibers," *Journal of Lightwave Technology*, vol. 17, p. 1649, 1999.
- [114] I. R. Matu, F. J. Arregui, and M. Lo, "Tapered optical-fiber-based pressure sensor," *Optical Engineering*, vol. 39, pp. 2241-2247, 2000.
- [115] A. Leung, P. Shankar, and R. Mutharasan, "Real-time monitoring of bovine serum albumin at femtogram/mL levels on antibody-immobilized tapered fibers," *Sensors and Actuators B: Chemical*, vol. 123, pp. 888-895, 2007.
- [116] A. M. R. Pinto, J. M. Baptista, J. L. Santos, M. Lopez-Amo, and O. Frazão, "Micro-Displacement Sensor Based on a Hollow-Core Photonic Crystal Fiber," *Sensors*, vol. 12, pp. 17497-17503, 2012.
- [117] O. Frazão, J. L. Santos, F. M. Araújo, and L. A. Ferreira, "Optical sensing with photonic crystal fibers," *Laser & Photonics Reviews*, vol. 2, pp. 449-459, 2008.
- [118] T. M. Monro, W. Belardi, K. Furusawa, J. C. Baggett, N. Broderick, and D. J. Richardson, "Sensing with microstructured optical fibres," *Measurement Science and Technology*, vol. 12, p. 854, 2001.
- [119] W. Jin, J. Ju, H. L. Ho, Y. L. Hoo, and A. Zhang, "Photonic crystal fibers, devices, and applications," *Frontiers of Optoelectronics*, vol. 6, pp. 3-24, 2013.
- [120] Y. L. Hoo, W. Jin, C. Shi, H. L. Ho, D. N. Wang, and S. C. Ruan, "Design and modeling of a photonic crystal fiber gas sensor," *Applied optics*, vol. 42, pp. 3509-3515, 2003.
- [121] NKT-Photonics-Group. (2013). *Photonic crystal fibres*. Available: [www.nktphotonics.com/](http://www.nktphotonics.com/)
- [122] H. Tai, H. Tanaka, and T. Yoshino, "Fiber-optic evanescent-wave methane-gas sensor using optical absorption for the 3.392- $\mu\text{m}$  line of a He-Ne laser," *Optics letters*, vol. 12, pp. 437-439, 1987.
- [123] F. Warken, E. Vetsch, D. Meschede, M. Sokolowski, and A. Rauschenbeutel, "Ultra-sensitive surface absorption spectroscopy using sub-wavelength diameter optical fibers," *Arxiv preprint cond-mat/0701264*, 2007.
- [124] A. S. Badru, "Optical Fibre Evanescent Field Techniques for Gas Detection," the University of Heriot-Watt and St Andrews University, 2008.
- [125] A. M. R. Pinto and M. Lopez-Amo, "Photonic Crystal Fibers for Sensing Applications," *Journal of Sensors*, vol. 2012, 2012.
- [126] B. Gupta and C. Singh, "Fiber-optic evanescent field absorption sensor: A theoretical evaluation," *Fiber & Integrated Optics*, vol. 13, pp. 433-443, 1994.

- [127] W. Jin, G. Stewart, M. Wilkinson, B. Culshaw, F. Muhammad, S. Murray, *et al.*, "Compensation for surface contamination in a D-fiber evanescent wave methane sensor," *Lightwave Technology, Journal of*, vol. 13, pp. 1177-1183, 1995.
- [128] L. Xiao, M. D. Grogan, S. G. Leon-Saval, R. Williams, R. England, W. J. Wadsworth, *et al.*, "Tapered fibers embedded in silica aerogel," *Optics letters*, vol. 34, pp. 2724-2726, 2009.
- [129] S. F. Silva, L. Coelho, O. Frazão, J. L. Santos, and F. X. Malcata, "A Review of Palladium-Based Fiber-Optic Sensors for Molecular Hydrogen Detection," *Sensors Journal, IEEE*, vol. 12, pp. 93-102, 2012.
- [130] C. Singh and B. Gupta, "Detection of gases with porous-clad tapered fibers," *Applied optics*, vol. 34, pp. 1019-1023, 1995.
- [131] J. Villatoro, D. Monzón-Hernández, and E. Mejía, "Fabrication and modeling of uniform-waist single-mode tapered optical fiber sensors," *Applied optics*, vol. 42, pp. 2278-2283, 2003.
- [132] J. Villatoro and D. Monzón-Hernández, "Fast detection of hydrogen with nano fiber tapers coated with ultra thin palladium layers," *Optics Express*, vol. 13, pp. 5087-5092, 2005.
- [133] N. Vukovic, N. G. Broderick, M. Petrovich, and G. Brambilla, "Novel method for the fabrication of long optical fiber tapers," *Photonics Technology Letters, IEEE*, vol. 20, pp. 1264-1266, 2008.
- [134] N. P. Group. (2013). *Photonic crystal fibres*. Available: [www.nktphotonics.com/](http://www.nktphotonics.com/)
- [135] R. Yang, Y. S. Yu, C. Chen, Q. D. Chen, and H. B. Sun, "Rapid fabrication of microhole array structured optical fibers," *Optics letters*, vol. 36, pp. 3879-3881, 2011.
- [136] Y. Lai, K. Zhou, L. Zhang, and I. Bennion, "Microchannels in conventional single-mode fibers," *Optics Letters*, vol. 31, pp. 2559-2561, Sep 1 2006.
- [137] J. Huang, A. Alqahtani, J. Viegas, and M. S. Dahlem, "Fabrication of optical fiber gratings through focused ion beam techniques for sensing applications," in *Photonics Global Conference (PGC), 2012*, 2012, pp. 1-4.
- [138] A. R. Mosier, "Soil processes and global change," *Biology and Fertility of Soils*, vol. 27, pp. 221-229, Jul 1998.
- [139] K. Zhou, X. Chen, Y. Lai, K. Sugden, L. Zhang, and I. Bennion, "In-fiber polymer-glass hybrid waveguide Bragg grating," *Optics letters*, vol. 33, pp. 1650-1652, 2008.
- [140] T. Ritari, J. Tuominen, H. Ludvigsen, J. Petersen, T. Sørensen, T. Hansen, *et al.*, "Gas sensing using air-guiding photonic bandgap fibers," *Optics Express*, vol. 12, pp. 4080-4087, 2004.
- [141] C. Charlton, B. Thompson, and B. Mizaikoff, "Hollow waveguide infrared spectroscopy and sensing," *Frontiers in Chemical Sensors*, pp. 133-167, 2005.
- [142] A. Van Brakel, C. Grivas, M. N. Petrovich, and D. J. Richardson, "Micro-channels machined in microstructured optical fibers by femtosecond laser," *Optics Express*, vol. 15, pp. 8731-8736, 2007.
- [143] H. Yu, W. Jin, H. Ho, K. Chan, C. Chan, M. Demokan, *et al.*, "Multiplexing of optical fiber gas sensors with a frequency-modulated continuous-wave technique," *Applied optics*, vol. 40, pp. 1011-1020, 2001.
- [144] W. Jin, H. Xuan, and H. Ho, "Sensing with hollow-core photonic bandgap fibers," *Measurement Science and Technology*, vol. 21, p. 094014, 2010.
- [145] H. Ho, Y. Hoo, W. Jin, J. Ju, D. Wang, R. Windeler, *et al.*, "Optimizing microstructured optical fibers for evanescent wave gas sensing," *Sensors and Actuators B: Chemical*, vol. 122, pp. 289-294, 2007.
- [146] Y. Hoo, W. Jin, H. Ho, J. Ju, and D. Wang, "Gas diffusion measurement using hollow-core photonic bandgap fiber," *Sensors and Actuators B: Chemical*, vol. 105, pp. 183-186, 2005.
- [147] C. M. Cordeiro, E. M. Dos Santos, C. B. Cruz, C. J. de Matos, and D. S. Ferreira, "Lateral access to the holes of photonic crystal fibers-selective filling and sensing applications," *Opt. Express*, vol. 14, pp. 8403-8412, 2006.
- [148] K. Zhou, D. Webb, C. Mou, M. Farries, N. Hayes, and I. Bennion, "Optical fibre cavity ring down measurement of refractive index with a microchannel drilled by femtosecond laser," in *20th International Conference on Optical Fibre Sensors*, 2009, pp. 75035Y-75035Y-4.

- [149] W. Jin, S. Liu, L. Jin, Y. L. Hoo, and H. L. Ho. (2010, In-line, microstructured optical-fiber devices for sensing applications. *SPIE Sensing & Measurement*. Available: <http://spie.org/x40786.xml?pf=true&ArticleID=x40786>
- [150] R. R. Gattass and E. Mazur, "Femtosecond laser micromachining in transparent materials," *Nature Photonics*, vol. 2, pp. 219-225, 2008.
- [151] C. Volkert and A. Minor, "Focused ion beam microscopy and micromachining," *Mrs Bull*, vol. 32, pp. 389-395, 2007.
- [152] Y. Fu and L. Wang, "Focused Ion Beam Machining and Deposition," *Ion Beams in Nanoscience and Technology*, pp. 265-290, 2010.
- [153] A. A. Tseng, "Recent developments in micromilling using focused ion beam technology," *Journal of Micromechanics and Microengineering*, vol. 14, p. R15, 2004.
- [154] C. Martelli, P. Olivero, J. Canning, N. Groothoff, B. Gibson, and S. Huntington, "Micromachining structured optical fibers using focused ion beam milling," *Optics letters*, vol. 32, pp. 1575-1577, 2007.
- [155] X. Li, J. Liang, and T. Ueda, "Applied technique of focused ion beam milling based on microstructure of photonic bandgap fiber," *The International Journal of Advanced Manufacturing Technology*, pp. 1-7, 2013.
- [156] L. S. Rothman, I. Gordon, A. Barbe, D. C. Benner, P. Bernath, M. Birk, *et al.*, "The HITRAN 2008 molecular spectroscopic database," in *Quantitative Spectroscopy and Radiative Transfer* vol. 110, ed, 2009, pp. 533-572.
- [157] A. Gladyshev, M. Belovolov, S. Vasiliev, E. Dianov, O. Medvedkov, A. Nadezhdinskii, *et al.*, "Tunable single-frequency diode laser at wavelength  $\lambda = 1.65 \mu\text{m}$  for methane concentration measurements," *Spectrochimica Acta Part A: Molecular and Biomolecular Spectroscopy*, vol. 60, pp. 3337-3340, 2004.
- [158] S. Li, T. Koscica, Y. Zhang, D. Li, and H. L. Cui, "Optical fiber remote sensing system of methane at 1645nm using wavelength-modulation technique," 2005, pp. 59950Y. 1-59950Y. 9.
- [159] T. Iseki, H. Tai, and K. Kimura, "A portable remote methane sensor using a tunable diode laser," *Measurement Science and Technology*, vol. 11, p. 594, 2000.
- [160] V. Zeninari, B. Parvitte, D. Courtois, V. Kapitanov, and Y. N. Ponomarev, "Methane detection on the sub-ppm level with a near-infrared diode laser photoacoustic sensor," *Infrared physics & technology*, vol. 44, pp. 253-261, 2003.
- [161] T. Iseki, "A portable remote methane detector using an InGaAsP DFB laser," *Environmental Geology*, vol. 46, pp. 1064-1069, 2004.
- [162] K. Ichimura, Y. YAMAUCHI, M. SOMA, T. SAKAI, T. NAKAMURA, Y. IKEDA, *et al.*, "Fiber optic methane gas detection system," *Hitachi Cable Rev (Web)*, 2006.
- [163] M. Cong, S. Guo, and Y. Wang, "A novel methane detection system based on InGaAsP distributed feedback laser," *Optica Applicata*, vol. 41, pp. 639-648, 2011.
- [164] A. M. Cubillas, O. M. Conde, M. Á. Quintela, A. Cobo, and J. M. López-Higuera, "Methane detection using Wavelength Modulation Spectroscopy and a multiline quantitation method," 2005, p. 59482J.
- [165] M. Vasilyev, V. Sacharov, and A. Shelyakin, "A Fiber-Optic Open-Path Methane Sensor," *LASER PHYSICS-LAWRENCE-*, vol. 9, pp. 940-942, 1999.
- [166] H. Wang, Q. Wang, J. Chang, X. Zhang, S. Zhang, and J. Ni, "Measurement technique for methane concentration by wavelength scanning of a distributed-feedback laser," *Laser Physics*, vol. 18, pp. 491-494, 2008.
- [167] J. Shemshad, S. Aminossadati, and M. Kizil, "Methane concentration measurement using tunable diode laser in near infrared spectrum," 2011, pp. 36-43.
- [168] NKT, "Hollow Core Photonic Bandgap Fiber HC-1550-02," ed, 2012.
- [169] J. Shemshad Shadbad, "Development of a sequential multipoint fibre optic methane measurement system for coal mines," Doctor of Philosophy, School of Mechanical and Mining Engineering, The University of Queensland, 2012.

- [170] R. Thapa, K. Knabe, K. Corwin, and B. Washburn, "Arc fusion splicing of hollow-core photonic bandgap fibers for gas-filled fiber cells," *Optics Express*, vol. 14, pp. 9576-9583, 2006.
- [171] K. P. Gaopeng Xin, Ruiqin Fan, Lu Liu, Zhimin Gu, and Xiaofeng Xu, "Refractive index sensor based on a step index multimode polymer optical fiber with a micro-hole created by a miniature numerical control machine," *中国光学快报: 英文版*, pp. 1-3, 2013.
- [172] G. Fu, K. Li, X. Fu, and W. Bi, "Temperature characteristics of fusion splicing Hollow Core Photonic Crystal Fiber by sinusoidal modulation CO<sub>2</sub> laser," *Optics & Laser Technology*, vol. 49, pp. 64-67, 2013.
- [173] S. Farsinezhad and F. E. Seraji, "Analysis of Fresnel Loss at Splice Joint Between Single-Mode Fiber and Photonic Crystal Fiber," *International Journal of Optics and Applications*, vol. 2, pp. 17-21, 2012.
- [174] H. Gong, C. C. Chan, Y. F. Zhang, W. C. Wong, and X. Dong, "Miniature refractometer based on modal interference in a hollow-core photonic crystal fiber with collapsed splicing (Journal Paper)," *Journal of Biomedical Optics*, vol. 16, p. 017004, 2011.
- [175] F. Benabid, "Photonic MircoCells based on hollow-core PCF," 2011.
- [176] F. Couny, F. Benabid, and P. Light, "Reduction of Fresnel back-reflection at splice interface between hollow core PCF and single-mode fiber," *Photonics Technology Letters, IEEE*, vol. 19, pp. 1020-1022, 2007.
- [177] F. Benabid, "Hollow-core photonic bandgap fibre: new light guidance for new science and technology," *Philosophical Transactions of the Royal Society A: Mathematical, Physical and Engineering Sciences*, vol. 364, pp. 3439-3462, 2006.
- [178] L. Xiao, M. Demokan, W. Jin, Y. Wang, and C. L. Zhao, "Fusion splicing photonic crystal fibers and conventional single-mode fibers: microhole collapse effect," *Journal of Lightwave Technology*, vol. 25, pp. 3563-3574, 2007.

## Appendix I: Risk Assessments

The approach to risk assessment in Australia is based on the AS/NZS 4360:2004: standard for risk management (Australian standard) and the AUSTRAC guidance note Risk management and AML/CTF programs. Risk assessment is required for all operations and experiments involved with hazardous material or equipment. Documentation is compulsory and contributes to reduction of risks by regular reviews. An appropriate risk assessment is expected to recognize possible hazards and outline the actions required to eliminate or reduce any risks linked to an operator's health.

The following steps are necessary for carrying out a risk assessment:

1. Identification of the hazardous materials, situations, and tasks.
2. Assessment of the likelihood of hazards.
3. Control and reduction of risks by defining procedures and precautions.

The risk matrix is used to categorise the risk level of each hazard. Based on this table, required actions are taken to deal with risks from higher priority to lower priority. Tables A1 and A2, respectively, show the risk matrix and its table of descriptions that are summarized from the mentioned standards.

**Table A1:** The risk matrix (CRCMining, 2011)

Likelihood	Risk Rating				
A Almost certain	15 (M)	10 (H)	6 (H)	2 (Ex)	1 (Ex)
B Likely	19 (M)	14 (M)	9 (H)	4 (Ex)	3 (Ex)
C Possible	22 (L)	18 (M)	13 (H)	8 (H)	5 (Ex)
D Unlikely	24 (L)	21 (L)	17 (M)	12 (H)	7 (H)
E Rare	25 (L)	23 (L)	20 (M)	16 (M)	11 (H)



**Table A2:** Description of the risk matrix (CRCMining, 2011)

Rating risk level	(E)	Extreme risk - detailed action/plan required
	(H)	High risk - needs senior management attention
	(M)	Moderate risk - specify management responsibility
	(L)	Low risk - manage by routine procedures
Likelihood	A	Almost certain - expected in most circumstances
	B	Likely - will probably occur in most circumstances
	C	Possible - could occur at some time
	D	Unlikely - not expected to occur
	E	Rare - exceptional circumstances only

**Table A3:** Description of hazard effect and consequences (CRCMining, 2011)

Loss Type	Hazard Effect/ Consequence				
	1	2	3	4	5
	Insignificant	Minor	Moderate	Major	Catastrophic
(P) Harm to People	Slight injury or health effects – first aid/ minor medical treatment level	Minor injury or health effects – restricted work or minor lost workday case	Major injury or health effects – major lost workday case/ permanent disability	Permanent total disabilities, single fatality	Multiple fatalities
(E) Environmental Impact	Environmental nuisance	Material environmental harm	Serious environmental harm	Major environmental harm	Extreme environmental harm
(A) Asset Damage & Other Consequential Losses	Slight damage <\$5000. No disruption to operation	Minor damage \$5000 to \$50,000. Brief disruption to operation	Local damage \$50,000 to \$500,000. Partial shutdown	Major damage \$500,000 to \$1M. Partial loss of operation	Extreme damage > \$1M. Substantial or total loss of operation
(R) Impact on Reputation	Slight impact – public awareness may exist but no public concern	Limited impact – some local public concern	Considerable impact – regional public concern	National impact – national public concern	International impact – international public attention

The following table (Table A4) summarises the results of the assessment of the risks associated with all-fibre gas sensing projects. Also the operation introduction of gas chamber and cylinders is attached next to the experimental setup in the laboratory.

Table A4: Result of risk assessment

Activity	Potential Hazard	Existing controls	Existing Risk				Additional Controls (Where control is a procedure, it is to be added to the Job Instruction)	With new Controls				
			Loss Type	Consequence	Likelihood	Risk Score		Risk	Consequence	Likelihood	Risk Score	Risk
Storage	Leaky gas bottle causes gas explosion	10% flammable volume 90% inert gas, Secure to holder via chain, stored in an upright position Gas volume very low compared to size of room,	P, A, R	3	D	17	Medium		3	D	17	Medium
	Gas explosion from gas leak caused by electrical equipment	10% flammable volume 90% inert gas, Secure to holder via chain, stored in an upright position Gas volume very low compared to size of room,	P, A, R	3	D	17	Medium		3	D	17	Medium
Design	Uncontrolled release causes gas explosion	10% flammable volume 90% inert gas, Secure to holder via chain, stored in an upright position Gas volume very low compared to size of room, Multiple valves in place	P, A, R	2	C	18	Medium	Job instruction to detail correct operation of valves for different sequences, Secure gas bottle handle away from the bottle when not in use. Job Instruction to include that the vessel is left in a safe state to ensure a release is vented to the outside.	2	D	21	Low
	Unauthorised use causes gas explosion	Secure access lab with restricted entry	P, A, R	2	D	21	Low		2	D	21	Low
	Eye injury from laser operation	Very low powered laser goggles are available if required	P	2	D	21	Low		2	D	21	Low
	Gas pressure builds up beyond the rated capacity of the vessel causing gas release	Pressure relief on dedicated output:45PSI Vessel tested in workshop	P	2	D	21	Low		2	D	21	Low
	Gas released by vent tube lit by a smoker	Methane is lighter than air, tube mounted over 2m from floor level No smoking policy at UQ	P	2	D	21	Low		2	D	21	Low
	small External explosion cause gas bottle to <u>explode</u>	Check valve installed close to the gas bottle and a check valve installed by the vessel	P	2	D	21	Low		2	D	21	Low
	Gas leaks from faulty valve	Choice of valve made to ensure the gas does not degrade the valve seals (non-oil type)	A	2	E	23	Low		2	E	23	Low
Operation	Uncontrolled release of gas during operation	10% flammable volume 90% inert gas, Secure to holder via chain, stored in an upright position Gas volume very low compared to room size Multiple valves in place	P, A, R	2	C	18	Medium	Job instruction to detail correct operation of valves for different sequences, Secure gas bottle handle away from the bottle when not in use. Job Instruction to include that the vessel is left in a safe state to ensure a release is vented to the outside.	2	D	21	Low
	System damaged by incorrect operation valves		P, A	2	C	18	Medium	Job instruction to detail correct operation of valves for different sequences,	2	D	21	Low
	Pressure in vessel keeps rising passed the relief pressure setting; vessel to leak	Outlet tube twice the diameter of the inlet tube	P, A	2	D	21	Low		2	D	21	Low

The tables below (Tables A5 and A6) are the risk assessment details for using the FEI Quanta 3D SEM/FIB Dual Beam System in the Australian Microscopy & Microanalysis Research Facility at the Queensland University of Technology. Users are to be specially trained and signed off before they are allowed to operate the machine. The SOP for the machine is provided.

**Table A5:** Description of the risk matrix (QUT Risk management plan, 2013)

<b>Likelihood: How likely is it to happen?</b>	<b>Consequences: How severely it hurts someone (if it happens)?</b>				
	<b>Insignificant</b> (no injuries; no damage)	<b>Minor</b> (first aid treatment only; damage / spillage contained at site)	<b>Moderate</b> (medical treatment; damage / spillage contained but with outside help)	<b>Major</b> (extensive injuries; loss of production; significant impact)	<b>Catastrophic</b> (death; toxic release of chemicals; extensive damage)
Almost certain – expected to occur in most circumstances	3 H	3 H	4 A	4 A	4 A
Likely – Occurs frequently in most circumstances	2 M	3 H	3 H	4 A	4 A
Possible – Has been known to occur in certain circumstances	1 L	2 M	3 H	4 A	4 A
Unlikely – could occur at some time but improbable	1 L	1 L	2 M	3 H	4 A
Rare - may occur but only in exceptional circumstances	1 L	1 L	2 M	3 H	3 H
<b>Score and Statement</b>	<b>Action</b>				
<b>4</b> <b>A: Acute</b>	ACT NOW to eliminate or reduce risk – URGENT - do something about the risks immediately. Refer to management if outside your scope to control. Proceed only with the greatest caution.				
<b>3</b> <b>H: High</b>	Implement controls to remove or reduce the risk before proceeding. Refer to management if outside your scope to control. Seek advice, stay focused and remain aware.				
<b>2</b> <b>M: Moderate</b>	Proceed with caution and monitor progress closely. Follow safe work procedures. Stay focused and remain aware.				
<b>1</b> <b>L: Low</b>	Proceed with activity. Record and review if any equipment/ people/ materials/ work processes or procedures change. Remain aware.				

**Table A6: Result of risk assessment (FEI Quanta 3D SEM/FIB Dual Beam System)**

Activity	Existing Risk			New Risk level		Notes / Remarks 1) Who is responsible to implement controls? 2) Latest implementation date? 3) Other relevant detail.
	Hazard, Activity, Task, or Process (Go to Hazard Categories)	Identified Risks	Risk Level Initial	Proposed Control Measures (All control measures must comply with legislative requirements and follow the Control Hierarchy.)	Residual Risk Level	
1	Tripping over hoses or leads behind microscopes	Trip and fall, resulting in hitting the floor or equipment.	2M	Inform all clients that they are not to walk around the back of microscopes (access restricted to specific personnel).	1L	There may be leads and vacuum hoses on the floor behind the scanning electron microscope that are required for its operation and which are unable to be relocated.
2	Powered Equipment	Individual removes panel and contacts exposed high voltage cable or components. Electrocutation	2M	All powered equipment will be used according to the manufacturer's standards. All powered equipment will be "tested and tagged" according to current regulations. All high voltage components are enclosed. Room access is restricted to users trained in correct operation of microscope. Restricted access to the rear of the microscope. Only qualified service personnel are allowed to access restricted zones and remove panels or modify microscope.	1L	SEM contains high voltages capable of serious or fatal shocks to individual users.
3	Ionizing radiation exposure	Individual removes shielding or replaces viewing port with non-lead glass which allows ionizing radiation to escape.	2M	Microscope design features of multiple interlocks that prevent users from exposure to low energy ionizing radiation	1L	Interactions between the electron beam and sample/stage generate ionizing radiation during normal operation. The relatively low kV of standard SEM beams results in low energy x-ray production. Engineering features isolate hazardous ionizing radiation from the operator to minimise exposure to this radiation.
4	Sample & Microscope interactions	Specimen is inserted into microscope and releases components or physically contacts delicate internal microscope parts which subsequently require cleaning/replacement.	2M	Written safe working procedure. Access restricted to trained individuals.	1L	Sample properties must be considered before use in the microscope. Interaction with the beam or vacuum may liberate volatile components/loose particles which may affect/ damage microscope parts.
5	Ergonomic Issues Including: Visual fatigue Prolonged sitting Keyboard and mouse use	Eyestrain Prolonged periods of uninterrupted sitting results in lower back, neck and shoulder pain during and after task completion. A chair without seat height adjustment, backrest angle tilt and backrest height is used; awkward and unsupported posture results. Strain of the shoulder, forearm and wrist.	1L	Bookings are restricted to 3 hours (generally) during prime time.	1L	Persons using the scanning electron microscope spend most of the session time viewing a CRT or LCD screen. Computer operation is usually performed in a seated posture. Prolonged poor posture will increase the risk of musculoskeletal injury particularly to the back and shoulders when sitting for most of the hours worked.
6	Liquid Nitrogen extremely low temperature (-196°C) Climbing ladder/step with liquid nitrogen to refill EDAX	severe burn-like damage to the skin either by contact with the fluid, surfaces cooled by the fluid or evolving gases. (Comparable to boiling water) Skin can freeze and adhere to liquid nitrogen cooled surfaces causing tearing on removal. Thermal stress damage may shatter containers explosive reaction with oxidisable material Splashing and dripping from the bucket as well as the funnel	2H	Do not touch with bare skin Lab coats, covered footwear and chemical splash goggles or full face shield must be worn. Long cryo gloves should be worn Insure the dewar is secured to the trolley Cold Burns treatment - immerse in luke warm water, do not rub. Use only containers or fittings (pipes, tongs etc.) that have been designed specifically for use with cryogenic liquids Do not overfill the bucket Ask users to move away from the microscope	2M	Regular checks should be made to ensure that the venting mechanism on the container is still operable. Regularly check receptical for cracks Leave door to the room open so that the room is properly ventilated.
7	nitrogen gas in enclosed area displaces oxygen	Asphyxiation, dizziness, nausea, vomiting, unconsciousness, confusion, and death.	2H	Contact QUT Health Services ext 82321 emergency 88888 Spillages – ensure area is well ventilated, consider evacuation and dilute with water if can be safely done.	2M	Leave the door open

## Appendix II: Certificates of Merit Awarded During Study

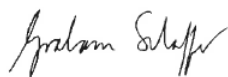
Faculty of Engineering, Architecture and  
Information Technology

*Engineering Postgraduate Research Conference 2013*

The Faculty is pleased to congratulate:

***Mohammad Amanzadeh***

The Professor Klaus Bremhorst Prize for  
Best Presentation Related to Mining Engineering  
and Energy



Professor Graham Schaffer  
Executive Dean  
Faculty of Engineering, Architecture and Information Technology  
June 2013




THE UNIVERSITY OF QUEENSLAND  
AUSTRALIA

*Nature Photonics*  
Best Student Paper Award

Mohammad Amanzadeh

Presented to

*Photonics Global Conference 2012*  
*13-16 December 2012*  
*Singapore*



Rachel Pei Chin Won, PhD  
Chief Editor, *Nature Photonics*

nature  
photonics

nature publishing group 

# 2012 Australian Mining Technology Conference

“Reducing energy intensity through operational efficiency”

8 - 10 October 2012, Perth, Western Australia



## Most Outstanding Student Paper

**Mohammad Amanzadeh**



# Appendix III: Hollow Core Fibre Specification Sheet



Crystal Fibre • *aeroLASE* • Koheras • SuperK

## HC-1550-02

*Hollow Core Photonic Bandgap Fiber*

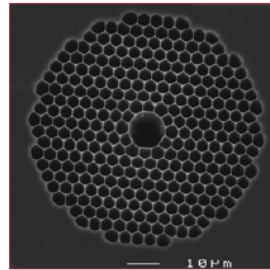
- >95% of optical power located in air
- Quasi-Gaussian fundamental mode
- Can be filled with gas
- Low bend loss down to few mm bend radius
- Fresnel reflection to air at the end faces  $<10^{-4}$
- Up to 75% of fiber cross section composed of solid silica, facilitating fusion splicing to conventional fibers
- Undoped silica for good temperature stability

Photonic Bandgap Fibers guide light in a hollow core, surrounded by a microstructured cladding formed by a periodic arrangement of air holes in silica. Since only a small fraction of the light propagates in glass, the effect of material nonlinearities is significantly reduced and the fibers do not suffer from the same limitations on loss as conventional fibers made from solid material alone.

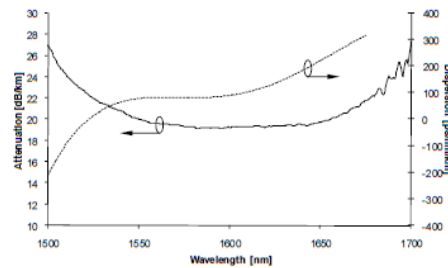
While hollow core PCF holds the promise to become the next generation ultra-low loss transmission fiber, it already finds important applications in power delivery, pulse shaping and compression, sensors and non-linear optics.

Physical properties	
Core diameter <sup>(1)</sup>	10 $\mu\text{m} \pm 1 \mu\text{m}$
Pitch	3.8 $\mu\text{m}$
Air filling fraction in the holey region <sup>(2)</sup>	> 90%
Diameter of holey region	70 $\mu\text{m}$
Cladding diameter	120 $\mu\text{m}$
Coating diameter (single layer acrylate)	220 $\mu\text{m}$

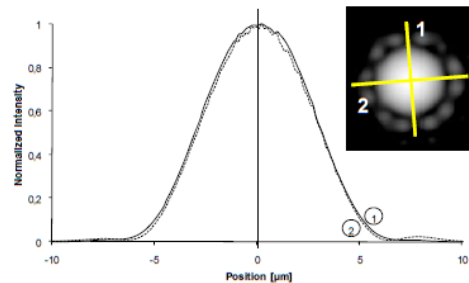
Optical properties	
Center wavelength <sup>(3)</sup>	1550 nm
Attenuation @ 1550 nm	< 0.03 dB/m
Dispersion @ 1550 nm	97 ps/nm/km
Dispersion slope @ 1550 nm	0.5 ps/nm <sup>2</sup> /km
Dispersion slope @ zero disp. wavelength	4.8 ps/nm <sup>2</sup> /km
Width of transmission band <sup>(4)</sup>	> 200 nm
Fraction of light in air <sup>(5)</sup>	> 95%
Mode field diameter <sup>(6)</sup>	7.5 $\mu\text{m}$
Numerical aperture <sup>(7)</sup>	0.2
Effective mode index <sup>(8)</sup>	~0.99
Mode shape overlap with std. SMF <sup>(9)</sup>	> 85%



Typical attenuation and dispersion



Typical near field intensity



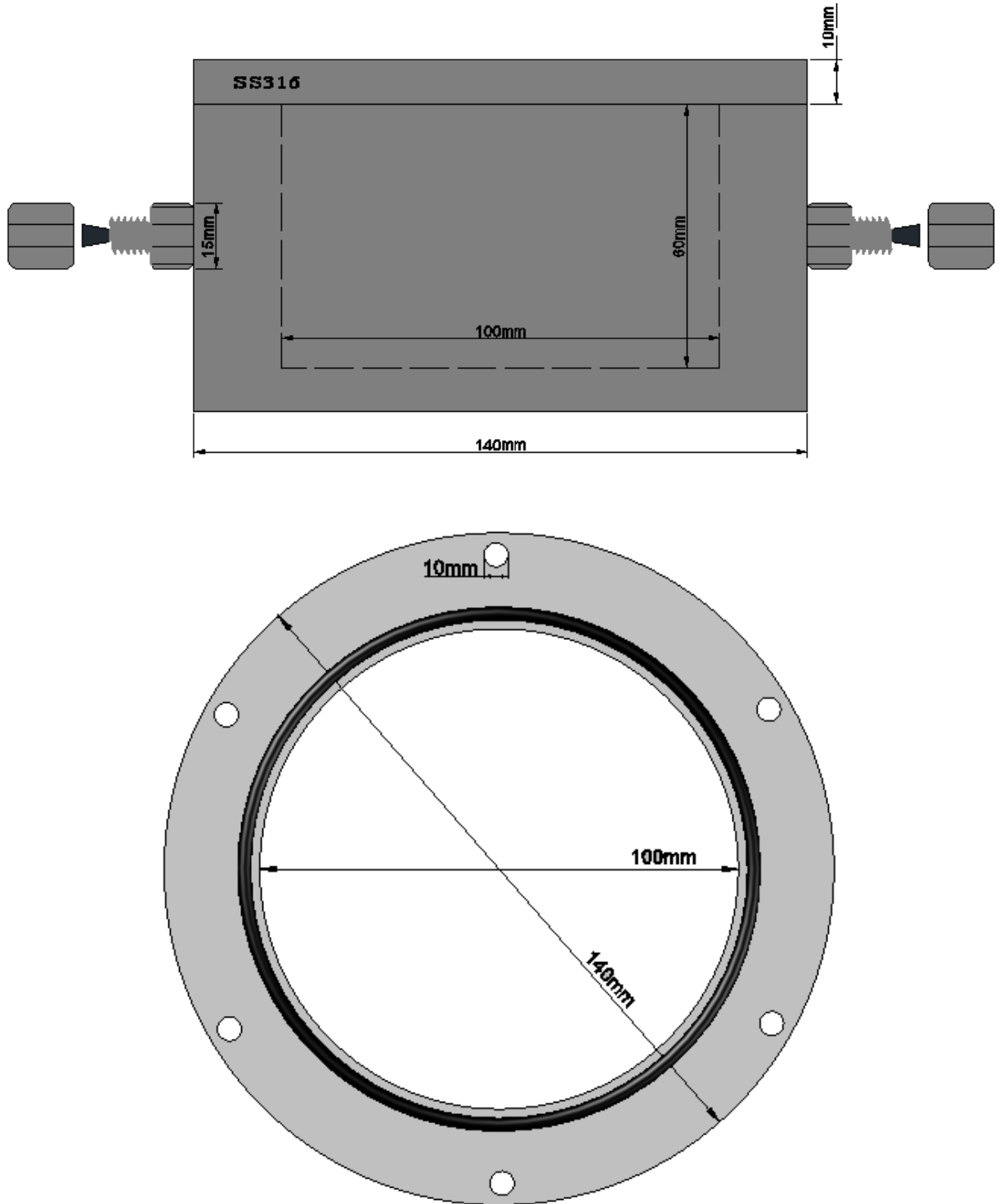
1. Core formed by removing 7 hexagonal unit cells of the cladding
2. Excluding core and outermost ring of holes
3. Other wavelengths available on request
4. Bandwidth over which loss < 0.1 dB/m
5. Derived from numerical model
6. Full 1/e-width of the near field intensity distribution
7. Sine of half angle at which a Gaussian fit to the far field intensity distribution has dropped to 1% of its peak value.
8. Derived from numerical model
9. Mode field diameters matched to provide best overlap

HC-1550-02-100.409



## Appendix IV: Gas Concentration Setup

Gas Chamber AutoCAD drawings:



Gas mixture manufacturer certificate:




## ISO Guide 34 Reference Material Certificate BETA Standard

Customer Details		Order Details	
Account Number:	2103271	Sales Order:	128970257
Name:	CRC Mining	Purchase Order:	
Address:	Cooper Road St Lucia 4072	Primary Use:	Calibration
Certificate Details		Cylinder Details	
Number:	000000131169/1	Cylinder Barcode:	9202395766
Date of Issue:	28.09.2011	Outlet (AS 2473):	TYPE 20
Expiry Date:	28.09.2015	Pressure (15°C):	13700kPa
Cylinder No:	ALQY1.158	Gas Volume:	1.2m <sup>3</sup> (15°C, 101.3kPa)
Minimum storage/usage temperature		Minimum utilisation pressure	
0°C		700kPa	
Material	Description		
<b>288167D</b>	<b>BETA 10% CH4 IN N2</b>		


When re-ordering please call Customer Service on 1800-658-278 and quote the material number.

The property value of the Reference Material is traceable to the SI through the Reference Standards used to analyse this material, which are traceable to the Australian National Standard of Mass.

## Appendix V: Single Mode Fibre Specification Sheet



### Single Mode Fiber: 1260 to 1620 nm




**SMF-28-1000**

---

### Description

Thorlabs' single mode SMF-28e fiber jacketed with 900  $\mu\text{m}$  yellow Hytrel tubing delivers high performance across a broad spectral range in the telecom region, and also features exceptional core / clad concentricity specifications.



---

### Specifications

Geometrical & Mechanical	
Core Diameter	8.2 $\mu\text{m}$
Cladding Diameter	125 $\pm$ 0.7 $\mu\text{m}$
Coating Diameter	245 $\pm$ 5 $\mu\text{m}$
Core-Clad Concentricity	<0.5 $\mu\text{m}$
Coating-Clad Concentricity	<12 $\mu\text{m}$
Fiber Curl	$\geq$ 4.0 m Radius of Curvature
Operating Temperature	-60 to 85 $^{\circ}\text{C}$
Proof Test Level (245 coat)	$\geq$ 100 kpsi (0.7 GN/m <sup>2</sup> )
Fiber Length	1000 meters

Optical	
Numerical Aperture (nominal)	0.14
Attenuation*	0.33 - 0.35 dB/km @ 1310 nm 0.31 - 0.35 dB/km @ 1383 nm** 0.21 - 0.24 dB/km @ 1490 nm 0.19 - 0.20 dB/km @ 1550 nm 0.20 - 0.23 dB/km @ 1625 nm
Operating Wavelength	1260 - 1620 nm
Mode Field Diameter	9.2 $\pm$ 0.4 $\mu\text{m}$ @ 1310 nm 10.4 $\pm$ 0.5 $\mu\text{m}$ @ 1550 nm
Dispersion	$\leq$ 18.0 ps/(nm·km) @ 1550 nm $\leq$ 22.0 ps/(nm·km) @ 1625 nm
Polarization Mode Dispersion, Link Design Value	$\leq$ 0.06 ps//km
Polarization Mode Dispersion, Maximum Individual Fiber	$\leq$ 0.2 ps//km
Bend Loss per Turn on 32 mm Mandrel	$\leq$ 0.03 dB @ 1550 nm

\*Maximum specified attenuation value available within the stated ranges.  
 \*\* Attenuation values at this wavelength represent post-hydrogen aging performance.

US, Canada, & South America: +1-973-300-3000 | Europe: +49 (0) 8131-5956-0 | UK & Ireland: +44 (0)1353-65440  
 France: +33 (0) 970 44 48 44 | Scandinavia: +46-31-733-30-00 | Japan & Asia: +81-3-5979-8889 | China: +86 (0)21-32513486

Specifications Subject  
to Change without Notice

www.thorlabs.com

April 28, 2011  
2291-S01, Rev B

## Single Mode Fiber: 1260 nm to 1625 nm

### Features

- Shipped from Stock, No Minimums
- Acrylate Coating
- SMF-28-J9 has a Ø900 µm Tight Buffer Outer Jacket
- Core-Clad Concentricity
  - <0.5 µm for SMF-28-J9, 1310BHP, and 1550BHP;
  - ≤0.75 µm for SM1250G80 and SM1500G80
- 1310BHP, and 1550BHP Offer Tight Second Mode Cutoff Tolerances
- SM1250G80 and SM1500G80 Offer Enhanced Bend Insensitivity
- Recommended Stripping Tools (See Page 1154):
  - T04S10 (Ø80 µm Cladding)
  - T06S13 (Ø125 µm Cladding, Use T08S40 for SMF-28 Series)

ITEM #	OPERATING WAVELENGTH	MODE FIELD DIAMETER	CLADDING DIAMETER	COATING DIAMETER	CUTOFF WAVELENGTH	SHORT- (LONG-) TERM BEND RADIUS	ATTENUATION MAXIMUM	NA
SMF-28-J9	1260 - 1620 nm	9.2 ± 0.4 µm @ 1310 nm 10.4 ± 0.5 µm @ 1550 nm	125 ± 0.7 µm	245 ± 5 µm	<1260 nm	-	<0.35 dB/km @ 1310 nm <0.20 dB/km @ 1550 nm	0.14
1310BHP	1300 - 1625 nm	8.6 ± 0.5 µm @ 1310 nm 9.7 ± 0.5 µm @ 1550 nm	125 ± 1.0 µm	245 ± 15 µm	1260 ± 30 nm	≥6 mm (≥13 mm)	0.5 dB/km @ 1310 nm 0.5 dB/km @ 1550 nm	0.13
SM1 250G80	1260 - 1650 nm <sup>a</sup>	9.0 µm @ 1310 nm 10.5 µm @ 1550 nm	80 ± 1.0 µm	175 µm ± 5%	1150 - 1250 nm	≥5 mm (≥12 mm or 38 mm for 25 Year Life)	≤2 dB/km @ 1310 nm and 1550 nm	0.12 <sup>b</sup>
1550BHP	1460 - 1620 nm	9.5 ± 0.5 µm @ 1550 nm	125 ± 1.0 µm	245 ± 15 µm	1400 ± 50 nm	≥6 mm (≥13 mm)	0.5 dB/km @ 1550 nm	0.13
SM1 500G80	1550 - 1700 nm <sup>a</sup>	6.4 µm @ 1550 nm	80 ± 1.0 µm	175 µm ± 5%	1350 - 1500 nm	≥5 mm (≥12 mm or 38 mm for 25 Year Life)	≤2 dB/km @ 1550 nm	0.20 <sup>c</sup>

<sup>a</sup> Wavelength range is illustrative and not guaranteed. <sup>b</sup> 0.11 ≤ NA ≤ 0.13 <sup>c</sup> 0.19 ≤ NA ≤ 0.21

### Popular Compatible Connectors (See Page 1142)

CLADDING DIAMETER	FC/PC CONNECTOR	FC/APC CONNECTOR*
80 µm	30080D1	N/A
125 µm	30126D1	30126K1 (Ø900 µm) 30126F1 (Ø3 mm)

\*Furcation Tubing Diameter is given in Parentheses

### Standard Length Pricing (Longer Lengths Available)

ITEM #	\$	£	€	RMB	DESCRIPTION
SMF-28-10	\$ 8.06	£ 5.80	€ 7.01	¥ 64.24	10 m SMF-28-J9 w/ Ø900 µm Jacket
SMF-28-100	\$ 51.51	£ 37.09	€ 44.81	¥ 410.53	100 m SMF-28-J9 w/ Ø900 µm Jacket
SMF-28-1000	\$ 464.60	£ 334.51	€ 404.20	¥ 3,702.86	1000 m SMF-28-J9 w/ Ø900 µm Jacket

ITEM #	PRICE/m*	\$	£	€	RMB
SMF-28-J9	1 to >100 m	\$ 0.70	£ 0.50	€ 0.61	¥ 5.58
	1 to 9 m	\$ 4.80	£ 3.46	€ 4.18	¥ 38.26
	10 to 49 m	\$ 4.08	£ 2.94	€ 3.55	¥ 32.52
1310BHP	50 to 249 m	\$ 3.36	£ 2.42	€ 2.93	¥ 26.78
	1 to 9 m	\$ 4.60	£ 3.32	€ 4.01	¥ 36.67
	10 to 49 m	\$ 3.91	£ 2.82	€ 3.41	¥ 31.17
SM1 250G80	50 to 249 m	\$ 3.22	£ 2.32	€ 2.81	¥ 25.67
	1 to 9 m	\$ 4.80	£ 3.46	€ 4.18	¥ 38.26
	10 to 49 m	\$ 4.08	£ 2.94	€ 3.55	¥ 32.52
1550BHP	50 to 249 m	\$ 3.36	£ 2.42	€ 2.93	¥ 26.78
	1 to 9 m	\$ 4.60	£ 3.32	€ 4.01	¥ 36.67
	10 to 49 m	\$ 3.91	£ 2.82	€ 3.41	¥ 31.17
SM1 500G80	50 to 249 m	\$ 3.22	£ 2.32	€ 2.81	¥ 25.67

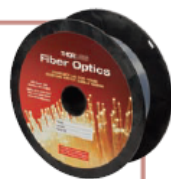
\*Call for Quantities Over 250 m

## Bend-Insensitive Single Mode Fiber: 1260 nm to 1625 nm

ITEM #	OPERATING WAVELENGTH	MODE FIELD DIAMETER	CLADDING DIAMETER	COATING DIAMETER	CUTOFF WAVELENGTH	SHORT- (LONG-) TERM BEND RADIUS	ATTENUATION MAXIMUM	NA
CCC1310-J9	1260 - 1625 nm	8.6 ± 0.4 µm @ 1310 nm 9.8 ± 0.5 µm @ 1550 nm	125.0 ± 0.7 µm	242.0 ± 5.0 µm	≤1260 nm	-	≤0.35 dB/km @ 1310 nm ≤0.21 dB/km @ 1550 nm	0.14

### Features

- Microbend Loss 10.0 mm Radius, 1 Turn
  - 0.50 dB @ 1550 nm
  - 1.5 dB @ 1625 nm
- Dispersion [ps/(nm \* km)]
  - ≤18.0 @ 1550 nm
  - ≤22.0 @ 1625 nm
- Polarization Mode Dispersion (ps/√km)
  - PMD Link Design Value ≤ 0.06
  - Maximum Individual Fiber PMD ≤ 0.1
- Ø900 µm Jacket
- Recommended Stripping Tool: T08S40 (Page 1154)



This bend-insensitive single mode fiber has enhanced macrobend features leading to superior performance when confined to a small radius compared to other single mode fibers. This fiber exceeds the ITU-T recommendation G.657.A1 in addition to remaining fully compliant with ITU-T Recommendation G.652.D. Our bend-insensitive optical fiber is also compatible with the installed base of SMF-28e and SMF-28+ fiber.

### Popular Compatible Connectors (See Page 1142)

CLADDING DIAMETER	FC/PC CONNECTOR	FC/APC CONNECTOR
125 µm	30126D1	30126K1

ITEM #	PRICE/m*	\$	£	€	RMB
CCC1310-J9	1 to 9 m	\$ 3.50	£ 2.52	€ 3.05	¥ 27.90
	10 to 49 m	\$ 2.98	£ 2.15	€ 2.59	¥ 23.72
	50 to 249 m	\$ 2.45	£ 1.77	€ 2.14	¥ 19.53

\*Call for Quantities Over 250 m


Do you need...

SMF-28-J9 and 1550BHP Patch Cables



See pages 1006 - 1009

# Appendix VI: DFB Laser Source Datasheets and Drawings

<b>Production and Quality Control</b>			
<b>Data Sheet DL 100 DFB_01216</b>			
QM-Form: F-192	Date Form: 19.07.10	Version: 01	Page 1 of 4

## 01 General

Order Number:	VB.10.0937	Customer:	University of Queensland
SN DL 100 DFB:	01216	Production Date:	23.09.2010

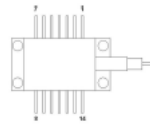
## 02 Customer's Specifications

Wavelength:	1666.0 nm	Output Power:	10.0 mW
Mode Hop Free Tuning:			

## 03 Laser Diode

Article Number:	#LD-1665-0010-DFB-1
Serial Number:	10026406

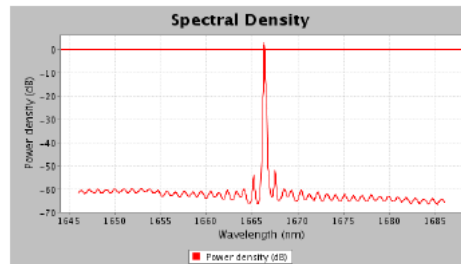
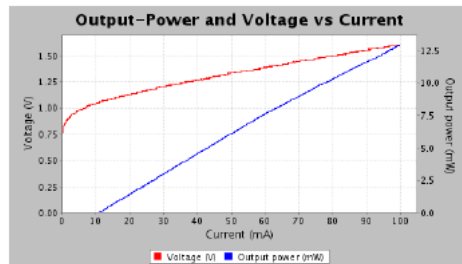
### Laser Diode Pinning :



- Pin1: Thermistor
  - Pin2: Thermistor
  - Pin3: LD Cathode, DC
  - Pin4: PD Anode
  - Pin5: PD Cathode
  - Pin6: TEC+
  - Pin7: TEC (-)
  - Pin8: Case GND
  - Pin9: Case GND
  - Pin10: n.c
  - Pin11: LD Anode, Case
  - Pin12: LD Cathode, AC
  - Pin13: LD Anode, Case
  - Pin14: n.c
- Floating Laser Diode  
(Bottom View)

## 04 Diode Laser Operation

Slope Efficiency:	0.145 W/A	Lasing Threshold:	11 mA
Output Power vs. Current Characteristics		Optical Spectrum	



### Factory Settings:

Set Current:	82.0 mA
Set Temperature:	26.1 °C
Set Power:	10.7 mW **
Set Wavelength:	1666.0 nm

### Maximum Values:

Maximum Current:	100 mA
Maximum Voltage:	1.9 V *
Maximum Power:	12.9 mW **

\*This value is adjusted at the DCC 110 module and includes 0.3 V offset.  
\*\*Laser output power is less behind optical isolator and fiber (see chapters 09 and 10).

# Production and Quality Control Data Sheet *DL 100 DFB\_01216*



QM-Form: F-192

Date Form: 19.07.10

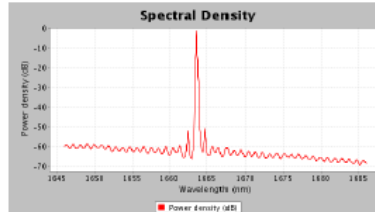
Version: 01

Page 2 of 4

## 05 Coarse Tuning

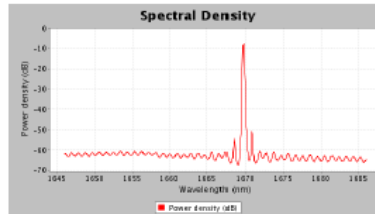
Minimum Wavelength: 1663.19 nm  
 Lasing Threshold: 7 mA  
 Minimum Temperature: 3.0 °C \*  
 Maximum Power: 13.2 mW  
 Maximum Current: 83 mA \*\*

Optical Spectrum



Maximum Wavelength: 1669.25 nm  
 Lasing Threshold: 23 mA  
 Maximum Temperature: 48.0 °C  
 Maximum Power: 8.0 mW  
 Maximum Current: 100 mA

Optical Spectrum



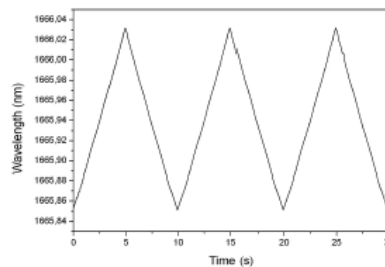
\*If temperature is set to values < 15 °C make sure the laser diode is switched on.

\*\*When cooling down the laser diode reduce the maximum current in order not to exceed the maximum power. (This is to avoid optical failure as the output power increases when the diode is cooled down.)

## 06 Tuning Rates

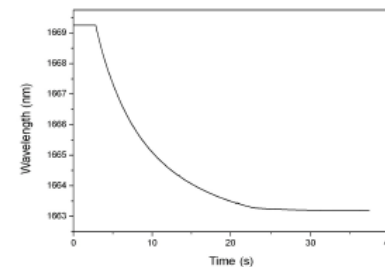
Current Tuning Rate: 1.0 GHz/mA  
 0.0090 nm/mA  
 Tuned Range (pp): 19 GHz  
 Temperature: 25.0 °C  
 Current: 90 mA  
 Mod. Current (pp): 20 mA  
 Mod. Frequency: 0.1 Hz

Current Tuning



Temperature Tuning Rate: 14.5 GHz/K  
 0.13 nm/K  
 Current: 82 mA  
 T<sub>max</sub> / λ<sub>max</sub>: 48.0 °C / 1669.25 nm  
 T<sub>min</sub> / λ<sub>min</sub>: 3.0 °C / 1663.19 nm  
 MHFTR: 655 GHz

Temperature Tuning



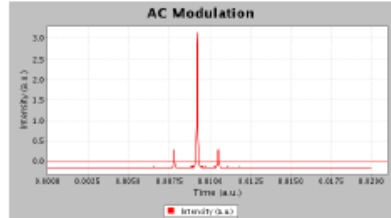
# Production and Quality Control Data Sheet *DL 100 DFB\_01216*



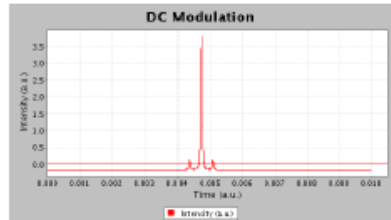
QM-Form: F-192	Date Form: 19.07.10	Version: 01	Page 3 of 4
----------------	---------------------	-------------	-------------

## 07 RF-Modulation

**Via Bias-T:**  
**Modulation Frequency:** 100 MHz  
**RF Power (50 Ω - Source):** -24.0 dBm



**Via FET:**  
**Modulation Frequency:** 30 MHz  
**RF Power (50 Ω - Source):** -23.0 dBm



## 09 Integrated Isolator

**Isolator:** Diode features internal isolator (30 dB)

## 10 Integrated Fiber Coupling

**Fiber Coupler:** Fiber Coupler not installed

**Fiber:** Fiber not installed

# Production and Quality Control Data Sheet DL 100 DFB\_01216



QM-Form: F-192	Date Form: 19.07.10	Version: 01	Page 4 of 4
----------------	---------------------	-------------	-------------

## 11 Laser Optics

Collimator Lens:	no	$\lambda / 2$ waveplate:	no
Anamorphic Prism Pair:	no		

## 12 Serial Numbers Electronics

DC 110/12":	01263
DC 110 Mon:	02930
DCC 110/0,5A:	02600
DTC 110 TO3:	03132

## 13 Jumper Settings Plug-in Modules

DCC 110:	External input via DA# 0 backplane line.
DTC 110:	External input not set.

## 14 Comments

The POS/NEG switch on the DCC module has to be set to NEG.




## 15 Quality Control

Production: \_\_\_\_\_ Date: 23.09.2010  
Schindler Stephanie

Final Check: \_\_\_\_\_ Date: 23.09.2010  
Horst Kreibich





 Lechner, Schlegel D-82166 Geretsching <a href="http://www.toptica.com">www.toptica.com</a> Phone: +4910185 65831-0 Fax: +4910185 65831-200	page: scale: <b>DIN 6-1</b>  	dimensions are in mm	dimensions without tolerance indication:
	title: <b>DL DFB BFY</b>	DIN ISO 2768 mH	The information contained in this drawing is the sole property of TOPTICA Photonics AG. Any reproduction in part or in whole without the written permission of TOPTICA Photonics AG is prohibited.